BRUNEL UNIVERSITY

AGATA ZUZANNA GAŁKA

PHYSICALLY BASED CONSTITUTIVE MODEL FOR DAMAGE IN COMPOSITES UNDER DYNAMIC LOADS

DEPARTAMENT OF MECHANICAL AND AEROSPACE ENGINEERING

PhD Thesis
Academic Year: 2019 – 2020

Supervisors:
Professor Rade Vignjevic
Dr Nenad Djordjevic

December 2020

BRUNEL UNIVERSITY

Department of Mechanical and Aerospace Engineering

PhD Thesis
Academic Year 2019 – 2020

AGATA ZUZANNA GAŁKA

PHYSICALLY BASED CONSTITUTIVE MODEL FOR DAMAGE IN COMPOSITES UNDER DYNAMIC LOADS

Supervisors:
Professor Rade Vignjevic
Dr Nenad Djordjevic

The thesis is submitted in partial fulfilment of the requirements
for the degree of PhD

Abstract

The complex nature of fibre reinforced composites, their non-homogeneity and anisotropy make their modelling a very challenging task. Although the linear – elastic behaviour of composites is well understood, there is still a significant uncertainty regarding prediction of the damage initiation, damage evolution and material failure especially for the tri-axial state of stress or strain. Therefore, simplifying assumptions are inevitable in the constitutive modelling.

This work shows development of a new composite damage constitutive model. The model is based on the concept of spectral decomposition of the stiffness tensor of a material. Spectral decomposition leads to identification of the number of the strain energy modes. They are used to define the material strain energy limits. Present material model is thermodynamically consistent and was developed in the framework of irreversible thermodynamics with internal state variables. The development process was supported by the mesoscale model analysis. The purpose of mesoscale models was twofold. Firstly, it allowed to understand of the mesoscale damage effects on the continuum (macroscopic) material behaviour. Secondly, it provided invaluable insight into the stress and strain state of the composite loaded in different deformation eigenmodes. The mesoscale modelling resulted in postulating a simplifying assumption that principal stiffnesses of the material are invariant for the composite subjected to damage in the applicability range. Moreover, the mesoscale model analysis was used to determine the strain energy limits in the material.

The model is capable of predicting dynamic material response by coupling with equation of state. The form of the equation of state used in this work is applicable to anisotropic materials.

The model was implemented in Dyna3D and was validated against the experimental data showing good agreement of damage extent shock wave propagation.

Keywords

composite, CFRP, damage, failure criteria, dynamic response, constitutive model, thermodynamic framework, equation of state

To the memory of my beloved grandmother Gabriela,
the first engineer in the family and the kindest person I knew
who had a great influence on who I am.

Acknowledgements

First of all, I would like to thank my supervisors – Professor Rade Vignjevic and Dr Nenad Djordjevic for the opportunity of working on this project and for their invaluable support, encouragement and advice. I appreciate their patience and guidance that allowed me to carry out this work. I would also like to thank them for their kindness and understanding. I would also like to acknowledge great help I got from Nenad with model implementation.

Secondly, many thanks to my husband Maciek, who supported me during the most difficult time of my PhD. Without his care, belief and understanding it would be hard to find motivation to finish the PhD. I would also like to thank him for all the discussions about my project that greatly contributed to its final form.

I would also like to thank my parents for the fact that they were always there when I needed them. Thanks for all the words of comfort and encouragement. Also, for advice, support and care. I really appreciate that they always believe in me. I am also grateful to Filip and Helena – my siblings who can always cheer me up.

Many thanks to all my friends – both in UK and in Poland. They greatly contributed to my well-being and healthy work-life balance during the PhD.

Last but not least, I would like to express my gratitude to Catherine Wells, who greatly supported me with admin work and was always there with helping hand, useful advice and kind words.

Table of contents

List of figures

List of tables

List of symbols

$\mathbf{A}$	Arbitrary second order tensor
$A, A_D, \tilde{A}$	Total load carrying area, damage area, effective load carrying area
a	Coefficient in Gruneisen equation of state
$\mathbf{b}$	Left Cauchy green deformation tensor
b	Variable introduced for convenience (no physical meaning)
$\mathrm{C}, C_{ijkl}, \mathrm{C}_0$	Fourth order stiffness tensor in symbolic and index notation, fourth order undamaged material stiffness tensor of fourth order
$\mathbf{C}, C_{\alpha\beta}, \mathbf{C}_0$	Second order (contracted) stiffness tensor in symbolic and index notation, undamaged material stiffness tensor of second order (contracted)
$\mathbf{C}$	Right Cauchy green deformation tensor
C	Mie-Gruneisen EOS constant (speed of sound in the material)
c	Constant
c_v	Heat capacity at constant volume
$\mathrm{D}, \mathbf{D}$	Arbitrary damage tensor, second order damage tensor
$\mathbf{D}, \mathbf{D}^S, \mathbf{D}^H$	Damage tensors defining degradation of material, shift in damage surface and damage surface evolution
d, d^i	Scalar damage variable, modal scalar damage variable
E, E_i	Young's moduli
$\mathbf{E}$	Green Lagrange strain tensor
e_k	Conjugate displacement
e	Euler number
$F_\alpha, F_{\alpha\beta}$	Strength tensors
$\mathbf{F}$	Deformation gradient
F	Parameter characteristic for a material anisotropy in Hill criterion
$\mathbf{f}\ f_i$	Force vector in symbolic and index notation

f	Arbitrary function, damage initiation function
G , G_{ij}	Shear moduli
G	Parameter characteristic for a material anisotropy in Hill criterion
g_i	Degeneracy
H	Damage potential function
H	Parameter characteristic for a material anisotropy in Hill criterion
h , h^i	Damage hardening variable, modal damage hardening variable
h	Planck's constant $(h \approx 6.626*10^{-34} m^2 kgs^{-1})$
I , $\mathbf{I}$	Fourth and second order identity tensors
K , K_ψ	Bulk modulus
k	Boltzmann's constant $(k \approx\sim 1.38*10^{-23} JK^{-1})$
L^i	Lagrange function in i-th mode
L	Parameter characteristic for a material anisotropy in Hill criterion
M	Parameter characteristic for a material anisotropy in Hill criterion
$\mathbf{M}$, M_{ijkl}	Damage effect tensor
m	Number of moles
m^i	Microstructure influence coefficient of proportionality
N	Parameter characteristic for a material anisotropy in Hill criterion
n	Energy level
$\mathbf{n}$ n_j	Surface normal in tensor and index notation
P_i , p_i	Probability functions: absolute probability, relative probability
$\mathbf{P}^i$	Projection operator tensor
p , p_{0K} , p_H	Pressure, pressure at temperature $0\ K$, pressure on the Hugoniot curve (reference pressure)

$\tilde{p}$, p_{EOS}	Alternative pressure, pressure calculated from EOS
R	Ideal gas constant
S , S_{ijkl} , S_0	Fourth order compliance tensor in symbolic and index notation, fourth order undamaged material compliance tensor of fourth order
$\mathbf{S}$, $S_{\alpha\beta}$, $\mathbf{S}_0$	Second order (contracted) compliance symbolic in tensor and index notation, undamaged material compliance tensor of second order (contracted)
S_1, S_2, S_3	Coefficients of Mie-Gruneisen EOS
S_4, S_5, S_6	Material shear strength in YZ (4), ZX (5) and XY (6) planes
$\mathbf{s}_d$, s_{ij} , $\tilde{s}_{ij}$	Deviatoric stress tensor, alternative deviatoric stress tensor
s	Entropy
t	Time
$\mathbf{t}$	Traction force
U_S, U_P	Shock and particle velocities
u	Specific internal energy (internal energy per unit volume)
u , u_{0K} , u_H	Internal energy of the system, internal energy at temperature $0\ K$, internal energy at Hugoniot curve (reference)
$\tilde{u}$, $\tilde{u}_{vib}$	mean vibrational energy of the system, vibrational energy of the system including the ground state
$\hat{u}$, $\overline{u}$, $\overline{u}_i$	Energy of an oscillator, mean energy of oscillator, mean energy of i-th oscillator
V , V_0	Volume, initial volume
$\mathbf{v}^i$	I-th eigenvector
W	Strain energy
$\mathbf{X}$	Arbitrary tensor variable
X , X_t , X_c	Material strength in longitudinal (X) direction: t - tensile, c - compressive
x^i	Magnitude of strain
Δx	Distance between the gauges
$\mathbf{Y}$, $\mathbf{Y}^S$, $\mathbf{Y}^H$	Forces conjugate to damage variable $\mathbf{D}$, $\mathbf{D}^S$, $\mathbf{D}^H$

y_i, y_d^i, y_h^i	Conjugate force, force conjugate to damage variable d^i, force conjugate to hardening variable h^i
Y, Y_t, Y_c	Material strength in transverse (Y) direction: t - tensile, c - compressive
Y_m	Yield limit for matrix material
Z, Z_t, Z_c	Material strength in transverse (Y) direction: t - tensile, c - compressive
z^i	Coefficient accounting for microstructure influence on the principal strains
α	Material coefficient related to the first eigenvector
α_θ	Longitudinal thermal expansion coefficient
β	Material coefficient related to the third eigenvector
γ, γ_j	Gruneisen constant
δ_{ij}	Kronecker delta
$\delta_x, \delta_y, \delta_z$	Applied displacements
$\boldsymbol{\varepsilon}, \varepsilon_{ij}, \varepsilon_\alpha$	Euler-Almansi strain tensor in tensor, index and contracted index notation
$\boldsymbol{\varepsilon}^i, \varepsilon^i$	Modal strain vector, modal strain magnitude
ε_v	Volumetric strain
θ	temperature
κ	configuration
κ, κ^i	Damage hardening energy, modal damage hardening energy
$\dot{\Lambda}$	Lagrange multiplier
λ^i	I-th eigenvalue
μ	Compression parameter
ν, ν_{ij}	Poisson's ratio
ξ	Parameter defining the non-linear elastic behaviour in Chang and Chang failure criteria

ρ, ρ_0	Density, initial density
$\boldsymbol{\sigma}, \sigma_{ij}, \sigma_\alpha$	Cauchy stress, tensor, vector
$\boldsymbol{\sigma}^i, \sigma^i$	Modal stress vector, modal stress magnitude
$\sigma, \tilde{\sigma}$	Nominal stress, effective stress
Υ, Υ^i	Energy dissipation, energy dissipation in a mode
υ, υ_j	Vibration frequency, vibration frequency in one particle in one direction, average vibration frequency
Φ, Φ_1, Φ_2	Damage potential, loading potential, hardening potential
ϕ	Potential energy of the atoms (no vibration)
χ	motion
Ψ, Ψ^i	Helmholtz free energy, Helmholtz free energy in a mode
ψ_{ij}, ψ_α	Pressure tensor, pressure vector (contracted)
ω_0, ω_0^i	Damage energy threshold, modal damage energy threshold

Indices:

$(\ )_{ijkl}$	Components of a tensor
$(\ )^i$	Variable in i-th eigenmode
$(\ )_0$	Initial value of variable (corresponding to undamaged material)
$(\ )_{cr}$	Critical value of variable (corresponding to damage initiation)
${}^n(\ )$	Variables at time instance: $t = n$
${}^*(\ )$	Trial variable value

List of acronyms

2D, 3D, 6D	Two dimensional, three dimensional, six dimensional
CDM	Continuum Damage Mechanics
CFRP	Carbon fibre reinforced polymer
CT	Computed Tomography
EOS	Equation of state
FEA	Finite element analysis
HODO	Homogeneous of Degree One
NDT	Non-Destructive Testing
RUC	Repetitive unit cell
RVE	Representative volume element
WWFE	World Wide Failure Exercise

1 Introduction

1.1 Motivation

Rapid expansion of composite materials, especially in aerospace and automotive industries necessitates development of composite modelling tools to be able to assess the structure strength. Unfortunately, due to complex nature of composites, prediction of strength of the material and the failure characteristics is not a straightforward task. Intentional material anisotropy and existence of different constituents (and interfaces between them) significantly limit the application of tools and criteria developed for homogeneous materials. Development of the composite material models would allow for more reliable finite element analysis (FEA) which can replace the mechanical tests and decrease costs of composite structures. Moreover, better understanding of the composite failure may increase the design safety.

A number of constitutive composite models were developed recently, however they are rarely trusted by the practitioners (Soden, Kaddour and Hinton, 2004). Soden, Kaddour and Hinton, driven by lack of a reliable comparison between models and reality started the World-Wide Failure Exercise (WWFE) (Soden, Kaddour and Hinton, 2004) whose objective was to assess the capabilities of the existing composite models to predict the failure. The models were benchmarked against experimental data. One of the aims of the WWFE was to mend the knowledge gap between theoreticians and practitioners studying composite failure. Citing Soden, Kaddour and Hinton (2004) composite models were often developed because of 'academic curiosity'. So far, three editions of WWFE were finished. The first two editions of WWFE concentrated on 2D (two dimensional) and 3D (three dimensional) load cases. They identified a few more accurate theories; however, the general conclusion was that none of the theories developed to that date were capable of predicting the strength of material for all examined load cases. The third Failure Exercise focused mainly on progressive damage of composites (Kaddour, Hinton, Li, *et al.*, 2013; Kaddour, Hinton, Smith, *et al.*, 2013). The overall conclusion from WWFE-III was that the models are immature (Kaddour *et al.*, 2014).

Although WWFE covered a wide range of loading conditions it did not go beyond quasi-static loading. In aerospace, defence and automotive industries, identified as leading sectors using composites, material response to high strain rates (e.g. impact) is relevant and, although difficult to model and test experimentally, should not be neglected. As high velocity

phenomena result in shockwaves formation, quasistatic models cannot be used. Thus, determination of the state of the material behind a shock wave necessitates including an equation of state (EOS) in the model definition. Lack of equation of state in currently existing composite models is a significant limitation in their applicability.

1.2 Aims and objectives

The main aim of this work is to develop a composite material constitutive model capable of accurate prediction of material behaviour under dynamic loads. Such a model needs to account for major damage mechanisms evolving in the composite during impact. Furthermore, it should be thermodynamically consistent and allow coupling with EOS. The constitutive model described in this work assumes continuum level approach and hyperelastic material formulation. The model uses internal state variables to define its damage state. It is applicable to unidirectional composites with possibility of generalisation to other composite types.

The objectives were identified as:

- analysis of the material damage behaviour using the mesoscale models' simulations
- analysis of different deformation modes using the mesoscale models
- theoretical development of the composite constitutive model
- implementation of the model in Dyna3D
- validation of the model

1.3 Thesis outline

The thesis consists of seven chapters. The first three chapters present the background and the motivation for the research and developed composite model. Chapter 1 gives the motivation, aims and objectives of the project. Chapter 2 is dedicated to composites, their mechanics, damage behaviour and modelling approaches. The framework for the model is presented in Chapter 3. It includes continuum mechanics, thermodynamics, damage mechanics and EOS theory used in this work.

Chapters 4, 5 and 6 present the methods and research work completed in this project. The fourth chapter focuses on mesoscale modelling of damage. It was aimed at assessing the continuum scale damage effects. The use of the mesoscale models in investigation of the

constituents' states under different deformation modes is described in Chapter 5. The development of the material constitutive model is presented in Chapter 6. Additionally, Chapter 6 covers the model implementation and validation followed by a proposal of further development.

Chapter 7 provides the thesis summary including the comments on the developed model capabilities and limitations. Furthermore, it proposes possible future improvements of the model. In addition to the seven main chapters there are five appendices that provide supplementary information, derivations and detailed models characteristics.

An outline of the thesis structure is graphically presented in Figure 1.3.1. Spectral decomposition was original core idea for research, the investigations presented here follow from it.

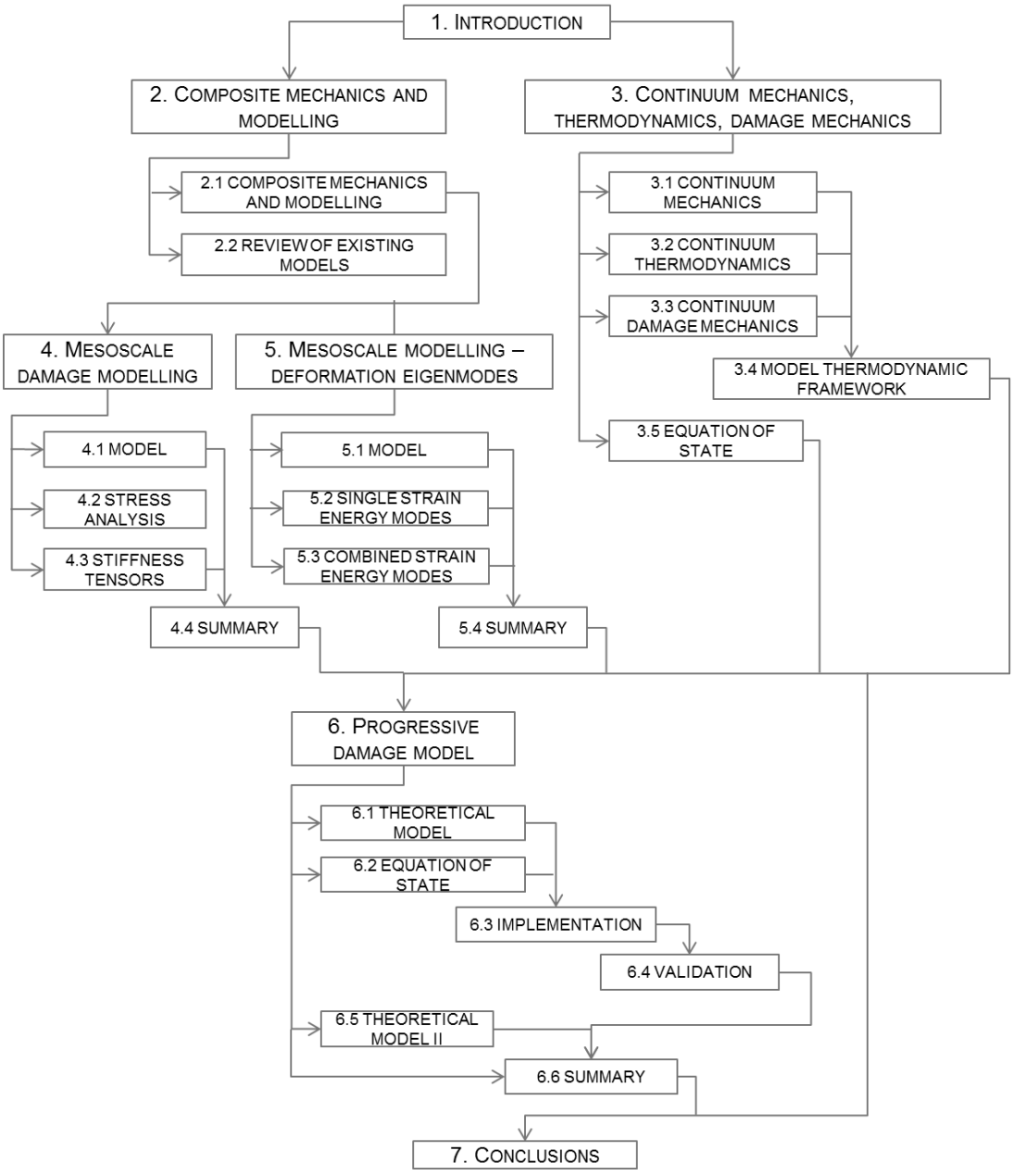

Figure 1.3.1 Thesis structure

2 Composite mechanics and modelling

Modelling of a material is the development of the set of equations that define its behaviour. The **constitutive equations** interrelate the material variables. Development of a good material model requires sound understanding of the material mechanics. This chapter provides general information about composites covering their mechanics, damage and commenting on existing composite failure criteria and constitutive models. What is also important, this chapter introduces the notation used in the model development.

The first part of the chapter (Section 2.1) gives short introduction to composites and damage mechanics. This helps to identify key features of the composite models and recognise capabilities and limitations of existing formulations. The spectral decomposition of the material stiffness tensor, which is fundamental in this work, is given in Section 2.1.4. The review of existing composite failure criteria and damage models is given in the second part of the chapter (Section 2.2).

2.1 Carbon fibre reinforced composites

Composites are materials composed of two or more constituents, which together give better (or more suitable) properties than each of the constituents separately. Among composites there are those existing naturally (e.g. bones) and human made (e.g. concrete). Composites can be manufactured to exhibit desired sets of material properties impossible to obtain with conventional materials. An example of such a composite is a carbon fibre reinforced polymer (CFRP). The high strength fibres assure required strength and stiffness while the matrix has its role in joining and protecting fibres. As a result, a composite formed of heavy fibres and light matrix has superior strength to specific weight ratio over other structural materials. These properties make CFRP a perfect choice for lightweight structures such as aircrafts.

In fibre reinforced composites the fibres' character plays significant role in the behaviour of material. The short fibres randomly arranged in matrix give almost isotropic macroscopic material behaviour. If long fibres are used, their alignment determine the macroscopic properties, which are usually strongly anisotropic. Long fibres can be either aligned in one direction (Figure 2.1.1 -a) or can form a weave (Figure 2.1.1 -b, -c). Unidirectional material has one high strength and stiffness direction (fibre direction) and is isotropic in other directions. Therefore, it can be described as the transversely isotropic material. Woven

composites have orthotropic or higher symmetries (e.g. tetragonal) depending on the weave pattern. The symmetries and resulting stiffness tensors for these materials are presented in Section 2.1.2. This work is mainly focused on unidirectional composites.

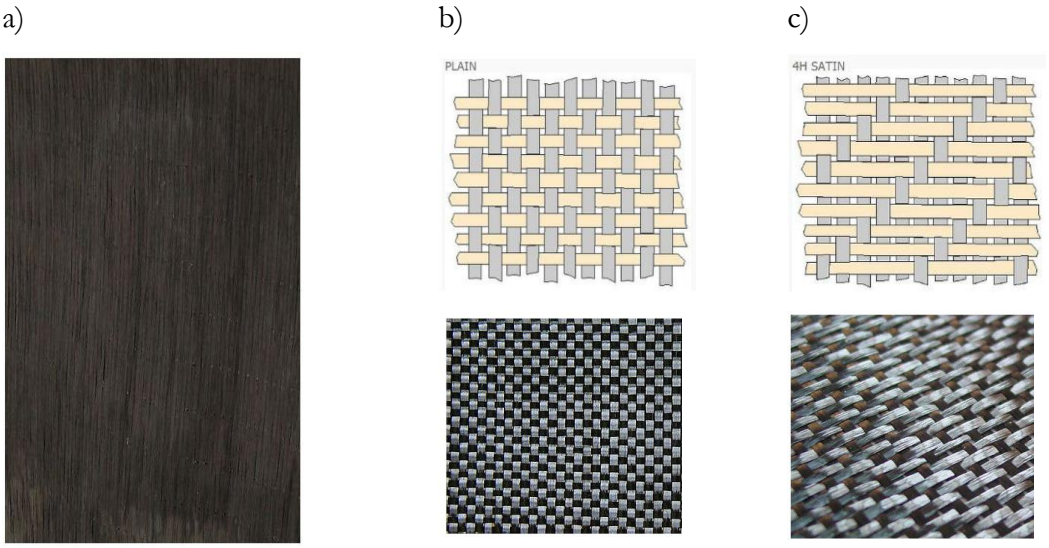

Figure 2.1.1 Fibre allignment: a) unidirectional, b) plain weave, c) 4H weave (*Carbon Fiber - All Patterns Explained*, 2015)

CFRPs demonstrate anisotropy both in strength and stiffness with the highest values for the fibre direction. The variation of the strength of the material with respect to its direction is clearly explained in Figure 2.1.2.

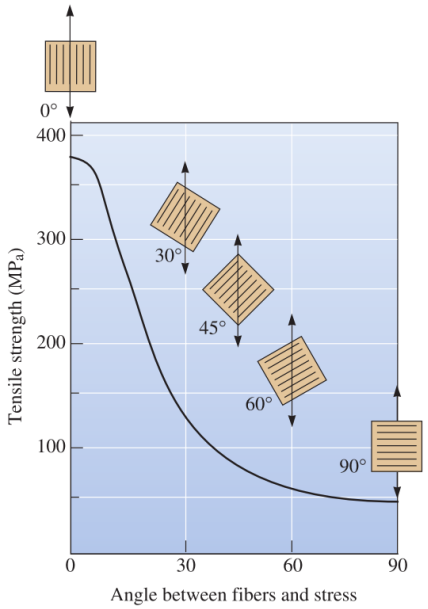

Figure 2.1.2 Variation of composite strength depending on the loading direction for unidirectional composite (Askeland, Fulay and Wright, 2010, p.662)

2.1.1 Linear elastic behaviour of CFRP composites

Because of anisotropy, the stress-strain relation of composites cannot be fully described by single Hooke's Law curve. For an arbitrary, anisotropic material in which no planes of symmetry can be identified the relation is defined by Equation 2.1.1, which is referred to as a generalised Hooke's law:

$$\boldsymbol{\sigma} = \mathbf{C} : \boldsymbol{\varepsilon}, \tag{2.1.1}$$

where $\boldsymbol{\sigma}$ and $\boldsymbol{\varepsilon}$ are second order **stress and strain tensors** respectively. A tensor that describes the relation between stress and strain is the fourth order stiffness tensor $\mathbf{C}$. The generalised Hooke's law, stated using second and fourth order tensors has the form:

$$\begin{bmatrix} \sigma_{11} & \sigma_{12} & \sigma_{13} \\ \sigma_{21} & \sigma_{22} & \sigma_{23} \\ \sigma_{31} & \sigma_{32} & \sigma_{33} \end{bmatrix} = \begin{bmatrix} C_{1111} & C_{1122} & C_{1133} & C_{1123} & C_{1131} & C_{1112} & C_{1132} & C_{1113} & C_{1121} \\ C_{2211} & C_{2222} & C_{2233} & C_{2223} & C_{2231} & C_{2212} & C_{2232} & C_{2213} & C_{2221} \\ C_{3311} & C_{3322} & C_{3333} & C_{3323} & C_{3331} & C_{3312} & C_{3332} & C_{3313} & C_{3321} \\ C_{2311} & C_{2322} & C_{2333} & C_{2323} & C_{2331} & C_{2312} & C_{2332} & C_{2313} & C_{2321} \\ C_{3111} & C_{3122} & C_{3133} & C_{3123} & C_{3131} & C_{3112} & C_{3132} & C_{3113} & C_{3121} \\ C_{1211} & C_{1222} & C_{1233} & C_{1223} & C_{1231} & C_{1212} & C_{1232} & C_{1213} & C_{1221} \\ C_{3211} & C_{3222} & C_{3233} & C_{3223} & C_{3231} & C_{3212} & C_{3232} & C_{3213} & C_{3221} \\ C_{1311} & C_{1322} & C_{1333} & C_{1323} & C_{1331} & C_{1312} & C_{1332} & C_{1313} & C_{1321} \\ C_{2111} & C_{2122} & C_{2133} & C_{2123} & C_{2131} & C_{2112} & C_{2132} & C_{2113} & C_{2121} \end{bmatrix} : \begin{bmatrix} \varepsilon_{11} & \varepsilon_{12} & \varepsilon_{13} \\ \varepsilon_{21} & \varepsilon_{22} & \varepsilon_{23} \\ \varepsilon_{31} & \varepsilon_{32} & \varepsilon_{33} \end{bmatrix} \tag{2.1.2}$$

Equation 2.1.2 can be simplified as a consequence of the symmetries of stress tensor and strain tensor (Cowin and Mehrabadi, 1992). These are postulated by the equivalence of the stiffness tensor components as shown below:

$$C_{ijkm} = C_{jikm} = C_{ijmk}. \tag{2.1.3}$$

This results in reducing the number of independent stiffness tensor variables from 81 to 36. The symmetries allow for rewriting the stress – strain relation in commonly used Voigt notation, which assigns the indices as presented below:

$$\begin{array}{llll} \sigma_{11} = \sigma_1 & \sigma_{12} = \sigma_{21} = \sigma_4 & \varepsilon_{11} = \varepsilon_1 & \varepsilon_{12} = \varepsilon_{21} = \varepsilon_4 = \frac{1}{2}\gamma_4 \\ \sigma_{22} = \sigma_2 & \sigma_{13} = \sigma_{21} = \sigma_5 & \varepsilon_{22} = \varepsilon_2 & \varepsilon_{13} = \varepsilon_{21} = \varepsilon_5 = \frac{1}{2}\gamma_5 \\ \sigma_{33} = \sigma_3 & \sigma_{23} = \sigma_{32} = \sigma_6 & \varepsilon_{33} = \varepsilon_3 & \varepsilon_{23} = \varepsilon_{32} = \varepsilon_6 = \frac{1}{2}\gamma_6 \end{array} \tag{2.1.4}$$

$$\begin{bmatrix}\sigma_1\\ \sigma_2\\ \sigma_3\\ \sigma_4\\ \sigma_5\\ \sigma_6\end{bmatrix}=\begin{bmatrix}C_{11} & C_{12} & C_{13} & C_{14} & C_{15} & C_{16}\\ C_{21} & C_{22} & C_{23} & C_{24} & C_{25} & C_{26}\\ C_{31} & C_{32} & C_{33} & C_{34} & C_{35} & C_{36}\\ C_{41} & C_{42} & C_{43} & C_{44} & C_{45} & C_{46}\\ C_{51} & C_{52} & C_{53} & C_{54} & C_{55} & C_{56}\\ C_{16} & C_{62} & C_{63} & C_{64} & C_{65} & C_{66}\end{bmatrix}.\begin{bmatrix}\varepsilon_1\\ \varepsilon_2\\ \varepsilon_3\\ \gamma_4\\ \gamma_5\\ \gamma_6\end{bmatrix} \quad \textbf{2.1.5}$$

Note that in Voigt notation the engineering shear strains are used instead of true strains. The additional symmetry in the stiffness tensor is the major tensor symmetry with respect to the main diagonal. This symmetry is the consequence of the thermodynamic requirement that no work can be generated by the elastic deformation of the material in the closed loading cycle (Cowin and Mehrabadi, 1985). It is expressed as:

$$C_{ijkm} = C_{kmij}\,. \quad \textbf{2.1.6}$$

Accounting for the major symmetry of the stiffness tensor it can be rewritten as:

$$\mathbf{C}=\begin{bmatrix}C_{11} & C_{12} & C_{13} & C_{14} & C_{15} & C_{16}\\ C_{12} & C_{22} & C_{23} & C_{24} & C_{25} & C_{26}\\ C_{13} & C_{23} & C_{33} & C_{34} & C_{35} & C_{36}\\ C_{14} & C_{24} & C_{34} & C_{44} & C_{45} & C_{46}\\ C_{15} & C_{25} & C_{35} & C_{45} & C_{55} & C_{56}\\ C_{16} & C_{26} & C_{36} & C_{46} & C_{56} & C_{66}\end{bmatrix} \quad \textbf{2.1.7}$$

Voigt notation does not map the stress and strain tensors from 3D space to 6D space (Cowin and Mehrabadi, 1992; Helbig, 1994). Despite the use of six indices, it does not have a tensorial character (Mehrabadi and Cowin, 1990). In Voigt notation the contraction of the stress and stiffness vectors with themselves does not give the same result as the contraction of the second order stress and strain tensors in full notation (using summation over repeated indices):

$$\sigma_\alpha\sigma_\alpha \neq \sigma_{ij}\sigma_{ij}\,,$$
$$\varepsilon_\alpha\varepsilon_\alpha \neq \varepsilon_{ij}\varepsilon_{ij}\,. \quad \textbf{2.1.8}$$

So, the tensor norms are not preserved, which is a serious limitation. An alternative tensor contraction representation is presented in Equation 2.1.9.

$$\begin{bmatrix} \sigma_1 \\ \sigma_2 \\ \sigma_3 \\ \sqrt{2}\sigma_4 \\ \sqrt{2}\sigma_5 \\ \sqrt{2}\sigma_6 \end{bmatrix} = \begin{bmatrix} C_{11} & C_{12} & C_{13} & \sqrt{2}C_{14} & \sqrt{2}C_{15} & \sqrt{2}C_{16} \\ C_{12} & C_{22} & C_{23} & \sqrt{2}C_{24} & \sqrt{2}C_{25} & \sqrt{2}C_{26} \\ C_{13} & C_{23} & C_{33} & \sqrt{2}C_{34} & \sqrt{2}C_{35} & \sqrt{2}C_{36} \\ \sqrt{2}C_{14} & \sqrt{2}C_{24} & \sqrt{2}C_{34} & 2C_{44} & 2C_{45} & 2C_{46} \\ \sqrt{2}C_{15} & \sqrt{2}C_{25} & \sqrt{2}C_{35} & 2C_{45} & 2C_{55} & 2C_{56} \\ \sqrt{2}C_{16} & \sqrt{2}C_{26} & \sqrt{2}C_{36} & 2C_{46} & 2C_{56} & 2C_{66} \end{bmatrix} . \begin{bmatrix} \varepsilon_1 \\ \varepsilon_2 \\ \varepsilon_3 \\ \sqrt{2}\varepsilon_4 \\ \sqrt{2}\varepsilon_5 \\ \sqrt{2}\varepsilon_6 \end{bmatrix} \quad \text{2.1.9}$$

In this tensor, the norms are preserved:

$$\sigma_\alpha \sigma_\alpha = \sigma_{ij}\sigma_{ij}, \quad \text{2.1.10}$$

$$\varepsilon_\alpha \varepsilon_\alpha = \varepsilon_{ij}\varepsilon_{ij} .$$

It is used throughout this work as the mapping of the tensors from 3D space to 6D space.

2.1.2 Material symmetries and stiffness tensors

The equations given in Section 2.1.1 represent linear elastic behaviour of any anisotropic material. If symmetry planes can be found in the material, the stiffness tensor can be simplified. There are 34 symmetry classes recognised by geologists (Cowin and Mehrabadi, 1985) such as isotropy, tetragonal or triclinic etc. However, only few of them are important for fibre reinforced composites. The symmetry classes that are relevant for this work are described in the following paragraphs.

Orthotropy is the symmetry class in which three perpendicular symmetry planes can be identified (note, that if there are at least two orthogonal planes of symmetry, the third one must exist) (Cowin and Mehrabadi, 1985). Example of an orthotropic material is a woven composite with different fibre properties of warp and weft fibres. Following the contracted tensor notation, the stiffness tensor of the orthotropic material can be represented as:

$$C_{\alpha\varepsilon} = \begin{bmatrix} C_{11} & C_{12} & C_{13} & 0 & 0 & 0 \\ C_{12} & C_{22} & C_{23} & 0 & 0 & 0 \\ C_{13} & C_{23} & C_{33} & 0 & 0 & 0 \\ 0 & 0 & 0 & 2C_{44} & 0 & 0 \\ 0 & 0 & 0 & 0 & 2C_{55} & 0 \\ 0 & 0 & 0 & 0 & 0 & 2C_{66} \end{bmatrix} \quad \text{2.1.11}$$

In orthotropic materials there is no coupling between shear and normal stresses and strains. Furthermore, the shear stresses are also decoupled.

The materials in which another symmetry plane exists are called **tetragonal** materials. Excellent example of this kind of symmetry is a woven CFRP with the same properties in two fibre directions. For such materials the following relations hold:

$$C_{22} = C_{33}, \qquad C_{55} = C_{66}, \qquad C_{12} = C_{13}. \tag{2.1.12}$$

Therefore, the stiffness tensor simplifies to:

$$C_{\alpha\varepsilon} = \begin{bmatrix} C_{11} & C_{12} & C_{12} & 0 & 0 & 0 \\ C_{12} & C_{22} & C_{23} & 0 & 0 & 0 \\ C_{12} & C_{23} & C_{22} & 0 & 0 & 0 \\ 0 & 0 & 0 & 2C_{44} & 0 & 0 \\ 0 & 0 & 0 & 0 & 2C_{66} & 0 \\ 0 & 0 & 0 & 0 & 0 & 2C_{66} \end{bmatrix} \tag{2.1.13}$$

Another class of symmetry is **transverse isotropy.** Transversely isotropic materials have one plane of isotropy (exhibit the same properties in one plane regardless the direction). An example of such is a unidirectional composite. For transversely isotropic materials, the symmetry imposes an additional constraint:

$$2C_{44} = C_{22} - C_{23}. \tag{2.1.14}$$

So, the stiffness tensor becomes:

$$C_{\alpha\varepsilon} = \begin{bmatrix} C_{11} & C_{12} & C_{12} & 0 & 0 & 0 \\ C_{12} & C_{22} & C_{23} & 0 & 0 & 0 \\ C_{12} & C_{23} & C_{22} & 0 & 0 & 0 \\ 0 & 0 & 0 & C_{22} - C_{23} & 0 & 0 \\ 0 & 0 & 0 & 0 & 2C_{66} & 0 \\ 0 & 0 & 0 & 0 & 0 & 2C_{66} \end{bmatrix} \tag{2.1.15}$$

The last symmetry class described here is **isotropy**. For isotropic materials the stiffness tensor is given by:

$$C_{\alpha\varepsilon} = \begin{bmatrix} C_{11} & C_{12} & C_{12} & 0 & 0 & 0 \\ C_{12} & C_{11} & C_{12} & 0 & 0 & 0 \\ C_{12} & C_{12} & C_{11} & 0 & 0 & 0 \\ 0 & 0 & 0 & C_{11}-C_{12} & 0 & 0 \\ 0 & 0 & 0 & 0 & C_{11}-C_{12} & 0 \\ 0 & 0 & 0 & 0 & 0 & C_{11}-C_{12} \end{bmatrix} \quad \textbf{2.1.16}$$

There are only two independent stiffness tensor members in isotropic materials. The graphical representation of the described symmetry classes is presented in Figure 2.1.3.

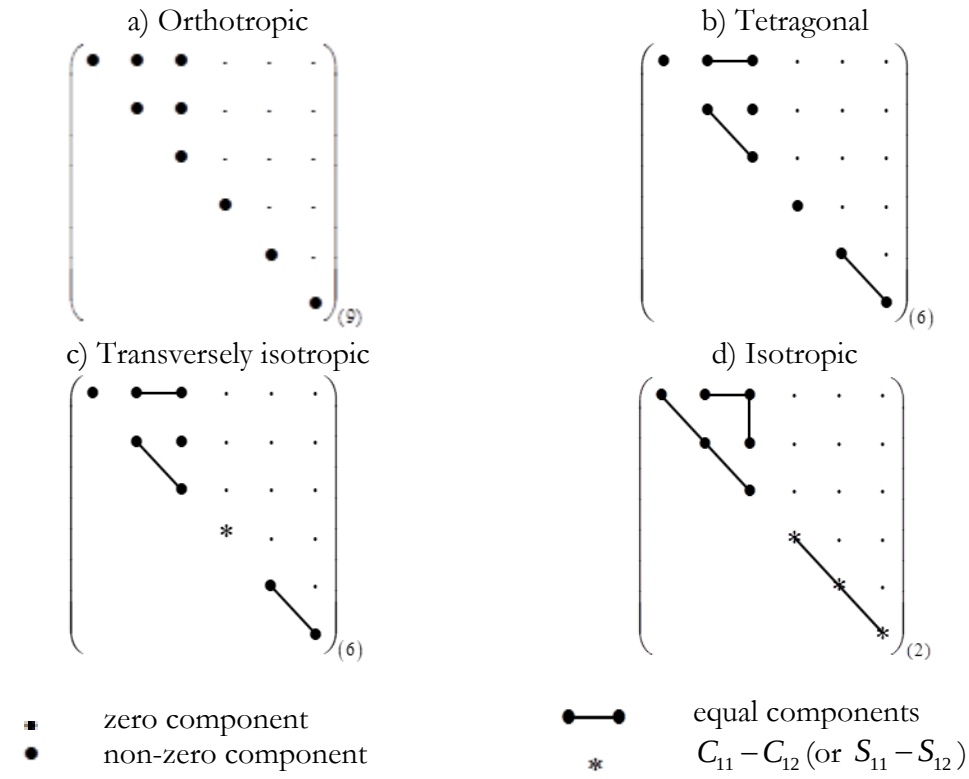

Figure 2.1.3 Graphical representation of stiffness tensors of: a) orthotropic, b) tetragonal, c) transversely isootropic and d) isotropic material. The numbers in brackets indicate the number of independent parameters needed to define the material stiffness tensor (after Nye (1985))

2.1.3 Compliance tensor and engineering constants constraints

Although, the stiffness tensor sufficiently describes the material's linear elastic behaviour it is convenient to introduce the **compliance tensor**, which is an inverse of the stiffness tensor. Compliance tensor is related to the macroscopic material constants of the composites (e.g. Young's moduli – E_i, Poisson's ratio – ν_{ij} and shear moduli – G_{ij}) in a more straightforward way than the stiffness tensor.

The compliance tensor for an orthotropic material is given by:

$$S_{\alpha\varepsilon} = \begin{bmatrix} S_{11} & S_{12} & S_{13} & 0 & 0 & 0 \\ S_{12} & S_{22} & S_{23} & 0 & 0 & 0 \\ S_{13} & S_{23} & S_{33} & 0 & 0 & 0 \\ 0 & 0 & 0 & \frac{1}{2}S_{44} & 0 & 0 \\ 0 & 0 & 0 & 0 & \frac{1}{2}S_{55} & 0 \\ 0 & 0 & 0 & 0 & 0 & \frac{1}{2}S_{66} \end{bmatrix} =$$

$$= \begin{bmatrix} \frac{1}{E_1} & -\frac{\nu_{21}}{E_2} & -\frac{\nu_{31}}{E_3} & 0 & 0 & 0 \\ -\frac{\nu_{12}}{E_1} & \frac{1}{E_2} & -\frac{\nu_{32}}{E_3} & 0 & 0 & 0 \\ -\frac{\nu_{13}}{E_1} & -\frac{\nu_{23}}{E_2} & \frac{1}{E_3} & 0 & 0 & 0 \\ 0 & 0 & 0 & \frac{1}{2G_{23}} & 0 & 0 \\ 0 & 0 & 0 & 0 & \frac{1}{2G_{31}} & 0 \\ 0 & 0 & 0 & 0 & 0 & \frac{1}{2G_{12}} \end{bmatrix} \quad \textbf{2.1.17}$$

For tetragonal materials the following conditions apply:

$$S_{22} = S_{33}, \qquad S_{55} = S_{66}, \qquad S_{12} = S_{13}. \quad \textbf{2.1.18}$$

They lead to the following constraints on the engineering constants:

$$E_2 = E_3, \qquad G_{12} = G_{31}, \qquad \nu_{12} = \nu_{13}, \qquad \nu_{23} = \nu_{32}, \qquad \nu_{21} = \nu_{31}. \quad \textbf{2.1.19}$$

Moreover, for transversely isotropic materials the following is true:

$$\frac{1}{2}S_{44} = S_{22} - S_{23}, \qquad G_{23} = \frac{E_2}{2(1-\nu_{23})}. \quad \textbf{2.1.20}$$

In this case plane 23 is the isotropy plane of a material. Note that Equation 2.1.20 is the relation between Young's and shear moduli for an isotropic material.

The fact that work done by all the stresses must be positive imposes a constraint on the engineering constants. Thus, both stiffness and compliance tensors must be positive-definite (Lempriere, 1968), which leads to the following set of requirements for stiffness tensors (Jones, 1998):

$$C_{11}, C_{22}, C_{33}, C_{23}, C_{31}, C_{12} > 0. \quad \textbf{2.1.21}$$

As a result, the following set of constraints apply:

$$E_1, E_2, E_3, G_{23}, G_{31}, G_{12} > 0. \qquad \textbf{2.1.22}$$

Furthermore, the off diagonal terms must satisfy the following relations:

$$|S_{23}| < \sqrt{S_{22}S_{33}}, \qquad |S_{13}| < \sqrt{S_{11}S_{33}}, \qquad |S_{12}| < \sqrt{S_{11}S_{22}}.$$

It can also be expressed as a set of constraints on Poisson's ratios (Jones, 1998):

$$\begin{aligned} &|\nu_{12}| < \sqrt{\frac{E_1}{E_2}}, \quad |\nu_{23}| < \sqrt{\frac{E_2}{E_3}}, \quad |\nu_{31}| < \sqrt{\frac{E_3}{E_1}}, \\ &|\nu_{21}| < \sqrt{\frac{E_2}{E_1}}, \quad |\nu_{32}| < \sqrt{\frac{E_3}{E_2}}, \quad |\nu_{13}| < \sqrt{\frac{E_1}{E_3}}. \end{aligned} \qquad \textbf{2.1.23}$$

The Poisson's ratios for majority of homogeneous, isotropic materials vary between 0 and 0.5. Note, that for composite materials the theoretical limits are much higher. According to Equations 2.1.23, for material with strong anisotropy manifested by $E_1 \gg E_2$ the Poisson's ratio ν_{12} can attain values much higher than one, which is the theoretical limit for isotropic materials.

2.1.4 Spectral decomposition of the stiffness tensor

The idea of a decomposition of the stiffness tensor was attributed by Rychlewski (1984) and Cowin and Mehrabadi (1992) to Lord Kelvin (Thomson, 1857). Every symmetric, second order tensor can be represented as a symmetric, positive definite matrix and therefore can be diagonalized. Diagonalization allows representing a tensor in terms of its eigenvalues (principal values) and eigenvectors (principal vectors):

$$\mathbf{A} = \sum_{i=1}^{3} \lambda^i \mathbf{v}^i \otimes \mathbf{v}^i, \qquad \textbf{2.1.24}$$

where $\mathbf{A}$ is a symmetric tensor, $\mathbf{v}^i$ is an eigenvector and λ^i is an eigenvalue of the tensor. Conveniently, mapping to six-dimensional space, as described in Section 2.1.1, reduces the order of the stiffness tensor from fourth to second (and stress and strain second order tensors to vectors).

The stiffness tensor of any material can therefore be given as:

$$\mathbf{C} = \sum_{i=1}^{6} \lambda^i \mathbf{v}^i \otimes \mathbf{v}^i \,, \qquad \textbf{2.1.25}$$

with λ^i being the i-th eigenvalue (or principal stiffness) and $\mathbf{v}^i$ being the corresponding eigenvector (in six dimensions). To avoid confusion with the spatial indices, the modes are denoted with upper indices and roman numbers in this work.

The symmetries of the material, as explained in Section 2.1.2, reduce the number of distinct eigenvalues. Direct solutions for eigenvalues and eigenvectors for woven and tetragonal materials (in terms of stiffness tensor members) are presented in Table 2.1.1.

Table 2.1.1 Eigenvalues and eigenvectors of tetragonal and transversely isotropic materials

Eigenvalues	Eigenvectors
$\lambda^I = \frac{1}{2}\left[(C_{11}+C_{22}+C_{23}) + \sqrt{(C_{11}-C_{22}-C_{23})^2 + 8(C_{12})^2} \right]$	$\mathbf{v}^I = \frac{1}{\sqrt{2+\alpha^2}} \begin{bmatrix} \alpha & 1 & 1 & 0 & 0 & 0 \end{bmatrix}^T$
$\lambda^{II} = C_{22} - C_{23}$	$\mathbf{v}^{II} = \frac{1}{\sqrt{2}} \begin{bmatrix} 0 & -1 & 1 & 0 & 0 & 0 \end{bmatrix}^T$
$\lambda^{III} = \frac{1}{2}\left[(C_{11}+C_{22}+C_{23}) - \sqrt{(C_{11}-C_{22}-C_{23})^2 + 8(C_{12})^2} \right]$	$\mathbf{v}^{III} = \frac{1}{\sqrt{2+\beta^2}} \begin{bmatrix} \beta & 1 & 1 & 0 & 0 & 0 \end{bmatrix}^T$
$\lambda^{IV} = 2C_{44}$	$\mathbf{v}^{IV} = \begin{bmatrix} 0 & 0 & 0 & 1 & 0 & 0 \end{bmatrix}^T$
$\lambda^{V} = 2C_{66}$	$\mathbf{v}^{V} = \begin{bmatrix} 0 & 0 & 0 & 0 & 1 & 0 \end{bmatrix}^T$
$\lambda^{VI} = 2C_{66} = \lambda^V$	$\mathbf{v}^{VI} = \begin{bmatrix} 0 & 0 & 0 & 0 & 0 & 1 \end{bmatrix}^T$

For transversely isotopic materials an additional relation $\lambda^{IV} = C_{22} - C_{23} = \lambda^{II}$ holds. Coefficients α and β are:

$$\alpha = \frac{2C_{12}}{\lambda^I - C_{11}}, \qquad \beta = \frac{2C_{12}}{\lambda^{II} - C_{11}}, \qquad \alpha\beta = -2\,. \qquad \textbf{2.1.26}$$

In case of a tetragonal material the stiffness tensor can be defined as:

$$\begin{aligned}\mathbf{C} &= \sum_{i=I}^{VI} \lambda^i \mathbf{v}^i \otimes \mathbf{v}^i = \\ &= \lambda^I \mathbf{v}^I \otimes \mathbf{v}^I + \lambda^{II} \mathbf{v}^{II} \otimes \mathbf{v}^{II} + \lambda^{III} \mathbf{v}^{III} \otimes \mathbf{v}^{III} + \\ &\quad + \lambda^{IV} \mathbf{v}^{IV} \otimes \mathbf{v}^{IV} + \lambda^V (\mathbf{v}^V \otimes \mathbf{v}^V + \mathbf{v}^{VI} \otimes \mathbf{v}^{VI})\end{aligned} \qquad \text{2.1.27}$$

And for a transversely isotropic material:

$$\begin{aligned}\mathbf{C} &= \sum_{i=I}^{VI} \lambda^i \mathbf{v}^i \otimes \mathbf{v}^i = \\ &= \lambda^I \mathbf{v}^I \otimes \mathbf{v}^I + \lambda^{III} \mathbf{v}^{III} \otimes \mathbf{v}^{III} + \lambda^{II} (\mathbf{v}^{II} \otimes \mathbf{v}^{II} + \mathbf{v}^{IV} \otimes \mathbf{v}^{IV}) + \\ &\quad + \lambda^V (\mathbf{v}^V \otimes \mathbf{v}^V + \mathbf{v}^{VI} \otimes \mathbf{v}^{VI})\end{aligned} \qquad \text{2.1.28}$$

By definition, eigenvectors $\mathbf{v}^i$ have the unit length. Mathematically this is postulated by:

$$\mathbf{v}^i \cdot \mathbf{v}^i = 1. \qquad \text{2.1.29}$$

The eigenvector solution for the general orthotropic material is lengthy and requires the number of simplifying assumptions to be determined explicitly. Neither of the references on eigensystems of materials (Cowin and Mehrabadi, 1985, 1992; Mehrabadi and Cowin, 1990; Sutcliffe, 1992; Mehrabadi, Cowin and Horgan, 1993; Schreyer and Zuo, 1995) present the direct eigenvalue solution for the orthotropic symmetry. Nevertheless, it is not vital for this work, as the materials considered have the tetragonal or higher symmetries.

Spectral decomposition of the isotropic material stiffness tensor gives two distinct modes. One of them is a volumetric (or spherical) mode and the other one is a deviatoric mode. They are defined as:

$$\begin{aligned}\lambda^v &= C_{11} + 2C_{12}, & \mathbf{v}^v &= \frac{1}{\sqrt{3}}\begin{bmatrix}1 & 1 & 1 & 0 & 0 & 0\end{bmatrix}^T, \\ \lambda^d &= C_{11} - C_{12}, & \mathbf{v}^d &= \begin{bmatrix}\frac{-2}{\sqrt{6}} & \frac{1-\sqrt{3}}{\sqrt{6}} & \frac{1+\sqrt{3}}{\sqrt{6}} & 1 & 1 & 1\end{bmatrix}^T.\end{aligned} \qquad \text{2.1.30}$$

2.1.5 Damage in composites

Damage in a material depends on its life cycle starting with design process, through manufacturing, assembly and, finally, exploitation. Design, manufacturing and assembly are

complex processes. They depend on a large number of parameters, which determine the final material quality. An example is generation of residual stresses between fibres and matrix due to different thermal expansion during curing process. Design and manufacturing of composites, although important for the material quality, lies beyond the scope of this work. This work focuses on the in-service performance of composites.

The extent and character of damage in composites depends on many aspects e.g. composite structure, properties of its constituents, loading rates and load types. Among in-service composite damage, impact induced damage is one of the most severe and detrimental. Depending on the loading rate low and high velocity impact (HVI) are distinguished. In **low velocity impact** structures respond globally – time scales allow for impact energy transfer from the impact zone to the rest of the structure. Low velocity impacts are typically modelled as quasi-static events, where inertial and strain rate effects are neglected (Orlowski, 2014). Low velocity impact is characterised by velocities much lower than the speed of sound in the material. In the case of low velocity impact danger does not lie in an instantaneous collapse of the structure but in reduction of its stiffness, strength and reduction in fatigue life combined with low detectability. The commonly used example of low velocity impact is tool dropping which can lead to material delamination. This type of damage is difficult to detect as it usually forms under material surface leaving no visible trace. Nevertheless, it can cause serious strength and stiffness reduction and undetected is a significant threat to the safety of the structure. Composite behaviour under low velocities has been widely studied to provide an insight into dominant damage mechanisms evolving at different impact stages (Wu and Tsai, 2000). Kim (2000) reports three principal damage modes – interlaminar, intralaminar and fibre breaking. Interlaminar damage (delamination) affects the interface between layers of composite and is dependent on matrix properties and the properties of the fibre-matrix interface. Intralaminar damage between fibres, also driven by matrix and fibre-matrix interface properties, is affecting the material within one ply by matrix cracking and fibre-matrix debonding. Last damage mode identified by the author is intralaminar damage across the fibres such as fibre breaking in tension and fibre buckling in compression.

Investigation of damage in composites under **high velocity impact** is far more complicated, but equally important. Because of short time scales of the impact, difficulties arise in experiment design especially in terms of constraining the specimen and observation of damage effects (Reid and Zhou, 2000). Understanding materials' high velocity impact

behaviour is most important for sectors where high velocities are encountered such as aeronautics, aerospace, automotive, military and defence. Some typical examples of high velocity impact are bird and debris impact. Both can lead to fatal accidents – one tragic example is Concorde accident in Paris in 2000. Debris from the runway hit the fuel tank of the aircraft leading to fire. In case of wind turbines, the blades can be destroyed by hailstones during heavy storms.

Existence of at least two constituents in composite materials necessitates existence of the additional feature which is the interface between the constituents. The interface properties differ from properties of the constituents. Damage mechanisms that evolve in the material can be related to either of the phases or their interface. Among damage mechanisms described in (Talreja and Singh, 2012) there are matrix microcracking, fibre breakage, fibre micro-buckling, interfacial debonding and delamination (interlaminar cracking).

Matrix microcracking of composite is a damage mechanism identified within a ply of a laminate. It affects solely the matrix phase but can sometimes promote other damage mechanisms. Matrix microcracks are typically consequence of tensile, cyclic or thermal loading as well as errors in manufacturing. This damage mechanism does not affect the stiffness properties significantly.

In contrast, the overall material performance is strongly affected by **fibre breaking**. This significantly reduces the fibre direction stiffness and residual strength. Fibre breaking usually occurs under tensile loading in the fibre direction. Due to uncertainties in manufacturing and assembly processes, as well as the fibre material microstructure defects that have a statistical nature the strengths of different fibres may not be equal. Following failure of the weakest fibres the stress is redistributed to the remaining fibres, which now need to carry higher loads. It is also important to note, that breaking of the fibre often promote matrix cracking or fibre matrix delamination.

Fibre micro-buckling is a damage mechanism induced by the compressive loading in plane of fibres. It is a consequence of the initial fibre misalignment generated during the manufacturing process. Misalignment leads to fibres bending resulting in their buckling and finally structural collapse. As in case of fibre breaking, fibre micro-buckling can contribute to matrix cracking.

Damage mechanism characteristic for the interface between fibres and matrix is **interfacial debonding**. It can be either the result of manufacturing faults in bonding between fibres and matrix or solely the result of loads acting on the material. Interfacial debonding starts with matrix cracking around the fibre, which results in different deformation of the constituents. Higher deformation of the fibre results in higher Poisson's contraction, which can be high enough to cause debonding between the fibre and the matrix (Talreja and Singh, 2012).

Delamination is damage mechanism which develops between the adjacent plies. It may be seen as matrix cracking which occurs in the plane of the interface between the two composite layers. Delamination does not need high energy to evolve (Wu and Tsai, 2000) but can cause significant reduction in stiffness of the material.

The fact that the material is composed of at least two phases and their interface whose mechanical properties differ (often significantly) makes predictions of damage character very difficult. It is also important to note that damage in one phase can promote damage in the other. These interactions make the physics of damage in composites complex and difficult to model or predict.

2.2 Review of existing material models

Previous section gave an overview of the composite (elastic and damage) behaviour and introduced the necessary terminology and notation. It also provided the list of damage mechanisms. These allow identifying the most important features of a composite constitutive model. First of all, the model should be able to accurately represent the linear elastic behaviour of the composite and reliably predict the damage onset, damage evolution and failure. Whilst linear elastic behaviour is well described by the generalised Hooke's Law, modelling of the damage is much more complex. Hence, second important aspect in constitutive models is damage and more specifically its evolution and influence on materials' properties.

This section focuses on evaluation of existing composite models highlighting their main features, assumptions, accuracies and limitations. A number of frequently used composite constitutive models is reviewed showing different approaches used for damage onset and evolution modelling.

Over the last decades a large number of researchers tried to address these issues and developed relevant theories and models. These models can be generally classified into three groups: **phenomenological**, **physically based** and **statistical** models (Krajcinovic and Silva, 1982; Puck and Schürmann, 1998). The review presented here is mainly limited to the theories and models implemented in LS-Dyna or Dyna3D and the models otherwise relevant to this work.

2.2.1 Damage initiation criteria used in composite constitutive models

Basic material characterisation consists in defining its stiffness and strength. Standard tests are designed to characterise the material under *a priori* defined stress state. The stress state in an elastic, isotropic, homogeneous material is easy to define. Stress-strain relation for anisotropic material is given by generalised Hooke's Law (Section 2.1.1). Lack of homogeneity, however, is the factor significantly complicating the strength analysis. The macroscopic state of stress established for the representative volume does not give the information about the stress variations due to material micro- or mesostructure. Naturally arising question is how to define the load carrying capability under complex load case knowing the material strength in different directions. It is usually expressed by failure criteria. There are number of failure mechanisms in composites as described in Section 2.1.5, which can be associated with different loading conditions.

Special care was taken to use the consistent notation in this paragraph. Stresses are denoted using the contracted notation (σ_i, $i = 1, 2, ..., 6$). X, Y and Z are used as labels for the normal strengths in 1, 2 and 3 directions that can be determined from the uniaxial stress tests. The subscripts t and c indicate tension and compression. The shear strengths are denoted by S_i with the subscript corresponding to the shear plane $(i = 4, 5, 6)$.

The most basic damage initiation criteria are **maximum stress** and **maximum strain** criteria. They assume that the material fails under the stress or strain that exceeds material's strength or critical strain in a given direction. These are accurate for plane stress or plane strain load cases respectively. However, if a complex triaxial stress or strain state is generated in the material, maximum stress and strain criteria overestimate the material load carrying capacity by not taking into account interaction between different stress or strain components (Echaabi, Trochu and Gauvin, 1996) both for isotropic and anisotropic materials. Nevertheless, the maximum stress criterion was found to be accurate for predicting

longitudinal strength of composites and was used in failure criteria such as Hashin's failure criterion (Hashin, 1980) or LaRC03 (Dávila and Camanho, 2003).

For isotropic materials probably the most common elastic limit criterion is **von Mises yield** criterion (or Maxwell–Huber–Hencky–von Mises theory). Although the von Mises criterion is directly applicable only to isotropic materials, the possibility of extending the formulation to anisotropic materials was postulated by number of researchers, starting with **Hill** (1950). He suggested that yield criterion for anisotropic metals can be defined by:

$$2f(\sigma_\alpha) = F(\sigma_2-\sigma_3)^2 + G(\sigma_3-\sigma_1)^2 + H(\sigma_1-\sigma_2)^2 + \\ + 2L\sigma_4^2 + 2M\sigma_5^2 + 2N\sigma_6^2 = 1. \qquad \textbf{2.2.1}$$

where F, G, H, L, M and N are the parameters characteristic for a material anisotropy. The coefficients are dependent on the material yield strengths in the material's anisotropy directions:

$$2F = \frac{1}{Y_t^2} + \frac{1}{Z_t^2} - \frac{1}{X_t^2}, \qquad 2L = \frac{1}{S_4^2},$$

$$2G = \frac{1}{Z_t^2} + \frac{1}{X_t^2} - \frac{1}{Y_t^2}, \qquad 2M = \frac{1}{S_5^2}, \qquad \textbf{2.2.2}$$

$$2H = \frac{1}{X_t^2} + \frac{1}{Y_t^2} - \frac{1}{Z_t^2}, \qquad 2N = \frac{1}{S_6^2}.$$

The criterion was proposed for the orthotropic material in which the hydrostatic/isotropic stress (calculated as $p = (\sigma_1+\sigma_2+\sigma_3)/3$) does not contribute to yielding. Note that different definition of pressure is used in this work (Section 3.5.1).

A systematic approach to define failure in anisotropic materials was suggested by **Tsai and Wu** (1971). The basic assumption of Tsai and Wu failure criterion was the existence of a function defining the failure surface (with summation over repeated indices):

$$f(\sigma) = F_\alpha\sigma_\alpha + F_{\alpha\beta}\sigma_\alpha\sigma_\beta = 1, \qquad \textbf{2.2.3}$$

where F_α and $F_{\alpha\beta}$ are strength tensors of second and fourth order (in contracted notation they are vectors and second order tensors respectively).

The tensors can be determined for an orthotropic composite using compressive, tensile and shear strengths as follows:

$$F_\alpha = \begin{Bmatrix} \frac{1}{X_t} - \frac{1}{X_c} \\ \frac{1}{Y_t} - \frac{1}{Y_c} \\ \frac{1}{Z_t} - \frac{1}{Z_c} \\ 0 \\ 0 \\ 0 \end{Bmatrix} \qquad F_{\alpha\beta} = \begin{Bmatrix} \frac{1}{X_t X_c} & F_{12} & F_{13} & 0 & 0 & 0 \\ F_{12} & \frac{1}{Y_t Y_c} & F_{23} & 0 & 0 & 0 \\ F_{13} & F_{23} & \frac{1}{Z_t Z_c} & 0 & 0 & 0 \\ 0 & 0 & 0 & \frac{1}{S_4^2} & 0 & 0 \\ 0 & 0 & 0 & 0 & \frac{1}{S_5^2} & 0 \\ 0 & 0 & 0 & 0 & 0 & \frac{1}{S_6^2} \end{Bmatrix} \qquad \textbf{2.2.4}$$

Note, that if the expressions below are satisfied the Tsai and Wu criterion simplifies to Hill's criterion (Equation 2.2.1).

$$\begin{aligned} X_t = X_c = X \qquad & F_{12} = -\frac{1}{2}\left(\frac{1}{X^2} + \frac{1}{Y^2} - \frac{1}{Z^2}\right) \\ Y_t = Y_c = Y \qquad & F_{13} = -\frac{1}{2}\left(\frac{1}{Z^2} + \frac{1}{X^2} - \frac{1}{Y^2}\right) \\ Z_t = Z_c = Z \qquad & F_{23} = -\frac{1}{2}\left(\frac{1}{Y^2} + \frac{1}{Z^2} - \frac{1}{X^2}\right) \end{aligned} \qquad \textbf{2.2.5}$$

Tsai – Wu failure criterion can also be simplified if the composite is unidirectional with fibres in direction X subjected to the plane state of stress. This simplification yields the commonly used form of Tsai and Wu criterion:

$$f = \frac{\sigma_1^2}{X^2} - \frac{\sigma_1 \sigma_2}{X^2} + \frac{\sigma_2^2}{Y^2} + \frac{\sigma_6^2}{S^2} = 1. \qquad \textbf{2.2.6}$$

Chang and Chang (1987) suggested failure criteria with three in plane failure modes – matrix cracking, fibre – matrix shearing and fibre breaking. **Chang-Chang** criteria are based on failure criteria proposed by (Yamada and Sun, 1978), but are generalised to account for non-linear elastic behaviour. Failure criterion for matrix cracking is given by Equation 2.2.7. Fibre-matrix shearing and fibre breaking failure modes are described by the same Equation 2.2.8.

$$f_m = \left(\frac{\sigma_2}{X_t}\right)^2 + \frac{\left(\frac{\sigma_6^2}{2G_{12}}\right) + \frac{3}{4}\xi\sigma_6^4}{\left(\frac{S^2}{2G_{12}}\right) + \frac{3}{4}\xi S^4} \qquad \textbf{2.2.7}$$

$$f_f = \left(\frac{\sigma_1}{X_t}\right)^2 + \frac{\left(\frac{\sigma_6^2}{2G_{12}}\right) + \frac{3}{4}\xi\sigma_6^4}{\left(\frac{S^2}{2G_{12}}\right) + \frac{3}{4}\xi S^4} \qquad \textbf{2.2.8}$$

In case of linear elastic behaviour of a laminate $\xi = 0$ and Equations 2.2.7 and 2.2.8 simplify to Equation 2.2.9, which is the failure criterion proposed by Yamada and Sun (1978):

$$f_m = \left(\frac{\sigma_2}{Y_t}\right)^2 + \left(\frac{\sigma_6}{S_6}\right)^2 \qquad \textbf{2.2.9}$$

$$f_f = \left(\frac{\sigma_1}{X_t}\right)^2 + \left(\frac{\sigma_6}{S_6}\right)^2$$

Chang and Chang (1987) considered, to some extent, the progressive damage of material. The authors suggested that fibre damage results in reduction of the longitudinal Young's modulus following the Weibull distribution. The matrix related failure modes were assumed to lead to reduction of Young's modulus and Poisson's ratios to zero with no change in longitudinal and shear stiffness properties.

Significant progress in predicting composites failure was development of the **Hashin** failure criterion (Hashin, 1980). Hashin introduced two major failure modes: one connected to matrix and the other to fibre failure. Each of them is treated separately for tension and compression. It is important to note that the criteria developed by Hashin are empirical, i.e. an approximation based on a best fit to empirical data, not a physically based failure theory. In his approximation, Hashin used quadratic curves justifying it by their good fitting capabilities and lower computational cost compared to higher order equations.

Hashin suggested two equations (2.2.10 and 2.2.11) for fibre tensile failure. First one accounts for shear strengths influence, the second is simply maximum stress criterion.

$$f_{ft} = \left(\frac{\sigma_1}{X_t}\right)^2 + \left(\frac{\sigma_5}{S_5}\right)^2 + \left(\frac{\sigma_6}{S_6}\right)^2 = 1 \qquad \textbf{2.2.10}$$

$$f_{ft} = \left(\frac{\sigma_1}{X_t}\right)^2 = 1 \qquad \textbf{2.2.11}$$

Fibre tensile failure mode assumes that only stress components: σ_1, σ_5 and σ_6 influence the mode. Corresponding tensile (X_t) and shear strengths $(S_5$ and $S_6)$ are used to define the fibre failure.

For fibre failure in compression Hashin suggested maximum stress criterion:

$$f_{fc} = \left(\frac{\sigma_1}{X_c}\right)^2 = 1. \qquad \textbf{2.2.12}$$

Hashin's matrix failure criterion is described by the quadratic formulation given by Equation 2.2.13, which takes into account interaction between transverse normal stresses and shear stresses in all planes.

$$f_{mt} = \left(\frac{\sigma_2 + \sigma_3}{Y_t}\right)^2 + \left(\frac{\sigma_4^2 - \sigma_2\sigma_3}{S_4^2}\right) + \left(\frac{\sigma_5}{S_5}\right)^2 + \left(\frac{\sigma_6}{S_6}\right)^2 = 1 \qquad \textbf{2.2.13}$$

Hashin's matrix failure in compression is given by:

$$f_{mc} = \left(\frac{\sigma_2 + \sigma_3}{Y_c}\right)\left(\frac{Y_c^2}{2S_4} - 1\right)\left(\frac{\sigma_2 + \sigma_3}{2S_4}\right)^2 + \frac{\sigma_4^2 - \sigma_2\sigma_3}{S_4^2} + \left(\frac{\sigma_5}{S_5}\right)^2 + \left(\frac{\sigma_6}{S_6}\right)^2 = 1 \qquad \textbf{2.2.14}$$

According to Hashin (1980) the best results for matrix failure would be given by finding the plane of the maximum principal stress (Mohr's failure theory), but at that time it appeared to be too complex to use in computations. This idea was evaluated later by Puck and Schürmann (1998).

LaRC03 failure criteria were developed by Dávila and Camanho (2003). These are the phenomenological failure criteria which are based on works by Hashin (1980) and Puck and Schürmann (1998). Authors analysed how different load cases influence the strength of a material. For transverse matrix compression the failure criteria were based on the Mohr –

Coulomb criterion. Following the Mohr's circle maximum stresses in material were established by:

$$\tau_{eff}^{T} = \left\langle \left| \tau^{T} \right| + \eta^{T} \sigma_{n} \right\rangle, \qquad \tau_{eff}^{L} = \left\langle \left| \tau^{L} \right| + \eta^{L} \sigma_{n} \right\rangle, \tag{2.2.15}$$

where η^{T} and η^{L} are respectively transverse and longitudinal influence coefficients (determined experimentally), σ_n is stress normal to the fracture surface, τ^{L} and τ^{T} are longitudinal and transverse components of stress lying on the fracture plane that can be determined from σ_2, σ_6 and fracture angle α (Figure 2.2.1).

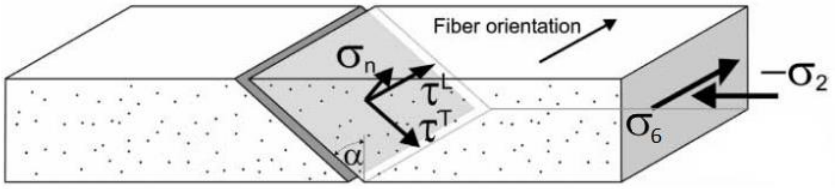

Figure 2.2.1 Fracture of a unidirectional lamina subjected to transverse compression and in-plane shear (adjusted from Dávila, Camanho and Rose, 2005)

Failure criterion proposed by Dávila and Camanho (2003) is given by:

$$f_1 = \left(\frac{\tau_{eff}^{T}}{S_4} \right)^2 + \left(\frac{\tau_{eff}^{L}}{S_6^{is}} \right)^2 = 1, \tag{2.2.16}$$

where S_4 and S_6^{is} denote transverse shear strength and longitudinal *in situ* shear strength. *In situ* effect stands for increased strength of composite layer lying between other layers of different orientation.

For transverse matrix failure in tension authors suggest use of:

$$f_2 = (1-r)\frac{\sigma_2}{Y_t} + g\left(\frac{\sigma_2}{Y_t} \right)^2 + \left(\frac{\sigma_6}{S_6} \right)^2 = 1, \tag{2.2.17}$$

where r is given by:

$$r = \frac{G_{Ic}}{G_{IIc}} = \frac{\Lambda_2^0}{\Lambda_6^0}\left(\frac{Y_t^{is}}{S_6^{is}} \right)^2, \qquad \Lambda_2^0 = 2\left(\frac{1}{E_2} - \frac{\nu_{21}^2}{E_1} \right), \qquad \Lambda_6^0 = \frac{1}{G_{12}}, \tag{2.2.18}$$

where Y_t^{is} is *in situ* transverse strength in tension and S_6^{is} *in situ* longitudinal shear strength; E_1, E_2, G_{12}, ν_{12} are Young moduli in longitudinal and transverse directions, longitudinal shear modulus and Poisson's ratio respectively. It is worth noticing that if $r=1$ Equation 2.2.17 simplifies to form in Equation 2.2.16, which can be also seen as 2D case of Hashin's failure criterion (Dávila, Camanho and Rose, 2005). The only difference is that Equation 2.2.17 uses the *in-situ* strengths rather than ply strengths.

Fibre failure under tension is assumed to occur under the maximum strain criterion:

$$f_3 = \frac{\varepsilon_1}{\varepsilon_1^{cr}} = 1. \qquad \textbf{2.2.19}$$

Fibre failure under longitudinal compression was attributed to fibre kinking, which is phenomenon of generation of shear stress between the fibres due to initial misalignment (see Figure 2.2.2).

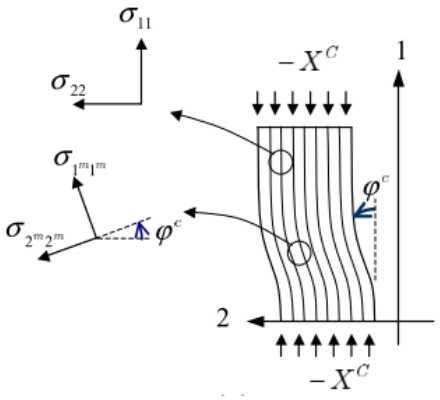

Figure 2.2.2 Fibre misalignment (adapted from Dávila and Camanho (2003))

An important effect included in the model is reduction of the effects of kinking by transverse compression, whilst transverse tension promotes it. Thus, there are two criteria to describe kinking failure. Equation 2.2.20 gives the criterion for compressive transverse stress and Equation 2.2.21 the criterion for tensile transverse stress.

$$f_4 = \frac{\left|\tau_{12}^m\right| + \eta^L \sigma_2^m}{S_{is}^L} = 1, \qquad \textbf{2.2.20}$$

$$f_5 = (1-r)\left(\frac{\sigma_2^m}{Y_t^{is}}\right) + g\left(\frac{\sigma_2^m}{Y_t^{is}}\right)^2 + \left(\frac{\sigma_6^m}{S_6^{is}}\right)^2 = 1, \qquad \textbf{2.2.21}$$

where superscript m denotes the change of coordinate system to the misalignment frame using the stress components σ_1, σ_2, σ_6 and misalignment angle (Figure 2.2.2) that yields:

$$\sigma_1^m = \cos^2\varphi\,\sigma_1 + \sin^2\varphi\,\sigma_2 + 2\sin\varphi\cos\varphi\,\sigma_6,$$

$$\sigma_2^m = \sin^2\varphi\,\sigma_1 + \cos^2\varphi\,\sigma_2 - 2\sin\varphi\cos\varphi\,\sigma_6, \qquad \textbf{2.2.22}$$

$$\sigma_6^m = -\sin\varphi\cos\varphi\,\sigma_1 + \sin\varphi\cos\varphi\,\sigma_2 + \left(\cos^2\varphi - \sin^2\varphi\right)\sigma_6.$$

The last case of damage analysed by Dávila and Camanho (2003) was high transverse compression coupled with moderate longitudinal compression. Under these conditions the kink band is not likely to form, so damage would occur as matrix damage. The criterion is given by:

$$f_6 = \left(\frac{\tau_{eff}^{mT}}{S^T}\right)^2 + \left(\frac{\tau_{eff}^{mL}}{S_{is}^L}\right)^2 = 1, \qquad \textbf{2.2.23}$$

where stresses in the misalignment frame are defined by:

$$\tau_{eff}^{mT} = \left\langle -\sigma_2^m \cos\alpha\left(\sin\alpha - \eta^T\cos\alpha\right)\right\rangle,$$

$$\tau_{eff}^{mL} = \left\langle \cos\alpha\left(\left|\sigma_6^m\right| + \eta^L\sigma_2^m\cos\alpha\right)\right\rangle. \qquad \textbf{2.2.24}$$

Note that the criterion definition is exactly the same as the matrix failure criterion (Equation 2.2.16) but is calculated in the material misalignment frame. LaRC03 failure criteria were used for composite constitutive models developed by Pinho, Iannucci and Robinson (2006a) and Maimí *et al.* (2007a).

The last failure criterion that is most important for this work is another approach to generalisation of von Mises yield criterion. It was suggested by Mehrabadi and Cowin (1990) and mathematically derived by Schreyer and Zuo (1995). If von Mises criterion is treated as the maximum distortional strain energy criterion it can be obtained by the spectral decomposition of the stiffness tensor of an isotropic material and calculation of the modal strain energy. The same procedure can be followed for the non-isotropic material stiffness tensor. This leads to identification of the strain energy modes corresponding to each of the principal stiffnesses. In case of isotropic materials decomposition yields two distinct modes

that can be identified as spherical and deviatoric. The deviatoric mode in the case of material isotropy is the exact form of von Mises Yield criterion. In case of non-isotropic materials there are at most six distinct strain energy modes. For some material symmetries (transverse isotropy, tetragonal) the number of the modes decreases as a result of repeated eigenvalues.

Direct procedure of the derivation of the yield surface was described by Schreyer and Zuo (1995). Following this approach six strain energy modes can be defined for each material. Assuming that the material fails if the strain energy in a mode exceeds its limit, six scalar failure criteria can be defined for each material. Schreyer and Zuo (1995) proposed definition of the eigenstresses characteristic for each mode (here in contracted notation):

$$\boldsymbol{\sigma}^i = \mathbf{P}^i \cdot \boldsymbol{\sigma} = \left(\mathbf{v}^i \cdot \boldsymbol{\sigma}\right)\mathbf{v}^i = \sigma^i \mathbf{v}^i, \qquad \textbf{2.2.25}$$

where tensor $\mathbf{P}^i$ is the projection operator tensor corresponding to the i-th eigenmode defined as the tensor product of two eigenvectors $\mathbf{v}^i$. For the materials with tetragonal symmetry and transverse isotropy the explicit solution for eigenstresses is possible (Schreyer and Zuo, 1995):

$$\bar{\sigma}^{I\,2} = \boldsymbol{\sigma}^I : \boldsymbol{\sigma}^I = \frac{1}{\left(2+\alpha^2\right)}\left[\alpha\sigma_1 + \sigma_2 + \sigma_3\right]^2, \qquad \alpha = \frac{2C_{12}}{\lambda^I - C_{11}},$$

$$\bar{\sigma}^{II\,2} = \boldsymbol{\sigma}_2 : \boldsymbol{\sigma}_2 = \frac{1}{2}\left(\boldsymbol{\sigma}_2 - \boldsymbol{\sigma}_3\right)^2,$$

$$\bar{\sigma}^{III\,2} = \boldsymbol{\sigma}^{III} : \boldsymbol{\sigma}^{III} = \frac{1}{\left(2+\beta^2\right)}\left[\beta\sigma_1 + \sigma_2 + \sigma_3\right]^2, \qquad \beta = \frac{2C_{12}}{\lambda^{III} - C_{11}}, \qquad \textbf{2.2.26}$$

$$\bar{\sigma}^{IV\,2} = \boldsymbol{\sigma}^{IV} : \boldsymbol{\sigma}^{IV} = 2\left(\sigma_4\right)^2,$$

$$\bar{\sigma}^{V\,2} = \boldsymbol{\sigma}^V : \boldsymbol{\sigma}^V + \boldsymbol{\sigma}^{VI} : \boldsymbol{\sigma}^{VI} = 2\sigma_5^2 + 2\sigma_6^2.$$

For transversely isotropic materials there are only four modes. First, third and fifth (which becomes fourth) modes remain the same as in Equations 2.2.26 and the second mode is a combination of the second and the fourth mode from Equation 2.2.26, i.e.:

$$\bar{\sigma}^{II\,2} = \boldsymbol{\sigma}^{II} : \boldsymbol{\sigma}^{II} + \boldsymbol{\sigma}^{IV} : \boldsymbol{\sigma}^{IV} = \frac{1}{2}\left(\sigma_2 - \sigma_3\right)^2 + 2\left(\sigma_4\right)^2. \qquad \textbf{2.2.27}$$

Following Schreyer and Zuo (1995) suggestion, the experiments can be designed to activate only one strain energy mode. Subsequently, the strengths related to each of the modes can be determined for a given material. The similar approach was used by Hebda (2006) for the laminae (in 2D).

The failure criteria presented in this section represent a small selection of many other developed over the years. A more complete list of failure criteria was provided by Orifici, Herszberg and Thomson (2008). Furthermore, comprehensive evaluation of the composite failure theories was the aim of the World-Wide Failure Exercise (WWFE) (Soden, Kaddour and Hinton, 2004). The exercise compared and contrasted the range of failure theories against each other and experimental data for the number of load cases. It revealed lack of the universally accurate and robust theory.

The approach used in this work is based on the definition of the strain energy modes. The only difference is that failure criteria are defined in strain rather than stress domain in this work (see Section 5.1). Such failure criteria have benefit of being physically sound and consistent with theory applicable to arbitrary loading conditions.

2.2.2 Material progressive damage models

The most basic material models include failure models that are not capable of modelling progressive damage. In these models the engineering constants are set to zero resulting in zero stress after failure criterion is reached. The example of such a model is Chang-Chang Composite Failure Model (e.g. MAT_022 in LS-Dyna).

The other type of models includes progressive damage models which can describe material gradual deterioration. Examples of such models are (Pinho, Iannucci and Robinson, 2006b, 2006a; Maimí *et al.*, 2007a, 2007b; Gama, 2015; Zhao *et al.*, 2018) among many others. Majority of progressive damage models are based on the continuum damage mechanics (Section 3.3).

Matzenmiller, Lubliner and Taylor, (1995); Maimí *et al.*, (2007a); Gama, (2015) model progressive damage by modifying the elements of the compliance tensor. Each of failure criteria activates separate damage variables which adjust diagonal terms of the compliance tensor as show in Equation 2.2.28. Within this general idea different failure criteria were

considered. In case of Maimí *et al.* (2007a) LaRC03 criteria were used. Gama (2015) used Hashin failure criterion for fibres and he developed his own failure criteria for matrix.

$$\mathbf{S}=\begin{bmatrix} \frac{1}{\left(1-d_{E_1}\right)E_1} & \frac{-\nu_{21}}{E_2} & \frac{-\nu_{31}}{E_3} & 0 & 0 & 0 \\ \frac{-\nu_{12}}{E_1} & \frac{1}{\left(1-d_{E_2}\right)E_2} & \frac{-\nu_{32}}{E_3} & 0 & 0 & 0 \\ \frac{-\nu_{13}}{E_1} & \frac{-\nu_{23}}{E_2} & \frac{1}{\left(1-d_{E_3}\right)E_3} & 0 & 0 & 0 \\ 0 & 0 & 0 & \frac{1}{\left(1-d_{E_4}\right)G_{23}} & 0 & 0 \\ 0 & 0 & 0 & 0 & \frac{1}{\left(1-d_{E_5}\right)G_{31}} & 0 \\ 0 & 0 & 0 & 0 & 0 & \frac{1}{\left(1-d_{E_6}\right)G_{12}} \end{bmatrix} \quad \textbf{2.2.28}$$

An interesting approach to modelling of progressive damage was presented by Zhang *et al.*, (2016) and improved by Zhao *et al.*, (2018). They suggested seven Hashin-based failure criteria: fibre tension (FT), fibre compression (FC), matrix tension (MT), matrix compression (MC), fibre-matrix shear-out (FMs), interlaminar tension (IT) and interlaminar compression (IC). Each of the criteria activates a corresponding damage mode. In this model damage is defined by the number of damage factors applied to material elastic constants (presented in Table 2.2.1). Unlike in previously described models, this damage model affects also off-diagonal terms of the compliance and stiffness tensors.

According to Zhao *et al.*, (2018) degradation factors d_y^x can be obtained from the mesoscale periodic models. In their analysis single fibre models were used. It was claimed, following Trias *et al.*, (2006) that it is sufficient to accurately model the degradation of a material.

Table 2.2.1 Mode dependent degradation model (Zhao *et al.*, 2018)

Failure mode	Degradation factors for elastic constants								
	E_1	E_2	E_3	G_{12}	G_{13}	G_{23}	ν_{12}	ν_{13}	ν_{23}
FT	$d_{E_{11}}^{FT}$	1	1	$d_{G_{12}}^{FT}$	$d_{G_{13}}^{FT}$	1	$d_{\nu_{12}}^{FT}$	$d_{\nu_{13}}^{FT}$	1
FC	$d_{E_{11}}^{FC}$	1	1	$d_{G_{12}}^{FC}$	1	1	$d_{\nu_{12}}^{FC}$	$d_{\nu_{13}}^{FC}$	1
MT	1	$d_{E_{22}}^{MT}$	1	$d_{G_{12}}^{MT}$	1	$d_{G_{23}}^{MT}$	$d_{\nu_{12}}^{MT}$	1	$d_{\nu_{23}}^{MT}$
MC	1	$d_{E_{22}}^{MC}$	1	$d_{G_{12}}^{MC}$	$d_{G_{13}}^{MC}$	$d_{G_{23}}^{MC}$	$d_{\nu_{12}}^{MC}$	1	$d_{\nu_{23}}^{MC}$
FMS	1	$d_{E_{22}}^{FMS}$	$d_{E_{33}}^{FMS}$	$d_{G_{12}}^{FMS}$	$d_{G_{13}}^{FMS}$	$d_{G_{23}}^{FMS}$	$d_{\nu_{12}}^{FMS}$	$d_{\nu_{13}}^{FMS}$	$d_{\nu_{23}}^{FMS}$
IT	1	1	$d_{E_{33}}^{IT}$	1	$d_{G_{13}}^{IT}$	$d_{G_{23}}^{IT}$	1	$d_{\nu_{13}}^{IT}$	$d_{\nu_{23}}^{IT}$
IC	1	1	$d_{E_{33}}^{IC}$	1	$d_{G_{13}}^{IC}$	$d_{G_{23}}^{IC}$	1	$d_{\nu_{13}}^{IC}$	$d_{\nu_{23}}^{IC}$

2.2.3 Models implemented in LS-Dyna

There are numerous constitutive models available in any FE software. There is no material model that is universally applicable to all materials and load cases. Some models are only suitable for elastic analysis and infinitesimal strains. Some more advanced models are applicable to large strains and include plasticity and damage effects. Another aspect that should be considered is the strain rate – some materials exhibit strain rate dependence, which can also be accounted for in material model. Furthermore, if high velocity phenomena are modelled the dynamic material response requires use of equation of state. All these aspects should be considered while choosing the material model suitable for analysis. The appropriate choice of the material constitutive model is therefore of vital importance to assure the meaningful result. Only few composite damage models such as Hashin, Tsai-Wu and Tsai-Hill failure criteria are available in commercial software. The model developed in this thesis is implemented in Dyna3D software, which focuses specifically on the dynamic modelling. Dyna 3D is a code developed by Lawrence Livermore National Laboratory (LLNL) in USA for which source code is available in house which allows implementing new subroutines, including new material models. The commercial version of this program,

LS Dyna currently supports eleven composite material models for structural analysis. Few most relevant models are described below. Equations defining damage criteria for these models are presented in Appendix A.

Material **MAT_COMPOSITE_DAMAGE** (**MAT_022**) uses Chang and Chang failure criterion. There are three failure modes considered – tensile fibre mode, tensile matrix mode and compressive matrix mode. The model requires five material strength parameters: longitudinal tensile strength, transverse tensile strength, in-plane shear strength, transverse compressive strength and nonlinear shear stress parameter. First four can be determined from simple mechanical tests and the latter from shear stress-strain measurements. Reaching failure criterion sets the selected material constants to zero.

Another composite model available in LS Dyna comes in two versions. Both are based on MAT_022. The model name is **MAT_ENHANCED_COMPOSITE_DAMAGE** (**MAT_054/MAT_055**). The models differ by the failure criterion for matrix failure. MAT_054 uses the Chang and Chang failure criterion (like MAT_022), and MAT_055 Tsai – Wu criterion. This material model is valid only with shell element formulation. There are five strength input parameters – tensile and compressive longitudinal and transverse stresses and in-plane shear stress. Additionally, the parameters that define the final failure, such as final rupture shear strain ot maximum damage can be specified for MAT_054.

Material **MAT_COMPOSITE_FAILURE** (**MAT_059**) is vaguely described in keyword manual (LSTC, 2014) and not at all in the Dyna theory manual (Hallquist, 2006). The material is shortly described in (Schweizerhof *et al.*, 1998), according to which the ellipsoidal failure surface is defined by failure surface similar to the Tsai-Wu criterion. It was suggested that this model works well for the materials whose different strengths do not differ significantly. Depending on the input the material can be either elastic – perfectly plastic, which results in constant stress after failure or elastic with damage, which results in setting the tensile strengths to zero (material can carry only compressive loads). The input parameters for the solid model are: tensile and compressive strengths in fibre, transverse and through thickness directions and three shear strengths.

Materials **MAT_COMPOSITE_MSC** (**MAT_161** and **MAT_162**) are the material models based on Hashin failure criteria. MAT_162 is the same as MAT_161, but it accounts for progressive damage. Progressive damage affects the normal and shear stiffnesses following

approach in Equation 2.2.28. There are ten strength parameters required for the model (longitudinal tensile strength, longitudinal compressive strength, transverse compressive strength, through thickness tensile strength, crush strength, fibre mode shear strength, matrix mode shear strengths in three planes). The critical values for damage parameter, compressive volume strain and tensile volume strain may be defined for final element failure (element erosion). The model MAT_161 correlates failure criteria with the set of stiffnesses. Tensile and shear failure criteria lead to instantaneous loss of load carrying capability of the layers. The compressive modes are treated differently. For fibre compressive failure, the residual strength is assumed and defined by the input scale factor. For matrix in compression normal stress is assumed to be linearly elastic, but the shear stresses are set to constant equal to fracture strength (like in perfect plasticity models, where stress is constant and equal to yield limit).

Material **MAT_LAMINATED_FRACTURE_DAIMLER_PINHO** (**MAT_261**) is the progressive damage model. The fibre failure was modelled by maximum stress for tensile failure and fibre compressive failure was based on LaRC03 (Dávila and Camanho, 2003). Matrix transverse tension and compression failure criteria were based on (Puck and Schürmann, 1998, 2002). The progressive damage was modelled by damage variables affecting the stress components. The damage variables evolve linearly basing on the fracture toughness. The model requires six strength parameters: tensile and compressive longitudinal and transverse strengths and longitudinal and in-plane shear strengths. Additional parameter defined in the input is the fracture angle in pure transverse compression and four fracture toughness that are used in the progressive damage part of the model.

Another model, **MAT LAMINATED FRACTURE DAIMPLER CAMANHO** (**MAT_262**) is similar to MAT_261. It also bases on the LaRC03 failure criteria and uses fracture toughness to control the progressive damage. The input parameters are the six strength parameters (tensile and compressive longitudinal and transverse strengths and longitudinal and in-plane shear strengths). Seven fracture toughnesses determine damage evolution.

2.3 Summary

This chapter provided necessary background on composite mechanics. It commented on the types of composites, their linear elastic behaviour and damage mechanisms. Furthermore, the notation used throughout this work was introduced as well as the spectral decomposition, which is crucial to the proposed model development.

The popular composite failure criteria were presented in this chapter. They are by no means all of the developed theories. The most popular theories were presented here. The large number of the theories and models makes it almost impossible to evaluate all of them at once. Different notation used in each of the theories additionally hinders recognising similarities between them. A very good evaluation of composite constitutive models was completed during WWFE by Soden, Kaddour and Hinton, (2004). It revealed that neither of sometimes very elaborate models was capable of predicting the strength of the material accurately in all load cases. Orifici, Herszberg and Thomson (2008) also provided a good list of failure theories. The large number of strength theories for the composites is not reflected in the number of available composite models in commercial FE software. There are few models available in LS-Dyna. Among the well-documented ones, for which the failure criteria can be easily tracked three models use the Chang and Chang (1987) failure theory (or closely related one). Two models use the Hashin failure criteria and two are strongly based on LaRC03 failure criteria. In LS-Dyna models damage is incorporated by changing material's elastic stiffnesses, which results in affecting the diagonal of the compliance tensor. Damage initiation criteria suggested in the model developed in the thesis uses a different approach. It was not directly compared to above mentioned formulations, nevertheless, it would be a natural next step in material behaviour comparison.

Summing up, the available theoretical and implemented material models have their limitations. Majority of the models assume *a priori* stiffness parameters that are affected by damage. One very significant limitation in all presented material models is lack of consideration for the high velocity impact as none of the models mentions coupling with equation of state. In contrast to above-mentioned empirical models, the model introduced in this work offers a consistent physical description of failure mechanisms. This allow incorporating an equation of state and in turn high velocity impact modelling.

3 Continuum mechanics, thermodynamics and damage mechanics framework

Modelling is an attempt to describe complex reality by a finite number of equations and variables. It aims at simplifying the physics laws so that they can be calculated effectively but still be able to accurately predict most important phenomena and capture materials' or structures behaviour. Therefore, derivation of material model should start with physics laws and rules. Along way simplifications and additional assumptions should be added to focus on the most important features and conditions. There are three main fields that aid material modelling, namely, **continuum mechanics**, **thermodynamics** and **damage mechanics**.

Continuum mechanics describes motion (translation and rotation) and deformation of materials using conservation laws (mass, momentum and energy). It also gives the necessary definitions for quantification of internal forces in the material (stresses) depending on the deformation (strains) through constitutive laws.

Continuum thermodynamic framework assures that the material model is thermodynamically consistent i.e. it does not violate the thermodynamic laws.

Damage mechanics provides a basis for representation of the micro- and mesoscale damage mechanisms at the continuum scale by the effect they have on the macroscopic material properties.

The constitutive model presented in this work is developed in the framework of continuum mechanics and thermodynamics. Damage in the model is represented by the damage (internal) variables that are defined consistently with the thermodynamic laws. This assures that every thermodynamic damage state in the material is physically admissible. All the important theories and concepts that were used in the model development are presented in this section for the sake of clarity and completeness.

3.1 Continuum mechanics

The fact that matter is built of atoms is obvious nowadays. However, analysis of a behaviour of a structure taken as a collection of atoms (or even more fundamental particles) is not practical. This is firstly due to the scale at which the structures are designed and observed, which is extremely large in comparison to the atomic scale. Secondly, the assessment of the

properties (e.g. by mechanical tests) is performed on the specimens, that have relatively large dimensions (Mase and Mase, 1999). These two facts justify the use of the concept of continuum, which postulates that the matter can be described as continuous with no regards to its discrete structure at large enough scales.

Detailed knowledge of the microscopic structure of a material is not required in continuum mechanics. The continuum is instead described by macroscopic field quantities such as density, temperature or velocity. Three main parts of continuum mechanics can be identified, i.e. the study of motion and deformation (**kinematics**), the study of stress (the **concept of stress**) and the mathematical description of the fundamental laws of physics governing the continuum motion (**balance principles**) (Holzapfel, 2000).

Continuum mechanics can be used to describe fluids and solids, which in turn identifies two main fields in continuum mechanics – fluid and solid mechanics. Only the latter is relevant for this work. The concepts and aspects of continuum mechanics that are essential in the model development are presented in the subsequent chapters.

3.1.1 Representative volume element

Continuum mechanics offers a convenient way of describing material's behaviour without insight into its microscopic structure. Treating material as a continuum requires homogenisation of its properties. This highlights an important concept which is the **Representative Volume Element** (RVE). There are several definitions of the RVE (conveniently listed in Gitman, Askes and Sluys (2007)). Generally, the RVE can be described as the minimum volume of the material that is capable of capturing material deformation processes accurately and giving the representative, mean response of the material (Ostoja-Starzewski, 2002; Kanit *et al.*, 2003; Khisaeva and Ostoja-Starzewski, 2006; Gitman, 2007; Gitman, Askes and Sluys, 2007; Li, Singh and Talreja, 2009; Kamiński and Pawlak, 2015). It is therefore required that the RVE is sufficiently large with respect to the microstructure of the material. The RVE is well defined under either of the two conditions: if a material has a periodic structure or the size is large enough to be statistically representative (consists of sufficiently large number of microscale elements) (Ostoja-Starzewski, 2002). This brings in a concept related to the RVE, a Repetitive Unit Cell (RUC), which is the material 'portion' whose structure is repeated throughout the material. Examples of RUC in a composite are presented in Figure 3.1.1.

a)

b)

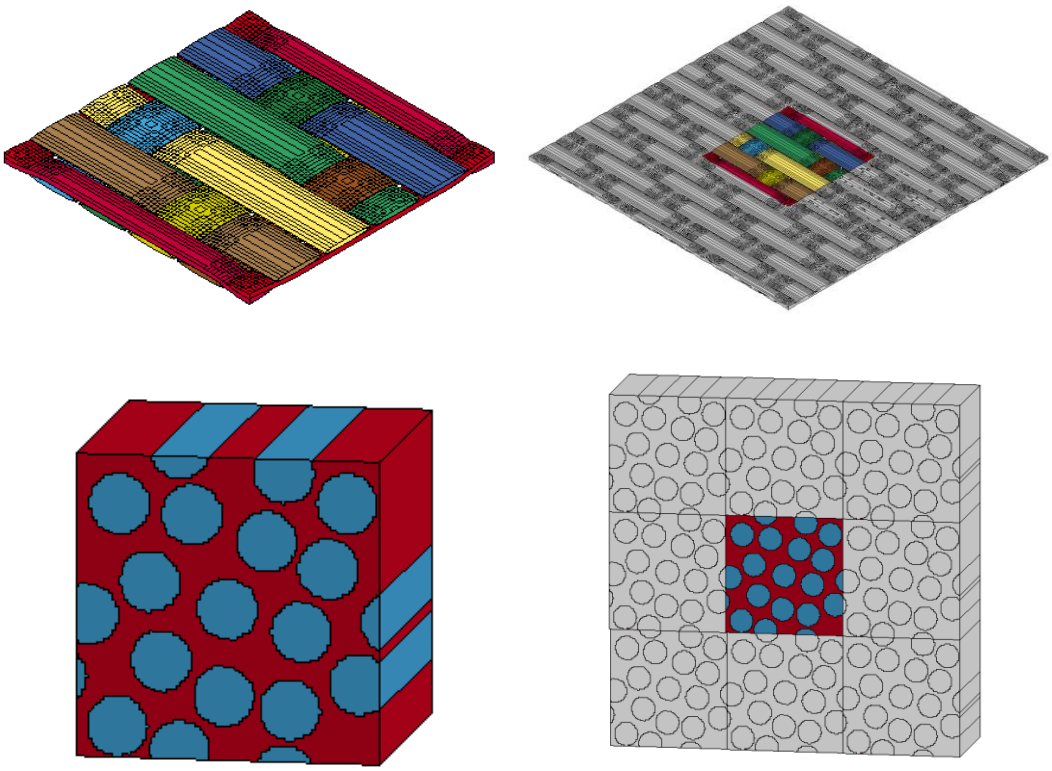

Figure 3.1.1 Repetitive Unit Cell: a) woven composite, b) unidirectional composite

3.1.2 Stress

Material loaded by the set of external forces maintains its integrity due to existence of the internal forces. If the body is in static equilibrium, the sum of the external and internal forces must be equal to zero. Figure 3.1.2 shows the imaginary cut of a material.

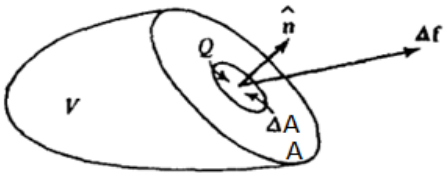

Figure 3.1.2 Forces acting on the imaginary cut in a material (Malvern, 1969, p.69, adjusted notation)

If a material is in static equilibrium, the internal force acting on the cut surface must balance the external forces. This holds for any point of the continuum. If elementary surface (ΔA) is considered, the traction vector (force per unit area) can be defined as:

$$\mathbf{t} = \lim_{\Delta A \to 0} \frac{\Delta \mathbf{f}}{\Delta A} \,. \qquad 3.1.1$$

Splitting of the traction vector into components collinear with Cartesian coordinate system leads to identification of the stress state as presented in (Figure 3.1.3).

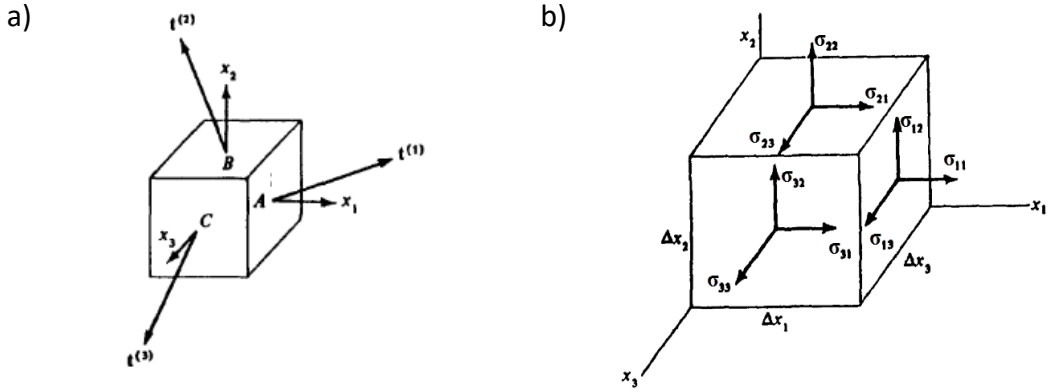

Figure 3.1.3 a) Traction vectors, b) cartesian stress tensor components (Malvern, 1969, pp. 70-71)

The stress tensor can be defined as:

$$\mathbf{f} = \boldsymbol{\sigma}\mathbf{n}, \qquad f_i = \sigma_{ij} n_j, \qquad \textbf{3.1.2}$$

where $\boldsymbol{\sigma}$ is the second order symmetric **Cauchy stress** tensor. The stress components for which the traction vector is collinear with the vector normal to the surface (σ_{11}, σ_{22} and σ_{33}) are called the normal stresses. All other stress components ($\sigma_{12} = \sigma_{21}$, $\sigma_{13} = \sigma_{31}$ and $\sigma_{23} = \sigma_{32}$) are known as tangential or shear stresses.

3.1.3 Displacement, deformation and strain

When the external force is applied to the material it changes its state. Depending on the conditions and material properties it can result in displacement, deformation or both. To determine how a material reacts to application of the external force, concepts of displacement, deformation and strain are necessary.

The simplest example of **displacement** is a rigid-body displacement (translation or rotation). In the rigid body particles do not change the relative position, and thus the body preserves its volume and shape. In other words, the rigid body motion can be defined by the changing material frame.

However, displacement is not limited to rigid bodies. On the contrary, an arbitrary displacement of a body, besides a rigid body displacement, includes **deformation**, i.e. change in shape or volume.

Displacement sequence that leads to the certain material state is called **motion**. Mathematically, it can be expressed as:

$$\mathbf{x} = \chi(\mathbf{X}), \tag{3.1.3}$$

where χ is motion, $\mathbf{x}$ is position of the point X at time t and $\mathbf{X}$ is position of the same point at the reference time. For hyperelastic materials motion is independent of time history. Definition of the deformation in a material requires introduction of another concept, namely, **deformation gradient** $\mathbf{F}$, which is given by the differential of Equation 3.1.3:

$$d\mathbf{x} = \frac{\partial \mathbf{x}}{\partial \mathbf{X}} d\mathbf{X}, \qquad \mathbf{F}(\mathbf{X}) = \frac{\partial \mathbf{x}}{\partial \mathbf{X}} = \frac{\partial \chi(\mathbf{X})}{d\mathbf{X}}. \tag{3.1.4}$$

For undeformed body, the deformation gradient simplifies to the identity tensor, giving.

$$d\mathbf{x} = d\mathbf{X}. \tag{3.1.5}$$

Deformation gradient is then used to define **strain tensors**. Left and right **Cauchy-Green deformation tensors** ($\mathbf{C}$ and $\mathbf{b}$ respectively) are defined by the product of deformation gradient as:

$$\mathbf{C} = \mathbf{F}^T\mathbf{F}, \qquad \mathbf{b} = \mathbf{F}\mathbf{F}^T. \tag{3.1.6}$$

The above tensors can be used as independent variables in the material constitutive model. However, often use of the strain tensors whose value equals to zero for an undeformed body is more convenient. The commonly used strain tensors are Green-Lagrange and Euler-Almansi strain tensors given respectively by:

$$\mathbf{E} = \tfrac{1}{2}\left(\mathbf{F}^T\mathbf{F} - 1\right) \qquad \boldsymbol{\varepsilon} = \tfrac{1}{2}\left(1 - \mathbf{F}^{-T}\mathbf{F}^{-1}\right) \tag{3.1.7}$$

Composites are the elastic-brittle materials with practically no plastic deformation. Consequently, the strains that are expected in the material can be described as infinitesimal. The strain tensor used in the constitutive model developed in this work is the Euler-Almansi strain tensor which is conjugate to the Cauchy stress tensor $(\boldsymbol{\sigma})$, which was introduced in the previous section.

3.2 Continuum thermodynamics

Thermodynamics is a study of energy and energy related phenomena. Two major branches can be identified within. **Statistical thermodynamics** deals with molecules and atoms and **classical (continuum) thermodynamics** is related to continuous matter. The latter is an obvious and consistent choice to be used along with continuum mechanics.

A deformed continuum possesses both thermal and mechanical energy. A **thermodynamic state** of a continuum is defined by macroscopic **thermodynamic state variables**. The necessity to consider thermodynamics in material constitutive model is dictated by the dissipative character of damage and need to model dynamic response of the material. During damage evolution energy is lost and entropy increases. To assure that the fundamental laws of physics are not violated and that the modelled material state is physically admissible, it is inevitable to consider thermodynamics.

3.2.1 Thermodynamics with internal variables

There are few thermodynamic theories used to describe the dissipative processes – **thermodynamics of irreversible processes**, **rational thermodynamics** and **thermodynamics with internal variables** (Ostoja-Starzewski, 2002). The latter is most appealing for this work. It does not have the limitation of being applicable only to the states close to equilibrium which is characteristic of the thermodynamics of irreversible processes (Djordjevic, 2011). Internal variables allow for definition of the fictitious thermodynamic equilibrium state. Therefore, determination of the current thermodynamic state is based on the current values of deformation gradient, temperature and set of internal variables without reference to the history of these variables (Holzapfel, 2000). This shows the superiority of thermodynamics with internal variables over rational thermodynamics in which the knowledge of the deformation history is essential.

In thermodynamics with internal variables the material state is described by two different types of variables: **external** and **internal**. External variables are typical thermodynamic quantities such as temperature or deformation gradient which can be easily measured and controlled. The other type of variables used in material modelling are the **internal variables** (or hidden variables), which are used to account for structural changes within the material at microscopic scale. These variables are more elusive and not as well defined as external variables. They may be the inelastic strains (often used to model plasticity in metals), damage

and dislocation densities among others (Holzapfel, 2000). Internal variables indirectly provide information about the material deformation history and thus are often called **history variables**. Internal variables can be neither directly measured nor controlled. However, they may be determined by phenomenological experiments (Holzapfel, 2000). They can be either scalar or tensor quantities. The choice of the set of history variables, their mathematical form and evolution laws is one of the challenges of material modelling.

3.2.2 Basic laws of thermodynamics

The principle laws of thermodynamics that are most important in constitutive modelling are the first and the second law of thermodynamics. The first law of thermodynamics, known as the energy balance principle, states that the rate of change of the energy within a system is equal to the energy supplied to the system minus the work the system performs on its surroundings. Thus, for any isolated system the total internal energy is constant but can change its form (e.g. thermal, mechanical, chemical etc.).

The second law of thermodynamics states that the entropy cannot decrease in time. It is particularly important in modelling of irreversible processes. The entropy maximum postulate is also widely used in material modelling (Fischer and Svoboda, 2007). It states that 'values assumed by the extensive parameters […] are those that maximise the entropy' (Callen, 1998). In other words, between the two material states the entropy rate have to be maximised to maximise the total entropy. Practically, this introduces an additional constraint needed for relating the internal variables.

3.2.3 State variables

Thermodynamics with internal variables makes use of the set of the quantities that uniquely define the state of the material. These quantities are called state variables. State variables, depending on their nature can be divided into **extensive** and **intensive** variables. Mass, entropy, volume, displacement and strain are the examples of the extensive quantities. The characteristic feature of extensive quantities is size-dependence. This distinguishes extensive variables from the intensive variables, which are e.g.: stress, temperature and pressure. The intensive quantities are sometimes referred to as **generalised forces** and extensive quantities – **generalised displacements** by the analogy with force and displacement giving the mechanical work.

An important notion which is often used with regard to state variables are **conjugate variables**. The variables are conjugate if their product gives the result in energy units (e.g. stress and strain, temperature and entropy or force and displacement).

The increment of energy (du) can therefore be defined as the sum of the conjugate forces (y_k) and displacements (de_k) product:

$$du = \sum_{k=1}^{N} y_k de_k \ . \qquad \textbf{3.2.1}$$

Consequently, the conjugate force can be defined as the partial derivative of the energy with respect to the conjugate variable:

$$y_k = \frac{\partial u}{\partial e_k} . \qquad \textbf{3.2.2}$$

In this work the forces conjugate to damage variables were used to define the damage potentials (defining the damage initiation and evolution).

3.2.4 State potentials

Thermodynamic **state potentials** are the scalar quantities that define the thermodynamic state of the material. State potentials are useful in definition of hyperelastic materials, as they can be explicitly defined by the current values of the state variables. First of the examples of the state potential is **internal energy**, which can be defined as the capacity of the material to release energy in the form of work or heat. Another example of the state potential is enthalpy. It is the measure of the energy that can be released in the form of non-mechanical (e.g. chemical) work and heat. **Gibbs energy** defines the amount of energy that can be released as non-mechanical work. The last state potential described in this work is the **Helmholtz free energy** which is the capacity of the material to release energy as work. The relation between the state potentials is presented in Figure 3.2.1.

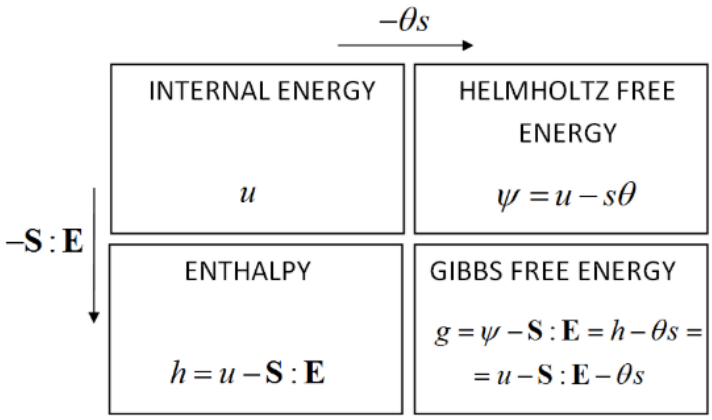

Figure 3.2.1 Relationship between thermodynamic potentials (Djordjevic, 2011)

Helmholtz free energy is the state potential commonly used in material modelling. It defines the material capability of performing work at constant temperature. Thus, not only is it inseparably connected to the strain energy, but also includes the chemical or damage potential. Helmholtz free energy is a function of strain and temperature:

$$\Psi(\mathbf{E},\theta) = u(\mathbf{E},s) - \theta s\,, \qquad 3.2.3$$

where $\mathbf{E}$ is Green-Lagrange strain tensor that is energy conjugate to Second Piola Kirchhoff stress tensor $\mathbf{S}$, θ is temperature and s is entropy. The specific definition of Helmholtz free energy used in this work is presented in Section 6.1.

3.2.5 Damage potentials

Initiation and evolution of internal damage variables is controlled by the so-called **pseudo** or **damage potentials**. The damage potentials consist of the loading potential and the limit function value which separate the elastic and inelastic (e.g. plastic or damage) material behaviour. The loading potential (Φ_1) is the function of the forces conjugate to variables defining the inelastic processes (y_i). It assumes different forms depending on the state potentials and damage variables used in the model. The hardening potential (Φ_2) depends on the forces conjugate to internal state variables defining hardening of the material (y_j) and controls the evolution of failure surface initially defined by ω_0. The general form of damage potential is expressed by:

$$\Phi\left(y_i, y_j\right) = \Phi_1\left(y_i\right) - \left(\Phi_2\left(y_j\right) + \omega_0\right). \quad \textbf{3.2.4}$$

Function Φ_2 is required for modelling of hardening and softening behaviour of materials whose material load limit varies with evolution of inelastic processes. The common approach in damage modelling is associative flow. It restricts the damage potential values to the non-positive values:

$$\Phi\left(y_i, y_j\right) = \Phi_1\left(y_i\right) - \left(\Phi_2\left(y_j\right) + \omega_0\right) \le 0. \quad \textbf{3.2.5}$$

Elastic material behaviour is observed when loading potential is lower than the limit:

$$\Phi_1\left(y_i\right) \le \Phi_2\left(y_j\right) + \omega_0. \quad \textbf{3.2.6}$$

If loading potential reaches a limit defined by hardening potential and initial failure threshold the material starts to behave non-elastically which results in evolution of the internal damage-related variables. During damage evolution the damage-related internal variables must satisfy Equation 3.2.7 as a consequence of associative flow:

$$\Phi\left(y_i, y_j\right) = \Phi_1\left(y_i\right) - \Phi_2\left(y_j\right) - \omega_0 = 0. \quad \textbf{3.2.7}$$

If material exhibits no hardening or softening behaviour (perfect inelastic behaviour), the hardening function equals to zero, so:

$$\Phi\left(y_i\right) = \Phi_1\left(y_i\right) - \omega_0 \le 0 \quad \textbf{3.2.8}$$

The hardening potential $\Phi_2\left(y_j\right)$ is greater than zero for the materials that exhibit hardening behaviour. Therefore, with damage evolution the allowed loading potential increases. The contrary behaviour – softening is associated with negative hardening potential $\Phi_2\left(y_j\right)$. The different behaviours are described by Figure 3.2.2.

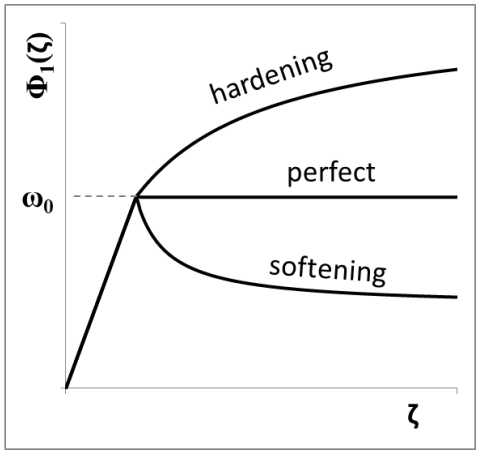

Figure 3.2.2 Different material beahviour – perfect, herdening and softening

The most commonly used loading potential is stress, which is the force conjugate to the strain. After reaching the critical value of stress, perfectly plastic materials stress is equal to its stress limit (Figure 3.2.3 - a)). It is associated with the evolution of plastic strain, which is the internal variable describing plastic deformation. If a material exhibits strain hardening the stress level behind the yield limit is higher (Figure 3.2.3 - b)) than for the equivalent strain for the perfectly plastic material. Strain softening results in lower stress after yield initiation (Figure 3.2.3 - c)).

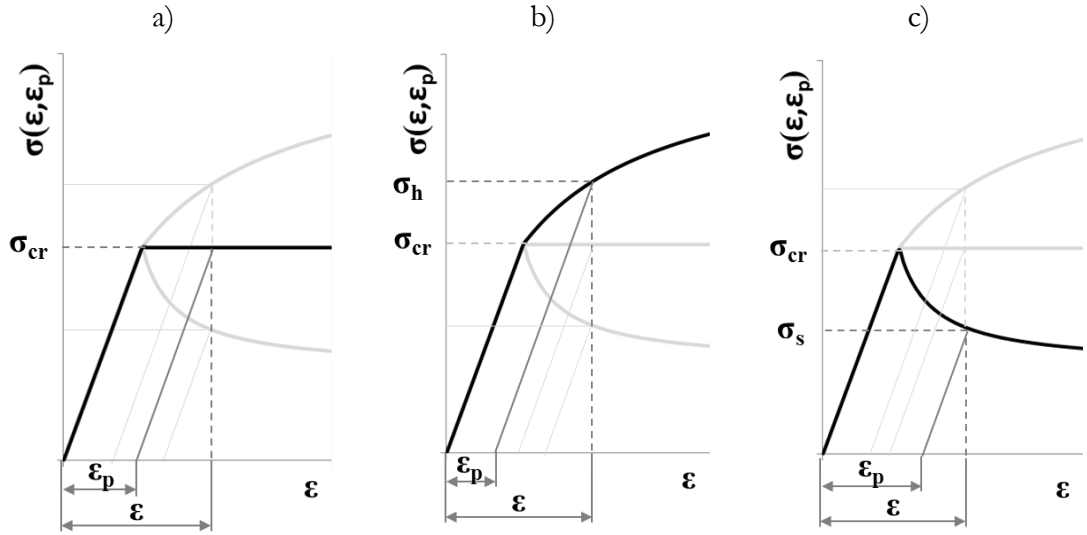

Figure 3.2.3 Plasticity: a) perfect plasticity, b) strain hardening, c) strain softening

The plasticity is the simplest example, as stress and are commonly used and well understood variables. However, such graphs are characteristic for any choice of conjugate force displayed on the vertical axis and the internal variable giving the magnitude of conjugate displacement on the horizontal one.

In case of this work, damage is defined by damage variable (not inelastic strain). Thus, the damage conjugate force is a function of strain energy instead of stress. For such a case, the damage potential with respect to squared strain can be represented by Figure 3.2.4 - a) and the corresponding stress vs strain graph by Figure 3.2.4 - b).

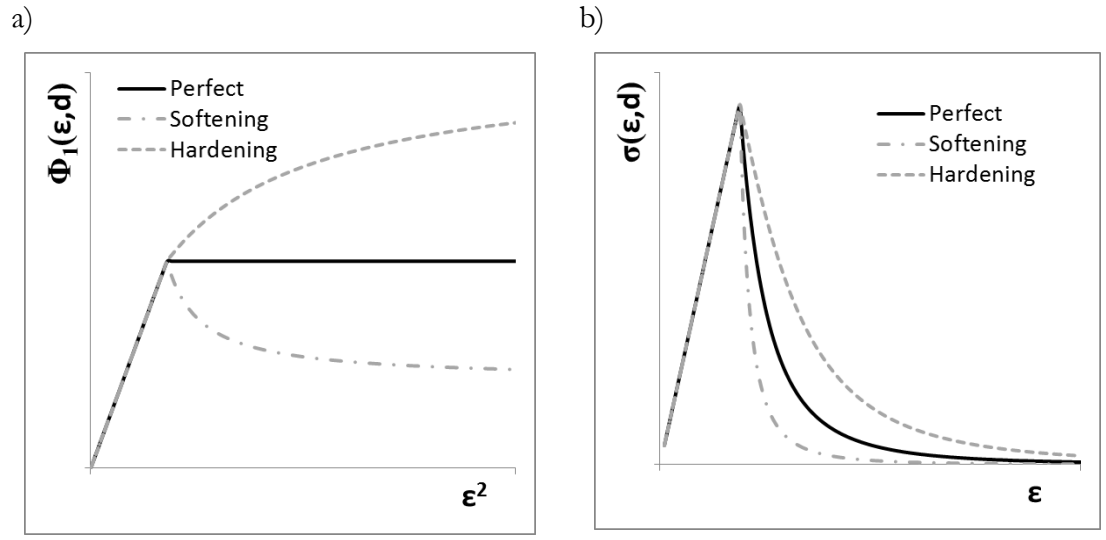

Figure 3.2.4 a) Loading potential vs squared strain and b) stress vs strain characteristic for the developed model

The graphs were presented here to avoid confusion between the stress - strain behaviour (being at the same time the damage potential graph) presented in Figure 3.2.3 and Figure 3.2.4 (where stress is not a damage potential). Note, that increase in stress after damage initiation is not observed in composite mechanical tests. Therefore, behaviour presented in Figure 3.2.4 - b) is typical of brittle composites. Hence, here terms hardening and softening are used in slightly different sense than usually. They refer to the deviation from the assumed perfect damage behaviour rather than the stress behaviour (drop or increase after damage/plasticity initiation). The specific form of the damage potential used in this work is given in Section 6.1.2.

3.3 Continuum damage mechanics

Damage is very often associated with the macroscale which is a natural scale to observe it as macroscopic cracks, scratches, voids etc. One should remember that it evolves from an atomic scale. The slips in the atomic structure, microcracks and voids are present in the material well before they can be observed at macroscopic level. They affect the material performance and can evolve to larger scales. The thorough analysis of material's damage

should start at atomic scale, where basic phenomena occur. It should be followed by the analysis of microscale damage and progressed to mesoscale analysis.

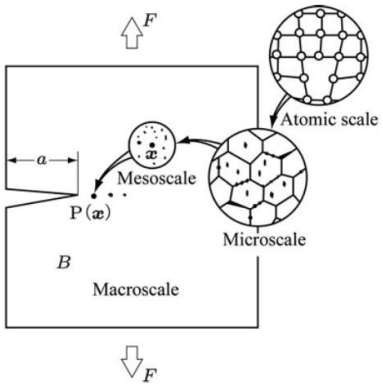

Figure 3.3.1 Scales of damage (Murakami, 2012, p.4)

All the scales mentioned above are important for understanding of the nature of damage. However, for engineering applications it would be difficult and inefficient to concentrate on atomic and microscales while evaluating the structures. Far more convenient is the approach of homogenisation and treating damage at a continuum scale by analogy to the continuum mechanics. Statistical nature of the materials justifies the use of the **continuum damage mechanics** (CDM). It allows for assessment of the extent of damage in the material without insight into its structure. The introduction of CDM is attributed to Kachanov (Krajcinovic and Silva, 1982; Lemaitre, 1985), whose ideas are presented in the Section 3.3.1. CDM is a representation of damage by its effects on material thermo-mechanical properties at a continuum scale. Typically, modelling of damage includes four steps – representing damage by the damage variable, defining damage growth (evolution equation), determination of a material response to damage and solving the equations for the particular case (Murakami, 2012).

3.3.1 Effective stress

Damage, unlike strain or force, cannot be directly measured. According to Chaboche (1988) one of approaches to measure an extent of damage is to investigate the materials' microstructure. Nevertheless, he recognised three major difficulties in this approach. The first one is the need to destroy material to be able to perform microstructural analysis. Secondly, the characterisation of the material initial state is difficult e.g. because of manufacturing defects. With increasing progress in all engineering branches it is nowadays possible to measure the extent of microstructural defects in a material by non-destructive tests (NDT) such as radiography (including computed tomography – CT), ultrasonics,

acoustic emission and infrared thermography (Kim, 2000). Thus, the two first difficulties can be solved. The final difficulty identified by Chaboche is need for the macroscopic variables corresponding to damage, which is more fundamental problem.

Alternative way of determination of a damage extent in a material was suggested by Kachanov (Kachanov, 1999). He proposed assessing damage by the effect it has on the material macroscopic properties. This idea became the foundation of CDM. Kachanov assumed the existence of the scalar function of 'continuity', which for the initial (undamaged) state of material is equal to one. With progressing damage, the continuity of a material reduces leading to rupture after reaching zero. Later the 'continuity' function was replaced for convenience by damage function ranging from zero for undamaged material, up to unity for fully destroyed one (Rabotnov, 1969; Murakami, 2012).

The above introduces one of the most important notions in CDM which is the **effective stress concept**. It follows directly from Kachanov's idea. He introduced the concept of effective stress as the 'mean density of forces acting on the elementary surface that effectively resists' external loading (Lemaitre, 1985).

It can be represented by:

$$\tilde{\sigma} = \frac{\sigma}{1-d}, \qquad \textbf{3.3.1}$$

where $\tilde{\sigma}$ is effective stress that is higher than nominal stress σ for positive damage variable d. Practically, this idea can be viewed as a reduction of the effective load carrying area caused by damage:

$$d = \frac{A_D}{A} = \frac{A-\tilde{A}}{A}, \qquad \textbf{3.3.2}$$

where A_D and $\tilde{A}$ are surface area of damaged and undamaged material respectively. The effective and nominal stress are linked by the following equation:

$$F = \sigma A = \tilde{\sigma}\tilde{A}, \qquad \textbf{3.3.3}$$

where $\tilde{\sigma}$ is effective stress in the material.

3.3.2 Damage variables

Following the introduction of CDM, the number of related theories evolved. Initially, isotropic damage (and what follows, scalar damage variable) was considered. However, later damage was generalised to anisotropic cases and in turn represented by tensors. Since the first definition of damage variable there has been significant amount of research in the field of continuum damage mechanics. One of the important considerations of the research in CDM field is the mathematical formulation of damage. Damage as a scalar is only applicable to the cases where the it can be assumed isotropic i.e. where there is a uniform distribution of cavities, voids etc. However, in reality damage is rarely isotropic (Schreyer, 1995). Several authors tried to represent damage in the form of vectors (e.g. Krajcinovic and Fonseka (1981)), second order tensors (e.g. Vakulenko and Kachanov (1971), Betten (1986, 1992), Cordebois and Sidoroff (1982)) and higher order tensors (e.g. Chaboche, Lesne and Maire (1995), Onat and Leckie, 1988)(Murakami, 1987).

It is highly relevant to choose an appropriate mathematical representation of damage, to be able to account for all its effects without extreme computational effort. According to Cauvin and Testa (1999) the proper choice of damage variables remains the most difficult part of development of material damage model.

The effective stress concept was introduced in scalar notation for one dimensional problem with scalar damage variable. However, it can be generalised for the tensor damage variable by (Murakami, 2012):

$$\tilde{\boldsymbol{\sigma}} = \left(\mathbf{I} - \mathbf{D}\right)^{-1} : \boldsymbol{\sigma}. \qquad \textbf{3.3.4}$$

Note that this equation implies that the effective stress tensor is not necessarily symmetric.

3.3.3 Equivalence hypotheses

Equivalence hypotheses are strictly related to the effective stress theory. Effective stress is a stress that results in the same material response in an undamaged material as an applied stress induces in a damaged one. Two equivalence hypotheses are commonly used – the elastic strain equivalence hypothesis and the elastic strain energy hypothesis (Hansen and Schreyer, 1994; Murakami, 2012).

Strain equivalence hypothesis states that the effective stress acting on an undamaged material gives the same strain as applied stress to a damaged material:

$$\boldsymbol{\varepsilon} = \mathbf{S}(\mathrm{D}) \cdot \boldsymbol{\sigma} = \mathbf{S}_0 \cdot \tilde{\boldsymbol{\sigma}} . \qquad \textbf{3.3.5}$$

where $\boldsymbol{\varepsilon}$, $\boldsymbol{\sigma}$ and $\tilde{\boldsymbol{\sigma}}$ are respectively strain, stress and effective stress tensors. $\mathbf{S}(\mathrm{D})$ and $\mathbf{S}_0$ are compliance tensors of damaged and undamaged material. Strain equivalence hypothesis is well illustrated by Figure 3.3.2.

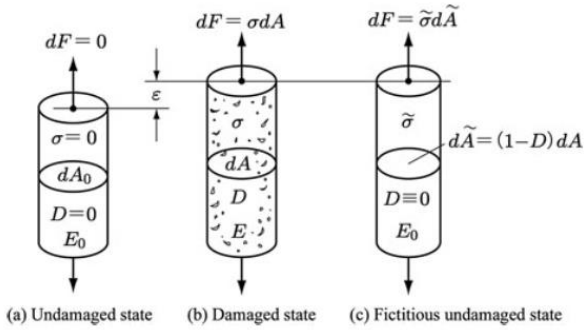

Figure 3.3.2 Concept of effective stress (Murakami, 2012 p.18)

The relation between a compliance tensor of a damaged and an undamaged material is:

$$\boldsymbol{\varepsilon} = \mathbf{S}_0 \cdot \tilde{\boldsymbol{\sigma}} = \mathbf{S}_0 \cdot (\mathbf{I} - \mathbf{D})^{-1} \cdot \boldsymbol{\sigma} = \mathbf{S}(\mathrm{D}) \cdot \boldsymbol{\sigma} \qquad \textbf{3.3.6}$$

Consequently, compliance and stiffness tensors of a damaged material can be respectively expressed as:

$$\mathbf{S}(\mathrm{D}) = \mathbf{S}_0 \cdot (\mathbf{I} - \mathbf{D})^{-1}, \qquad \mathbf{C}(\mathrm{D}) = \mathbf{C}_0 \cdot (\mathbf{I} - \mathbf{D}) . \qquad \textbf{3.3.7}$$

Strain energy equivalence hypothesis states that the strain energy (W) of the damaged material under applied stress is equal to the strain energy of an undamaged material under effective stress. This is postulated by:

$$2W = \boldsymbol{\sigma} \cdot \mathbf{S}(\mathrm{D}) \cdot \boldsymbol{\sigma} = \tilde{\boldsymbol{\sigma}} \cdot \mathbf{S}_0 \cdot \tilde{\boldsymbol{\sigma}} . \qquad \textbf{3.3.8}$$

After substitution of the effective stress from equation 3.3.4, the following relation is established:

$$\boldsymbol{\sigma} \cdot \mathbf{S}(\mathrm{D}) \cdot \boldsymbol{\sigma} = \boldsymbol{\sigma} \cdot (\mathbf{I} - \mathbf{D})^{-T} \cdot \mathbf{S}_0 \cdot (\mathbf{I} - \mathbf{D})^{-1} \cdot \boldsymbol{\sigma} . \qquad \textbf{3.3.9}$$

The damaged material compliance and stiffness tensors can therefore be defined as:

$$\mathbf{S}(\mathrm{D}) = (\mathbf{I}-\mathbf{D})^{-T} \cdot \mathbf{S}_0 \cdot (\mathbf{I}-\mathbf{D})^{-1}, \qquad \mathbf{C}(\mathrm{D}) = (\mathbf{I}-\mathbf{D})^{T} \cdot \mathbf{C}_0 \cdot (\mathbf{I}-\mathbf{D}). \qquad \textbf{3.3.10}$$

The difference between strain and strain energy equivalence hypotheses is illustrated in Figure 3.3.3. Material loaded from point 1 is within its elastic region up to point 2. Damage evolution results in reduction of the material load carrying capability. Upon further loading, material stress – strain state is described by point 3. The stress – strain relation defined by strain equivalence hypothesis is marked with point 7. It is clear that the effective stress acting on the undamaged material (with Young's modulus E_0) results in the same strain as the nominal stress on the damaged material (with reduced Young's modulus E). On the other hand, the strain energy equivalence hypothesis is marked with point 5 that identify the effective stress and strain. The energy equivalence hypothesis assures that the strain energy given by the equivalent stress and strain for the undamaged material Young's modulus (area between points 1, 5 and 4) is equal to the strain energy of the damaged material (area between points 1, 3, 6).

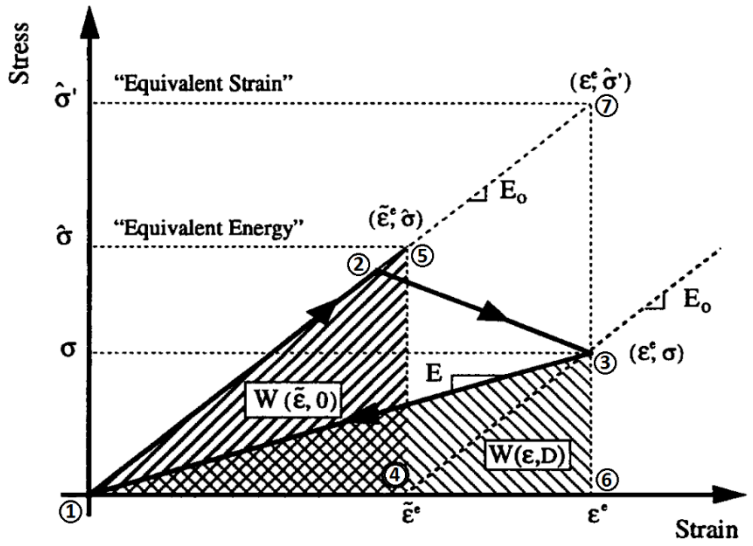

Figure 3.3.3 Difference between strain and strain energy equivalence hypotheses (Hansen and Schreyer, 1994)

3.4 Thermodynamic framework

Constitutive model is defined by the set of constitutive equations that interrelate model's variables. Different materials require different sets of equations to fully determine material's response to strain and/or temperature changes. If an elastic material state can be described by its' elastic energy, it is called the **hyperelastic** (or Green-elastic) material. The model

presented in this work is based on hyperelastic formulation. Thus, the constitutive laws can be derived using the irreversible thermodynamics with internal variables. Considering material's thermomechanical behaviour, it is convenient to use Helmholtz free energy. It defines material capability to perform work at constant temperature and thus is suitable as a material's thermodynamic potential.

3.4.1 State potential

Thermodynamic framework for the material model developed in this thesis was based on the general framework presented by Hansen and Schreyer (1994). The relation between the Helmholtz free energy and the internal energy densities is given by:

$$\Psi = u - s\theta, \tag{3.4.1}$$

where Ψ, u and s are respectively Helmholtz free energy, internal energy and entropy all given per unit volume and θ is temperature. The quantities defined per unit volume (densities) are convenient choice for FEA.

Following Hansen and Schreyer (1994) the isothermal assumption gives the fair approximation of the processes in which the amount of heat generated is not significant and those that occur rapidly. Helmholtz free energy density can be defined as a function of strain $(\boldsymbol{\varepsilon})$ and damage variables. In the most general form the damage variables are tensors. $\mathbf{D}$ defines the degradation of material integrity, $\mathbf{D}^S$ defines the shift of a damage surface and $\mathbf{D}^H$ defines the evolution of a damage surface.

$$\Psi = \Psi\left(\boldsymbol{\varepsilon}, \mathbf{D}, \mathbf{D}^S, \mathbf{D}^H\right). \tag{3.4.2}$$

The Helmholtz free energy density is a portion of energy stored in a material due to mechanical or chemical work. It consists of the strain energy density (W) and damage energy density (H):

$$\Psi\left(\boldsymbol{\varepsilon}, \mathbf{D}, \mathbf{D}^S, \mathbf{D}^H\right) \equiv W\left(\boldsymbol{\varepsilon}, \mathbf{D}\right) + H\left(\mathbf{D}^S, \mathbf{D}^H\right). \tag{3.4.3}$$

The strain energy depends on strain and stiffness of a material. Following the effective stress concept, the stiffness of a material reduces due to damage, so the strain energy of a material can be expressed as:

$$W\left(\boldsymbol{\varepsilon},\mathbf{D}\right)=\frac{1}{2}\boldsymbol{\varepsilon}:\mathrm{C}\left(\mathbf{D}\right):\boldsymbol{\varepsilon}, \qquad \textbf{3.4.4}$$

where stiffness tensor $\mathrm{C}\left(\mathbf{D}\right)$ is a function of a damage variable. A form of a damage potential strongly depends on the damage mechanism of the material (e.g. reorganisation of chains in polymers or slip in the atomic structure in metals etc.).

3.4.2 Energy dissipation, damage conjugate forces, damage potential

Damage is a dissipative process, which means that the initial material's state cannot be recovered without performing work. The energy dissipation due to damage can be explained by necessity to break interatomic bonds to create a crack or dislocation in a material. The total Helmholtz free energy rate can be defined as:

$$\dot{\Psi}=\frac{\partial\Psi}{\partial\boldsymbol{\varepsilon}}:\dot{\boldsymbol{\varepsilon}}+\frac{\partial\Psi}{\partial\mathbf{D}}:\dot{\mathbf{D}}+\frac{\partial\Psi}{\partial\mathbf{D}^{S}}:\dot{\mathbf{D}}^{S}+\frac{\partial\Psi}{\partial\mathbf{D}^{H}}:\dot{\mathbf{D}}^{H}. \qquad \textbf{3.4.5}$$

The dissipation of the Helmholtz free energy (per unit volume) is defined by the rate of change of the state potential related to the damage variables:

$$\dot{\Upsilon}=-\frac{\partial\Psi}{\partial\mathbf{D}}:\dot{\mathbf{D}}-\frac{\partial\Psi}{\partial\mathbf{D}^{S}}:\dot{\mathbf{D}}^{S}-\frac{\partial\Psi}{\partial\mathbf{D}^{H}}:\dot{\mathbf{D}}^{H}. \qquad \textbf{3.4.6}$$

Recalling the definition of Helmholtz free energy (Equation 3.2.3) and differentiating it with respect to time:

$$\dot{u}=\dot{\Psi}+\theta\dot{s}=0, \qquad \textbf{3.4.7}$$

the entropy rate can be determined as:

$$\dot{s}=\frac{\dot{\Upsilon}}{\theta}=\frac{1}{\theta}\left(\frac{\partial\Psi}{\partial\mathbf{D}}:\dot{\mathbf{D}}+\frac{\partial\Psi}{\partial\mathbf{D}^{S}}:\dot{\mathbf{D}}^{S}+\frac{\partial\Psi}{\partial\mathbf{D}^{H}}:\dot{\mathbf{D}}^{H}\right). \qquad \textbf{3.4.8}$$

The forces conjugate to damage variables are identified as:

$$\mathbf{Y}=-\frac{\partial\Psi}{\partial\mathbf{D}}, \qquad \mathbf{Y}^{S}=-\frac{\partial\Psi}{\partial\mathbf{D}^{S}}, \qquad \mathbf{Y}^{H}=-\frac{\partial\Psi}{\partial\mathbf{D}^{H}}. \qquad \textbf{3.4.9}$$

The damage potential function is a function of damage conjugate forces. $\mathbf{Y}^S$ is the force resulting in the shift of damage surface and $\mathbf{Y}^H$ results in the damage surface evolution.

$$\Phi\left(\mathbf{Y},\mathbf{Y}^S,\mathbf{Y}^H\right)\equiv\Phi_1\left(\mathbf{Y}-\mathbf{Y}^S\right)-\Phi_2\left(\mathbf{Y}^H\right)-\omega_0\le 0. \qquad \textbf{3.4.10}$$

According to Hansen and Schreyer, (1994) scalar components of a damage potential should be homogeneous functions of degree one (HODO) of their arguments. The function F is called a homogenous function of degree one if the following holds:

$$F\left(cx,cy\right)=cF\left(x,y\right) \qquad \textbf{3.4.11}$$

An important property of a HODO function that is used later is:

$$\left(\frac{\partial\Phi_i\left(\mathbf{X}\right)}{\partial\mathbf{X}}\right):\mathbf{X}=\Phi_i\left(\mathbf{X}\right). \qquad \textbf{3.4.12}$$

It was already pointed out in Section 3.2.5 that damage potential is the function controlling the damage initiation and evolution in the material. It serves the function of both damage criterion and constraint in damage evolution laws.

3.4.3 Damage variables evolution

A relation between damage variables is established using the maximum energy dissipation rule. It states that among all the possible states the material assumes the one that maximises the entropy (Hansen and Schreyer, 1994). Therefore, evolution of the internal, damage related variables must maximise the energy dissipation rate.

Maximum energy dissipation rate is found using the Lagrangian functional L and Lagrange multiplier $\dot{\Lambda}$. This method allows for calculation of minimum of the function, given specific constraints. In this case the constraint comes from the associative flow i.e. damage potential during damage evolution equals to zero $\Phi=0$:

$$L=-\dot{\Upsilon}+\dot{\Lambda}\Phi \qquad \textbf{3.4.13}$$

Damage variable evolution is determined by calculation of the minimum of the Lagrangian functional (L):

$$\frac{\partial L}{\partial \mathbf{Y}} = -\dot{\mathbf{D}} + \dot{\Lambda}\frac{\partial \Phi_1\left(\mathbf{Y}-\mathbf{Y}^S\right)}{\partial \mathbf{Y}} = 0\,, \qquad \frac{\partial L}{\partial \mathbf{Y}^S} = -\dot{\mathbf{D}}^S + \dot{\Lambda}\frac{\partial \Phi_1\left(\mathbf{Y}-\mathbf{Y}^S\right)}{\partial \mathbf{Y}^S} = 0\,, \qquad \textbf{3.4.14}$$

$$\frac{\partial L}{\partial \mathbf{Y}^H} = -\dot{\mathbf{D}}^H + \dot{\Lambda}\frac{\partial \Phi_2\left(\mathbf{Y}^H\right)}{\partial \mathbf{Y}^H} = 0\,.$$

Consequently, rate of damage variables is equal to:

$$\dot{\mathbf{D}} = \dot{\Lambda}\frac{\partial \Phi_1\left(\mathbf{Y}-\mathbf{Y}^S\right)}{\partial \mathbf{Y}}, \qquad \dot{\mathbf{D}}^S = \dot{\Lambda}\frac{\partial \Phi_1\left(\mathbf{Y}-\mathbf{Y}^S\right)}{\partial \mathbf{Y}^S}, \qquad \dot{\mathbf{D}}^H = \dot{\Lambda}\frac{\partial \Phi_2\left(\mathbf{Y}^H\right)}{\partial \mathbf{Y}^H}\,. \qquad \textbf{3.4.15}$$

Explicit result for damage variables given in terms of the Lagrange multiplier requires knowledge about specific functions (Φ_1) and (Φ_2) that are characteristic for the model. The Lagrange multiplier value can be obtained from the initial constraint, i.e. $\Phi = 0$ and consistency condition $\dot{\Phi} = 0$.

General material constraints that define the loading and unloading conditions are defined using Kuhn-Tucker optimality conditions (Hansen and Schreyer, 1994):

$$\dot{\Lambda} \geq 0 \qquad \Phi \leq 0 \qquad \dot{\Lambda}\Phi = 0 \qquad \textbf{3.4.16}$$

The damage variables' rates $(\dot{\mathbf{D}})$ and $(\dot{\mathbf{D}}^S)$ can be easily related by observing that (using chain rule):

$$\frac{\partial \Phi_1\left(\mathbf{Y}-\mathbf{Y}^S\right)}{\partial\left(\mathbf{Y}-\mathbf{Y}^S\right)} = \frac{\partial \mathbf{Y}}{\partial\left(\mathbf{Y}-\mathbf{Y}^S\right)}\frac{\partial \Phi_1\left(\mathbf{Y}-\mathbf{Y}^S\right)}{\partial \mathbf{Y}} = \frac{\partial \Phi_1\left(\mathbf{Y}-\mathbf{Y}^S\right)}{\partial \mathbf{Y}}\,,$$

$$\frac{\partial \Phi_1\left(\mathbf{Y}-\mathbf{Y}^S\right)}{\partial\left(\mathbf{Y}-\mathbf{Y}^S\right)} = \frac{\partial \mathbf{Y}^S}{\partial\left(\mathbf{Y}-\mathbf{Y}^S\right)}\frac{\partial \Phi_1\left(\mathbf{Y}-\mathbf{Y}^S\right)}{\partial \mathbf{Y}^S} = -\frac{\partial \Phi_1\left(\mathbf{Y}-\mathbf{Y}^S\right)}{\partial \mathbf{Y}^S}\,, \qquad \textbf{3.4.17}$$

thus:

$$\frac{\partial \Phi_1\left(\mathbf{Y}-\mathbf{Y}^S\right)}{\partial\left(\mathbf{Y}\right)} = -\frac{\partial \Phi_1\left(\mathbf{Y}-\mathbf{Y}^S\right)}{\partial\left(\mathbf{Y}^S\right)}\,. \qquad \textbf{3.4.18}$$

It leads to the following relation between the damage variables $\dot{\mathbf{D}}$ and $\dot{\mathbf{D}}^S$:

$$\dot{\mathbf{D}}^S = -\dot{\mathbf{D}}. \tag{3.4.19}$$

Recalling that damage functions are HODO functions the dissipation rate can be rewritten using Equations 2.1.9, 2.1.11, 2.1.15 and 2.1.22 as:

$$\begin{aligned}
\dot{\Upsilon} &= \mathbf{Y}:\dot{\mathbf{D}} + \mathbf{Y}^S:\dot{\mathbf{D}}^S + \mathbf{Y}^H:\dot{\mathbf{D}}^H = \\
&= \mathbf{Y}:\dot{\Lambda}\frac{\partial\Phi_1\left(\mathbf{Y}-\mathbf{Y}^S\right)}{\partial\mathbf{Y}} - \mathbf{Y}^S:\dot{\Lambda}\frac{\partial\Phi_1\left(\mathbf{Y}-\mathbf{Y}^S\right)}{\partial\mathbf{Y}} + \mathbf{Y}^H:\dot{\Lambda}\frac{\partial\Phi_2\left(\mathbf{Y}^H\right)}{\partial\mathbf{Y}^H} = \\
&= \dot{\Lambda}\left[\left(\mathbf{Y}-\mathbf{Y}^S\right):\frac{\partial\Phi_1\left(\mathbf{Y}-\mathbf{Y}^S\right)}{\partial\mathbf{Y}} + \mathbf{Y}^H:\frac{\partial\Phi_2\left(\mathbf{Y}^H\right)}{\partial\mathbf{Y}^H}\right] = \\
&= \dot{\Lambda}\left[\Phi_1\left(\mathbf{Y}-\mathbf{Y}^S\right)+\Phi_2\left(\mathbf{Y}^H\right)\right] = \dot{\Lambda}\left[\Phi\left(\mathbf{Y},\mathbf{Y}^S,\mathbf{Y}^H\right)+\omega_0\right]
\end{aligned} \tag{3.4.20}$$

Optimality conditions given by Equation 3.4.16, allow simplification of the dissipation rate:

$$\dot{\Upsilon} = \dot{\Lambda}\omega_0. \tag{3.4.21}$$

Finally, entropy production per unit volume is defined as a function of one argument as:

$$\dot{s} = \frac{\dot{\Upsilon}}{\theta} = \frac{\dot{\Lambda}\omega_0}{\theta}. \tag{3.4.22}$$

3.5 Equation of state

In contemporary hydrocodes (codes for modelling of shock wave propagation) constitutive models typically separate material compressibility effects from strength effects which enables a consistent calculation of stresses. Further, this allows for the mean pressure to be defined through a scalar equation of state. These concepts were originally developed for isotropic materials with limited amount of research on anisotropic materials such as composites.

Quasi-static deformation process can be, with high degree of accuracy, defined as the isothermal process. In the isothermal process the change of pressure in the material is dependant only on the change of its volume (as the temperature is constant). Parameter that describes this relation is the bulk modulus (K). It relates the volumetric strain (ε_v) and pressure (p) by:

$$p = -3K\varepsilon_v , \qquad \text{3.5.1}$$

where volumetric strain is:

$$\varepsilon_v = \left(\varepsilon_1 + \varepsilon_2 + \varepsilon_3\right)/3 . \qquad \text{3.5.2}$$

Bulk modulus of an isotropic material is defined from other material parameters such as Young's modulus and Poisson's ratio e.g.:

$$K = \frac{E}{3\left(1-2\nu\right)} . \qquad \text{3.5.3}$$

If deformation process is dynamic, the assumption of constant temperature within the material is no longer valid and the deformation process is defined as adiabatic. Thus, pressure (p) is not only a function of volume (V) or volumetric strain (ε_v) but also of temperature (θ). The equation that relates pressure, volume and temperature is called **equation of state** (EOS). The general form of EOS is:

$$f\left(p, V, \theta\right) = 0 , \qquad \text{3.5.4}$$

where the function f is defined by the specific form of equation of state. The most well-known equation of state is the ideal gas EOS:

$$pV = mR\theta \qquad \text{3.5.5}$$

where m is number of moles and R is ideal gas constant. This EOS, however, is only applicable to the limited number of substances (characterised as ideal gases) under specific conditions (e.g. moderate temperatures). The equation of state accurately describing all kinds of matter regardless their physical state and conditions does not exist. The choice of an appropriate form of EOS for the specific material and loading case is therefore of vital importance. There is a large number of already developed equations of states. It was not in the scope of this work to thoroughly analyse them, nor to develop a new one. Equation of state chosen for this work is the Gruneisen EOS. It is commonly used to model solids, and was proved to be accurate in modelling of non-isotropic solids under dynamic loads (Vignjevic *et al.*, 2008; Vignjevic and Djordjevic, 2010). One of the noteworthy advantages of the Gruneisen EOS is that it has an analytical derivation. Furthermore, it has well established methods for defining the material constants and the large number of materials

was already characterised (Marsh, 1980; Steinberg, 1996). The theoretical bases of the Gruneisen EOS are presented in Appendix B.

3.5.1 Definition of pressure in non-isotropic materials

It was already pointed out that in order to model material's dynamic behaviour a material model needs to be coupled with equation of state. In this work, Gruneisen equation of state was chosen. This section expands the EOS theory to account for material anisotropy.

Definition of pressure in a non-isotropic material is more challenging than in an isotropic one. In isotropic materials pressure is the average of three normal stresses:

$$p(\sigma_\alpha) = -(\sigma_1 + \sigma_2 + \sigma_3)/3. \qquad \textbf{3.5.6}$$

Alternatively, it can be defined using normal strains and the bulk modulus (K):

$$p(\varepsilon_\alpha) = -K(\varepsilon_1 + \varepsilon_2 + \varepsilon_3). \qquad \textbf{3.5.7}$$

For isotropic materials equations 3.5.6 and 3.5.7 are identical, so either can be used to define pressure yielding the same result. However, it does not hold for non-isotropic materials.

It was postulated by Anderson *et al.*, (1994) that pressure in orthotropic materials is an average of normal stress components (Equation 3.5.6). Therefore, it depends not only on the volumetric strain but also on the shear strain:

$$\begin{aligned} p = -\frac{1}{3b}\Big\{ & E_1(1-\nu_{23}\nu_{32}) + E_2(1-\nu_{13}\nu_{31}) + E_3(1-\nu_{12}\nu_{21}) \\ & + 2\Big[E_1(\nu_{21}+\nu_{31}\nu_{23}) + E_1(\nu_{31}+\nu_{21}\nu_{32}) + E_2(\nu_{32}+\nu_{31}\nu_{12})\Big]\Big\}\varepsilon_v \\ & + \frac{E_1}{3b}\Big[(1-\nu_{23}\nu_{32}) + (\nu_{21}+\nu_{31}\nu_{23}) + (\nu_{31}+\nu_{21}\nu_{32})\Big]\varepsilon_1^d \\ & + \frac{E_2}{3b}\Big[(1-\nu_{13}\nu_{31}) + (\nu_{32}+\nu_{12}\nu_{31}) + (\nu_{21}+\nu_{31}\nu_{23})\Big]\varepsilon_2^d \\ & + \frac{E_3}{3b}\Big[(1-\nu_{12}\nu_{21}) + (\nu_{32}+\nu_{12}\nu_{31}) + (\nu_{31}+\nu_{21}\nu_{32})\Big]\varepsilon_3^d, \end{aligned} \qquad \textbf{3.5.8}$$

where: $b = 1-\nu_{12}\nu_{21}-\nu_{13}\nu_{31}-\nu_{23}\nu_{32}-\nu_{12}\nu_{23}\nu_{31}-\nu_{13}\nu_{21}\nu_{32}$.

Note that EOS defines pressure as a function of volume change; therefore, definition 3.5.7 seems more appropriate choice as it defines pressure in terms of volumetric strain. In fact, it

was proved that such an approach can give more accurate results for dynamically loaded orthotropic materials (Vignjevic *et al.*, 2008). Two methods for obtaining pressure were evaluated and discussed in (Vignjevic *et al.*, 2008). The one that was found more accurate was chosen for this model and is presented below. It is suggested that pressure in non-isotropic materials is a vector and can be defined (in full tensor notation) by:

$$-p\psi_{ij} = C_{ijkl}\delta_{kl}\varepsilon_{ss}/3, \qquad \textbf{3.5.9}$$

where p and ψ_{ij} are pressure magnitude and vector respectively, C_{ijkl} is a stiffness tensor, δ_{kl} is Kronecker delta and $\varepsilon_{ss}/3$ is volumetric strain – ε_v (with summation over repeated indices). Volumetric strain definition was already introduced in Equation 3.5.2 but the form, which is later used (in contracted notation) is repeated here for convenience:

$$\varepsilon_v = \left(\varepsilon_1 + \varepsilon_2 + \varepsilon_3\right)/3. \qquad \textbf{3.5.10}$$

Equation 3.5.9 in a matrix (contracted) notation is:

$$p\begin{bmatrix}\psi_1\\ \psi_2\\ \psi_3\\ 0\\ 0\\ 0\end{bmatrix} = -\begin{bmatrix}C_{11} & C_{12} & C_{13} & 0 & 0 & 0\\ C_{12} & C_{22} & C_{23} & 0 & 0 & 0\\ C_{13} & C_{23} & C_{33} & 0 & 0 & 0\\ 0 & 0 & 0 & 2C_{44} & 0 & 0\\ 0 & 0 & 0 & 0 & 2C_{55} & 0\\ 0 & 0 & 0 & 0 & 0 & 2C_{66}\end{bmatrix}\cdot\begin{bmatrix}\varepsilon_v\\ \varepsilon_v\\ \varepsilon_v\\ 0\\ 0\\ 0\end{bmatrix}. \qquad \textbf{3.5.11}$$

From this, pressure magnitude p is equal to:

$$p = \sqrt{\frac{\left(C_{11}+C_{12}+C_{13}\right)^2 + \left(C_{12}+C_{22}+C_{23}\right)^2 + \left(C_{13}+C_{23}+C_{33}\right)^2}{3}}\varepsilon_v = -3K_\psi\varepsilon_v, \qquad \textbf{3.5.12}$$

where K_ψ is bulk modulus of orthotropic material. Pressure vector ψ_i is defined as:

$$\psi_i = \frac{\left(C_{i1}+C_{i2}+C_{i3}\right)}{\sqrt{\frac{\left(C_{11}+C_{12}+C_{13}\right)^2 + \left(C_{12}+C_{22}+C_{23}\right)^2 + \left(C_{13}+C_{23}+C_{33}\right)^2}{3}}}. \qquad \textbf{3.5.13}$$

This leads to decomposition of the stress vector to volumetric and deviatoric parts by:

$$\sigma_{ij} = C_{ijkl}\delta_{kl}\varepsilon_{ss}/3 + C_{ijkl}\varepsilon^{d}_{kl} = -p\psi_{ij} + s_{ij}\,. \qquad \textbf{3.5.14}$$

In such a definition the stresses generated by volumetric and deviatoric strains are not perpendicular, i.e. $p\psi_{ij}s_{ij} \neq 0$. To assure that volumetric and deviatoric parts of stress are independent, they should be redefined as follows:

$$\sigma_{ij} = -p\psi_{ij} + s_{ij} = -\tilde{p}\psi_{ij} + \tilde{s}_{ij}\,. \qquad \textbf{3.5.15}$$

Consequently, pressure and deviatoric stress assumes the form:

$$\tilde{p} = p - \frac{s_{ij}\psi_{ij}}{3} = -\frac{\sigma_{ij}\psi_{ij}}{3}, \qquad \textbf{3.5.16}$$

$$\tilde{s}_{ij} = s_{ij} - \frac{s_{kl}\psi_{kl}}{3}\psi_{ij} = \sigma_{ij} - \tilde{p}\psi_{ij}\,.$$

In such a definition the part of a deviatoric stress that is perpendicular to pressure vector ψ_{ij} is considered as pressure. The same part must be deduced from the stress vector obtained from deviatoric strain s_{ij}. This assures that deviatoric and volumetric stress vectors are mutually perpendicular and their sum equals to the total stress vector.

The total stress vector consists of pressure and deviatoric part, where pressure part should be obtained from the EOS:

$$\sigma_{ij} = p_{EOS}\psi_{ij} + \tilde{s}_{ij} \qquad \textbf{3.5.17}$$

The Gruneisen EOS for compressed solids is (for details see Appendix B):

$$p_{EOS} = \frac{\rho_0 C^2 \mu\left[1 + \left(1 - \frac{\gamma_0}{2}\right)\mu - \frac{a}{2}\mu^2\right]}{\left[1 - (S_1 - 1)\mu - S_2\frac{\mu^2}{\mu+1} - S_3\frac{\mu^3}{(\mu+1)^2}\right]} + (\gamma_0 + a\mu)u\,, \qquad \textbf{3.5.18}$$

where u is initial internal energy density, C is the intercept of the shock-particle velocity curve (described in more detail in Section 6.2), S_1, S_2, S_3 are slope coefficients of this curve,

ρ_0 is initial density, γ_0 is initial Gruneisen constant and a is volume correction to γ_0. Last variable in the equation, μ accounts for relative change in volume.

For large number of materials the relation between the particle and shock velocity which is defined by constants C, S_1, S_2 and S_3 using the cubic approximation is in in fact linear.

Thus, assuming $S_2 = S_3 = 0$ the expression can be simplified to:

$$p_{EOS} = \frac{\rho_0 C^2 \mu \left[1 + \left(1 - \frac{\gamma_0}{2}\right)\mu - \frac{a}{2}\mu^2\right]}{1 - (S_1 - 1)\mu} + (\gamma_0 + a\mu)u \qquad \textbf{3.5.19}$$

For solids under tension Gruneisen EOS is:

$$p_{EOS} = \rho_0 C^2 \mu + (\gamma_0 + a\mu)u, \qquad \textbf{3.5.20}$$

3.6 Summary

Chapter 3 introduces the most important concepts and provides the basis for development of the composite constitutive model. A few features, foundations and assumptions of the model can be identified following this chapter.

Firstly, the model is a continuum scale model in which damage is represented using effective stress concept and strain energy equivalence hypothesis (described in Section 3.3). Damage variables describe damage in the material as a reduction of stiffness whilst damage evolution variables control the evolution of damage limit (allowing for damage hardening or softening in the material). Damage evolution follows the maximum entropy production (maximum energy dissipation) rule.

Section 3.4 gives the thermodynamic framework of the model which is further expanded to incorporate spectral decomposition in Chapter 6. The equation of state theory is presented in Section 3.5. It introduces an approach to decompose stress into volumetric and deviatoric parts. The main feature of this decomposition is a definition of pressure as a stress that is generated by a volumetric deformation and assuring that deviatoric and volumetric stresses are orthogonal.

4 Mesoscale modelling of damage

As mentioned in previous chapters, the aim of modelling is to describe the material's behaviour at macroscopic scale accounting for most important phenomena occurring within (usually at microscopic level). This chapter describes the analysis of material at mesoscale, i.e. the scale at which anisotropy was introduced. Mesoscale modelling was intended to provide insight and help in understanding of the material behaviour, focusing on effect of damage in constituents on the material stiffness tensor.

Composite material with unidirectional fibre reinforcement was modelled at mesoscale i.e. fibres, matrix and their interface each having its own mechanical properties. This work bases on the mesoscale models available in the commercial code Digimat provided by e-Xtream. Damage effects are represented by reduction of the material stiffness in the selected elements within the representative volume element (RVE) models with results being averaged over RVE. Considerations of the following damage cases are presented in this work: fibre cracking, matrix microcracking and fibre-matrix debonding.

4.1 Model

RVE of a unidirectional composite comprised 16 fibres randomly distributed in a matrix (Figure 4.1.1). The modelled material was a repetitive unit cell (RUC), as presented in Figure 4.1.1 - b) and thus automatically satisfied the requirements of being the RVE (see Section 3.1.1).

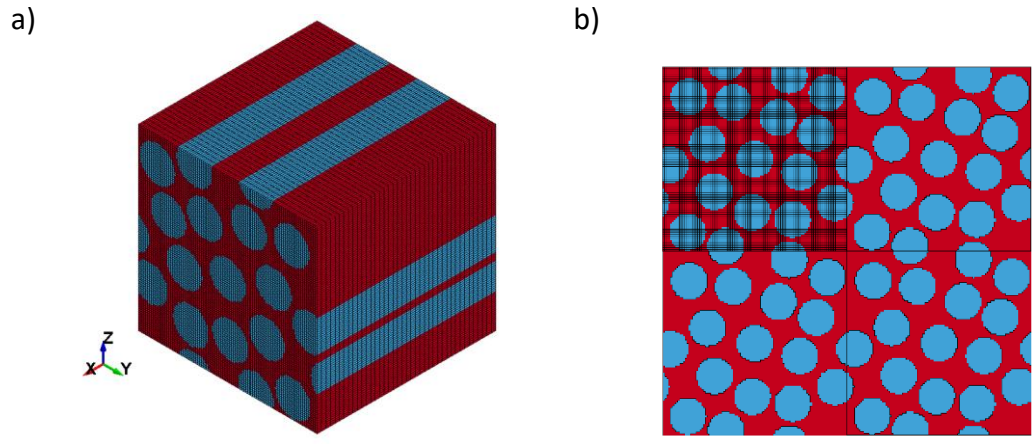

Figure 4.1.1 Unidirectional material model representative volume element a) isometric view, b) RVE

The model was a cube with an edge length of 0.026 mm. Fibres of 5 μm diameter constituted the 50% of the material volume. The model was divided into hexagonal elements of equal

size. Number of elements in the model and their aspect ratio depend on the damage mechanism modelled. Material model assigned to matrix constituent was MAT ELASTIC (MAT_001) and to fibres MAT ORTHOTROPIC ELASTIC (MAT_002). Material properties used for an undamaged model are listed in Table 4.1.1. They were provided by e-Xtream with the model.

Table 4.1.1 Matrix properties used for undamaged mesoscale model

	Matrix		
E	Young's modulus	4.7	GPa
ν	Poisson's ratio	0.400	MPa
	Fibres		
E_x	Young's modulus, x-direction	265	GPa
E_y	Young's modulus, y-direction	13	GPa
E_z	Young's modulus, z-direction	13	GPa
ν_{yz}	Poisson's ratio, yx-plane	0.0126	-
ν_{zx}	Poisson's ratio, zx-plane	0.0126	-
ν_{xy}	Poisson's ratio, yz-plane	0.2060	-
G_{yz}	Shear modulus, yz-plane	5.4	GPa
G_{zx}	Shear modulus, zx-plane	15.5	GPa
G_{xy}	Shear modulus, xy-plane	15.5	GPa

Unidirectional composite is a transversely isotropic material. Therefore, the corresponding symmetries in the stiffness, compliance and damage tensors are expected in the simulation results (see Section 2.1.2). However, they were not presumed – all elements of stiffness tensor were extracted separately and the symmetry check was used as a validation and an accuracy check of the simulations.

4.1.1 Loads and boundary conditions

Apart from defining desired geometry and material properties the vital aspect of the model is boundary conditions setting. Two types of boundary conditions are used in the models. The boundary conditions constraining cube faces force the plane strain state in the material, whilst periodic boundary conditions are used to model the continuity of the material. Periodic boundary conditions map the nodal displacements from one cube face to the corresponding nodes on the other face.

Plane strain state is generated in the material to determine material stiffness tensor based on simulation results. Each model was successively loaded by six displacements – three normal

displacements and three shear displacements. For normal load cases one face of the RVE was loaded in tension, while remaining faces were constrained from movement in the direction normal to them as schematically presented in Figure 4.1.2 for X direction plane strain. The load was applied by the set displacement of $\delta = 2.6 \cdot 10^{-5} mm$, which results in strain $\varepsilon_i = 1 \cdot 10^{-3}$.

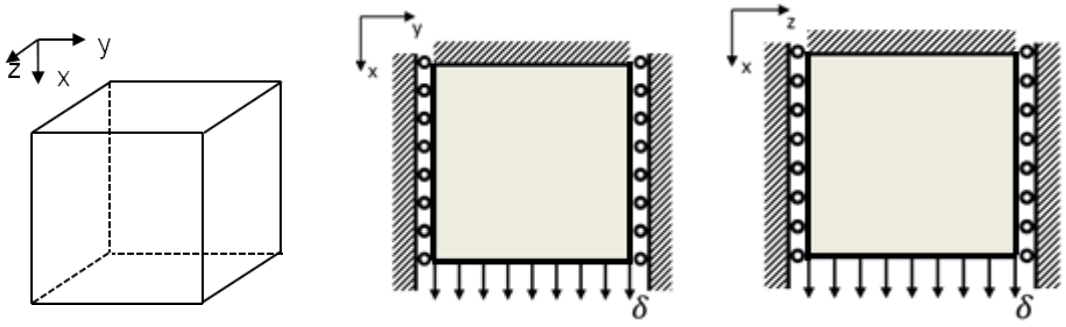

Figure 4.1.2 Loading and boundary conditions inducing plane strain in X direction

Plane shear strain was obtained by constraining one face in all directions and applying the load parallel to the opposite face (Figure 4.1.3). The load was applied as a set displacement of magnitude $\delta = 2.6 \cdot 10^{-5} mm$, which results in the shear strain $\varepsilon_{ij} = 5 \cdot 10^{-4}$ (or engineering shear strain $\gamma_{ij} = 1 \cdot 10^{-3}$).

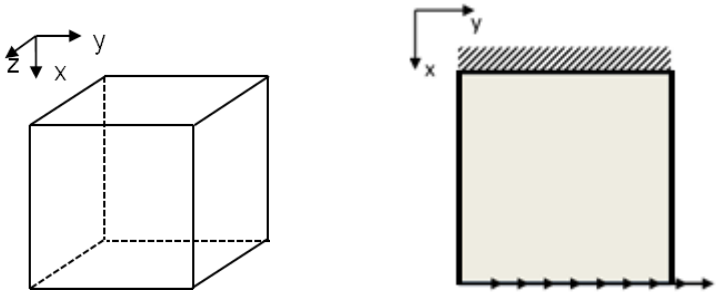

Figure 4.1.3 Loads and boundary conditions inducing shear in XY plane

The strain magnitudes used in plane strain loading were small enough to be considered as small strains.

Damage is modelled by reducing stiffness parameters of constituents by so-called damage factors. Different parameters are affected depending on the damage mechanism modelled (described in more detail in following sections). Damage factor of 1 describes the non-damaged constituent whilst damage factor of 100 means that constituent stiffness was reduced 100 times due to damage. Same loading and boundary conditions were used for all the cases regardless damage factor.

4.1.2 Fibre cracking damage mode

In unidirectional composite subjected to longitudinal tension the most important damage mechanism is fibre cracking. Fibre cracking was modelled by reducing the stiffness of the fibres elements lying in one plane (Figure 4.1.4). Following the effective stress concept, it can be interpreted as reduction of load carrying area of the fibres.

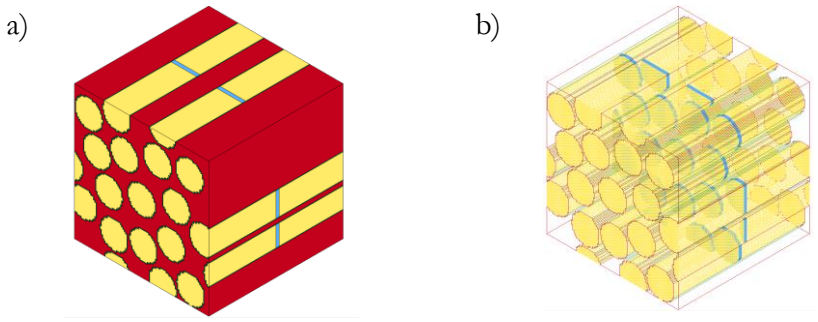

Figure 4.1.4 Mesoscale model with fibre cracking damage mechanism a) the whole model, b) highlighted elements with changed properties – the crack

The damaged fibre layer was modelled with MAT_ORTHOTROPIC_ELASTIC (MAT_002) material. Damage was introduced as degradation of all Young's and shear moduli by damage factor (see Appendix C). Seven damage factors were used in the broken fibres model. It resulted in 42 simulations – seven damage cases each requiring six simulations for the stiffness tensor determination.

4.1.3 Matrix uniform microcracking damage mode

Matrix damage is considered to be of lower importance than fibre damage as it usually does not have catastrophic consequences. However, it reduces the materials transverse and shear stiffnesses. Matrix microcracking was modelled by reducing Young's modulus of all matrix elements subsequently by the number of damage factors (see Appendix C). The Poisson's ratio remained unchanged, so the shear modulus of the material changed by the same factor as Young's modulus. In total 36 mesoscale simulations were performed for this damage mechanism – six for each damage factor.

4.1.4 Fibre-matrix interfacial debonding damage mode

One of the damage mechanisms that can seriously affect stiffness of a material is fibre matrix debonding. It is often preceded by cracking of matrix in proximity of fibres. It may start from shear in the plane of fibres and result in difference in displacements in the fibre-matrix interface. The modelling approach used for this damage mechanism was similar to the one

used for fibre cracking model. Debonding of the fibre matrix interface was modelled by stiffness reduction of the matrix elements adjacent to fibres (green elements in Figure 4.1.5).

a) b)

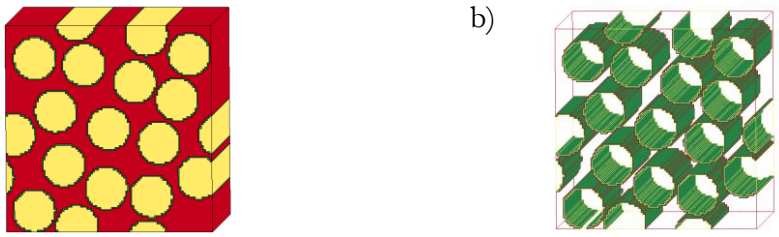

Figure 4.1.5 Mesoscale model with fibre-matrix debonding damage mechanism a) the whole model, b) elements with changed properties – debond layer

Debond layer was modelled with material model MAT_ORTHOTROPIC_ELASTIC (MAT_002) and the material properties were based on the reduced matrix properties (Appendix C). Despite the use of isotropic properties, MAT_002 was used here as, unlike MAT_001 it has the capability of modelling finite strains which were expected in the debond layer. Eight damage factors were used which resulted in 48 simulations of fibre-matrix debonding model.

4.1.5 Combined damage model

Interactions between several damage mechanisms are not easily predicted. To investigate the influence of joined fibre breaking and fibre-matrix interface damage mechanisms in the material a combined damage model was generated. The model was a superposition of fibre breaking model and fibre-matrix debonding mode. The same damage factor was used to reduce the properties of fibres and matrix (see fibres and matrix reduced properties in Appendix C).

4.2 Damage mode stress analysis

Stress analysis is highly relevant to assessment of damage. Loads in models were applied as set displacements. Therefore, with reduced stiffness of elements, stress was expected to decrease. The full stress analysis comprises an analysis of all damage models loaded subsequently by all the plane strains. For the sake of clarity only the most revealing and important results are presented here. This includes the fibre direction stress, displacement for broken fibre model and transverse direction stress and strains for matrix related damage mechanisms.

4.2.1 Broken fibres

Figure 4.2.1 shows stress distribution in the RVE models for the subsequent damage factors used. It can be observed that for lower values of damage factor the longitudinal load was transferred mainly through fibres resulting in high longitudinal stress in the fibres. The significant load transition from fibres to matrix is first observed for the damage factor close to 40 (Figure 4.2.1 - d)) and becomes more evident with increasing damage. For higher damage factors (see Figure 4.2.1 - e) and h)) stress around the cracked region was transferred mainly through the matrix. The fibre longitudinal stiffness in the simulations was approximately 57 times higher than the matrix stiffness. This suggests that the stress redistribution in the material starts to be pronounced when longitudinal stiffness approaches matrix stiffness.

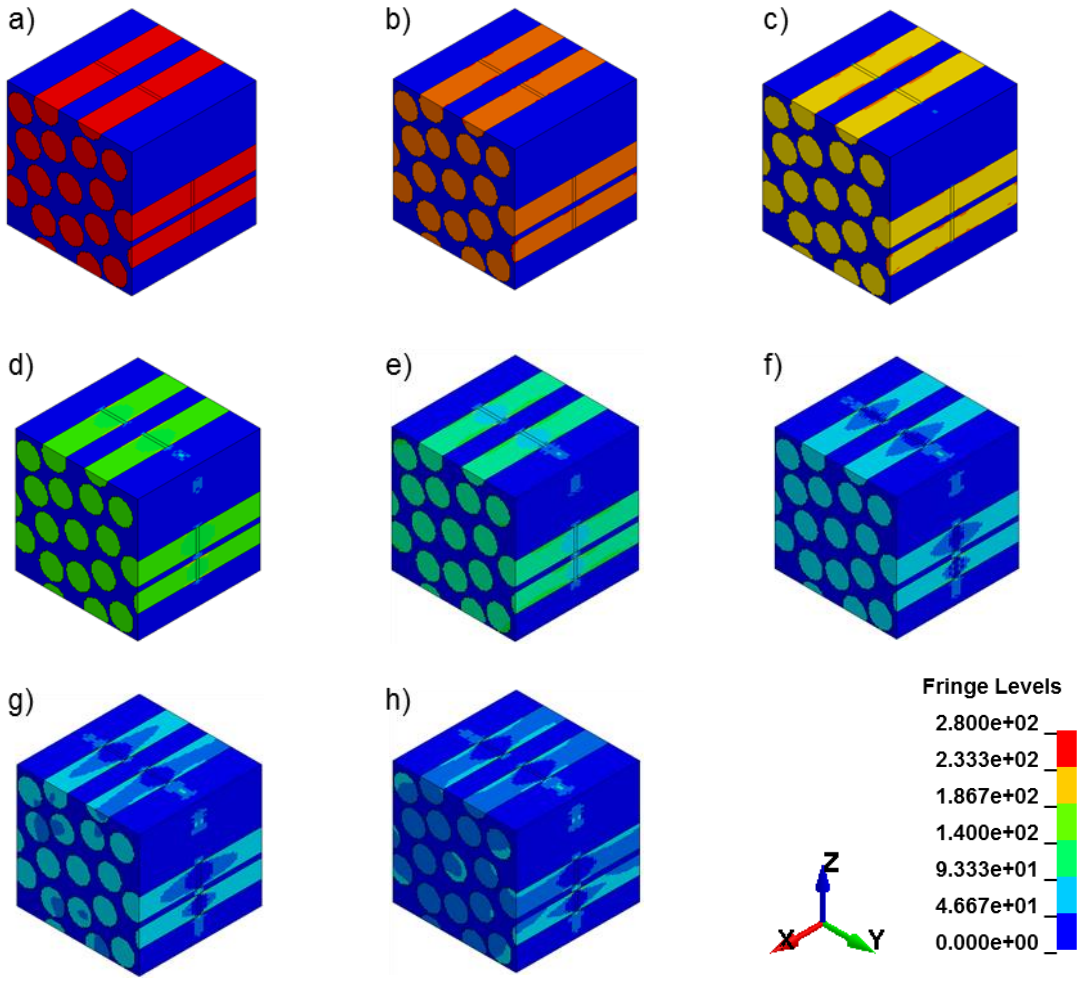

Figure 4.2.1 Distribution of X stress component of unidirectional model with broken fibres under X load for damage factor: a) 1 (no damage), b) 4, c) 10, d) 40, e) 100, f) 400, g) 1000, h) 10000

The X-displacements graphs are presented in Figure 4.2.2. Change in the nodal displacements starts to be significant at damage factor of 40. It is a consequence of a comparable stiffness of matrix and fibres for this damage factor. With increasing damage factor two distinct regions in the fibres are found. One with displacement 2.6e-5 and one with zero displacement. It suggests the complete failure of fibres as two disjoined fibre parts move separately – one remains constrained and the second moves due to applied displacements.

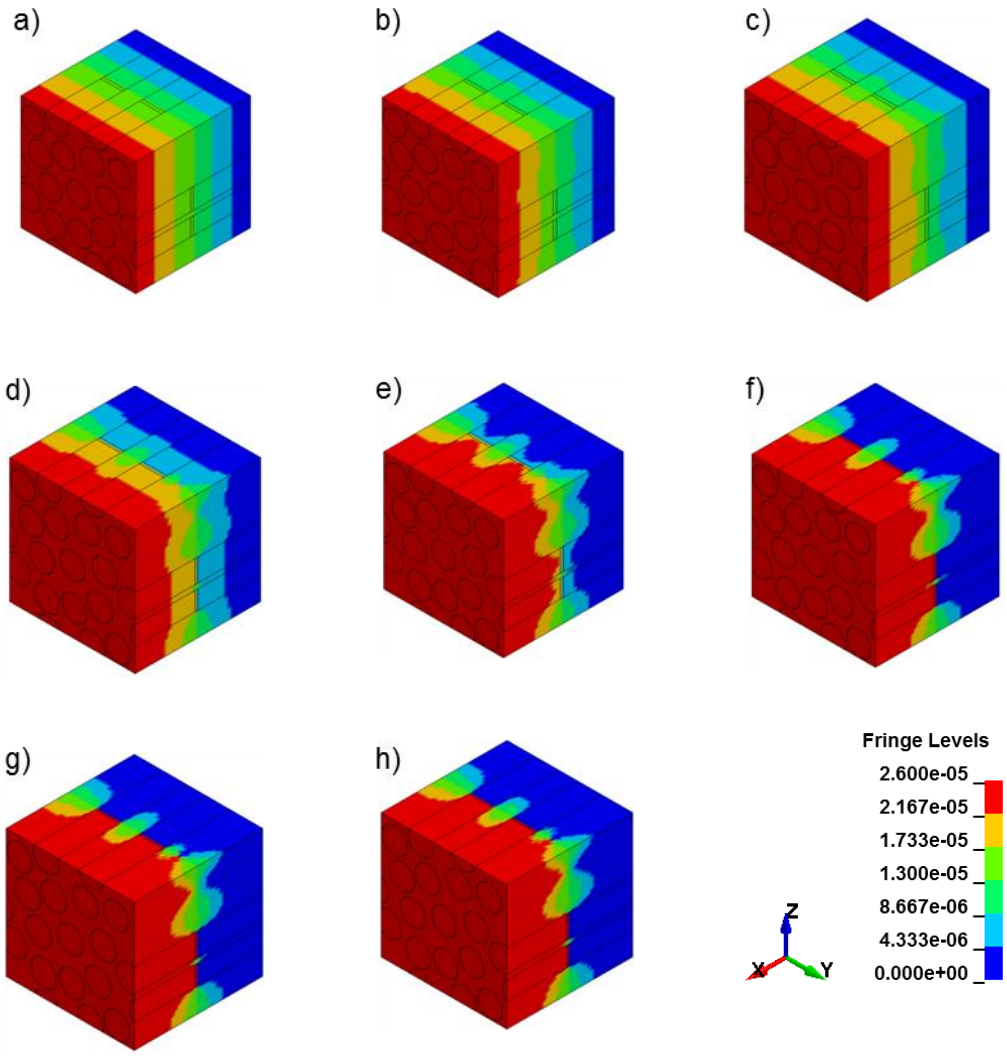

Figure 4.2.2 X-displacement of unidirectional model with broken fibres under X load for damage factor: a) 1 (no damage), b) 4, c) 10, d) 40, e) 100, f) 400, g) 1000, h) 10000

4.2.2 Matrix uniform microcracking

Figure 4.2.3 shows the Y stress component in the material under Y load direction. It is clear that matrix stiffness was the dominant in transverse direction. The high stress paths are

located in the regions, where the fibres are in line with the load direction. High stress paths are present in the matrix regardless of the damage magnitude, but they cannot be observed in Figure 4.2.3 - d) and e) because of the chosen scale (consistent for all damage factors to allow for direct comparison). The results confirm that the matrix is a key constituent for the transverse stiffness of unidirectional composite. Reduction of the matrix stiffness (resulting from evolution of voids and microcracks) significantly reduce the transverse stiffness of the whole composite.

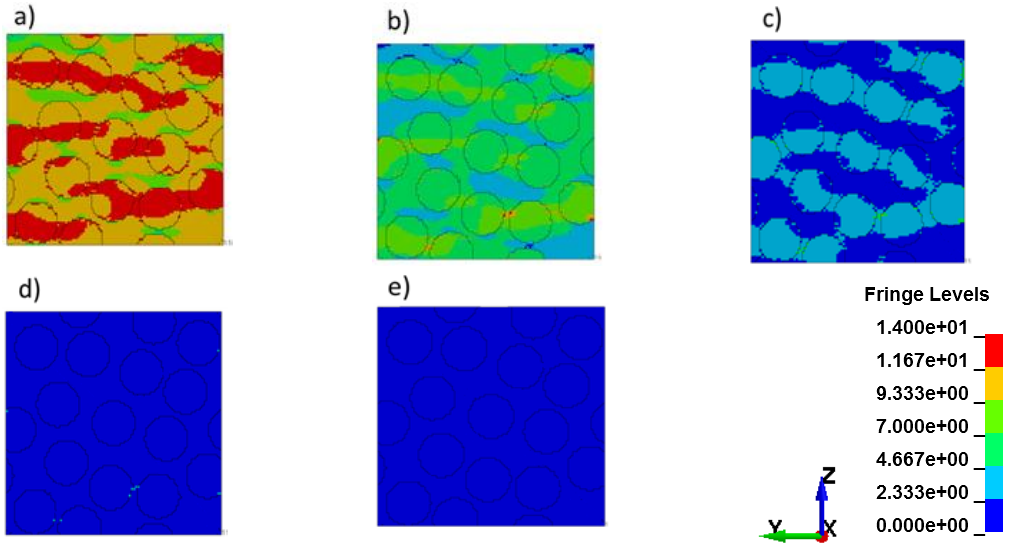

Figure 4.2.3 Y-stress of unidirectional model with damaged matrix under Y load for damage factor: a) 1 (no damage), b) 4, c) 10, d) 40, d) 100, 400, 1000 and 10000

Figure 4.2.4 shows stress distribution in fibre direction (X). Only two extreme cases are presented – case with no damage in matrix, and the one with matrix stiffness reduced by 10000. There is no change in stress distribution observed in fibres. Obviously, if matrix is analysed separately, it shows the difference in stress, but it is not significant for the whole RVE. This supports the statement, that the matrix state does not have a big influence on the fibre direction in the unidirectional composite material.

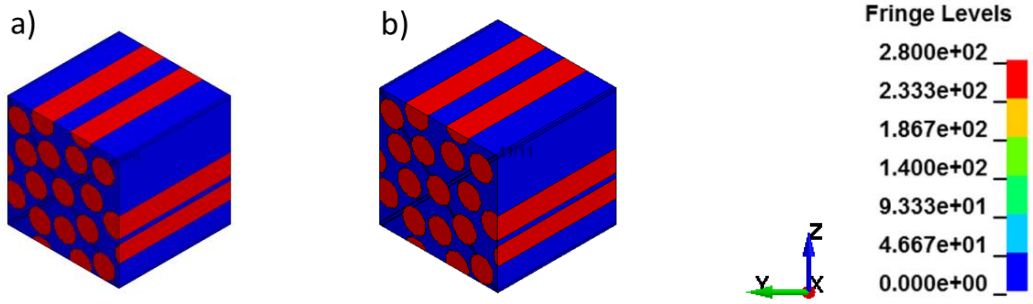

Figure 4.2.4 X-stress of unidirectional model with damaged matrix under X load for damage factor: a) 1, b) 10000

4.2.3 Fibre-matrix debonding

Stress distribution in a fibre-matrix debonding model, as expected, does not change for longitudinal (X) direction of load and therefore is not presented here. The analysis of the stresses in a fibre-matrix debonding model is based on the Y load direction. The model loaded in Z direction has similar stress distribution to the model loaded in Y direction and thus only one of them is described here. Figure 4.2.5 shows the Y stress component resulting from Y load for different damage factors.

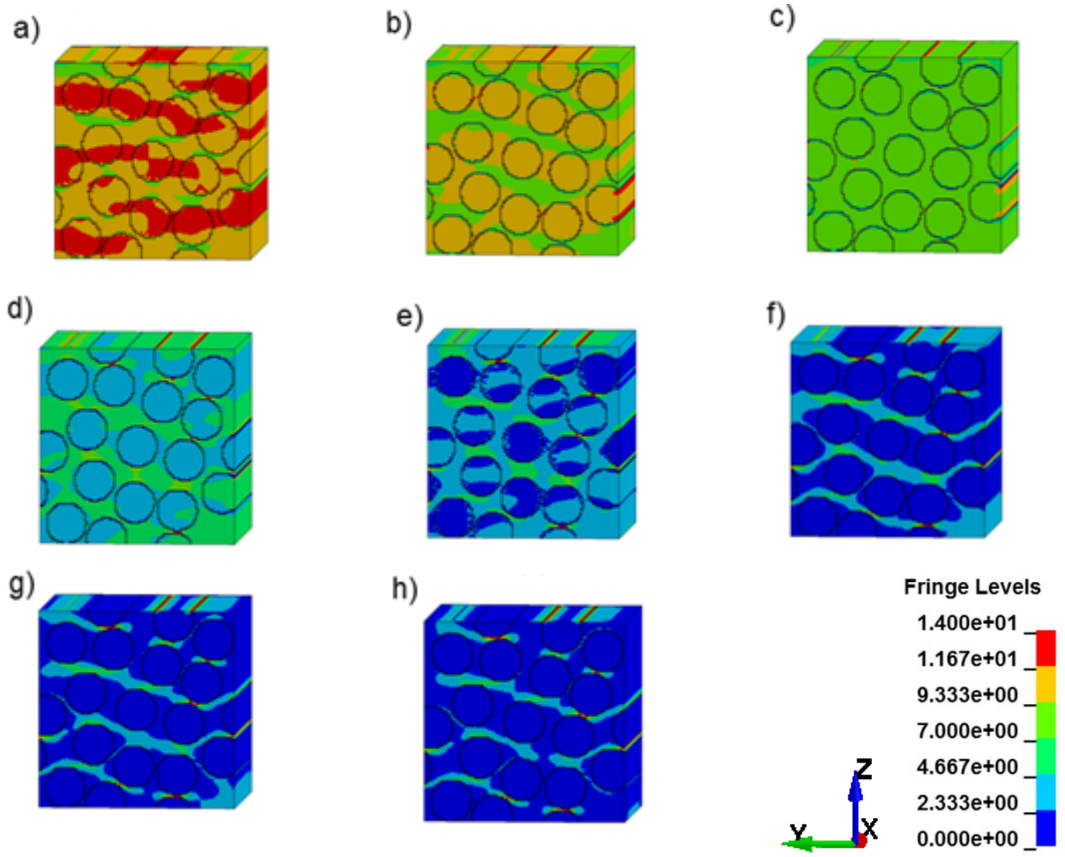

Figure 4.2.5 Distribution of Y stress component of unidirectional model with fibre-matrix debonding under Y load for damage factor: a) 1 (no damage), b) 4, c) 10, d) 40, e) 100, f) 400, g) 1000, h) 10000

High stress paths can be seen in Figure 4.2.5 - a). The paths are passing through the fibres arranged in line. Figure 4.2.5 - c) shows that for damage factor of 10 there were no high stress paths. The explanation for this behaviour can be given by a simple example by considering material as a system of springs. If the equivalent stiffness of the series of springs (matrix, fibres and debonds) is equal to the matrix stiffness there would be uniform stress distribution in the material as presented in Figure 4.2.5 - c). Damage factor for which the equivalent stiffness of the fibre with debonds is equal to the matrix stiffness is roughly equal to 20. For the higher damage factors (100 – 10000) stress distribution is different – stress is

transferred mainly through matrix. The high stress paths are located between the fibres rather than in line of fibres. The highest stresses in the matrix are found in regions, where distance between fibres is shortest, which gives the smallest load carrying area of matrix.

Figure 4.2.6 shows the displacements in the RVE. Figure 4.2.6 - f), g) and h) are the most revealing ones – they show that displacements within one fibre are equal. This suggests that the displacement in the fibres can be attributed to the rigid body motion of the fibres rather than their deformation.

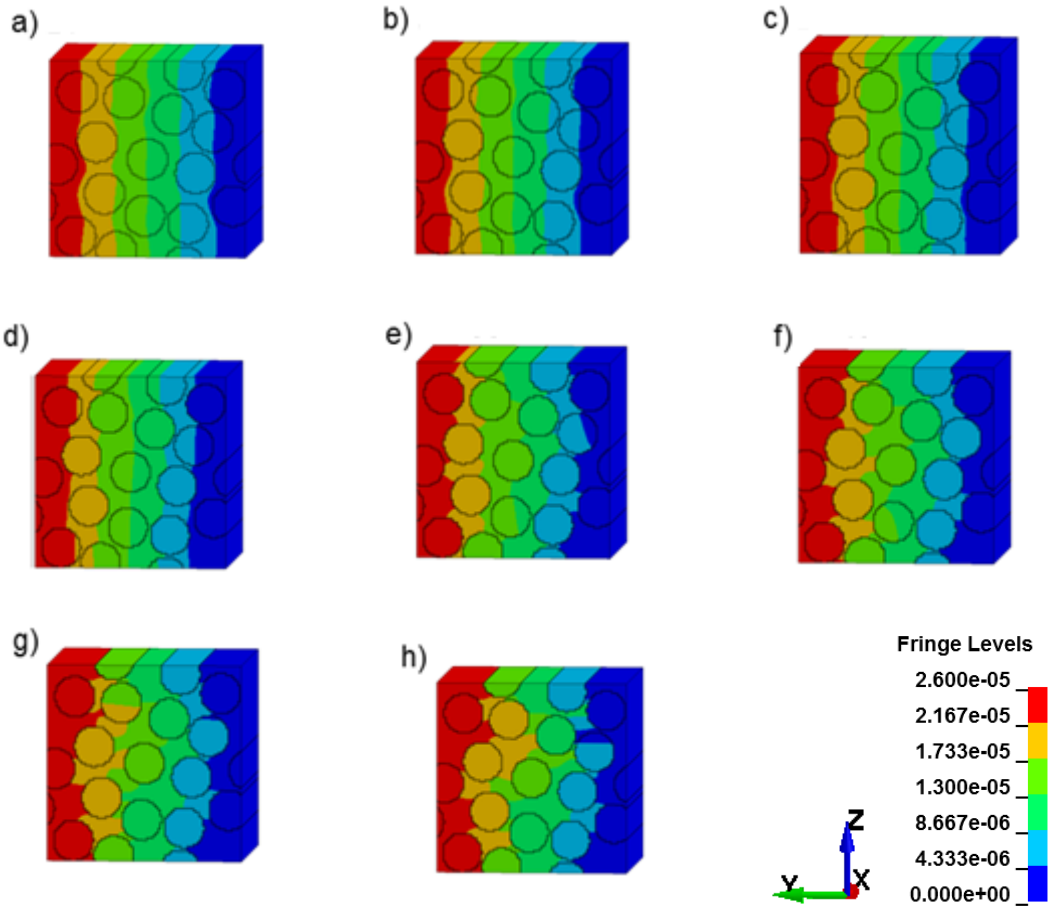

Figure 4.2.6 Y-displacement of unidirectional model with fibre-matrix debonding under Y load for damage factor: a) 1 (no damage), b) 4, c) 10, d) 40, e) 100, f) 400, g) 1000, h) 10000

This conclusion was confirmed by the strain results in the separate constituents (for fibres strains were equal to zero). The set displacement was applied to generate the RVE strain of 0.1%. As a result of material's inhomogeneity, the strain is not uniformly distributed in the element's volume. The average strain in the fibres does not exceed 0.015%. The highest strains are found in the debond layer and their average slightly exceeds 1% (note that debond layer mimic the discontinuity in the material, so it is hardly surprising that it experienced

highest strain). The strain in the matrix varied depending on the region. The highest strain in the matrix is over 0.5% and the average strain in the matrix part is around 0.05%.

4.2.4 Combined damage

In combined damage models damage effects are significant in all directions. At the first sight stress in the combined damage model under X plane strain (Figure 4.2.7) resembles the corresponding stress in the broken fibre model (Figure 4.2.1). However, the important difference is lack of significant stress redistribution from the broken fibres to the matrix in combined damage model. The longitudinal stress of fibres is reduced due to fibre fracture but because of no stress redistribution it remains constant within the fibre.

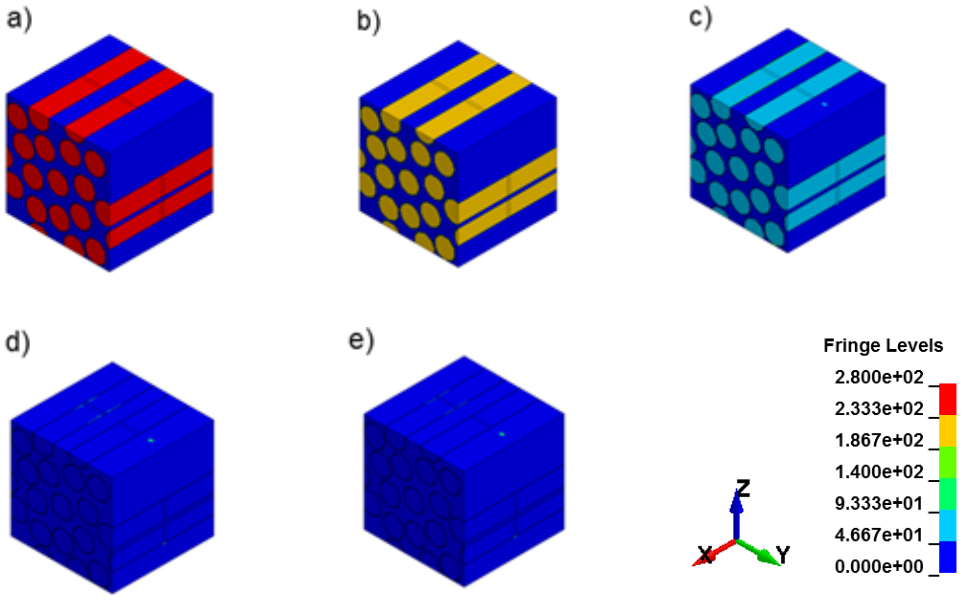

Figure 4.2.7 Distribution of X stress component of unidirectional model with combined damage X load for damage factor: a) 1 (no damage), b) 10, c) 100, d) 1000, e) 10000

Figure 4.2.8 shows the X displacement of combined damage model elements under longitudinal load. It is evident that fibres are fully disjoined from matrix for higher damage factors.

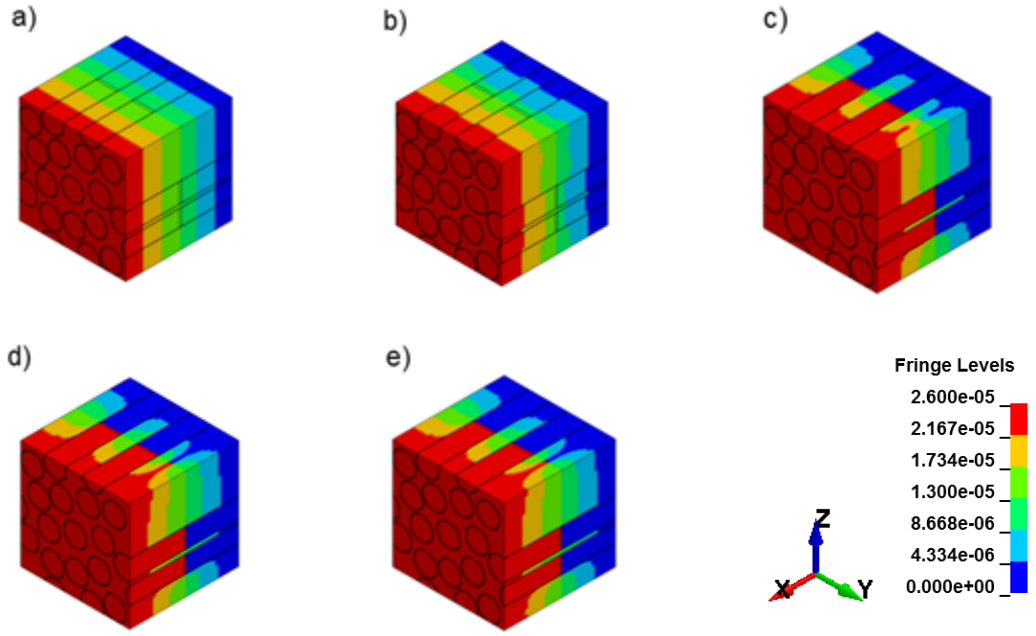

Figure 4.2.8 X-displacement of unidirectional model with combined damage under X load for damage factor: a) 1 (no damage), b) 10, c) 100, d) 1000, e) 10000

Stress distribution in the combined damage model (Figure 4.2.9) loaded in transverse direction (Y) does not vary significantly from the fibre-matrix debonding model (Figure 4.2.5). High stress paths are found for the fibres distributed in line with Y direction. Almost uniform stress is observed for the RVE for damage factor of 10 (Figure 4.2.9 - b)).

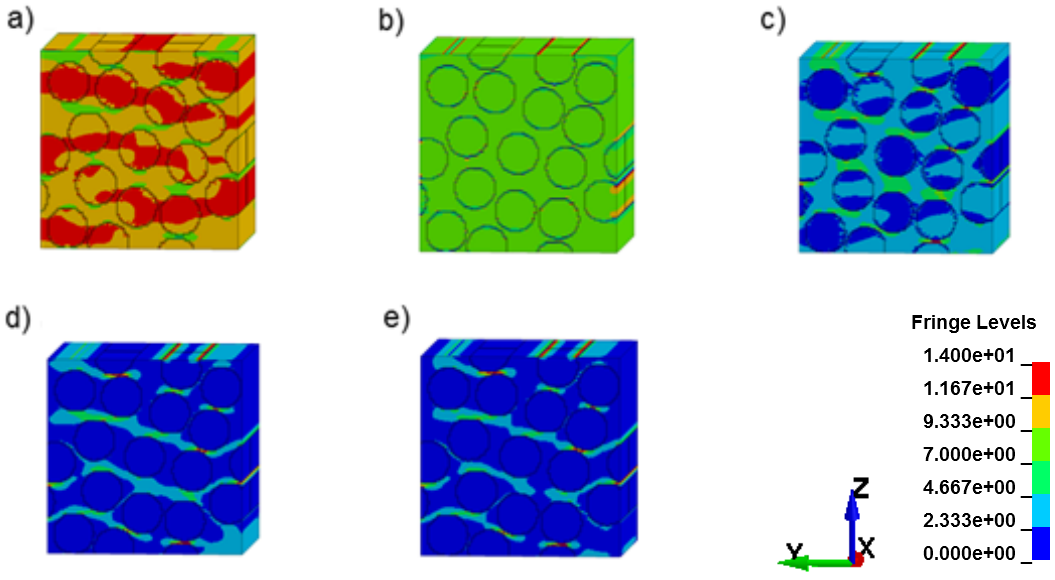

Figure 4.2.9 Distribution of Y stress component of unidirectional model with combined damage Y load for damage factor: a) 1 (no damage), b) 10, c) 100, d) 1000, e) 10000

For higher damage factors the high stress paths are located between the fibres. The stress level depends strongly on the distance between the fibres – the lower is the distance (in Z direction), the smaller is the load carrying area and subsequently the higher is the stress.

Deformation in transverse (Y) direction of the combined damage model is consistent with the fibre-matrix debonding model. However, for higher damage factors, the fibres are not deformed but moved – displacements in the fibres was uniform leading to no strain (Figure 4.2.10 - d) and e)).

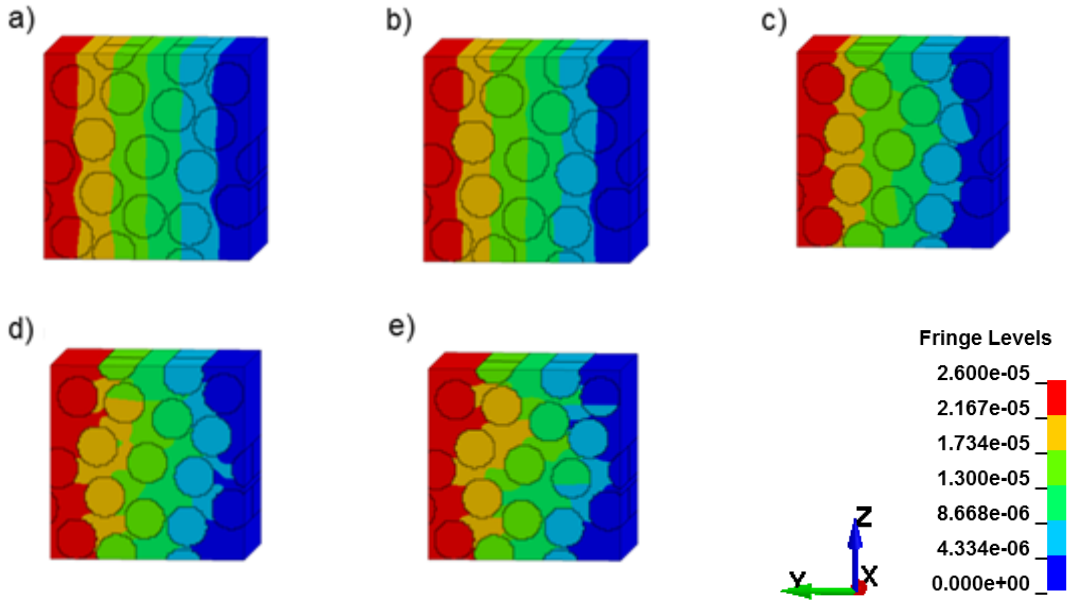

Figure 4.2.10 Y-displacement of unidirectional model with combined damage under Y load for damage factor: a) 1 (no damage), b) 10, c) 100, d) 1000, e) 10000

4.3 Stiffness tensors

One of the purposes of mesoscale modelling was to investigate the influence of damage mechanisms on the overall material stiffness. Stress analysis presented in the previous sections validated the model and damage mesoscale modelling approach by giving the expected material response. However, the main aim of mesoscale modelling was linking the mesoscale damage to its macroscopic effects. This can be done by extracting stiffness tensors of the damaged materials. A stiffness tensor of a transversely isotropic material consists of twelve non-zero elements, five of which are independent. Therefore, in order to construct a stiffness tensor six simulations are needed for each damage case. Each simulation result gives the stresses, which along with the known strain value allow to calculate of one column of a

stiffness tensor. The stress strain relation for a unidirectional strain in longitudinal direction can be written in a matrix form as:

$$\begin{bmatrix} \sigma_1 \\ \sigma_2 \\ \sigma_3 \\ \sqrt{2}\sigma_4 \\ \sqrt{2}\sigma_5 \\ \sqrt{2}\sigma_6 \end{bmatrix} = \begin{bmatrix} C_{11} & C_{12} & C_{13} & \sqrt{2}C_{14} & \sqrt{2}C_{15} & \sqrt{2}C_{16} \\ C_{21} & C_{22} & C_{23} & \sqrt{2}C_{24} & \sqrt{2}C_{25} & \sqrt{2}C_{26} \\ C_{31} & C_{32} & C_{33} & \sqrt{2}C_{34} & \sqrt{2}C_{35} & \sqrt{2}C_{36} \\ \sqrt{2}C_{41} & \sqrt{2}C_{42} & \sqrt{2}C_{43} & 2C_{44} & 2C_{45} & 2C_{46} \\ \sqrt{2}C_{51} & \sqrt{2}C_{52} & \sqrt{2}C_{53} & 2C_{54} & 2C_{55} & 2C_{56} \\ \sqrt{2}C_{61} & \sqrt{2}C_{62} & \sqrt{2}C_{63} & 2C_{64} & 2C_{65} & 2C_{66} \end{bmatrix} \cdot \begin{bmatrix} \varepsilon_1 \\ 0 \\ 0 \\ 0 \\ 0 \\ 0 \end{bmatrix} \quad \textbf{4.3.1}$$

This reduces to the following set of equations that allow to obtain a stiffness tensor column:

$$\sigma_1 = C_{11}\varepsilon_1 \Rightarrow C_{11} = \frac{\sigma_1}{\varepsilon_1}, \sigma_2 = C_{21}\varepsilon_1 \Rightarrow C_{21} = \frac{\sigma_2}{\varepsilon_1}, ..., \sqrt{2}\sigma_6 = \sqrt{2}C_{61}\varepsilon_1 \Rightarrow C_{61} = \frac{\sigma_6}{\varepsilon_1}. \quad \textbf{4.3.2}$$

The symmetries in the stiffness tensor were not pre-assumed. All the data in the model was collected separately disregarding the major symmetry of stiffness tensor. This allowed for the accuracy check of the model. As a consequence of transverse isotropy symmetry, the elements of the stiffness tensor are constrained by:

$$\begin{aligned} C_{22} &= C_{33}, & C_{55} &= C_{66}, \\ C_{12} &= C_{21} = C_{13} = C_{31}, & C_{22} - C_{32} &= 2C_{44}, \\ C_{23} &= C_{32}, \end{aligned} \quad \textbf{4.3.3}$$

$$\begin{aligned} &C_{14} = C_{41} = C_{15} = C_{51} = C_{16} = C_{61} = C_{24} = C_{42} = C_{25} = C_{52} = C_{26} = C_{62} = \\ &= C_{34} = C_{43} = C_{35} = C_{53} = C_{36} = C_{63} = C_{45} = C_{54} = C_{46} = C_{64} = C_{56} = C_{65} = 0. \end{aligned}$$

The full stiffness tensor (repeated from Section 2.1.3 for convenience):

$$C = \begin{bmatrix} C_{11} & C_{12} & C_{13} & 0 & 0 & 0 \\ C_{12} & C_{22} & C_{23} & 0 & 0 & 0 \\ C_{13} & C_{23} & C_{33} & 0 & 0 & 0 \\ 0 & 0 & 0 & 2C_{44} & 0 & 0 \\ 0 & 0 & 0 & 0 & 2C_{55} & 0 \\ 0 & 0 & 0 & 0 & 0 & 2C_{66} \end{bmatrix} \quad \textbf{4.3.4}$$

Stiffness tensors are also analysed in decomposed form by their eigenvalues and eigenvectors. The spectral decomposition of stiffness tensors is described in Section 2.1.4. Eigenvalues of the stiffness tensor can be seen as the material principal stiffnesses. The investigated material is a transversely isotropic material for which two of the eigenvalues were repeated ($\lambda^{II} = \lambda^{IV}$ and $\lambda^{V} = \lambda^{VI}$).

Analysis of the eigenvalues without considering eigenvectors offers limited information in assessment of damage. As mentioned in the previous sections of this work, the shear related eigenvectors ($\mathbf{v}^{IV}$, $\mathbf{v}^{V}$ and $\mathbf{v}^{VI}$) of the stiffness tensor are known and do not depend on the eigenvalues. The eigenvectors that may change as a consequence of damage are eigenvectors $\mathbf{v}^{I}$, $\mathbf{v}^{II}$ and $\mathbf{v}^{III}$.

Generic expressions for eigenvalues and eigenvectors are presented in Section 2.1.4. Below, the specific results obtained from the mesoscale undamaged model simulations are presented:

$$C = \begin{bmatrix} 139.4 & 5.4 & 5.4 & 0 & 0 & 0 \\ 5.4 & 11.2 & 5.4 & 0 & 0 & 0 \\ 5.4 & 5.4 & 11.2 & 0 & 0 & 0 \\ 0 & 0 & 0 & 5.7 & 0 & 0 \\ 0 & 0 & 0 & 0 & 11.0 & 0 \\ 0 & 0 & 0 & 0 & 0 & 11.0 \end{bmatrix} GPa$$

$$\begin{aligned} \lambda^{I} &= 139.5\, GPa, & \mathbf{v}^{I} &= \begin{bmatrix} 0.998 & 0.044 & 0.044 & 0 & 0 & 0 \end{bmatrix}^{T}, \\ \lambda^{II} &= 5.8\, GPa, & \mathbf{v}^{II} &= \begin{bmatrix} 0 & -0.707 & 0.707 & 0 & 0 & 0 \end{bmatrix}^{T}, \\ \lambda^{III} &= 16.1\, GPa, & \mathbf{v}^{III} &= \begin{bmatrix} -0.062 & 0.706 & 0.706 & 0 & 0 & 0 \end{bmatrix}^{T}, \\ \lambda^{IV} &= 5.7\, GPa \cong \lambda^{II}, & \mathbf{v}^{IV} &= \begin{bmatrix} 0 & 0 & 0 & 1 & 0 & 0 \end{bmatrix}^{T}, \\ \lambda^{V} &= 11.0\, GPa, & \mathbf{v}^{V} &= \begin{bmatrix} 0 & 0 & 0 & 0 & 1 & 0 \end{bmatrix}^{T}, \\ \lambda^{VI} &= 11.0\, GPa = \lambda^{V}, & \mathbf{v}^{VI} &= \begin{bmatrix} 0 & 0 & 0 & 0 & 0 & 1 \end{bmatrix}^{T}. \end{aligned} \quad \text{4.3.5}$$

Recalling the generic form of the first and the third eigenvectors (repeated from Table 2.1.1) coefficients α and β can be determined:

$$\mathbf{v}^{I} = \frac{1}{\sqrt{2+\alpha^2}}\begin{bmatrix}\alpha & 1 & 1 & 0 & 0 & 0\end{bmatrix}^T, \qquad \mathbf{v}^{III} = \frac{1}{\sqrt{2+\beta^2}}\begin{bmatrix}\beta & 1 & 1 & 0 & 0 & 0\end{bmatrix}^T. \qquad \textbf{4.3.6}$$

For the investigated undamaged material coefficient α is equal to 22.73, and coefficient β is equal to -0.09. Note, that for undamaged material the first eigenvector is almost perfectly aligned with fibre direction.

For a transversely isotropic material the second and fourth eigenvalues should be equal. The discrepancy between their values obtained in the simulations does not exceed 3.0%. The discrepancy between the other pair of repeated eigenvalues, fifth and sixth, is lower than 0.2%. This indicates accuracy of the mesoscale model.

The results in the sections below are presented for normalised eigenvalues, i.e. the damaged material eigenvalues divided by the corresponding undamaged stiffness eigenvalues.

4.3.1 Broken fibres model

The stiffness change of the RVE due to the fibre damage was significant which is clearly observed in Figure 4.3.1.

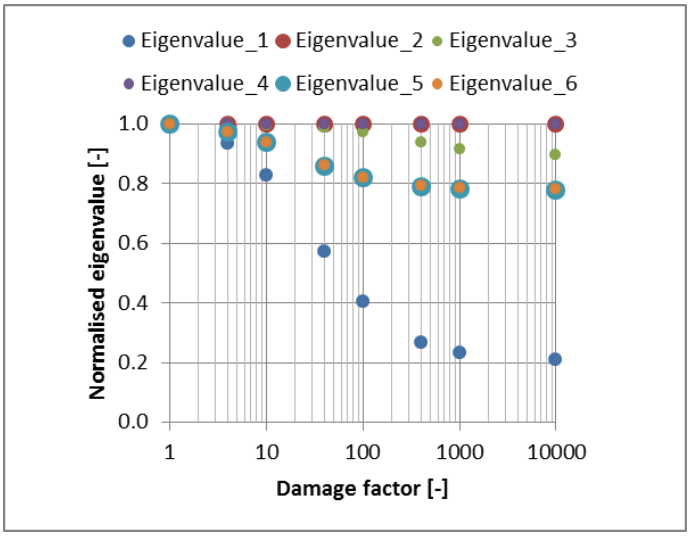

Figure 4.3.1 Normalised eigenvalues of the model with broken fibres

The most significant change is observed for the first eigenvalue, which is associated with fibre direction. Fibre breaking has a moderate influence on the fifth and sixth eigenvalue

(related to shear in fibre plane). Change in the third eigenvalue is observable. It is a direct consequence of the eigensystem rotation which is further commented below.

Figure 4.3.2 shows eigenvectors of the undamaged material and the material with damage factor of 10000. It is revealing in several ways. Firstly, despite the significant damage there is no observed change in the second eigenvector, which confirms the assumption that the material does not lose any of its symmetries. Eigenvectors v^I and v^{III} are rotated around vector v^{II} by the same angle. This is expected but noteworthy – eigenvectors must remain perpendicular, so if one of them is unchanged the other two must rotate by the same angle. The eigenvectors v^{IV}, v^V and v^{VI} are not shown in the figure, because they span the dimensions that cannot be represented in a 3D Cartesian coordinate system and are, by definition, perpendicular to the rest.

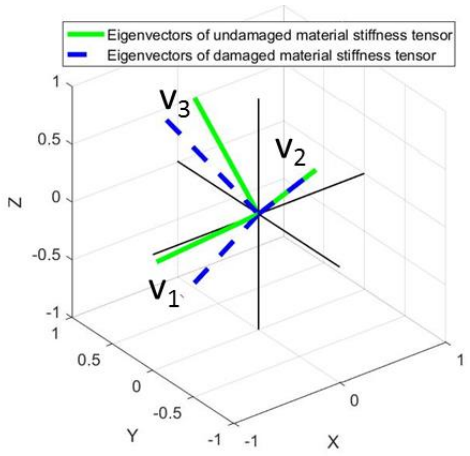

Figure 4.3.2 Eigenvectors in 3D space for broken fibre model for undamaged material (green) and material with damage factor 10000 (blue)

Figure 4.3.3 shows three first eigenvalues and rotation angles of eigenvectors. Increasing damage results in the first eigenvalue reduction and subsequently eigenvector rotation. This can be interpreted as loss of material's privileged high stiffness direction. The rotation of the eigenvectors started to be noticeable after the stiffness of the fibres approached the matrix stiffness.

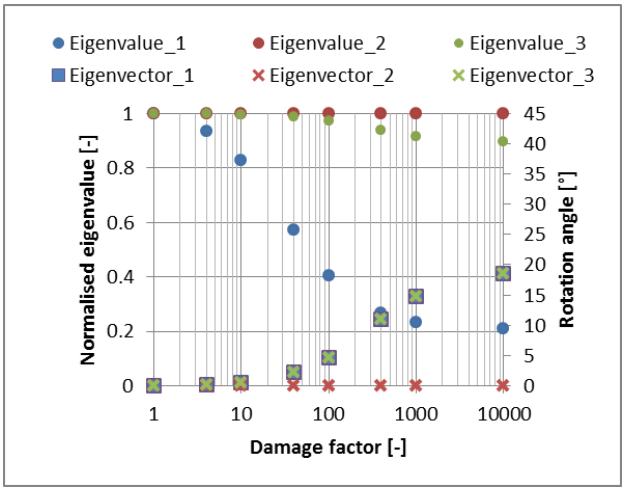

Figure 4.3.3 Eigenvalues and eigenvectors rotation angle of the model with broken fibres

Figure 4.3.3 clearly shows that rotation of the third eigenvector followed the rotation of the first one. Rotation of the eigenvector starts to be significant for damage factor 100. For lower values of damage factor the rotation did not exceed 5°. Figure 4.3.3 shows that for damage factor 100 the first eigenvalue which, with high degree of accuracy, describes the longitudinal direction was reduced by 60%.

The rotation of the eigenvectors is strictly connected to the change in value of coefficient α whose evolution due to damage is described below. The following equations are repeated from the previous sections of this work for the reader's convenience:

$$\alpha = \frac{2C_{12}}{\lambda^I - C_{11}},$$

$$\lambda^I = \frac{1}{2}\left[\left(C_{11}+C_{22}+C_{23}\right)+\sqrt{\left(C_{11}-C_{22}-C_{23}\right)^2+8(C_{12})^2}\right], \qquad \textbf{4.3.7}$$

$$\mathbf{v}^I = \frac{1}{\sqrt{2+\alpha^2}}\begin{bmatrix}\alpha & 1 & 1 & 0 & 0 & 0\end{bmatrix}^T.$$

Hypothetically, when the first element of stiffness tensor is much greater than the remaining elements $(C_{11} \gg C_{ij})$ its value becomes the first eigenvalue $(\lambda^I \to C_{11})$. Subsequently, coefficient α tends to a large number, which results in the first eigenvector being aligned with X axis $(v^I = \begin{bmatrix}1 & 0 & 0 & 0 & 0 & 0\end{bmatrix}^T)$. The situation is not far from reality. As long as the C_{11} element of a stiffness tensor is much higher than all other elements the direction of the eigenvector v^I would be close to direction of the X axis. When longitudinal stiffness is

reduced and fibre stiffness approaches matrix stiffness the influence of other stiffness tensor elements becomes more pronounced which leads to the first eigenvector being higher than the first tensor element $(\lambda^I > C_{11})$ and subsequently to reduction of coefficient α and rotation of the eigensystem.

4.3.2 Matrix uniform microcracking

Figure 4.3.4 shows the normalised eigenvalues of the stiffness tensor of models with uniform damage in matrix. The first eigenvalue, identified before as the one corresponding to the fibre direction is much higher than the other eigenvalues but its change due to matrix damage was minor. Significant reduction is observed in all other eigenvalues. The second, third and fourth eigenvalues are reduced by an order of magnitude for damage factor 40. What is interesting is that the second, third and fourth eigenvalues seems to be reduced by the same factor, which is evident in Figure 4.3.4. Second and fourth eigenvalues are equal, which suggests that material did not lose the transverse isotropy symmetry due to matrix uniform damage. The fact that the first eigenvalue did not change significantly due to matrix microcracking is not surprising.

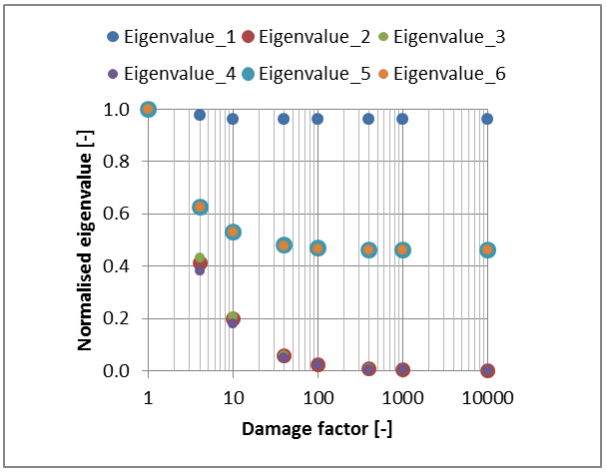

Figure 4.3.4 Normalised eigenvalues of the model with matrix uniform damage

Figure 4.3.5 shows eigenvalues of the stiffness tensor and rotation angles of the corresponding eigenvectors.

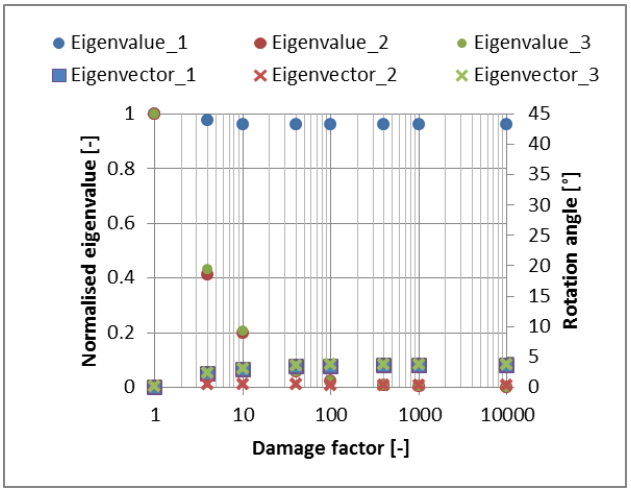

Figure 4.3.5 Eigenvalues and eigenvectors rotation angle of the model with matrix uniform damage

It can be observed in Figure 4.3.5 that first and third eigenvectors rotate by the same angle and that their rotation do not exceed 5° regardless damage factor used. Rotation of the second eigenvector is well below 1°.

4.3.3 Fibre-matrix debonding

Figure 4.3.6 shows the stiffness eigenvalues of the fibre-matrix debonding mesoscale model with respect to damage factor. It is clear from this plot, that the first eigenvalue is not significantly affected by interfacial debonding between fibres and matrix. On the other hand, all other eigenvalues seem to be considerably dependant on this damage mechanism. Figure 4.3.6 reveals slight discrepancy between second and fourth eigenvalues.

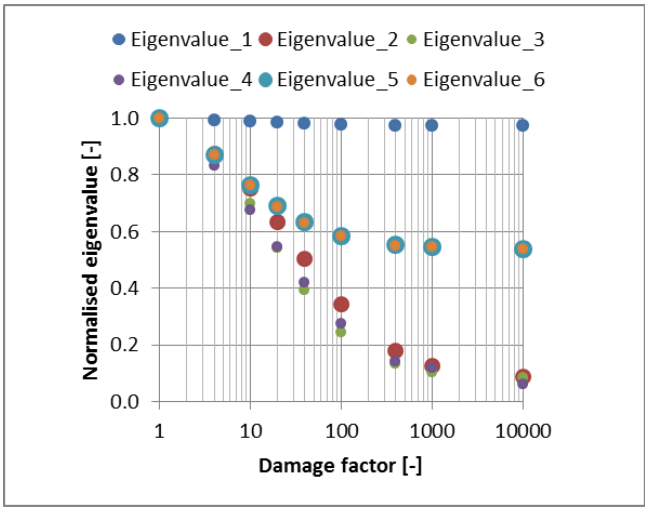

Figure 4.3.6 Normalised eigenvalues of the model with fibre-matrix debonding

Note that for fibre matrix debonding the longitudinal stiffness remains unchanged and much higher than other components. As evaluated earlier for the fibre cracking model, the higher is the first element of stiffness tensor (C_{11}) in comparison to other elements, the closer it is to the first eigenvalue (λ^I). Subsequently the angle between the first eigenvector and X direction becomes lower. Figure 4.3.7 shows eigenvectors of damaged and undamaged material. Second eigenvector does not rotate at all. Furthermore, there was only slight change in the first and the third eigenvectors despite the significant damage (factor 10000).

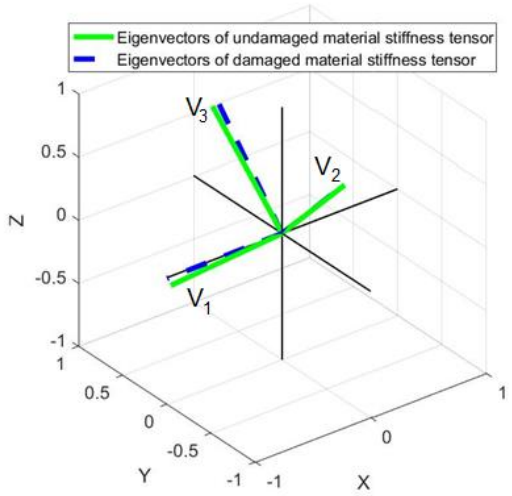

Figure 4.3.7 Eigenvectors in 3D space for fibre-matrix debonding model for undamaged material (green) and material with damage factor 10000 (blue)

Figure 4.3.8 shows the first three eigenvalues and corresponding eigenvectors rotation. It is clear that despite the significant change of second and third eigenvalues the rotation of the eigenvectors do not exceed the 5°, and therefore the material does not lose its symmetry.

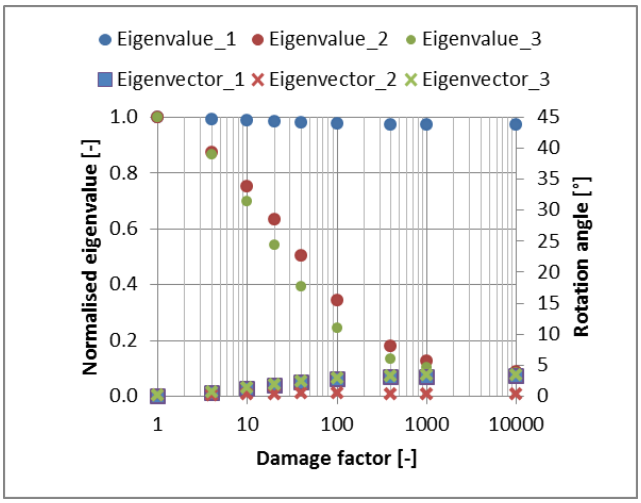

Figure 4.3.8 Eigenvalues and eigenvectors rotation angle of the model withfibre-matrix debonding

Note that the discrepancy between second and fourth eigenvalues (in Figure 4.3.6) may be a result of a slight rotation of the second eigenvector which may be caused by the numerical errors. If transverse material properties are reduced the difference between the eigenvalues (highest and lowest) can reach two orders of magnitude. It is significant and can lead to numerical inaccuracy.

4.3.4 Combined damage

Figure 4.3.9 shows the stiffness eigenvalues of the combined damage model. The combined damage was the damage mechanism affecting fibres and the interface between fibres and the matrix, so it is not surprising that all eigenvalues were affected.

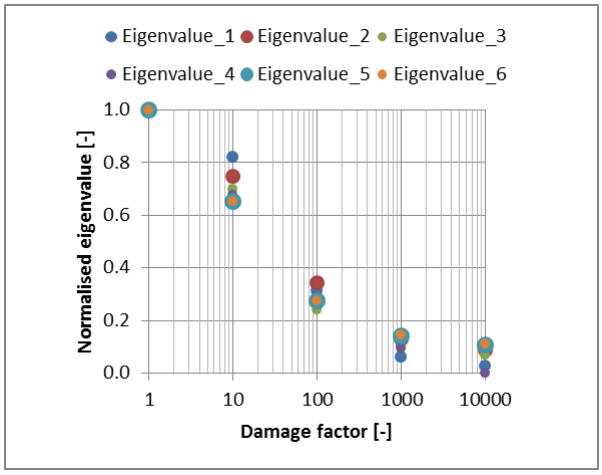

Figure 4.3.9 Normalised eigenvalues of the model with combined damage

Joined graphs of the first three eigenvalues and eigenvectors' rotation angles of combined damage model are presented in Figure 4.3.10. The figures show that the maximum rotation angle does not exceed 15° for the first and the third eigenvectors. It was also kept well below 5° for damage factor 1000 and below 2° for damage factor 100. The second eigenvalue rotation is insignificant as it does not exceed 0.5°.

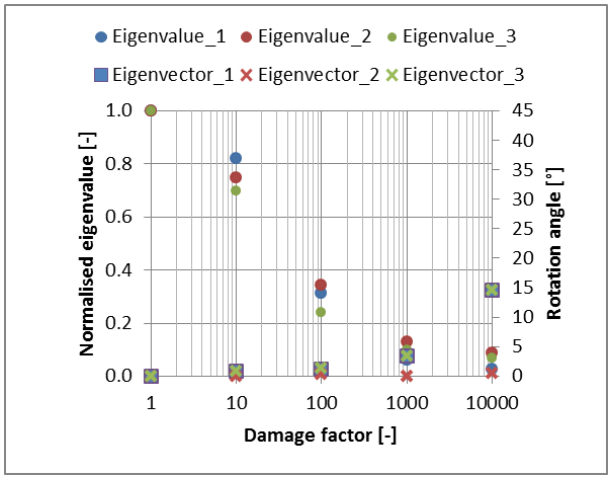

Figure 4.3.10 Eigenvalues and eigenvectors rotation angle of the model withfibre-matrix debonding

These results were presented to show, that the rotation of the eigenvectors in fibre and matrix damage model do not exceed the rotations observed with broken fibre model in Section 4.3.1.

4.4 Summary

The number of simulations of mesoscale damage models was performed. The considered damage mechanisms were fibre breaking, fibre-matrix interfacial debonding, matrix uniform damage and combined fibre breaking with interfacial debonding. Simulations were performed with different extent of damage that was controlled by the damage factor. Neither of the modelled damage cases violated the RVE conditions.

Results of this study demonstrate a clear trend of a gradual reduction of the stiffness tensor eigenvalues due to damage. In the case of fibre breaking it is followed by the rotation of the material eigensystem around the second eigenvector. However, it was found to be significant only for the reduction of the first principal stiffness by more than 60%. For such severe damage matrix starts to play a significant role in carrying load. At this point the material can be regarded as having no load carrying capacity and undergo final failure. In the matrix related damage mechanisms, the eigenvectors remained unchanged regardless the magnitude of damage. Therefore, the assumption of not rotating eigenvectors is valid for material with reasonable damage extent (not fully failed) and is one of the key assumptions of the model.

5 Mesoscale modelling - deformation eigenmodes

Previous chapter showed the mesoscale damage modelling results that aimed at better understanding of the changes brought by damage into the material at continuum level. It was also proved that damage can be successfully represented by changing stiffness eigenvalues. Second, but equally important purpose of the mesoscale modelling, which is addressed in this chapter, is an investigation of the state of material loaded in a single deformation mode (strain eigenmode). The analysis of the mesoscale simulations was based on the effect that continuum scale loading has on the material constituents. Knowledge of how the eigenstrain loading affects the material constituents allows to determine the strain energy limits and possible damage mechanisms.

The motivation for this analysis lies in a postulate given by Schreyer and Zuo (1995) that the material fails if the strain energy in a spectrally decomposed mode exceeds its limit value. For isotropic materials there are two modes i.e. volumetric and deviatoric. The deviatoric mode is the exact form of von-Mises yield criterion. For symmetries different than isotropy a number of modes can be defined and for each of them its strength limit can be determined. Whilst the postulate formulated by Schreyer and Zuo (1995) uses the eigenstresses (not to be confused with principal stresses) it is shown in Section 5.1.1 that eigenstrains can be used as well in the definition of strain energy. The authors suggested that the experiments can be designed so that the stresses (or strains) applied to the material activate only one of the strain energy modes. Whereas, it might be a challenge to design such mechanical tests it is straightforward to apply a specific deformation mode in FE. Simulations that activated the single strain energy mode are described in the following section. They were analysed in terms of the effect they have on the separate constituents.

In Section 5.1.1 the strain based eigenmodes characteristic for the modelled material are defined. The FEA was performed to check the state of a material loaded elastically in single strain energy mode. The simulations that activate single strain energy mode are described in Section 5.1.2. Results of the simulations are given in Section 5.2. Interaction between first three strain energy modes was also investigated by loading the material to activate two strain energy modes simultaneously. Similar analysis was not carried out for the fourth, fifth and sixth eigenmodes due to difficulty in modelling of those interactions.

5.1 Model

Geometry of a model used for the analysis of deformation eigenmodes is the same as the geometry used for modelling damage shown in Section 4.1 but for self-consistency of the chapter the main characteristics are repeated here. The RVE consists of 16 randomly arranged fibres surrounded by matrix. The fibre diameter is approximately 5μm. The whole RVE is a cube with edge length of 0.026mm. Matrix material is modelled with MAT_001 and fibre with MAT_002 (simple elastic and orthotropic elastic materials). The material properties can be found in Appendix C. Loads and boundary conditions that were applied to activate a single strain energy mode are presented in Section 5.1.2.

5.1.1 Definition of strain energy modes

Existence of strain, stress and stiffness modes allow to define modes of strain energy (Lubarda and Chen, 2009). Strain energy density for a material is equal to:

$$W = \frac{1}{2}\boldsymbol{\sigma}\cdot\boldsymbol{\varepsilon} = \frac{1}{2}\sum_{i=1}^{n}\boldsymbol{\sigma}\cdot\left(\mathbf{P}^i\cdot\boldsymbol{\varepsilon}\right) = \frac{1}{2}\sum_{i=1}^{n}\boldsymbol{\sigma}^i\cdot\boldsymbol{\varepsilon}^i = \frac{1}{2}\sum_{i=1}^{n}\lambda^i\boldsymbol{\varepsilon}^i\cdot\boldsymbol{\varepsilon}^i = \frac{1}{2}\sum_{i=1}^{n}\lambda^i\overline{\boldsymbol{\varepsilon}}^{i\,2}, \qquad \textbf{5.1.1}$$

with $\boldsymbol{\sigma}$ and $\boldsymbol{\varepsilon}$ being respectively stress and strain tensors, $\mathbf{P}$ is projection operator tensor and λ is eigenvalue. Superscript i denotes the i-th deformation mode. For a transversely isotropic material (material of tetragonal symmetry) the projection operator and subsequently strain vector in a mode is:

$$\boldsymbol{\varepsilon}^i = \mathbf{P}^i\cdot\boldsymbol{\varepsilon} = \left(\mathbf{v}^i\cdot\boldsymbol{\varepsilon}\right)\mathbf{v}^i, \qquad \textbf{5.1.2}$$

where $\mathbf{v}^i$ is eigenvector of i-th mode. It can be demonstrated that the single contraction of a modal strain vector with itself is:

$$\overline{\boldsymbol{\varepsilon}}^{i\,2} = \boldsymbol{\varepsilon}^i\cdot\boldsymbol{\varepsilon}^i = \left(\mathbf{v}^i\cdot\boldsymbol{\varepsilon}\right)\mathbf{v}^i\cdot\left(\mathbf{v}^i\cdot\boldsymbol{\varepsilon}\right)\mathbf{v}^i = \left(\mathbf{v}^i\cdot\boldsymbol{\varepsilon}\right)^2\mathbf{v}^i\cdot\mathbf{v}^i = \left(\mathbf{v}^i\cdot\boldsymbol{\varepsilon}\right)^2 = \varepsilon^{i\,2}, \qquad \textbf{5.1.3}$$

where the magnitude of the modal strain vector is:

$$\varepsilon^i = \mathbf{v}^i\cdot\boldsymbol{\varepsilon}. \qquad \textbf{5.1.4}$$

The explicit formulas that define the modal strain magnitudes in terms of the total strain vector members are presented below:

$$\overline{\boldsymbol{\varepsilon}}^{I2} = \varepsilon^{I2} = \frac{1}{2+\alpha^2}\left(\alpha\varepsilon_1 + \varepsilon_2 + \varepsilon_3\right)^2,$$

$$\overline{\boldsymbol{\varepsilon}}^{II2} = \varepsilon^{II2} = \frac{1}{2}\left(\varepsilon_2 - \varepsilon_3\right)^2,$$

$$\overline{\boldsymbol{\varepsilon}}^{III2} = \varepsilon^{III2} = \frac{1}{2+\beta^2}\left(\beta\varepsilon_1 + \varepsilon_2 + \varepsilon_3\right)^2, \qquad \textbf{5.1.5}$$

$$\overline{\boldsymbol{\varepsilon}}^{IV2} = \varepsilon^{IV2} = 2\varepsilon_4{}^2,$$

$$\overline{\boldsymbol{\varepsilon}}^{V2} = \varepsilon^{V2} = 2\varepsilon_5{}^2,$$

$$\overline{\boldsymbol{\varepsilon}}^{VI2} = \varepsilon^{VI2} = 2\varepsilon_6{}^2.$$

Roman numbers in upper indices in the equations denote the mode number. A single strain energy mode is activated if one of the modal strains is nonzero. Therefore, by solving the set of equations, where only one of the equations is nonzero, the relation between the strain components can be obtained for each eigenmode. Subsequently each modal strain can be defined by a single variable ε as presented in Table 5.1.1.

Table 5.1.1 Activation of a single strain energy mode

Activated mode	Strain component					
	ε_1	ε_2	ε_3	ε_4	ε_5	ε_6
$\overline{\boldsymbol{\varepsilon}}^{I2} \neq 0$	ε	$\frac{1}{\alpha}\varepsilon$	$\frac{1}{\alpha}\varepsilon$	0	0	0
$\overline{\boldsymbol{\varepsilon}}^{II2} \neq 0$	0	ε	$-\varepsilon$	0	0	0
$\overline{\boldsymbol{\varepsilon}}^{III2} \neq 0$	ε	$-\frac{\alpha}{2}\varepsilon$	$-\frac{\alpha}{2}\varepsilon$	0	0	0
$\overline{\boldsymbol{\varepsilon}}^{IV2} \neq 0$	0	0	0	ε	0	0
$\overline{\boldsymbol{\varepsilon}}^{V2} \neq 0$	0	0	0	0	ε	0
$\overline{\boldsymbol{\varepsilon}}^{VI2} \neq 0$	0	0	0	0	0	ε

Coefficient α is a material characteristic coefficient accounting for its anisotropy. It equals to 22.7 for the material used in mesoscale simulations. Because of such a high value (resulting from high anisotropy) the first strain mode is almost a plane strain in the fibre direction.

Figure 5.1.1 shows the graphical representation of strain energy modes of a transversely isotropic material. Note that for the negative value of ε the modes would be reversed, i.e. instead of tension there would be compression and instead of compression there would be tension. The signs of the modes were assigned arbitrarily, and are used consistently throughout this work.

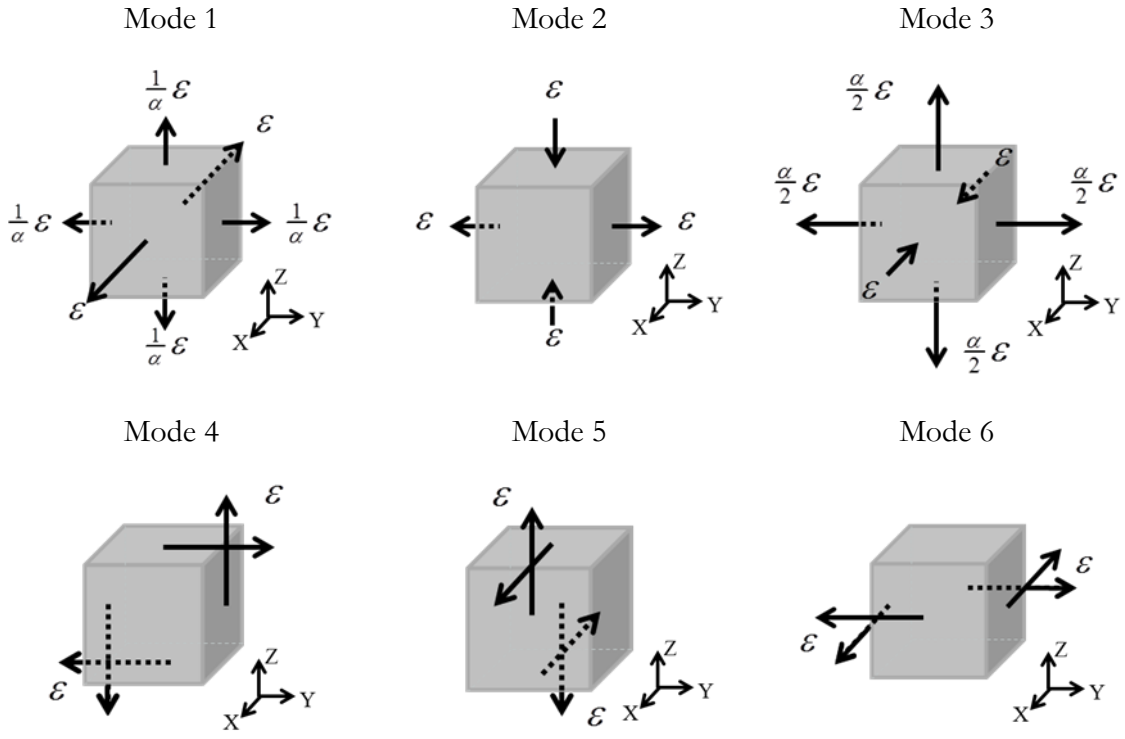

Figure 5.1.1 Graphical represetation of the strain vectors activating a single strain energy mode

For a transversely isotropic material the second and the fourth mode share the same eigenvalue and result in the same material loading type (shear deformation in the plane of isotropy (Figure 5.1.2). Although, they can be coupled, they were modelled separately in this chapter and their results were compared to check the modelling approach and accuracy.

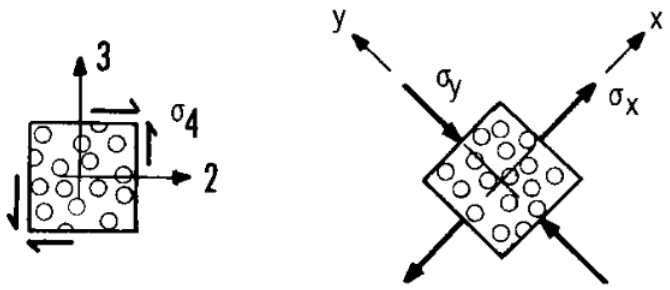

Figure 5.1.2 Equivalent states of stress in pure shear and tension-compression (Tsai and Wu, 1971)

The third mode is the transverse strain mode which has a small component in longitudinal direction. The longitudinal strain in this mode has different sign from the transverse strains.

Modes five and six are both the shear modes in the fibre plane. They share the same eigenvalue, and for a transversely isotropic material can be coupled. However, in simulation their equivalence was not assumed *a priori*, so they were modelled separately.

The strain modes are defined using the coefficient α, and therefore their applicability is limited to the material states that do not affect α significantly – the states for which material eigensystem (system of eigenvectors) does not rotate. It was demonstrated in the previous chapter that excluding significant fibre damage this requirement is fulfilled. It is accounted for in the material model development (Chapter 6) by setting a critical value for a fibre-related damage variable.

Similar approach to define strain energy modes was used by Schreyer and Zuo (1995). Instead of strain tensors they used the stress tensors in the definition, which is convenient for the plasticity models. For composites, however, strains seem a more reasonable choice.

5.1.2 Loads and boundary conditions

The strain vectors presented in Figure 5.1.1 were applied to the RVE of unidirectional composite to check its response to activation of a single strain energy mode. The loads were chosen so that the magnitude of the strain vector was 0.001 in all modelled cases. The strain vectors applied to the RVE are given below.

$$\boldsymbol{\varepsilon}^{I} = \begin{bmatrix} 0.998 & 0.044 & 0.044 & 0 & 0 & 0 \end{bmatrix}^{T} 10^{-3},$$

$$\boldsymbol{\varepsilon}^{II} = \begin{bmatrix} 0 & 0.707 & -0.707 & 0 & 0 & 0 \end{bmatrix}^{T} 10^{-3},$$

$$\boldsymbol{\varepsilon}^{III} = \begin{bmatrix} -0.064 & 0.706 & 0.706 & 0 & 0 & 0 \end{bmatrix}^{T} 10^{-3},$$

$$\boldsymbol{\varepsilon}^{IV} = \begin{bmatrix} 0 & 0 & 0 & 1 & 0 & 0 \end{bmatrix}^{T} 10^{-3},$$

$$\boldsymbol{\varepsilon}^{V} = \begin{bmatrix} 0 & 0 & 0 & 0 & 1 & 0 \end{bmatrix}^{T} 10^{-3},$$

$$\boldsymbol{\varepsilon}^{VI} = \begin{bmatrix} 0 & 0 & 0 & 0 & 0 & 1 \end{bmatrix}^{T} 10^{-3}. \qquad \textbf{5.1.6}$$

The boundary conditions applied to activate the first three modes were the same. Three faces X, Y and Z were constrained from movement along the normal direction as presented in Figure 5.1.3.

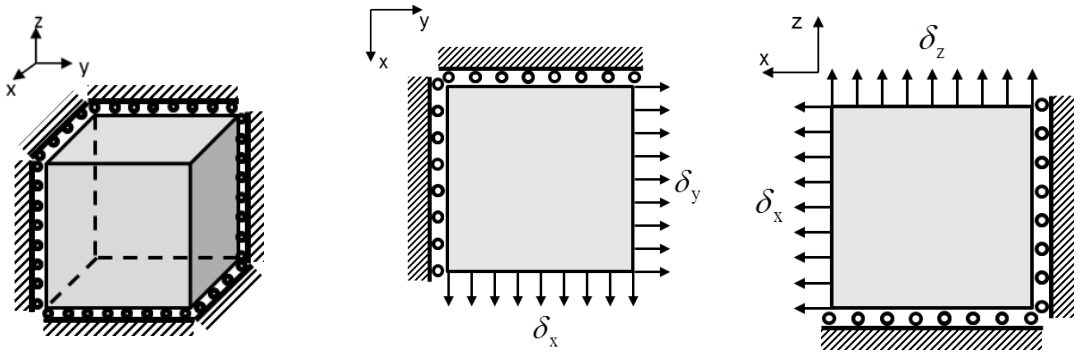

Figure 5.1.3 Boundary conditions for modes I, II and III

The three unconstrained faces were loaded by set displacements that result in the strain states given by Equations 5.1.6. The displacements for the modes are listed in Table 5.1.2.

Table 5.1.2 Displacements applied to RVE to activate a single strain energy mode

Mode I:	Mode II:	Mode III:
$\delta_x = 2.595\times10^{-5}$	$\delta_x = 0$	$\delta_x = -1.668\times10^{-6}$
$\delta_y = 1.142\times10^{-6}$	$\delta_y = 1.838\times10^{-5}$	$\delta_y = 1.835\times10^{-5}$
$\delta_z = 1.142\times10^{-6}$	$\delta_z = -1.838\times10^{-5}$	$\delta_z = 1.835\times10^{-5}$

Modes IV, V and VI were activated by constraining one face in all directions and loading the opposite face with set displacement as presented in Figure 5.1.4.

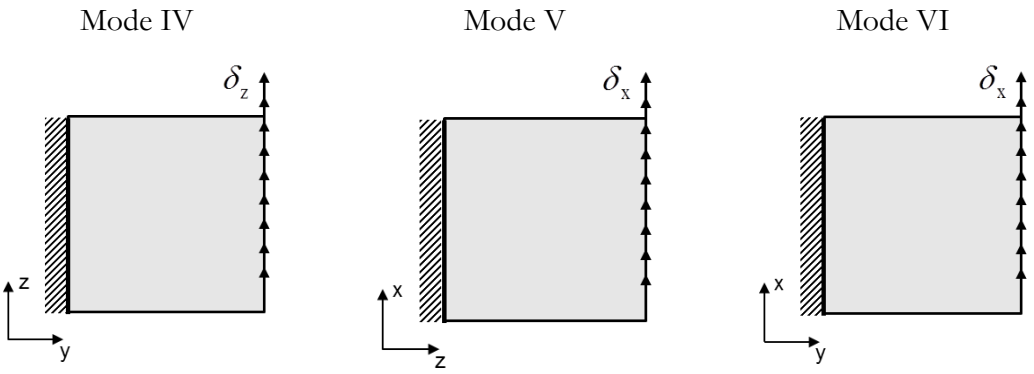

Figure 5.1.4 Loads and boundary conditions for modes IV, V and VI

Such loading condition generates the engineering state of strain in a material in YZ, ZX and XY planes respectively. The displacement that corresponds to the principal strain of magnitude 0.001 is equal to $\delta_i = 3.676*10^{-5}$. It was calculated considering the notation used, the edge length and fact that the engineering strain was generated instead of pure strain.

5.1.3 Mechanical tests that activate single strain energy mode

The possibility of designing the mechanical tests that activate single strain energy mode was already postulated in Section 5.1.1. The modes that are most easily activated by the mechanical test are fifth and sixth modes which are simple shear modes in fibre direction. The test that is commonly used to investigate the shear behaviour of composites is IOSIPESCU shear test (Walrath and Adams, 1983) – see Figure 5.1.5. Therefore, it can also be used to determine the strain energy limit in the fifth and sixth modes. The critical strain (or strain energy) values in these modes should be equal because of transverse isotropy of unidirectional composite. IOSIPESCU shear test can be also used to determine shear behaviour in the plane of material isotropy (mode IV critical energy).

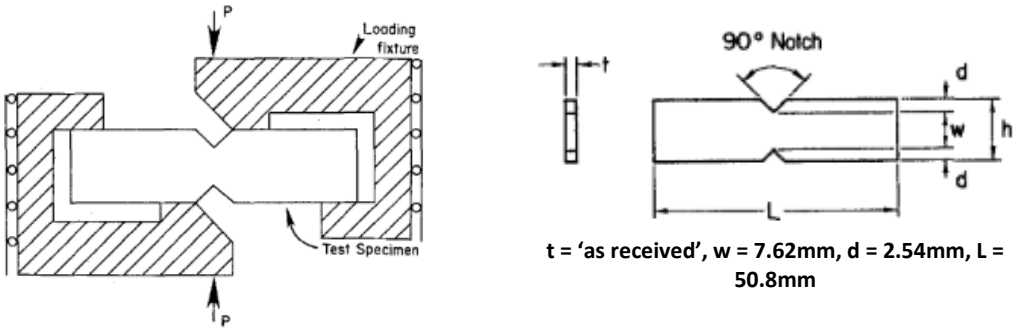

Figure 5.1.5 IOSIPESCU shear test and specimen (Broughton, K and Hull, 1990)

Equivalence of modes II and IV (presented in Section 5.1.1 in Figure 5.1.2) allows to determine only one strain energy limit for both modes. Moreover, the second mode can also be activated by biaxial tension – compression test (Van Hemelrijck *et al.*, 2008).

There are no standard tests that activate modes I and III. Mode I critical energy can be determined from known critical longitudinal strain of fibres by:

$$\omega_0^I = \lambda^I \overline{\boldsymbol{\varepsilon}}_{cr}^{f\,2} \qquad \textbf{5.1.7}$$

There are no standard and commonly used mechanical tests that can give the accurate value of the mode III threshold energy. Mode III threshold energy can be only approximated by

the biaxial tension – tension test while omitting the longitudinal strain in the mode. As a consequence, the mode I is also activated.

The tests presented here are only a suggestion – any mechanical activating a single strain energy mode can be used. In this work the threshold energies were determined using the mesoscale models' simulations.

5.2 Single strain energy modes results

The simulation results were analysed in terms of stresses generated in fibres and the matrix. The longitudinal (X) stress component was assumed to be critical for fibres. Therefore, all results for fibres are analysed in terms of longitudinal direction. The matrix material was analysed in terms of the X, Y and Z stress components. Moreover, pressure and von Mises stress were investigated. The maximum stresses in the fibres (maximum longitudinal (X) stress) and the matrix (maximum von Mises (VM) stress) were determined by averaging the 20 highest values in the middle cross-section of constituents. The von-Mises stress is the second mode eigenstress for an isotropic material (see Section 2.2.1). It is a measure of distortional strain energy in the material, and thus is consistent with energy and spectral decomposition approach adopted in this work. The elements lying on boundaries of the model were disregarded, as the stress values in them might be affected by boundary conditions. Maximum strain and strain energy values were obtained assuming proportionality of stress and strain in linear elastic analysis.

The limit stress values for fibres and matrix were obtained from the manufacturer's data. Assumed fibre strength was 4900 MPa (Hexcel Corporation, 2016), and the yield limit of matrix 81 MPa (Cytec Engineered Materials, 2012). Knowledge of both the maximum stress in a material (for known strain magnitude) and the stress limit allows to calculate the limit strain and consequently limit strain energy in each mode.

5.2.1 Mode I

In the first mode a dominant direction is the fibre direction. The RVE was loaded by set displacements in X, Y and Z directions. The resultant displacements (Figure 5.2.1) show that the state of strain required for activation of the first mode was achieved.

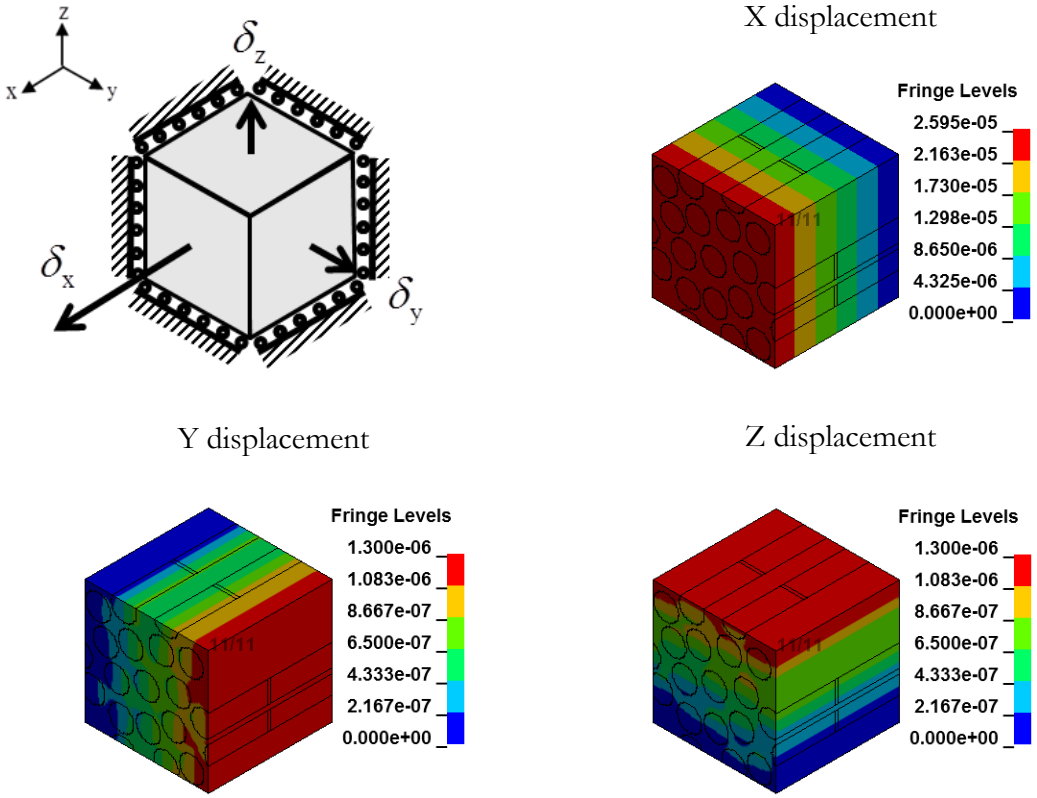

Figure 5.2.1 Mesoscale model loaded in the first mode

The first eigenvector is almost collinear with fibre direction, so this mode is almost perfectly longitudinal, i.e. the load in X direction is much higher than that in Y and Z directions. Therefore, it is not surprising that the longitudinal stress in fibres was highest. Fibres were loaded equally up to stress 268.6 MPa (Figure 5.2.2).

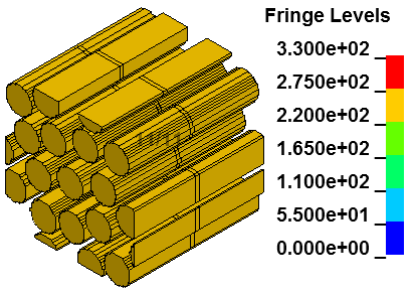

Figure 5.2.2 RVE loaded in the first deformation mode – X stress component in fibres

Stress in matrix in longitudinal direction ranged from 9.4 MPa to 10.2 MPa, but the vast majority of elements were stressed up to 9.8 MPa (Figure 5.2.3 - a)). Matrix stresses in Y and Z direction ranged from 5.1 MPa to 7.0 MPa (Figure 5.2.3 - b) and c)).

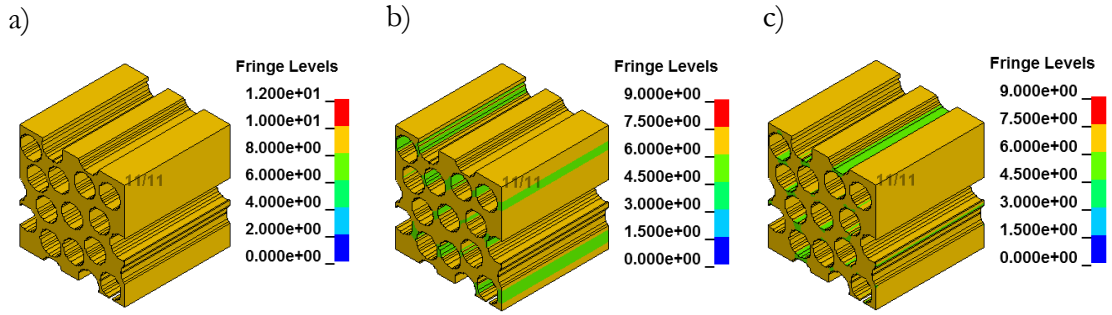

Figure 5.2.3 RVE loaded in the first deformation mode: a) X stress component, b) Y stress component, c) Z stress component in matrix

Due to equality of transverse stresses and the fact that the longitudinal stress in matrix was of the same order of magnitude there was a high pressure component in the matrix (Figure 5.2.4 - a)). Note that all the stress components were tensile, which in LS-Dyna gives negative pressure. The magnitude of the pressure was 7.0 MPa and it was uniform within the RVE matrix elements. The von Mises stress in the RVE ranged from 3.3 to 3.7 MPa.

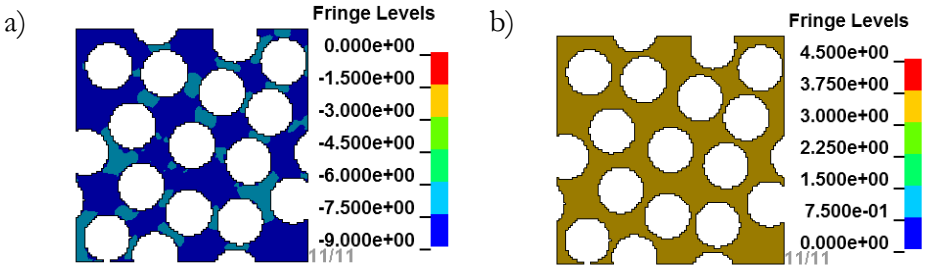

Figure 5.2.4 RVE loaded in the first deformation mode: a) pressure, b) von Mises stress in matrix

Table 5.2.1 shows the averaged stress results obtained for 20 most loaded elements in fibres and matrix, strength of the constituents and calculated limit strain. The limit strain was determined by multiplying the input strain by the ratio of strength and stress.

Table 5.2.1 Mesoscale modelling of the first deformation mode results

	Input strain [%]	Stress [MPa]	Strength [MPa]	Limit strain [%]
Fibre	0.1	268.6	4900	1.82
Matrix	0.1	3.8	81	2.13

Note that the limit strain calculated for fibres is 1.82%, which is close to 1.70% – limit strain for carbon fibres reported in (Hexcel Corporation, 2016). Strain limit for matrix is higher than that of fibres, therefore it can be stated that the principal damage mechanism in the first mode is fibre breaking. However, matrix damage cannot be neglected. Straining the material

in the first mode up to failure of fibres results in the matrix stress being 67.3 MPa, which is 83% of its strength.

5.2.2 Mode II

The second mode is a shear mode in the isotropy plane (YZ). Figure 5.2.5 shows the displacements in the RVE that activated a second deformation mode. Displacement and subsequently strain in longitudinal direction were zero. Displacements in transverse directions were equal in magnitude but opposite in sign. This resulted in equal but opposite strains.

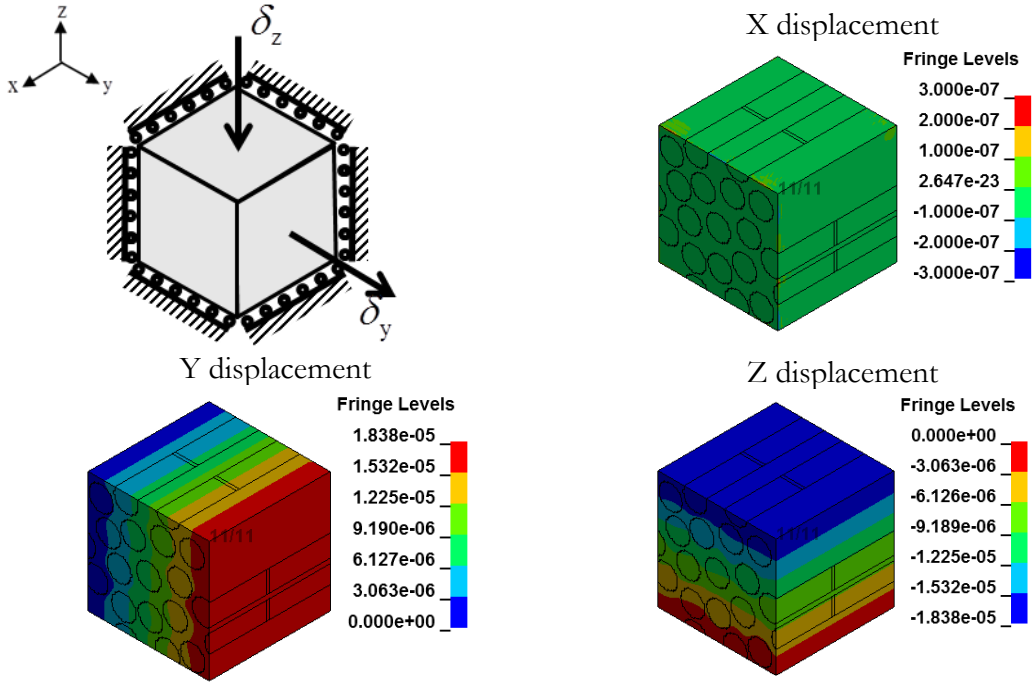

Figure 5.2.5 Load and displacements in the second mode

Figure 5.2.6 - a) shows the X stress component in fibres. Disregarding the slight boundary effects, the longitudinal stress in fibres was equal to zero. The fibre stresses in Y and Z directions were more significant – up to 10 MPa in tension (Y stress component) and compression (Z stress component). Nevertheless, they were neglected in the analysis. The first reason is the difficulty in defining the fibre transverse strength – it can hardly be determined by the mechanical tests. Secondly, as fibre transverse stress was comparable to matrix transverse stress, the latter is of greater importance for the overall material strength as matrix strength is undoubtedly lower than fibre strength.

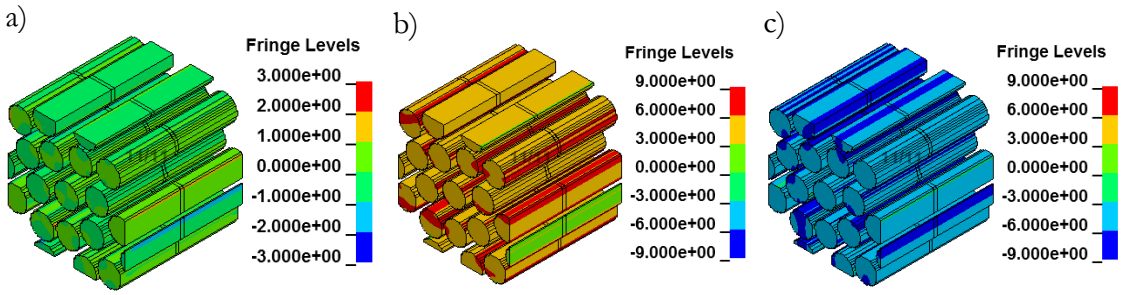

Figure 5.2.6 RVE loaded in the second deformation mode: a) X stress component, b) Y stress component and c) Z stress component in fibres

Figure 5.2.7 shows the stress in matrix of the RVE loaded in the second deformation mode. X stress component in the matrix varied from 4 MPa in compression to 4 MPa in tension as presented in Figure 5.2.7 - a). The highest Y and Z stresses were found between the fibres aligned with deformation direction as shown in Figure 5.2.7 - b) and c). Y stress components were tensile whilst Z stress components were compressive. The maximum stress magnitude in both directions was smaller than 9 MPa.

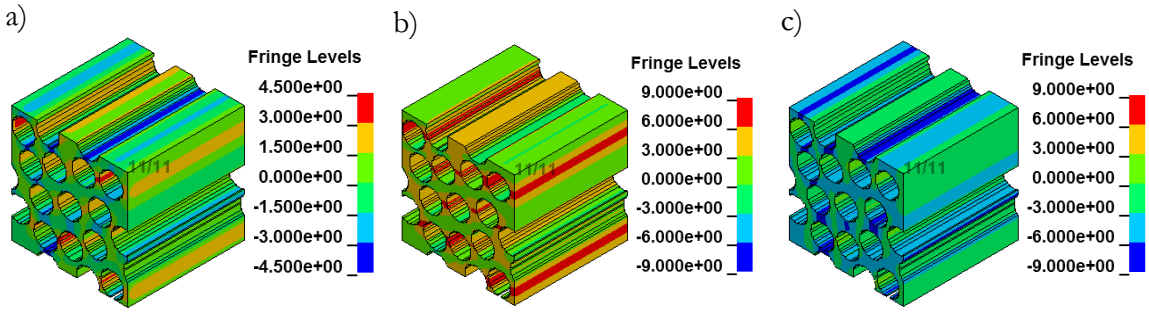

Figure 5.2.7 RVE loaded in the second deformation mode: a) X stress component, b) Y stress component, c) Z stress component in matrix

Pressure in matrix elements was not uniform. The highest pressure was found for the matrix elements located between the neighbouring fibres (Figure 5.2.8 - a)). Pressure did not exceed 5.1 MPa in tension and compression and for large number of elements was close to zero. Von Mises stress in matrix in the second mode reached 9.0 MPa (Figure 5.2.8 - b)). The highest von Mises stress was observed in the elements lying on the paths where the 45° direction distance between the fibres was shortest.

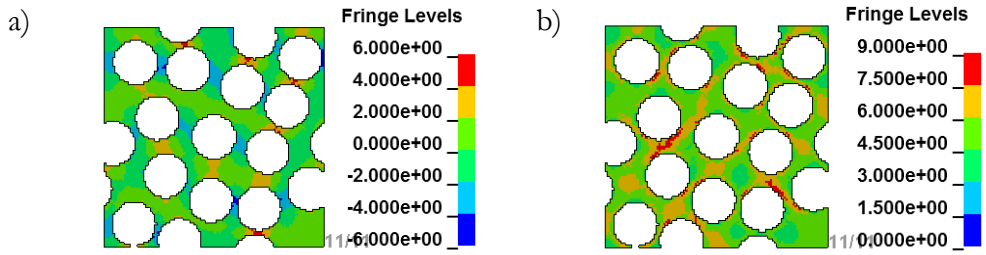

Figure 5.2.8 RVE loaded in the second deformation mode: a) pressure, b) von Mises stress in matrix

The stress results obtained for the second mode are presented in Table 5.2.2. Input strain of 0.1% resulted in matrix equivalent stress of 8.6 MPa and zero longitudinal fibre stress. Limit strain was calculated for the stress equal to strength of the material and is displayed in the last column of the table.

Table 5.2.2 Mesoscale modelling of the second deformation mode results

	Input strain [%]	Stress [MPa]	Strength [MPa]	Limit strain [%]
Fibre	0.1	0.0	4900	-
Matrix	0.1	8.6	81	0.94

The limit strain in the fibres tends to infinity, as the stress was close to zero. The maximum strain determined for matrix elements was 0.948%. The conclusion is that the second mode can be described as the matrix shear mode.

5.2.3 Mode III

The third mode is a three-dimensional strain mode for which the strain in longitudinal direction is more than ten times lower than the strain in both transverse directions as presented in Figure 5.2.9.

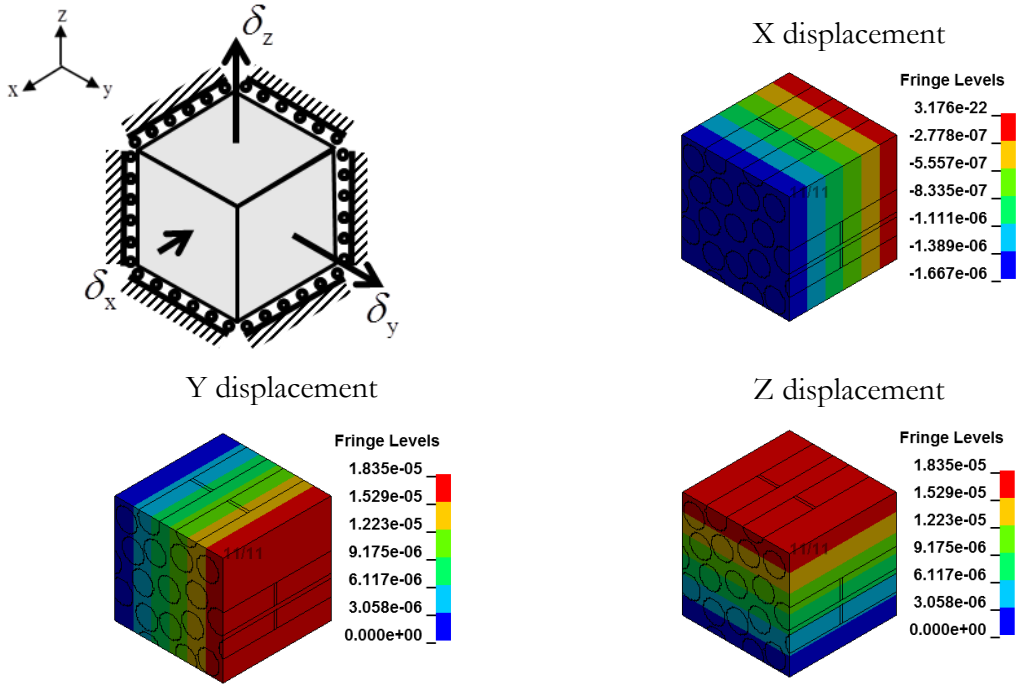

Figure 5.2.9 Load and displacements in the third mode

Figure 5.2.10 shows the longitudinal stress in the fibres obtained for the mesoscale RVE loaded in the third mode. The stress was uniform and equal to 11.2 MPa in compression for all elements.

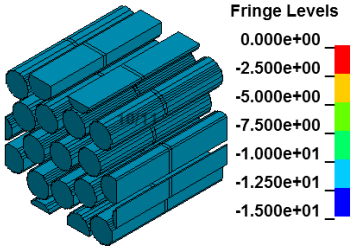

Figure 5.2.10 RVE loaded in the third deformation mode – X stress component in fibres

Matrix stresses are presented in Figure 5.2.11. Despite the compressive strain in longitudinal direction, the X stress component in matrix was positive and equal to 8.7 MPa for all elements (Figure 5.2.11 - a)). Transverse Y and Z stress components were equal to 10.8 MPa in all elements. The variation of stress between the elements did not exceed 0.01 MPa.

a) b) c)

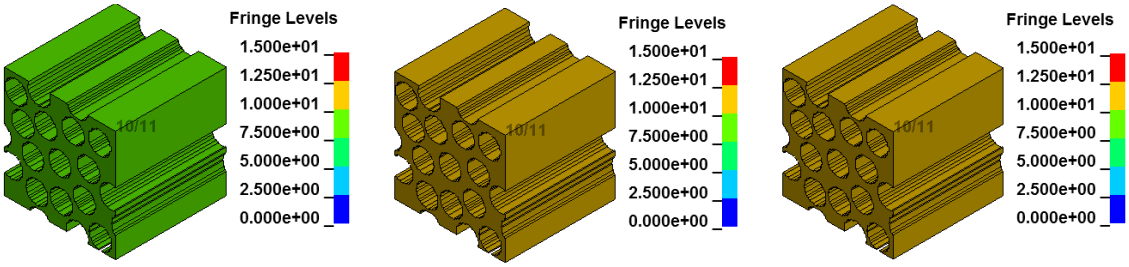

Figure 5.2.11 RVE loaded in the second deformation mode: a) X stress component, b) Y stress component, c) Z stress component in matrix

The fact that the compressive strain resulted in tensile stress, although at first surprising, is justified by Poisson's effect. Significant transverse strain would lead to higher contraction of the material in X direction was it unconstrained. Thus, the resultant X stress component in matrix was tensile.

The equality of Y and Z stress, and the fact that the longitudinal stress was tensile stress of the same order of magnitude resulted in a significant pressure in the matrix – equal to 10.0 MPa in tension (Figure 5.2.12 - a)). Von Mises stress in this mode was much lower – equal to 2.5 MPa (Figure 5.2.12 - b)).

a) b)

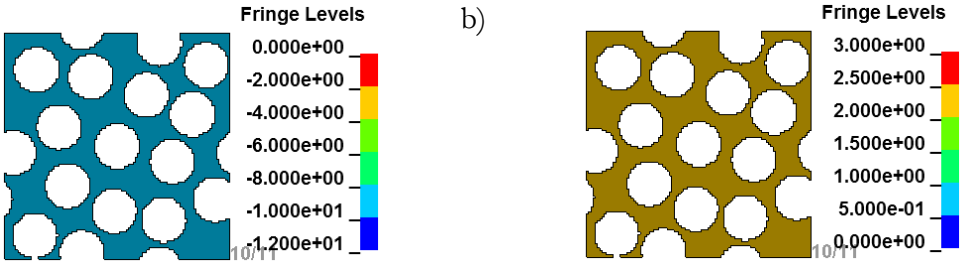

Figure 5.2.12 RVE loaded in the third deformation mode: a) pressure, b) von Mises stress in matrix

Table 5.2.3 shows input strain, stress in the elements, strength of constituents and resultant limit strain for fibres and matrix. Fibres tensile strength was used despite compressive character of load.

Table 5.2.3 Mesoscale modelling of the third deformation mode results

	Input strain [%]	Stress [MPa]	Strength [MPa]	Limit strain [%]
Fibre	0.1	11.2	4900	43.5
Matrix	0.1	2.5	81	3.1

It is clear that the third mode is the matrix-based mode, as the matrix limit strain is much lower than that of fibres. The magnitude of strain that would cause matrix damage is 3.1%, which is a very high value – the limit strain commonly used in aerospace industry is 0.4% (Tsai and Melo, 2014).

5.2.4 Mode IV

The fourth mode is the shear mode in the plane of isotropy (YZ). Ideally it should be combined with the second mode, as both share the same principal stiffness, however due to simulation convenience the modes were modelled separately. The RVE displacements that activated only the fourth mode of deformation are presented in Figure 5.2.13.

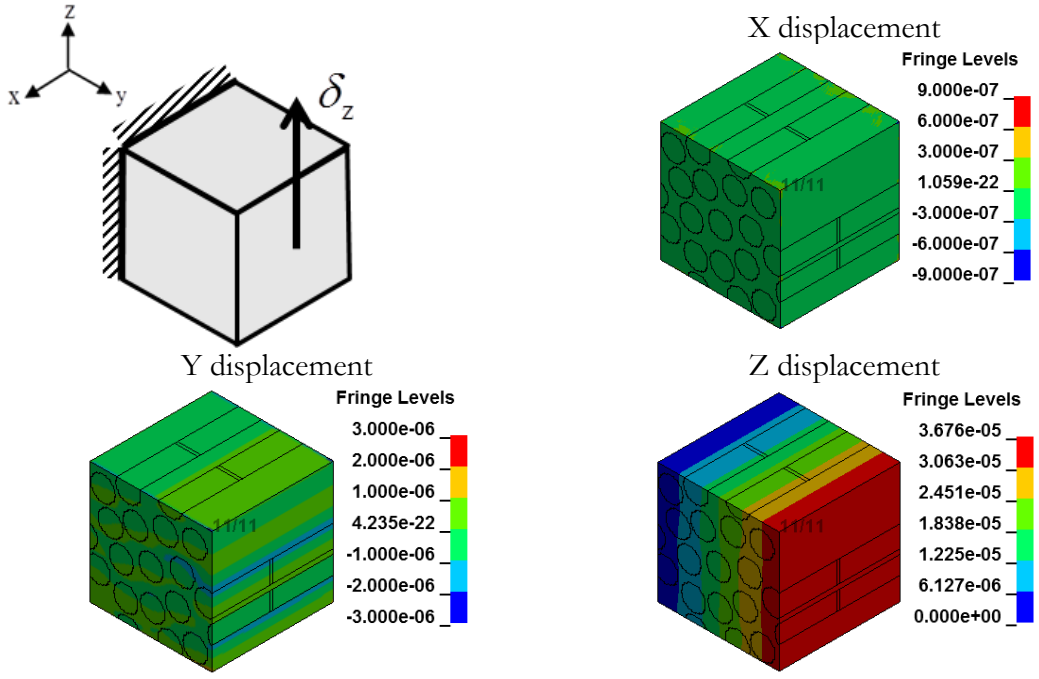

Figure 5.2.13 Loads and displacements in the fourth mode

Longitudinal component of stress in fibres was found to be insignificant. For the vast majority of the fibres it was close to zero as can be seen in Figure 5.2.14 - a). The highest

stress component in fibres was YZ stress presented in Figure 5.2.14 - b). It varied from 3.7 MPa to 5 MPa for the majority of elements, with some higher stress regions – up to 6.3 MPa.

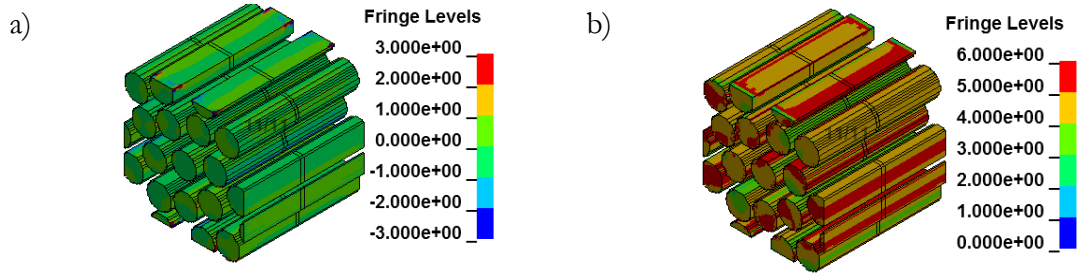

Figure 5.2.14 RVE loaded in the fourth deformation mode: a) X stress component in fibres, b) YZ stress component in fibres

The highest stress components in the matrix were Y, Z and YZ and thus they are displayed in Figure 5.2.15 - a), b) and c) respectively. Normal stresses varied from compressive to tensile in the range of -6.4 MPa to 5.6 MPa. The large number of elements had normal stresses equal to zero. In case of YZ stress component all elements were loaded in shear, vast majority in range 1.5 MPa to 4.5 MPa.

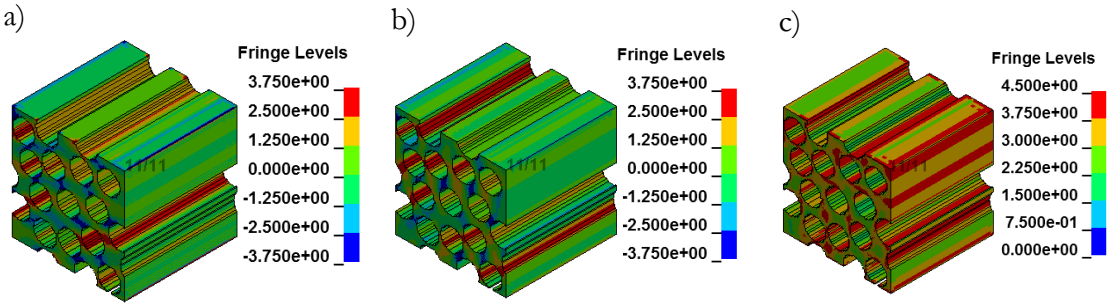

Figure 5.2.15 RVE loaded in the fourth deformation mode: a) Y stress component, b) Z stress component, c) YZ stress component in matrix

The highest pressure in the matrix component can be found between the fibres in 45° directions which can be observed in Figure 5.2.16 - a). On the other hand, the highest von Mises stress paths have an angle 0°/90° with respect to the coordinate axes. The von Mises stress varied between 2.7 MPa in low stress regions up to 9.0MPa in the high stress zones.

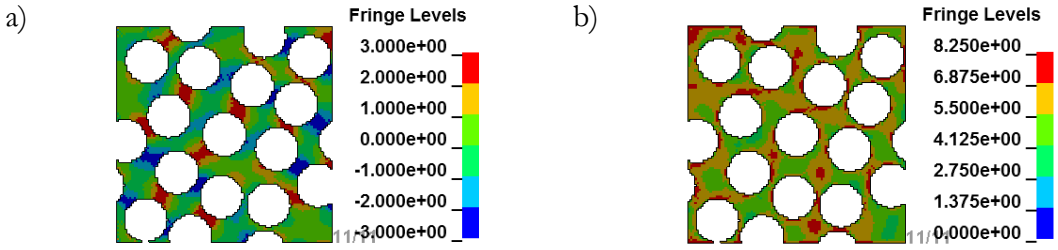

Figure 5.2.16 RVE loaded in the fourth deformation mode: a) pressure, b) von Mises stress in matrix

Table 5.2.4 shows the results of the limit strain calculated from the input strain multiplied by ratio of strength and stress. The limit strain for fibres is not shown as it greatly exceeds one. The limit strain for matrix material was calculated to be 0.95%.

Table 5.2.4 Mesoscale modelling of the fourth deformation mode results

	Input strain [%]	Stress [MPa]	Strength [MPa]	Limit strain [%]
Fibre	0.1	0.1	4900	-
Matrix	0.1	8.5	81	0.95

Note that the limit strain for matrix in the fourth mode (0.95%) was very close to the limit strain in the second mode (0.94%), which was expected as the modes are equivalent in terms of generated stress state.

5.2.5 Mode V

The fifth mode is a ZX shear mode. The RVE was constrained on the Z face and the opposite Z face was loaded with set displacement in X direction. The resultant displacements in the RVE are presented in Figure 5.2.17.

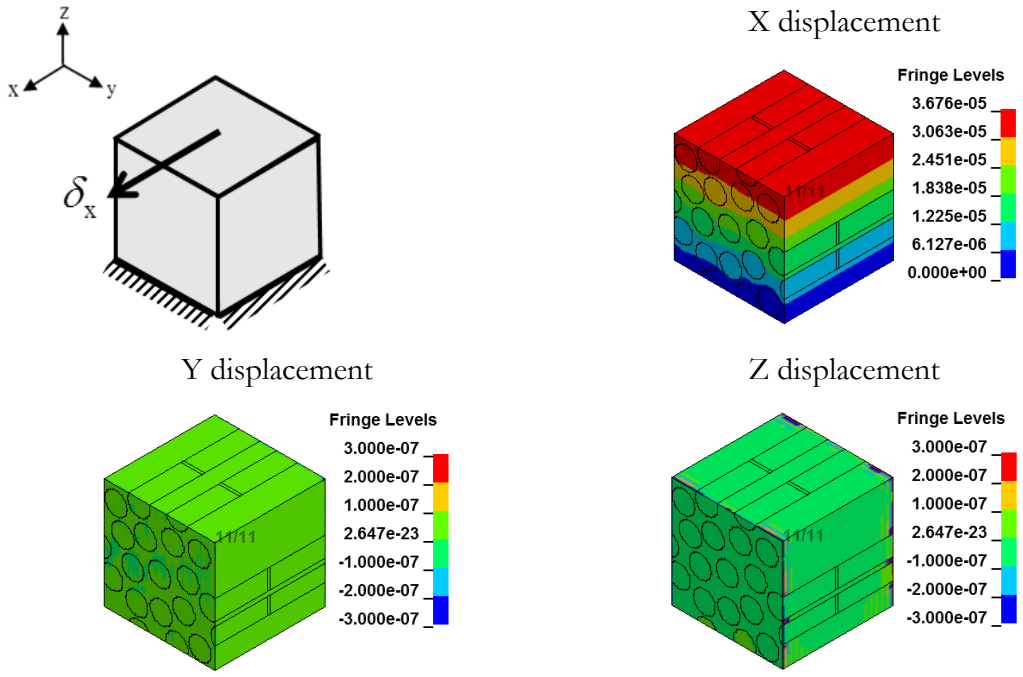

Figure 5.2.17 Loads and displacements in the fifth mode

The fibre X stress component was, for majority of elements close to zero as presented in Figure 5.2.18 - a). The only nonzero stress component in fibres was ZX stress, shown in Figure 5.2.18 - b). It varied from 3.4 MPa to 12.6 MPa. Majority of elements' stresses were in the range 5.0 MPa to 10.0 MPa.

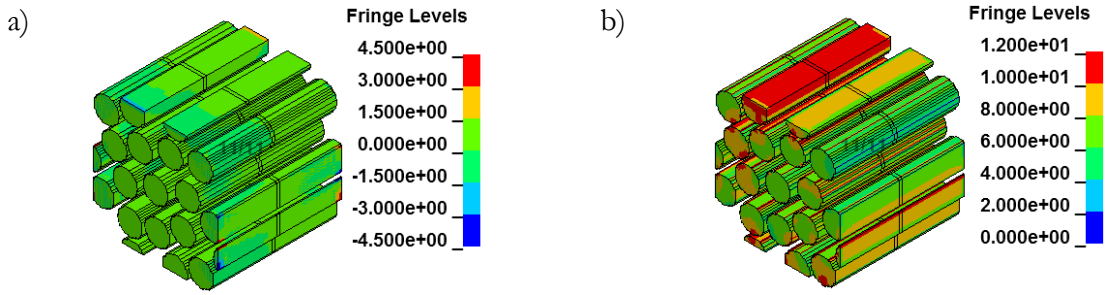

Figure 5.2.18 RVE loaded in the fifth deformation mode: a) X stress component in fibres, b) YZ stress component in fibres

The X and Z stress components in matrix were equal to zero if the boundary effects were ignored (Figure 5.2.19 - a)). The most significant stress component in this mode was ZX. Stress in matrix in majority of elements was between 0.5 MPa and 7.5 MPa. The elements with highest stresses were localised between the neighbouring fibres, where the distance between the fibres was smallest. This can be observed in Figure 5.2.19 - c).

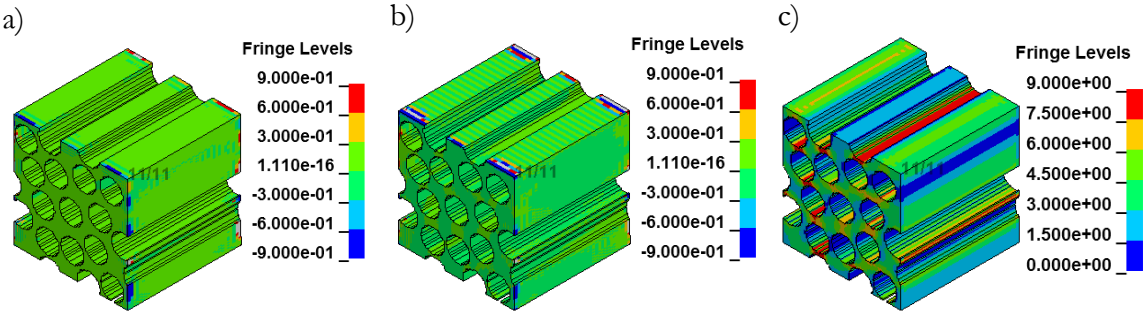

Figure 5.2.19 RVE loaded in the fourth deformation mode: a) X stress component, b) Z stress component, c) ZX stress component in matrix

Pressure part of the stress in the all elements (ignoring boundary effects) was equal to zero as presented in Figure 5.2.20 - a). The von Mises stress varied from 1.0 MPa to 22.2 MPa. The highest values of von Mises stress were found where the distance in Z direction between the fibres was shortest.

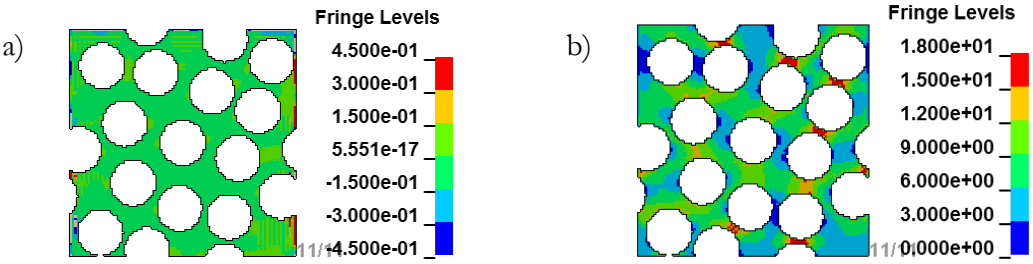

Figure 5.2.20 RVE loaded in the fifth deformation mode: a) pressure, b) von Mises stress in matrix

The resultant limit strain was calculated and presented in Table 5.2.5. The limit strain is not shown for fibres, as it greatly exceeds one. The matrix limit strain of was 0.39%.

Table 5.2.5 Mesoscale modelling of the fifth deformation mode results

	Input strain [%]	Stress [MPa]	Strength [MPa]	Limit strain [%]
Fibre	0.10	0.1	4900	-
Matrix	0.10	20.9	81	0.39

5.2.6 Mode VI

The sixth mode is the XY shear mode. Because of the transverse isotropy the material properties in YZ plane are the same. This results in the sixth mode being equivalent to the fifth mode. The RVE displacements are presented in Figure 5.2.21.

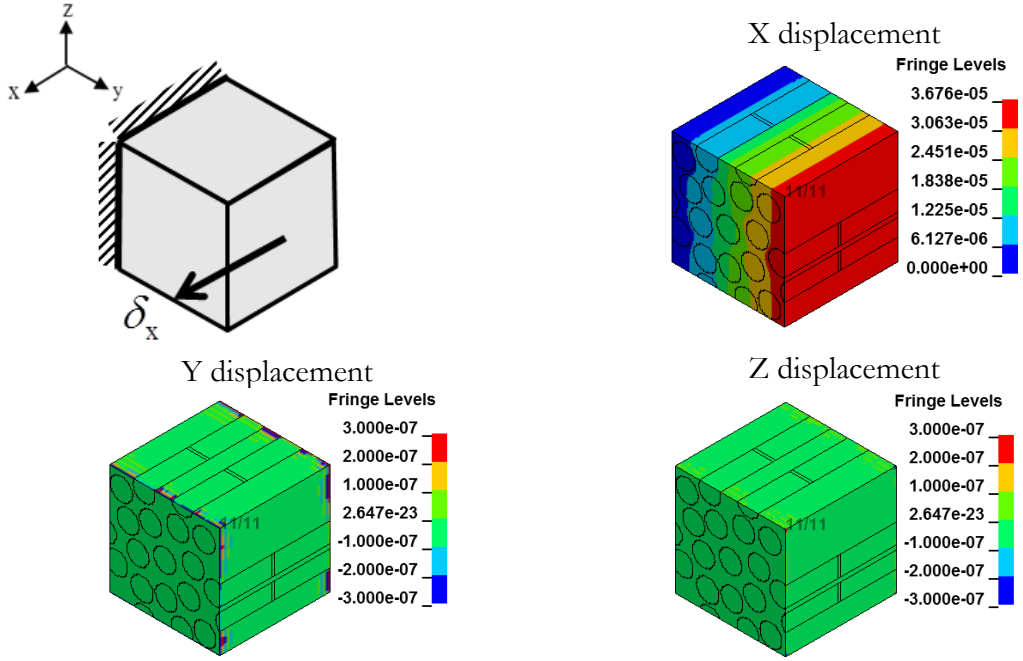

Figure 5.2.21 Loads and displacements in the sixth mode

Fibre longitudinal stress was equal to zero. The highest stress component in fibres was the XY stress. It ranged between 3.8 MPa and 13.6 MPa. Fibre stresses are displayed in Figure 5.2.22.

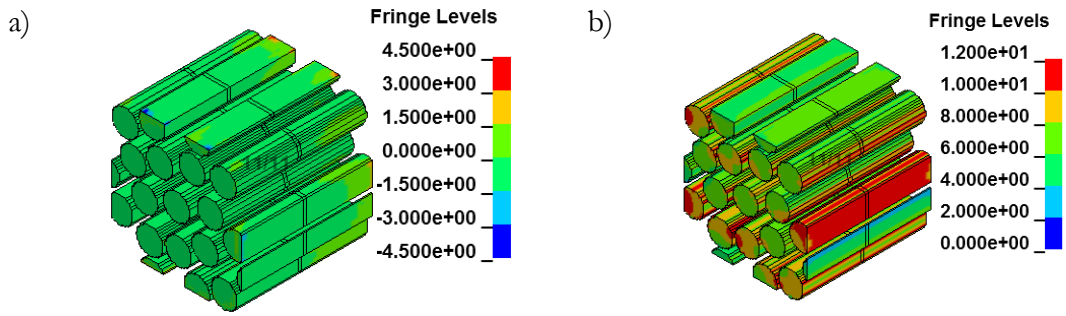

Figure 5.2.22 RVE loaded in the sixth deformation mode: a) X stress component in fibres, b) XY stress component in fibres

The normal stress components were equal to zero (ignoring small boundary effects). The X and Y stresses in Figure 5.2.23 - a) and b were given as an example. The most significant stress component in matrix was the XY shear stress. It ranged from 0.5 MPa to 8.6 MPa.

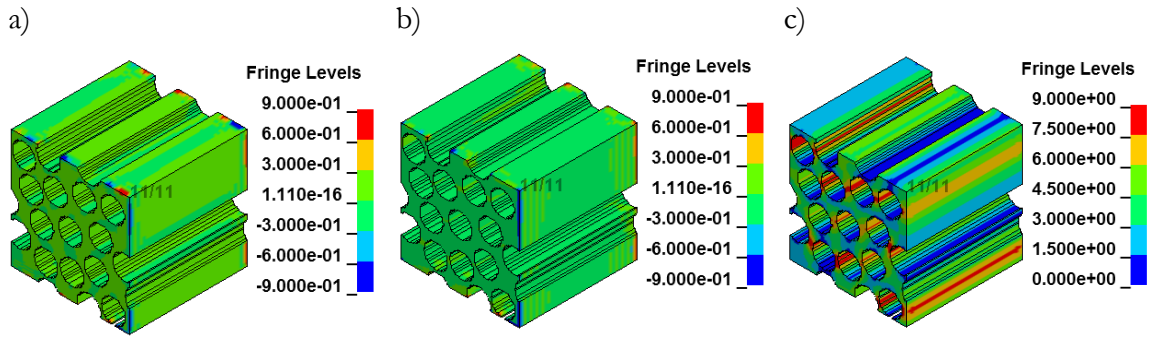

Figure 5.2.23 RVE loaded in the fourth deformation mode: a) X stress component, b) Z stress component, c) ZX stress component in matrix

Pressure component of stress was zero in the matrix constituent under the sixth deformation mode as is presented in Figure 5.2.24 - a). The von Mises stress in matrix was significant. The highest values were reached in the regions where the distance between the fibres in Y direction was smallest. The von Mises stress varied in this mode between 1.3 MPa to 22.0 MPa.

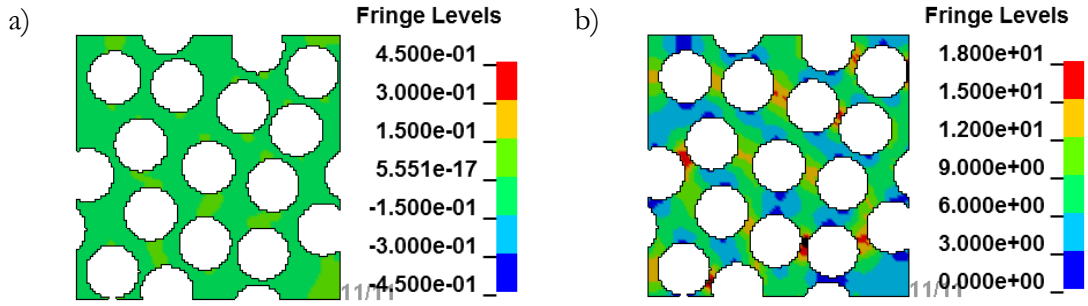

Figure 5.2.24 RVE loaded in the sixth deformation mode: a) pressure, b) von Mises stress in matrix

Stress averaged from the 20 most loaded elements was equal to 20.5 MPa, which resulted in the limit strain of 0.40%. Note that this limit strain is close to the limit strain obtained for the fifth deformation mode. Considering the equality of the modes, this result validates the model and the approach used.

Table 5.2.6 Mesoscale modelling of the sixth deformation mode results

	Input strain [%]	Stress [MPa]	Strength [MPa]	Limit strain [%]
Fibre	0.10	0.1	4900	-
Matrix	0.10	20.5	81	0.40

5.3 Combined strain energy modes

For the material treated as a continuum the strain energy modes are not interacting which is a consequence of the orthogonality of the eigenstresses and eigenstrains. Due to nonhomogeneity of CFRP, constituent stresses vary from continuum scale stresses. Thus, whilst there is no mode interaction at a continuum level, it exists at constituent level. Subsequently, it leads to elevated effective stress levels in separate constituents.

The previous section commented on the stresses in fibres and matrix under the single deformation mode loading. This section shows the similar analysis of the first three modes activated simultaneously in pairs. The aim of these simulations was the analysis of the joined mode loading on the constituent stress levels.

Activation of the two strain energy modes simultaneously was modelled using the boundary conditions that were used in single mode analysis (for convenience repeated in Figure 5.3.1).

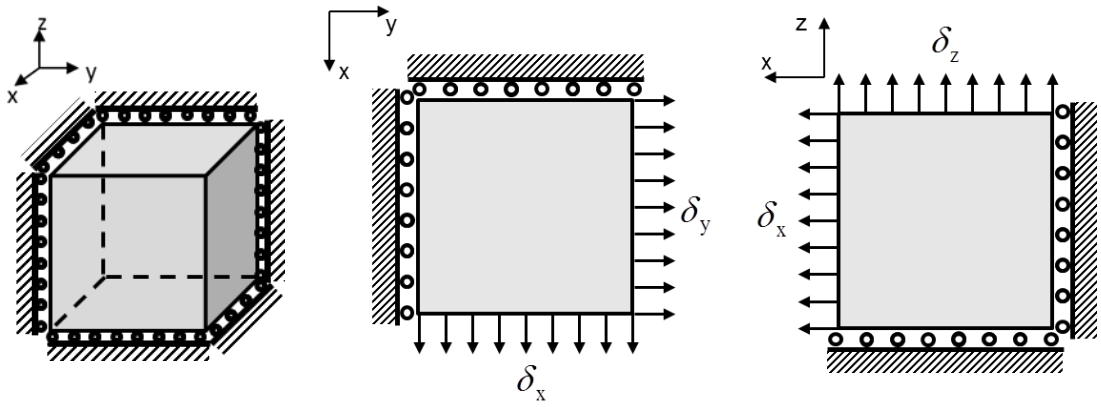

Figure 5.3.1 Boundary conditions for combined modes

The displacements that activate two strain energy modes were determined as the sum of displacements activating single strain energy modes. Note that each mode can be positive or negative, which results in four possible combinations of loading conditions for each pair. Only two of them are distinct for linear elastic simulation and assumption of no difference in compressive and tensile critical stresses and Young's moduli. The other two can be determined by reversing the signs of the strain vectors. This allows for reduction of the cases shown here to two for each pair of modes. The remaining load cases are characterised by the same stress levels but opposite stress character (tension/compression). This applies to X, Y and Z stress components and the pressure. The effective stress is by definition positive, and does not have any direction indication, therefore it does not change the sign for reversed

deformation cases. The combined modes in which two principal deformation modes have the same sign were designated by '+' and the modes with the opposite signs '-'. Note that the sign of the principal deformation mode was assigned arbitrarily and does not have any physical meaning. The displacements applied to the models combining the modes are presented in Table 5.3.1.

Table 5.3.1 Combined modes applied displacements

Mode I/II +	**Mode II/III +**	**Mode III/I +**
$\delta_x = 2.595\times10^{-5}$	$\delta_x = -1.668\times10^{-6}$	$\delta_x = 2.428\times10^{-5}$
$\delta_y = 1.953\times10^{-5}$	$\delta_y = 3.673\times10^{-5}$	$\delta_y = 1.949\times10^{-5}$
$\delta_z = -1.724\times10^{-5}$	$\delta_z = -3.787\times10^{-8}$	$\delta_z = 1.949\times10^{-5}$
Mode I/II -	**Mode II/III -**	**Mode III/I -**
$\delta_x = 2.595\times10^{-5}$	$\delta_x = -1.668\times10^{-6}$	$\delta_x = -2.762\times10^{-5}$
$\delta_y = -1.724\times10^{-5}$	$\delta_y = -3.787\times10^{-8}$	$\delta_y = 1.721\times10^{-5}$
$\delta_z = 1.953\times10^{-5}$	$\delta_z = 3.673\times10^{-5}$	$\delta_z = 1.721\times10^{-5}$

5.3.1 Modes I/II

The first mode is the 3D mode with the privileged longitudinal direction (X), the second mode is the shear mode in the isotropy plane (YZ) generated by transverse tension and compression. It can be observed that the second mode is insensitive to the sign change as in transversely isotropic material all transverse directions are equivalent. As a consequence also summation with the first mode does not yield the difference and modes I/II+ and I/II- are equal. The displacements obtained for the modes are presented in Figure 5.3.2.

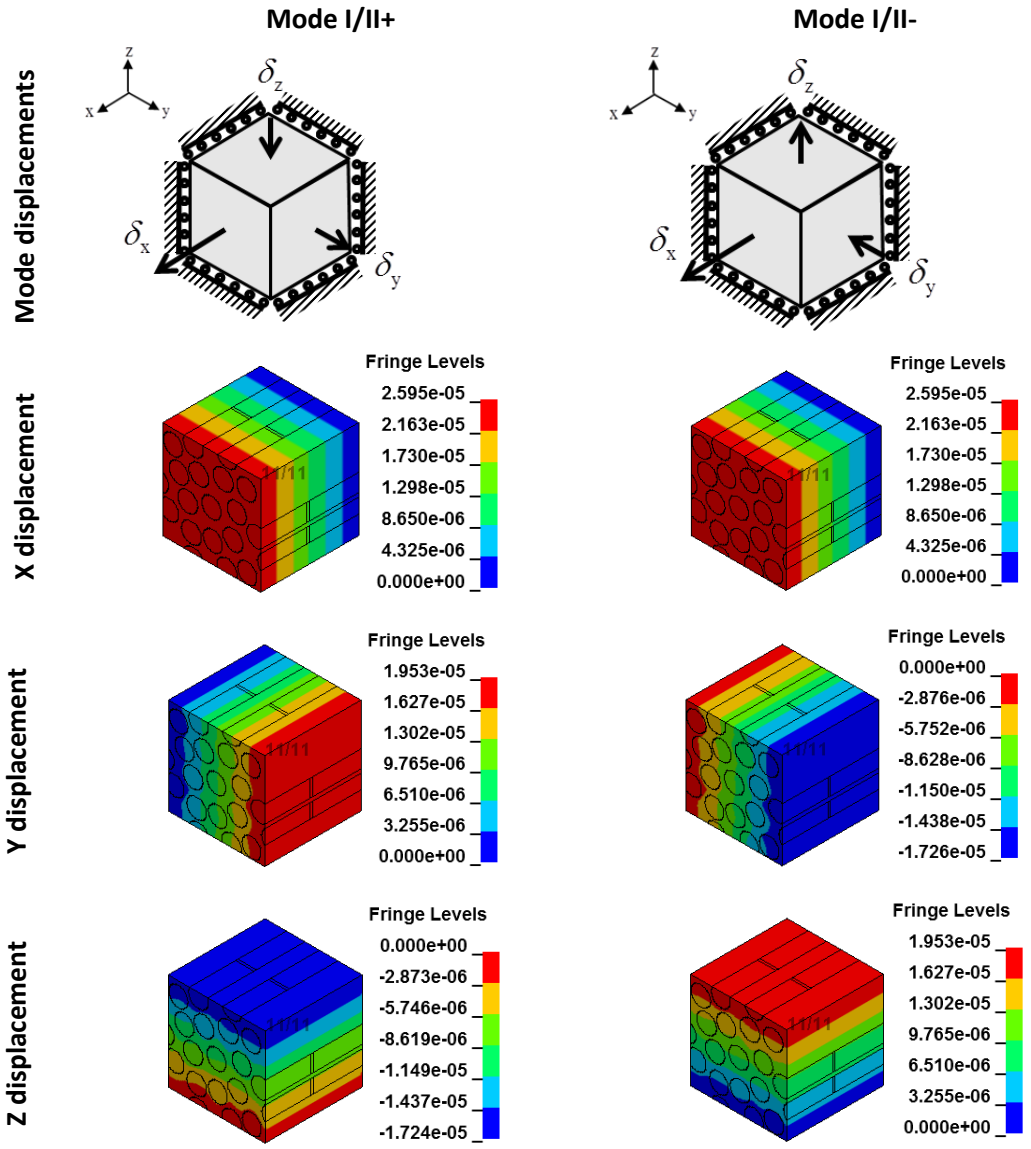

Figure 5.3.2 Mesoscale model loaded in the first and second mode (I/II+ ,I/II-)

Longitudinal stress component in the fibres obtained for joined mode did not differ from the stress in the fibres generated only by the first mode as presented in Figure 5.3.3.

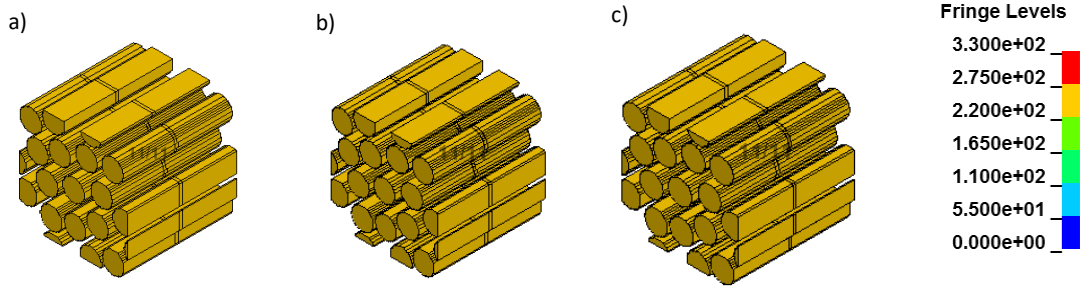

Figure 5.3.3 X stress component in fibres in the RVE loaded in: a) I mode, b) I/II+ mode and c) I/II- mode

The normal stress components in matrix are presented in Figure 5.3.4. The pictures clearly show that the modes I/II+ and I/II- are equivalent in the stress state. Moreover, exactly the

same stress would be obtained for the rotated coordinate system (for interchanged Y and Z directions). Despite this, the analysis was carried out for both joined modes for completeness. Furthermore, this can be another indication of mesoscale modelling accuracy.

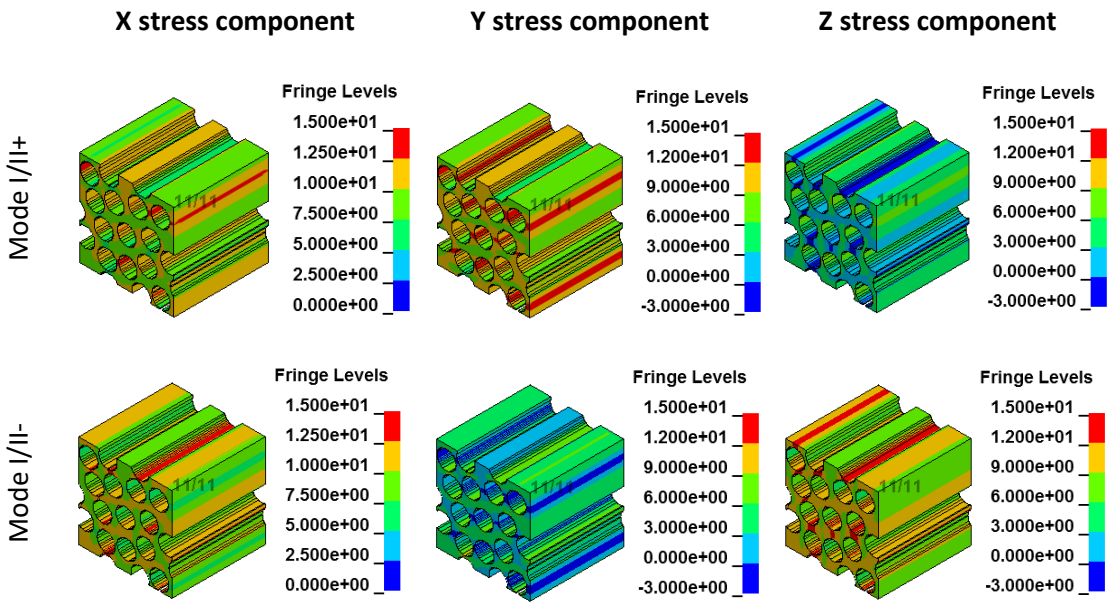

Figure 5.3.4 Normal stress components in matrix in RVE loaded in the first and second deformation modes (I/II+ and I/II-)

The most important aspect of the joined modes analysis was determination of the critical stresses for the modes in the presence of other modes. Figure 5.3.5 shows the pressure and effective stress for the combined modes. In mode I/II+ only the pressure in tension was observed. The highest pressure was found between the fibres in Y direction and was equal to 12.2 MPa (in tension). The opposite condition was observed for the mode I/II-, where pressure was higher for the regions between the fibres in Z direction. The highest pressure magnitude in I/II- mode was 12.2 MPa, which was equal to I/II+ pressure. The effective stress distribution for modes I/II+ and I/II- was similar and alike the second mode effective stress. However, the slight change in the direction of the high stress regions can be observed. The highest effective stress was 9.9 MPa for mode I/II+ and 10.2 MPa for mode I/II-. The discrepancy between the highest stresses observed in the elements results from the material microstructure. The effective stress levels averaged from the 20 elements with highest stresses were 9.5 MPa and 9.4 MPa for modes I/II+ and I/II- respectively.

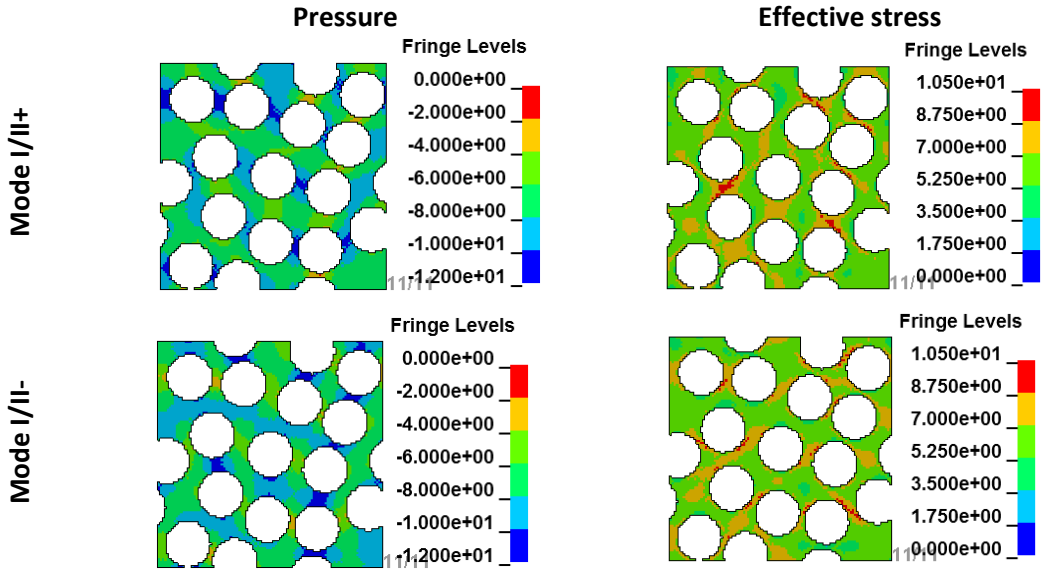

Figure 5.3.5 RVE loaded in the first and second deformation modes

The effect of the mode interaction on the constituent maximum stress levels is clearly presented in Figure 5.3.6. It shows the maximum longitudinal stress in fibres and maximum effective stress in matrix averaged from 20 highest stress elements.

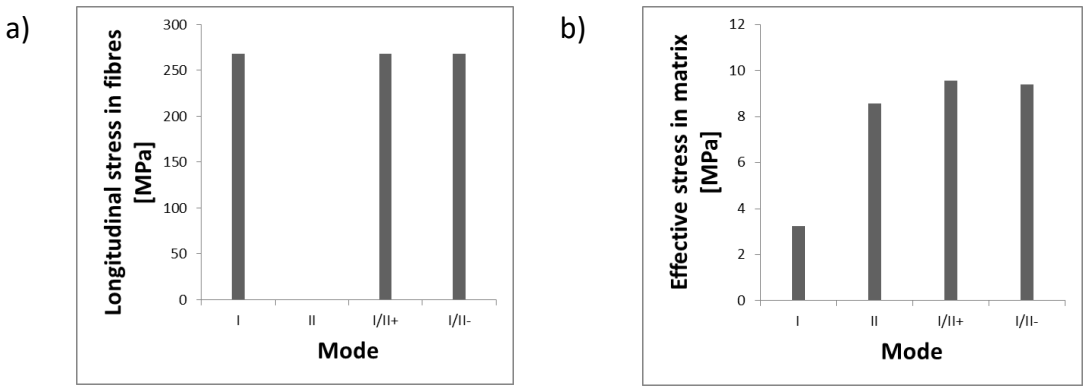

Figure 5.3.6 Comparison of maximum stress for one and two activated modes: a) longitudinal fibre stress, b) effective matrix stress

It is evident that the fibre stress depends only on the first mode, i.e. the combined mode fibre stress is equal to the first mode fibre stress as presented in Figure 5.3.6 - a). The case of matrix stress is more interesting, as the effective stress in combined modes is higher than for single modes. Figure 5.3.6 - b) shows that the first mode noticeably increases the maximum stress in matrix. Therefore, the first mode has an influence on the second mode. The exact interaction between the modal constituent stresses was established analytically and is presented in Section 6.4.

5.3.2 Modes II/III

The second and the third modes are both primarily related to matrix properties. The second mode is in-plane 2D mode and the third mode is the 3D mode. In the third mode the longitudinal (fibre) direction strain is an order of magnitude lower than the transverse strains. Using the same magnitudes of modal strains for both modes results in generating 2D strain state in the material (the third strain component is three orders of magnitude lower than the highest one). This is presented in Figure 5.3.7, where continuum Y displacement in modes II/III- and Z displacement in modes and II/III+ of the RVE is negligible.

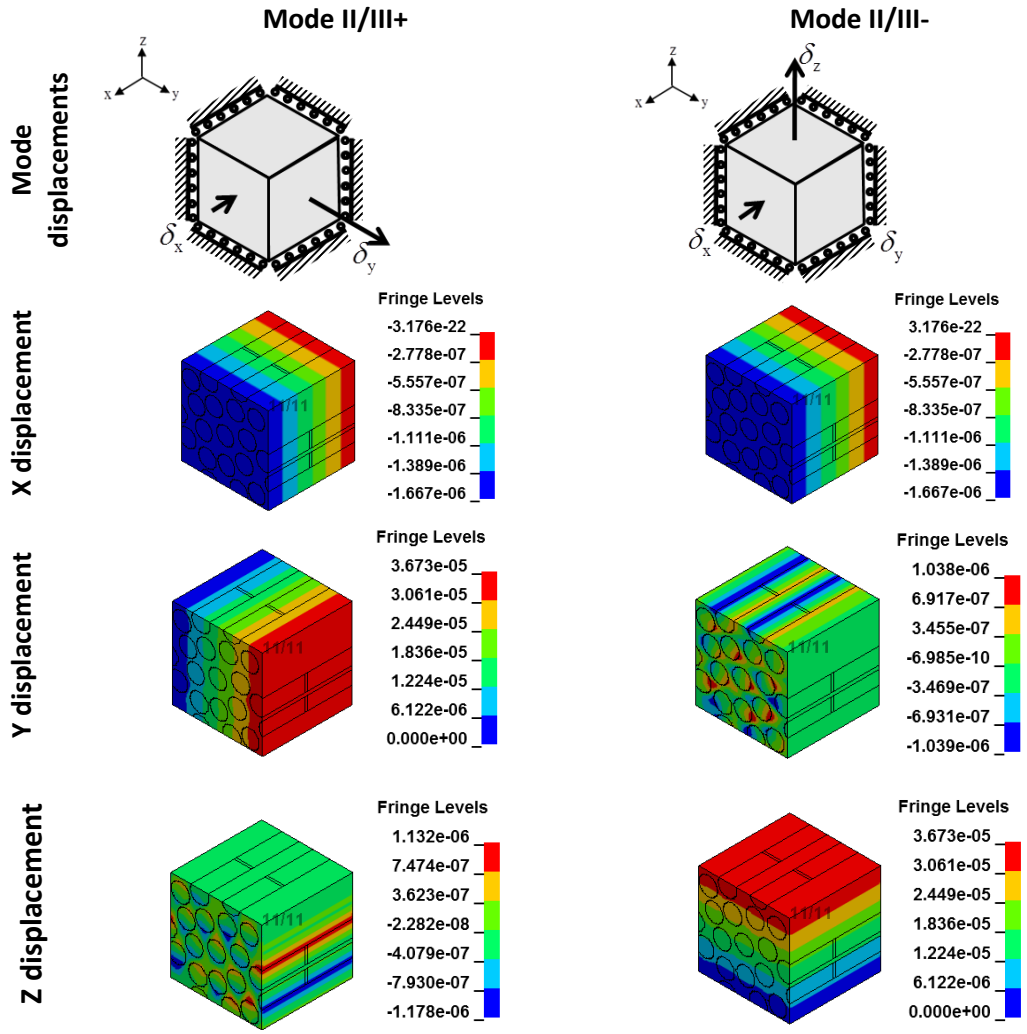

Figure 5.3.7 Mesoscale model loaded in the second and third mode (II/III+ ,II/III-)

The longitudinal stress in fibres generated by such a displacement was uniform within the fibre constituent and exactly the same as the longitudinal stress in fibres coming from mode III. The influence of the second mode on the longitudinal fibre stress cannot be observed.

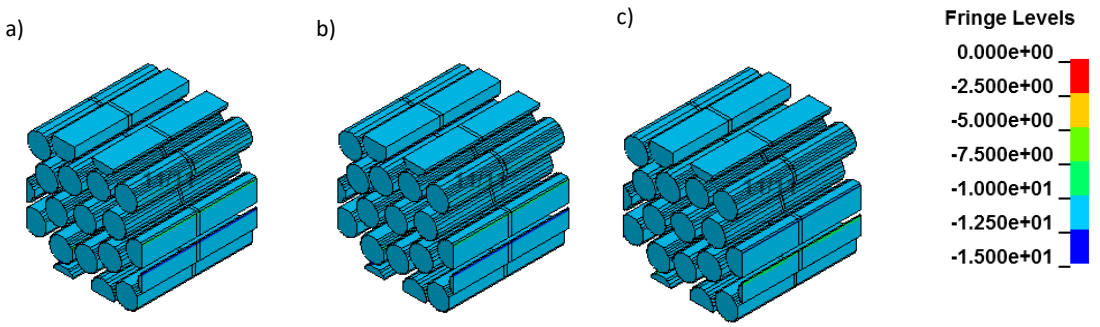

Figure 5.3.8 X stress component in fibres in the RVE loaded in: a) III mode, b) II/III+ mode and c) II/III- mode

Matrix normal stress components are presented in Figure 5.3.9. The modes II/III+ and II/III- can be treated as the equivalent modes, as the change of coordinate system would yield the similar stress distribution

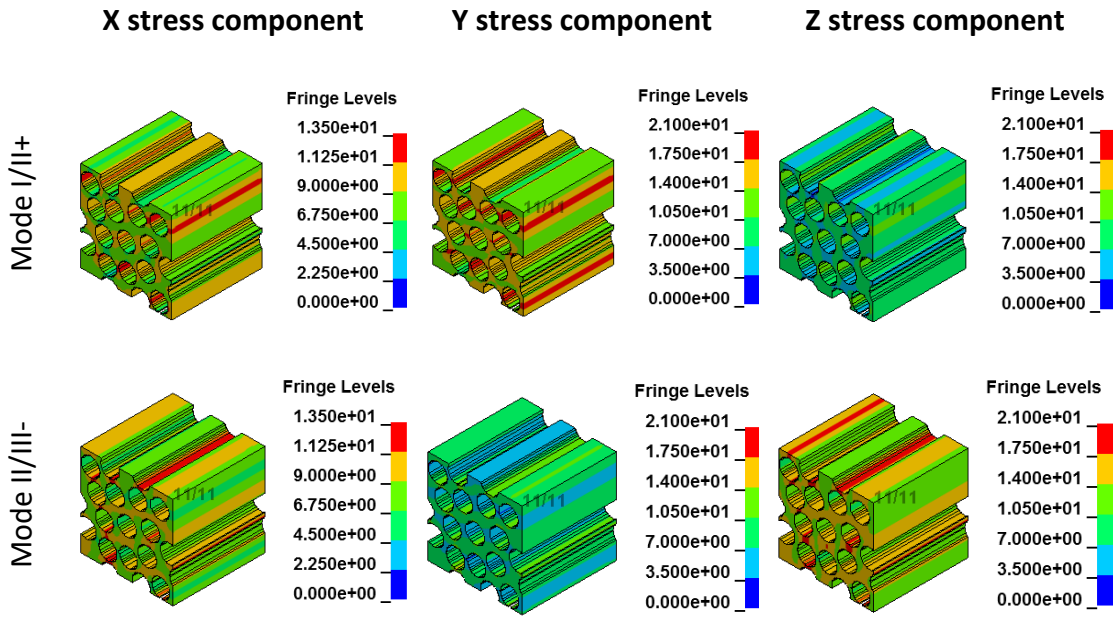

Figure 5.3.9 Normal stress components in matrix in RVE loaded in the first and second deformation modes (II/III+ and II/III-)

Pressure and effective stress results for combined modes II and III are presented in Figure 5.3.10. The highest pressure in the modes II/III+ was 15.6 MPa (tension). It was observed in the regions between the fibres neighbouring in Y direction. The highest pressure for modes II/III- was 15.6 MPa (tension) in the regions of shortest Z distance between the fibres. In the modes II/III+ the highest effective stress reached 9.5 MPa and in modes II/III- 9.6 MPa. Note that the high stress regions are very similar for modes II/III+ and II/III-.

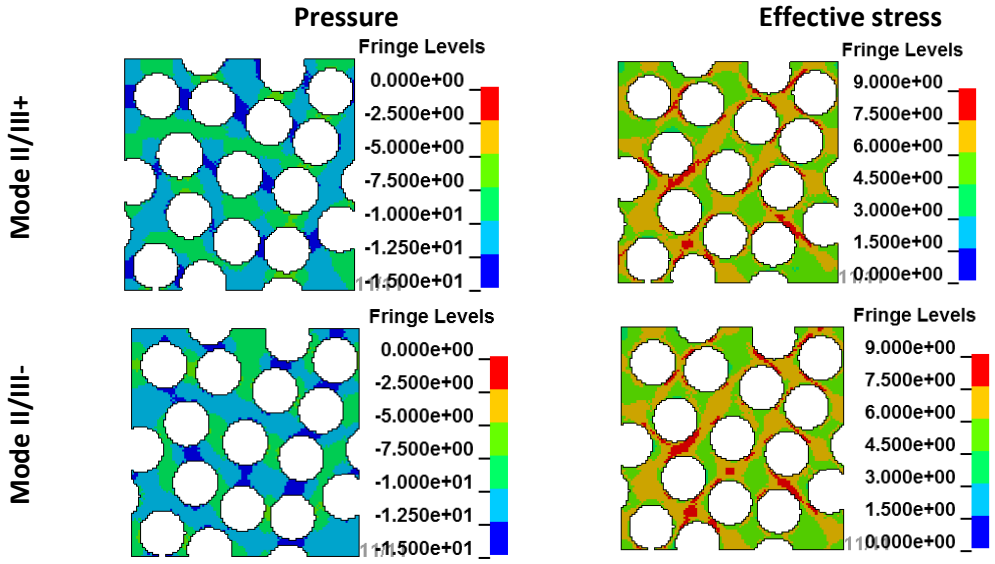

Figure 5.3.10 RVE loaded in the second and third deformation mode

The longitudinal stress results for fibre elements (uniform stress) and effective stresses results averaged for 20 most significantly stressed matrix elements are presented in Figure 5.2.11 - a) and b) respectively.

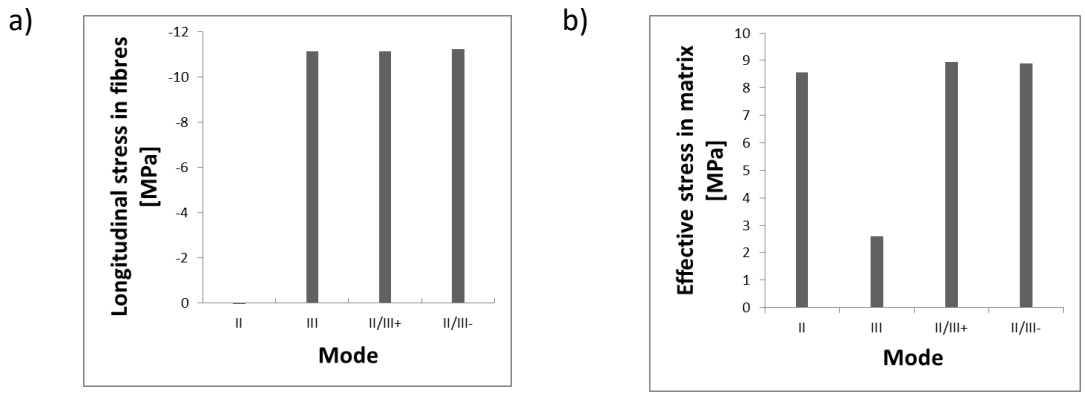

Figure 5.3.11 Comparison of maximum stress for the second and third mode and their combination: a) longitudinal fibre stress, b) effective matrix stress

It is transparent in Figure 5.2.11 - a) that the fibres stress depends only on the third mode. The influence of both modes on the matrix effective stress can be observed, however the second mode seems to be more significant.

Both modes II and III are the modes that are matrix dependant. However, the mode that affects the matrix effective stress most significantly is the second mode. Consequently, it was assumed to be matrix principal failure mode – i.e. the matrix fails in the second mode, unless its eigenstrain is zero. Only then the matrix is assumed to fail under the third mode. Exact expression for summation of the modes stresses is presented in Section 6.4.

5.3.3 Modes III/I

Both modes I and III are the 3D modes with equal transverse strains. Consequently, the transverse strains in the combined models are also equal. The displacements of the RVE are presented in Figure 5.3.12.

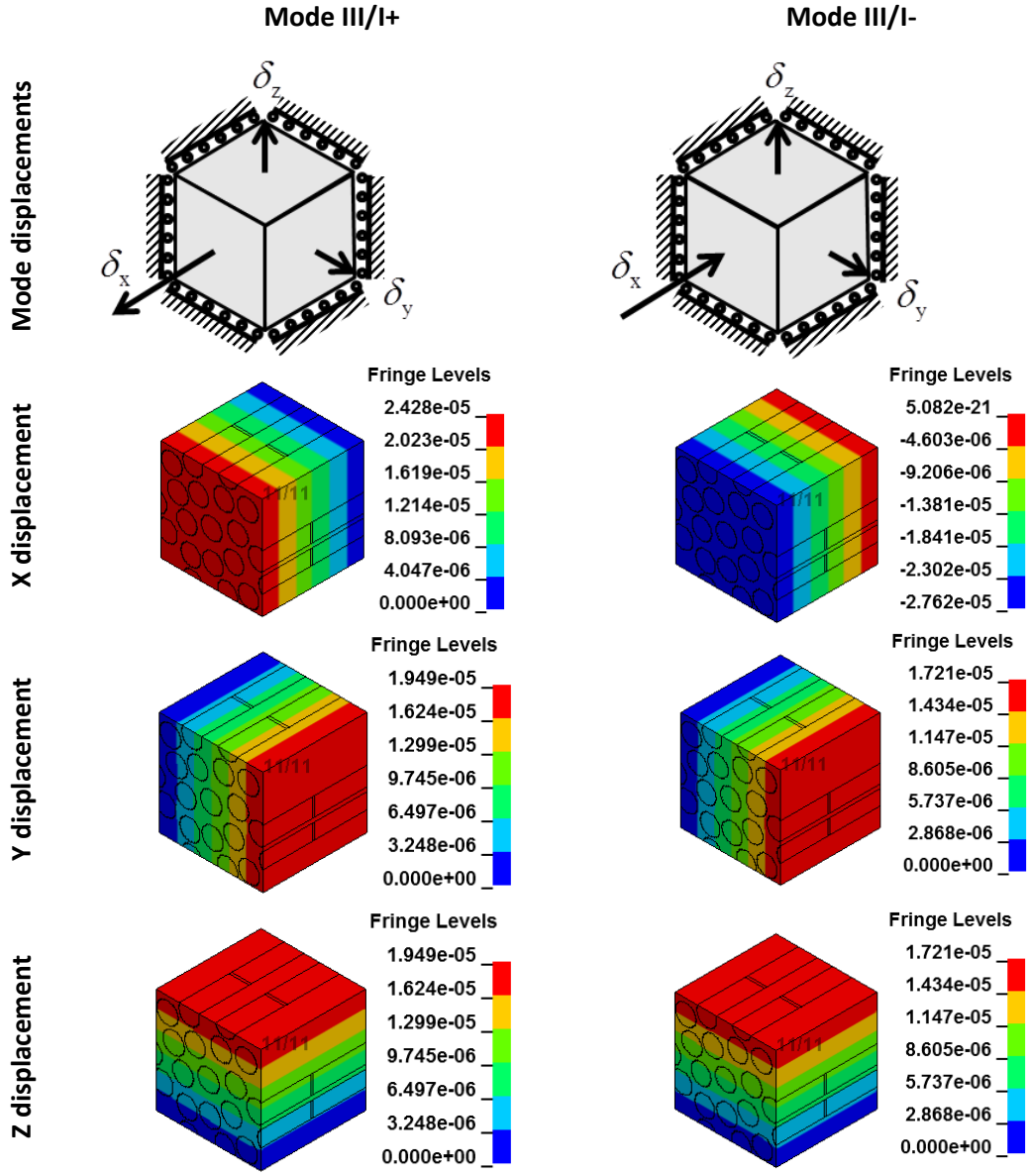

Figure 5.3.12 Mesoscale model loaded in the first and second mode (III/I+ ,III/I-)

The longitudinal stress in fibre elements was 256 MPa in tension in the vast majority of elements in the III/I+ mode and 278 MPa in compression in the III/I- mode (Figure 5.3.13). In mode III/I+ the longitudinal stresses in single modes had different signs, thus the addition lead to reduction of the stress magnitude. On the other hand, in mode III/I- the longitudinal

stresses in both modes were negative resulting in increase in the stress magnitude for the combined modes.

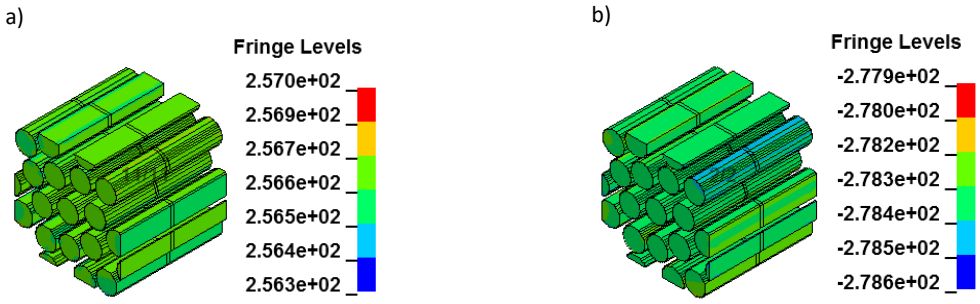

Figure 5.3.13 X stress component in fibres in the RVE loaded in: a) III/I+ mode, b) III/I- mode

The normal stress components in matrix for modes III/I+ and III/I- are presented in Figure 5.3.14. Longitudinal stress varied from 18.1 to 18.9 MPa in tension for III/I- mode. In mode III/I- majority of the elements were stressed between 0.9 to 1.2 MPa in compression. Transverse stresses varied from 16.5 to 18.3 MPa in both directions in mode III/I+. For mode III/I- the variation in transverse stresses was from 4.4 to 6.3 MPa.

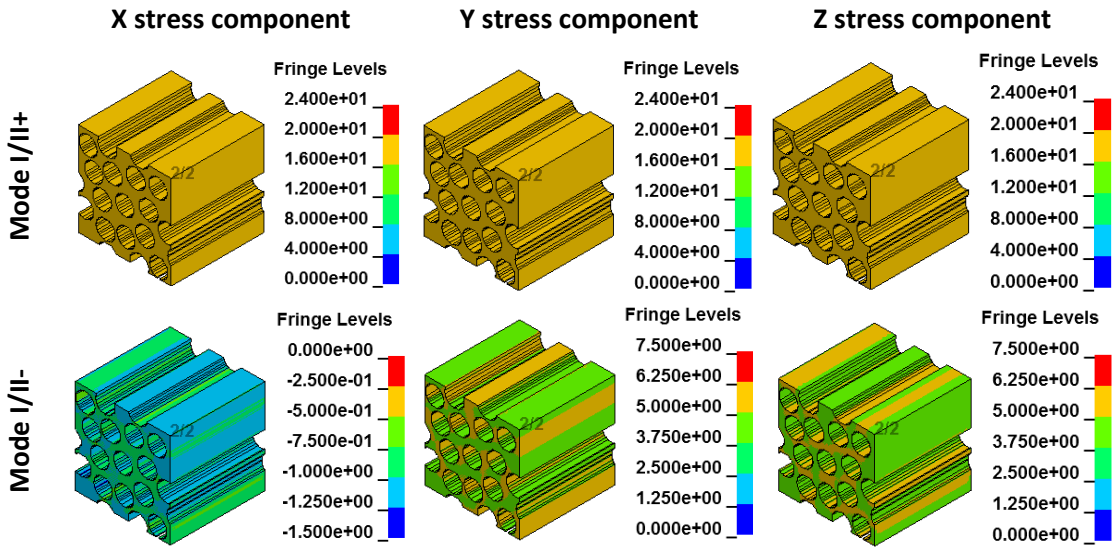

Figure 5.3.14 Normal stress components in matrix in RVE loaded in the third and first deformation modes (III/I+ and III/I-)

Pressure in matrix elements was almost uniform for both considered modes. In mode III/I+ it varied from 17.5 MPa to 18.4 MPa in tension and in mode III/I- from 2.6 to 3.5 MPa in tension. The maximum value of effective stress in mode III/I+ was 1.6 MPa. The critical stresses were found in the regions where distance between the fibres was smallest. The effective stress in the mode III/I- reached 6.2 MPa.

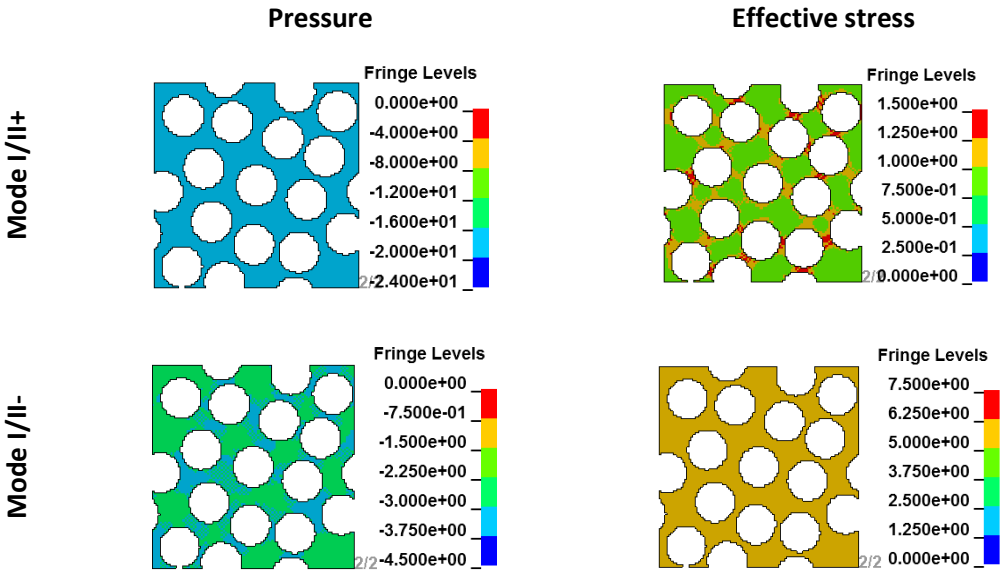

Figure 5.3.15 RVE loaded in the first deformation mode: a) pressure, b) von Mises stress in matrix

Longitudinal stress in fibres and effective stress in matrix in 20 highest stress elements are compared against the single modes results in Figure 5.3.16.

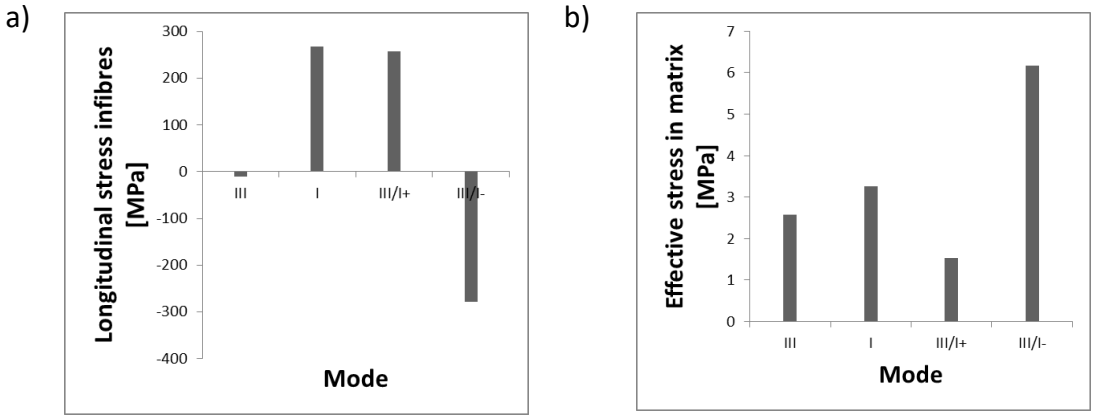

Figure 5.3.16 Comparison of maximum stress for one and two activated modes: a) longitudinal fibre stress, b) effective matrix stress

The fibre stress depends on both deformation modes. However, as the first mode is primary fibre mode, its influence is more significant than that of the third mode. The effective stress in matrix also depends on both modes. The more insight into how the modes interact is given in Section 6.5.

5.4 Summary

The mesoscale modelling of the deformation modes, presented in this chapter, aimed at understanding of the stress state in the material under single strain energy mode. Whilst the analytical solution for the stress state at continuum scale is trivial (defined by the

generalised Hooke's Law), the stress state in the separate constituents is not easy to predict. The mesoscale modelling gave an insight into the constituent scale stresses.

Moreover, by means of linear elastic analysis it provided the critical modal strain values characteristic for each mode, and subsequently, allowed to calculate of the critical strain energy densities required for the model definition. For convenience the set of results is presented in Table 5.4.1.

Table 5.4.1 Deformation eigenmodes mesoscale modelling results

Mode	Critical eigenstrain [%]	Principal stiffness [GPa]	Strain energy limit [kJ/m^3]	Damage mechanism
I	1.82	139.5	23104.0	fibre
II	0.94	5.8	256.2	matrix
III	3.12	16.1	7836.2	matrix
IV	0.95	5.7	257.2	matrix
V	0.39	11.0	83.7	matrix
VI	0.40	11.0	88.0	matrix

The combinations of the first three modes were analysed. They revealed that mixed mode loading increases the constituent stresses. Consequently, they may lead to reduction of the modal threshold energies, which is evaluated analytically in Section 6.4.

6 Progressive damage model

Work presented in the previous chapters was the foundation of the development of a new constitutive composite model. An overview of the continuum mechanics, thermodynamics and continuum damage mechanics gave a good framework for the mathematical formulation of the new material constitutive model. Development of the model was supported by the mesoscale models analysis (Chapter 4 and Chapter 5). It helped with understanding of the damage effect in the non-homogeneous composite and the stress state in the material where a single strain energy mode is present. Deformation process in the material was assumed to be adiabatic i.e. without temperature or matter transfer. For static deformation this is easily justified by insignificant temperature change and for dynamic deformation – the deformation time does not allow for heat transfer.

Spectral decomposition of the stiffness tensor was incorporated in the thermodynamic framework, giving six strain energy modes in the basic model. At continuum scale the modes are not interacting as the eigenvectors corresponding to modes form the orthogonal coordinate system. The basic model described in Section 6.1 was developed at continuum scale without insight into the mode interaction at mesoscale. The possibility of expanding the model to account for interaction between the modes at constituent scale was also evaluated. The suggested extension to the model is presented in Section 6.4.

6.1 Theoretical model

The model presented here is strongly inspired by the work of Schreyer (1995) and Schreyer and Zuo (1995). It uses spectral decomposition of a stiffness tensor to define the non-interacting strain energy modes. The assumption is made that damage does not change the material (stiffness) eigenvectors. This assumption is perfectly justified for the damage mechanisms that do not violate material symmetries and is additionally supported by the mesoscale model analysis (Chapter 4). Damage modes in the model are associated with strain energy modes.

6.1.1 Spectral decomposition of Helmholtz free energy potential

State potential that defines the material state in the model is the Helmholtz free energy. The Helmholtz free energy consists of the strain energy potential (W) and the sum of damage associated potentials (H):

$$\Psi = W + \sum H \qquad \textbf{6.1.1}$$

Strain energy potential is a measure of elastic strain energy stored in the material. It is the part of the free energy that can be recovered during material unloading (under condition of perfect elasticity). Damage potentials describe a non-recoverable part of the free energy that is associated with damage. They allow for modelling of the strain hardening and softening behaviour in the material.

Elastic strain energy (W) is defined by:

$$W(\boldsymbol{\varepsilon}) = \frac{1}{2}\boldsymbol{\varepsilon}\cdot\mathbf{C}\cdot\boldsymbol{\varepsilon}\,, \qquad \textbf{6.1.2}$$

where $\boldsymbol{\varepsilon}$ is strain vector and $\mathbf{C}$ is second order stiffness tensor. Application of the spectral decomposition (Equation 2.1.25, Section 2.1.4) leads to definition of the total strain energy as the sum of the modal strain energies:

$$W(\boldsymbol{\varepsilon}) = \frac{1}{2}\boldsymbol{\varepsilon}\cdot\mathbf{C}\cdot\boldsymbol{\varepsilon} = \frac{1}{2}\boldsymbol{\varepsilon}\cdot\left(\sum_{i=I}^{VI}\lambda^i\mathbf{P}^i\right)\cdot\boldsymbol{\varepsilon} = \frac{1}{2}\sum_{i=I}^{VI}\lambda^i\boldsymbol{\varepsilon}\cdot\mathbf{P}^i\cdot\boldsymbol{\varepsilon} = \frac{1}{2}\sum_{i=I}^{VI}\lambda^i\boldsymbol{\varepsilon}^i\cdot\boldsymbol{\varepsilon}^i = \sum_{i=I}^{VI}W^i\,, \qquad \textbf{6.1.3}$$

where λ is a stiffness tensor eigenvalue, $\mathbf{P}$ is a projection operator tensor and index i denotes the mode. The strain energy equivalence hypothesis is used to model the damage effect on stiffness of the material. It is defined in Section 3.3.2 as:

$$\mathbf{C}(\mathbf{D}) = (\mathbf{I}-\mathbf{D})^T\cdot\mathbf{C}_0\cdot(\mathbf{I}-\mathbf{D})\,, \qquad \textbf{6.1.4}$$

where $\mathbf{D}$ and $\mathbf{I}$ are damage and identity tensor respectively. Note that the basic assumption in the model is that the eigenvectors of the stiffness tensors do not change. Therefore, the damaged material stiffness tensor has the same projection operators and vary only by the eigenvalues from the undamaged one. Thus, the following relation holds:

$$\mathbf{C}(\mathbf{D}) = \sum_{i=I}^{VI}\lambda^i(\mathbf{D})\mathbf{P}^i(\mathbf{D}) = \sum_{i=I}^{VI}\lambda^i(\mathbf{D})\mathbf{P}^i\,. \qquad \textbf{6.1.5}$$

Substituting 6.1.5 into 6.1.4 gives:

$$\begin{aligned}\mathbf{C}(\mathbf{D}) &= \sum_{i=I}^{VI} \lambda^i(\mathbf{D})\mathbf{P}^i = (\mathbf{I}-\mathbf{D})^T \cdot \sum_{i=I}^{VI} \lambda_0^i \mathbf{P}^i \cdot (\mathbf{I}-\mathbf{D}) = \\ &= \sum_{i=I}^{VI} \lambda_0^i (\mathbf{I}-\mathbf{D})^T \cdot \mathbf{P}^i \cdot (\mathbf{I}-\mathbf{D}) = \sum_{i=I}^{VI} \lambda_0^i \mathbf{M}^T \cdot \mathbf{M} \cdot \mathbf{P}^i,\end{aligned} \qquad \textbf{6.1.6}$$

where $\mathbf{M}$ is a damage effect tensor $(\mathbf{M} = \mathbf{I} - \mathbf{D})$. Damage affects a single mode only if damage effect tensor $\mathbf{M}$ is collinear with projection operator corresponding to the mode. Therefore, damage effect tensor can be defined as:

$$\mathbf{M} = \sum_{i=I}^{VI} (1-d^i)\mathbf{P}^i\,, \qquad \textbf{6.1.7}$$

with damage effect being accounted for by a damage variable d. This allows to model damage by the set of scalar damage variables corresponding to the strain energy modes:

$$\mathbf{C}(d^i) = \sum_{i=I}^{VI} (1-d^i)^2 \lambda_0^i \mathbf{P}^i\,. \qquad \textbf{6.1.8}$$

Consequently, strain energy of a damaged material assumes the following form:

$$W(\boldsymbol{\varepsilon}, d^i) = \tfrac{1}{2} \sum_{i=I}^{VI} (1-d^i)^2 \lambda_0^i \bar{\boldsymbol{\varepsilon}}^{i2}\,, \qquad \textbf{6.1.9}$$

where:

$$\bar{\boldsymbol{\varepsilon}}^{i2} = \boldsymbol{\varepsilon}^i \cdot \boldsymbol{\varepsilon}^i = \varepsilon^{i2}\,, \qquad \varepsilon^i = \mathbf{v}^i \cdot \boldsymbol{\varepsilon}\,. \qquad \textbf{6.1.10}$$

It is of utmost importance to assure that the strain vector is defined consistently as a second order tensor projected on the 6D space (introduced in Section 2.1.1). Note that using the Voigt notation would lead to discrepancy between the double contraction of the (original) strain second order tensor and a contraction of a (reduced order) strain vector, which is unacceptable.

Damage potential in the model is assumed to be a quadratic function of damage hardening variable as suggested by Schreyer (1995). It is expressed by:

$$H(h) = \tfrac{1}{2}\kappa h^2\,, \qquad \textbf{6.1.11}$$

where κ is a material parameter and h is a damage evolution variable.

Both damage and damage evolution variables are unitless in the model. It follows, that the material parameter κ has a unit of energy and is later referred to as a damage evolution energy.

Damage hardening is a function associated with damage evolution, so it is assumed to be mode characteristic like damage variable. The final form of the Helmholtz free energy can be rewritten as:

$$\begin{aligned}\Psi\left(\boldsymbol{\varepsilon},d^i,h^i\right)&=\tfrac{1}{2}\sum_{i=I}^{VI}\left(1-d^i\right)^2\lambda_0^i\varepsilon^{i2}+\tfrac{1}{2}\sum_{i=I}^{VI}\kappa^i h^{i2}=\\&=\tfrac{1}{2}\sum_{i=I}^{VI}\left(\left(1-d^i\right)^2\lambda_0^i\varepsilon^{i2}+\kappa^i h^{i2}\right)=\sum_{i=I}^{VI}\Psi_i.\end{aligned}\qquad \textbf{6.1.12}$$

The above equation shows the possibility of decoupling the strain energy modes and treating them separately, which simplifies the model immensely. In the following section the model derivation is shown for a single mode.

6.1.2 Conjugate forces, damage potential and damage variables definition

The modal Helmholtz free energy for a single mode equals:

$$\Psi^i\left(\boldsymbol{\varepsilon},d^i,h^i\right)=\tfrac{1}{2}\left(1-d^i\right)^2\lambda_0^i\varepsilon^{i2}+\tfrac{1}{2}\kappa^i h^{i2},\qquad \textbf{6.1.13}$$

and its rate of change:

$$\dot{\Psi}^i\left(\boldsymbol{\varepsilon},d^i,h^i\right)=\frac{\partial\Psi^i}{\partial\varepsilon^i}\dot{\varepsilon}^i+\frac{\partial\Psi^i}{\partial d^i}\dot{d}^i+\frac{\partial\Psi^i}{\partial h^i}\dot{h}^i.\qquad \textbf{6.1.14}$$

The first element in the equation is an elastic non-dissipative strain energy rate. The variables that correspond to dissipative part are damage and damage evolution variables. The total energy dissipation can therefore be defined as:

$$\dot{\Upsilon}^i\left(\varepsilon^i,d^i,h^i\right)=\frac{\partial\Psi^i}{\partial\varepsilon^i}\dot{\varepsilon}^i-\dot{\Psi}^i=-\frac{\partial\Psi^i}{\partial d^i}\dot{d}^i-\frac{\partial\Psi^i}{\partial h^i}\dot{h}^i.\qquad \textbf{6.1.15}$$

This expression can be used to determine the conjugate forces and the rates of displacements. The forces conjugate to damage variable (d_i) and damage evolution variable (h_i) are defined respectively as:

$$y_d^i = -\frac{\partial \Psi^i}{\partial d^i} = \left(1 - d^i\right) \lambda_0^i \bar{\varepsilon}^{i\,2}, \qquad y_h^i = -\frac{\partial \Psi^i}{\partial h^i} = -\kappa^i h^i. \tag{6.1.16}$$

Both damage initiation and evolution are controlled by damage potential which makes the model associative damage model. Following the general thermodynamic framework (Hansen and Schreyer, 1994), damage potential for scalar damage variables should be a linear function of the conjugate forces:

$$\Phi^i \left(y_d^i, y_h^i\right) \equiv y_d^i - \left(y_h^i + \omega_0^i\right) \le 0, \tag{6.1.17}$$

where ω_0^i is a scalar constant that define damage threshold (and thus in this work is called damage threshold energy). Material is linear elastic as long as the damage potential function has a negative value. Damage initiates and evolves when the damage potential is equal to zero. Evolution of damage and damage evolution variables is defined by the maximum entropy production (or maximum dissipation) rule. The energy dissipation (Equation 6.1.15) is maximised in the models by Lagrange multipliers method. The function L^i is defined as:

$$L^i = -\dot{\Upsilon}^i + \dot{\Lambda}^i \Phi^i. \tag{6.1.18}$$

In the function the constraint Φ^i is multiplied by Lagrange multiplier $\dot{\Lambda}^i$. The constraint in the Lagrange function comes from the associative flow rule:

$$\Phi^i \left(y_d^i, y_h^i\right) = 0. \tag{6.1.19}$$

Solution for the minimum of the objective function L^i gives damage and damage evolution variables in terms of Lagrange multipliers:

$$\dot{d}^i = \dot{\Lambda}^i \frac{\partial \Phi^i}{\partial y_d^i} = \dot{\Lambda}^i, \qquad \dot{h}^i = \dot{\Lambda}^i \frac{\partial \Phi^i}{\partial y_h^i} = -\dot{\Lambda}^i = -\dot{d}^i. \tag{6.1.20}$$

Kuhn-Tucker optimality conditions constrain the variables and the damage function giving the loading and unloading conditions for the model (Hansen and Schreyer, 1994):

$$\dot{\Lambda}^i = \dot{d}^i \ge 0, \qquad \Phi^i \le 0, \qquad \dot{\Lambda}^i \Phi^i = 0. \tag{6.1.21}$$

To assure that during damage evolution material state does not violate Equation 6.1.17, the consistency condition must be satisfied, i.e. not only the damage function but also its time derivative must be equal to zero. This is postulated by:

$$\dot{\Phi}^i\left(\dot{y}_d^i, \dot{y}_h^i\right) \equiv \dot{y}_d^i - \dot{y}_h^i = 0. \qquad \textbf{6.1.22}$$

The rates of the forces conjugate to damage and damage evolution variables are defined by:

$$\dot{y}_d^i\left(\boldsymbol{\varepsilon}, d^i\right) = \frac{\partial y_d^i}{\partial d^i}\dot{d}^i + \frac{\partial y_d^i}{\partial \varepsilon^i}\dot{\varepsilon}^i = -\lambda_0^i \varepsilon^{i2}\dot{d}^i + 2\left(1-d^i\right)\lambda_0^i \varepsilon^i \dot{\varepsilon}^i,$$

$$\dot{y}_h^i\left(h^i\right) = \frac{\partial y_h^i}{\partial h^i}\dot{h}^i = -\kappa^i \dot{h}^i = \kappa^i \dot{\Lambda}^i = \kappa^i \dot{d}^i. \qquad \textbf{6.1.23}$$

Note that the convenient relation between the variables obtained in Equation 6.1.20 is used. After substitution into Equation 6.1.22 the following relation can be established:

$$\frac{1}{\left(1-d^i\right)}\dot{d}^i = \frac{2\lambda_0^i \varepsilon^i}{\kappa^i + \lambda_0^i \varepsilon^{i2}}\dot{\varepsilon}^i. \qquad \textbf{6.1.24}$$

Integration of this equation gives the explicit solution for the damage variable (the integration steps are presented in Appendix D):

$$d^i = 1 - \frac{1}{\left(\kappa^i + \lambda_0^i \bar{\boldsymbol{\varepsilon}}^{i2}\right)c}, \qquad \textbf{6.1.25}$$

where c is integration constant that can be determined knowing that damage function equals to zero (using Equations 6.1.25, 6.1.16 and 6.1.19). As $\dot{d}^i = -\dot{h}^i$ and $d^i{}_{t=0} = h^i{}_{t=0} = 0$ we can write that $d_i = -h_i$. Using this relation, the integration constant is further simplified and equals to:

$$c = \frac{1}{\omega_0^i + \kappa^i}. \qquad \textbf{6.1.26}$$

Finally, damage variable is established as:

$$d^i = \frac{\lambda_0^i \varepsilon^{i2} - \omega_0^i}{\lambda_0^i \varepsilon^{i2} + \kappa^i}. \qquad \textbf{6.1.27}$$

6.1.3 Failure criteria and damage variables for transversely isotropic material

Theoretical derivation of the model state potentials and variables was presented in the previous section. Derivation, in its most basic form assumed existence of (maximum) six number of strain energy modes. For transversely isotropic materials the number of modes can be reduced to four because of the repeated stiffness eigenvalues ($\lambda^{II} = \lambda^{IV}$ and $\lambda^{V} = \lambda^{VI}$). This allows to combine the modes that share the same eigenvalue. The Helmholtz free energy can therefore be split into four modes as:

$$\Psi^{I}\left(\boldsymbol{\varepsilon}, d^{I}, h^{I}\right) = \tfrac{1}{2}\left(1-d^{I}\right)^{2} \lambda_0^{I} \varepsilon^{I2} + \tfrac{1}{2}\kappa^{I} h^{I2},$$

$$\Psi^{II}\left(\boldsymbol{\varepsilon}, d^{II}, h^{II}\right) = \tfrac{1}{2}\left(1-d^{II}\right)^{2} \lambda_0^{II} \left(\varepsilon^{II2} + \varepsilon^{IV2}\right) + \tfrac{1}{2}\kappa^{II} h^{II2},$$

$$\Psi^{III}\left(\boldsymbol{\varepsilon}, d^{III}, h^{III}\right) = \tfrac{1}{2}\left(1-d^{III}\right)^{2} \lambda_0^{III} \varepsilon^{III2} + \tfrac{1}{2}\kappa^{III} h^{III2}, \qquad \textbf{6.1.28}$$

$$\Psi^{V}\left(\boldsymbol{\varepsilon}, d^{V}, h^{V}\right) = \tfrac{1}{2}\left(1-d^{V}\right)^{2} \lambda_0^{V} \left(\varepsilon^{V2} + \varepsilon^{VI2}\right) + \tfrac{1}{2}\kappa^{V} h^{V2}.$$

where the first and the third mode are the modes depending only on the first and third principal strain. The second mode is a function of the second and fourth principal strain and the fourth mode is a function of fifth and sixth principal strain. The four damage potentials that are the failure criteria in this model are:

$$\Phi^{I}\left(\boldsymbol{\varepsilon}, d^{I}, h^{I}\right) = \left(1-d^{I}\right)\lambda_0^{I}\varepsilon^{I2} - \kappa^{I} h^{I} - \omega_0^{I} = 0,$$

$$\Phi^{II}\left(\boldsymbol{\varepsilon}, d^{II}, h^{II}\right) = \left(1-d^{II}\right)\lambda_0^{II}\left(\varepsilon^{II2} + \varepsilon^{IV2}\right) - \kappa^{II} h^{II} - \omega_0^{II} = 0,$$

$$\Phi^{III}\left(\boldsymbol{\varepsilon}, d^{III}, h^{III}\right) = \left(1-d^{III}\right)\lambda_0^{III}\varepsilon^{III2} - \kappa^{III} h^{III} - \omega_0^{III} = 0, \qquad \textbf{6.1.29}$$

$$\Phi^{V}\left(\boldsymbol{\varepsilon}, d^{V}, h^{V}\right) = \left(1-d^{V}\right)\lambda_0^{V}\left(\varepsilon^{V2} + \varepsilon^{VI2}\right) - \kappa^{V} h^{V} - \omega_0^{V} = 0.$$

The damage variables are defined as:

$$d^{I} = \frac{\lambda_0^{I}\varepsilon^{I2} - \omega_0^{I}}{\lambda_0^{I}\varepsilon^{I2} + \kappa^{I}},$$

$$d^{II} = \frac{\lambda_0^{II}\left(\varepsilon^{II2} + \varepsilon^{IV2}\right) - \omega_0^{II}}{\lambda_0^{II}\left(\varepsilon^{II2} + \varepsilon^{IV2}\right) + \kappa^{II}},$$

$$d^{III} = \frac{\lambda_0^{III}\varepsilon^{III2} - \omega_0^{III}}{\lambda_0^{III}\varepsilon^{III2} + \kappa^{III}},$$

$$d^{V} = \frac{\lambda_0^{V}\left(\varepsilon^{V2} + \varepsilon^{VI2}\right) - \omega_0^{V}}{\lambda_0^{V}\left(\varepsilon^{V2} + \varepsilon^{VI2}\right) + \kappa^{V}}. \quad \textbf{6.1.30}$$

The first mode failure criterion is the fibre failure criterion because the first eigenvector (and subsequently the first mode strain) is aligned almost perfectly with fibres. It was also shown in the mesoscale model analysis (Chapter 5) that fibres are the weakest constituent under the first deformation eigenmode. The second mode is the isotropy plane shear mode that combines the two possible ways of generating the shear stress in the material. One of them is transverse tension-compression and the second pure shear. The third mode can be viewed as the volumetric matrix failure mode. The fifth mode is the shear failure mode in the plane of fibres.

6.2 Equation of state parameters determination

Accurate modelling of the material response to HVI necessitates including the equation of state in the model definition. EOS theory was presented in Section 3.5. The EOS parameters are established for a large number of commonly used materials (Marsh, 1980). This includes data for carbon (also carbon fibres specifically) and different types of epoxies (Munson and May, 1972; Marsh, 1980; Ahrens and Johnson, 1994; Millett, Bourne and Barnes, 2002; Hazell, Stennett and Cooper, 2008). However, determination of the shock EOS parameters for CFRP was done only by few researchers including (Riedel, Nahme and Thoma, 2004; Millett *et al.*, 2007; Hazell, Stennett and Cooper, 2009; Dattelbaum and Coe, 2012). Difficulty in composite materials lies in the fact that their properties depend on the specific constituents' properties used (e.g. different matrices), the specific manufacturing processes (e.g. curing of the epoxy) and the material geometry (e.g. weave and layup). Furthermore, the

impact direction is also of significance. One of the objectives of this work was to develop a model suitable for HVI modelling. The accuracy check of the model should include a validation of the impact response of the material, which requires determination of dynamic material properties. Data presented below was collected in the EXTREME project. The following chapters shortly comment on the experiments that were performed by the project partner. They also show the method and calculations of the EOS parameters of the unidirectional CFRP through thickness direction done in this work.

6.2.1 Plate impact tests

The plate impact test is a test performed to characterise a shock wave propagation in a material. It allows the determination of constants (C, S_1, S_2 and S_3) needed for the Gruneisen EOS. Typically, an impactor made of material with known dynamic properties is fired against the target made of a material to be characterised. The impact results in generation of the shock wave in the target. Measurements in the test allow measurement of relation between the shock and particle velocity in the material and between pressure and particle velocity (EOS). Due to inertial constraints the state induced in the material is the uniaxial strain state in which the only non-zero strain component is in the impact direction. The plate impact test setup is schematically presented in Figure 6.2.2.

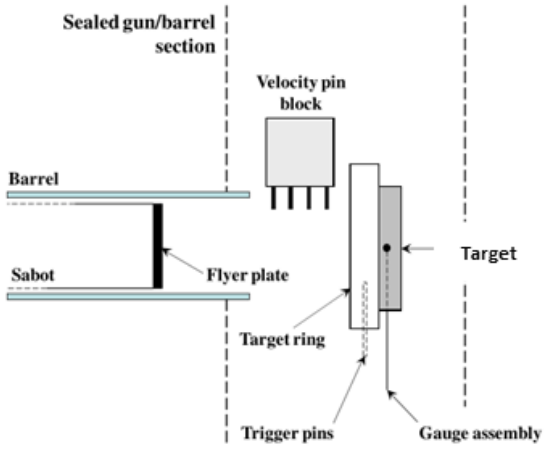

Figure 6.2.1 Plate impact test experimental setup (adjusted from Appleby-Thomas, Hazell and Stennett, 2009)

Two types of flyer plates were used in the experiments: aluminium and copper. Velocity of the flyer plate was measured by a velocity pin block situated before the target. The cover plate of a matching material was used to avoid impedance mismatch at the impact surface.

The back surface of the specimen was supported by a 12 mm thick polymethyl-methacrylate (PMMA) backing plate. A schematic representation of the target is presented in Figure 6.2.2.

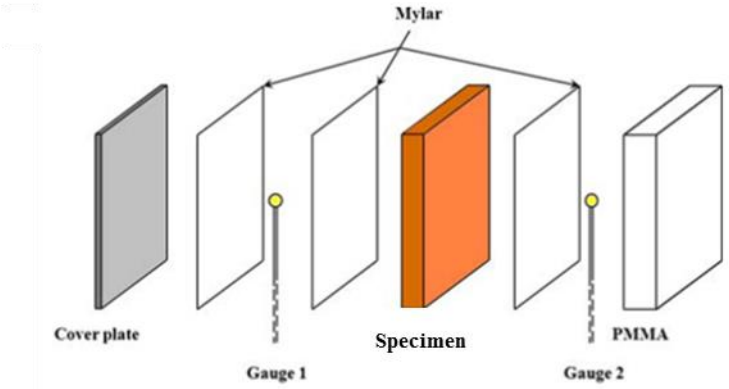

Figure 6.2.2 Plate impact test target (adjusted from Appleby-Thomas, Hazell and Stennett, 2009)

Manganin pressure gauges were calibrated according to Rosenberg (Rosenberg, Yaziv and Partom, 1980). They were located at the front and the back surfaces of the specimen. The front gauge was insulated by a 25 μm film made of biaxially-oriented polyethylene terephthalate (boPET commercially known as Mylar) from the 1 mm thick cover plate (Al or Cu – matching the impactor) and the specimen. The back gauge was insulated by boPET from the specimen and it was supported by the PMMA backing plate.

The specimens used in the experiment were 6mm thick CFRP panels comprising 23 plays of a unidirectional CFRP laminae aligned in 0° direction. The material density was 1.54 g/cm^3. CYCOM® 997 epoxy resin was used. The experiment programme, with the impact velocities recorded by the pin block, is presented in Table 6.2.1.

Table 6.2.1 Plate impact test programme

Specimen	Impact direction [km/s]	Impactor material [km/s]	Impact velocity [km/s]
UD CFRP 1	Through thickness	Aluminium	0.352
UD CFRP 2	Through thickness	Aluminium	0.463
UD CFRP 3	Through thickness	Copper	0.625
UD CFRP 4	Through thickness	Copper	0.806

6.2.2 Results

The stress traces, recorded by front and rear gauges, are shown in Figure 6.2.3. Front gauge recording clearly shows the formation of the shock wave – the stress rise time was well below 200 ns for all of the shots. The shock arrival to the back gauge is also well defined. Note that the stress recorded by the back gauge for velocity of 0.625 kms^{-1} degraded to zero rapidly after reaching the maximum value, which suggests that the gauge was damaged by impact. However, it is assumed that up to the failure point its readings were correct and can be used for determination of shock parameters, although the results should be treated with caution.

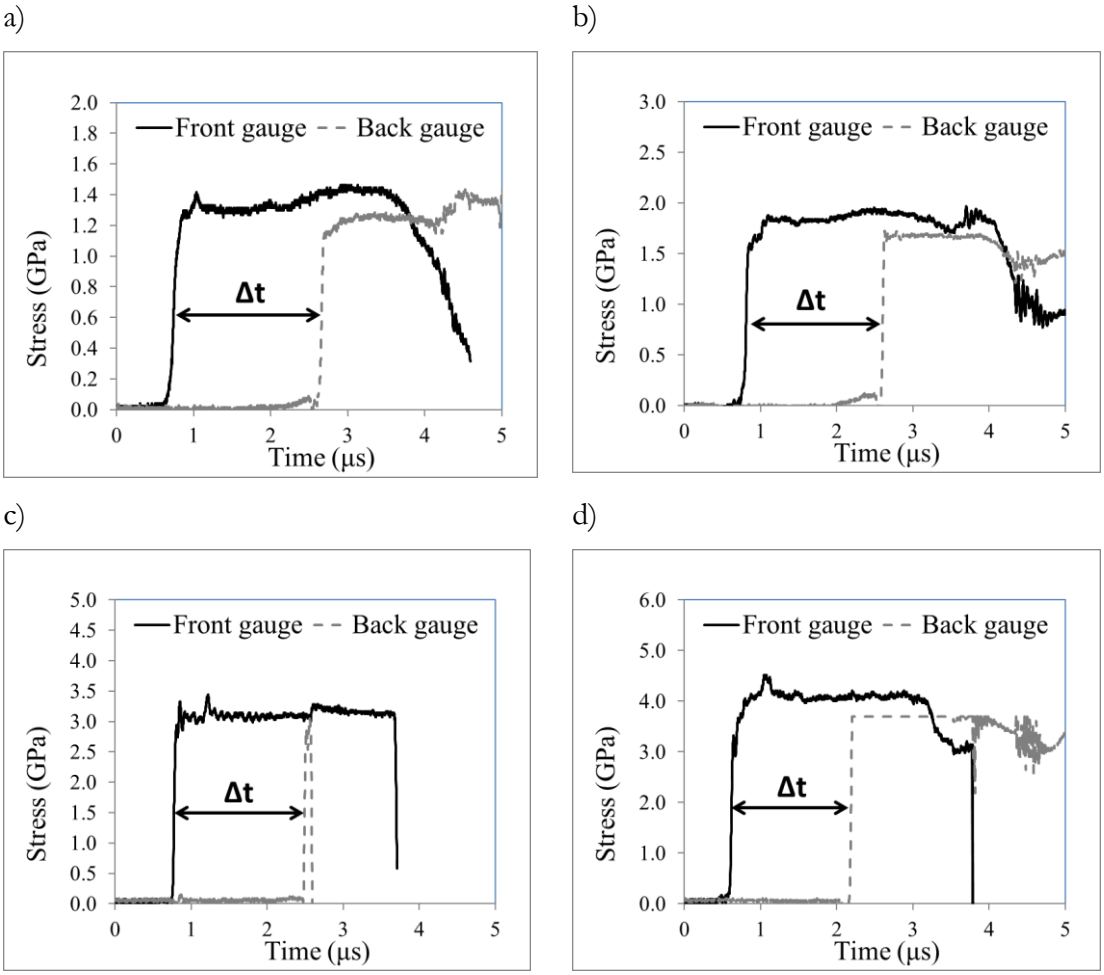

Figure 6.2.3 Shock wave propagation in the specimens hit with the impact velocity: a) 0.352 kms^{-1} , b) 0.463 kms^{-1}, c) 0.625 kms^{-1}, d) 0.806 kms^{-1}

The stress behind the shockwave, also known as the Hugoniot stress, was calculated by taking a mean value of the plateau readings. These results are presented in Table 6.2.2. There is a strong correlation between the impact velocity and the Hugoniot stress, which is an expected result.

Table 6.2.2 Plate impact test results

Impact velocity [km/s]	Shock velocity [km/s]	Particle velocity [km/s]	Rise time - front gauge [ns]	Rise time - back gauge [ns]	Hugoniot stress [GPa]
0.352 (Al)	3.186	0.256	176	106	1.297
0.463 (Al)	3.391	0.334	80	64	1.832
0.625 (Cu)	3.504	0.541	86	40	3.088
0.806 (Cu)	3.882	0.690	51	61	4.078

Velocities were calculated by dividing the known distance between the gauges (Δx) by a time interval required for the shock to arrive at the back gauges (Δt):

$$U_S = \Delta x / \Delta t \,. \qquad \textbf{6.2.1}$$

The shock velocity increased with increasing velocity of impact. This trend was also observed for the particle velocities. The particle velocities were found by impedance-match technique (Meyers, 1994) using the known density of the target, known shock properties of the flyer material (Marsh, 1980) and calculated shock velocity. Impedance-match technique is based on the two physical restrictions at the shock interface. These are equality of pressure and equality of particle velocities at the target-flyer interface.

Shock velocities and particle velocities were used to construct a $U_S - U_P$ plot in Figure 6.2.4. Following Ruoff (1967), Davison and Graham (1979) and Meyers (1994) the linear relation between particle and shock velocities can be determined for majority of materials, giving the shock velocity as:

$$U_S = C + S_1 U_P \,. \qquad \textbf{6.2.2}$$

This approximation was successfully applied to composites by a number of researchers (Riedel, Nahme and Thoma, 2004; Millett *et al.*, 2007; Hazell, Stennett and Cooper, 2008, 2009; Appleby-Thomas, Hazell and Stennett, 2009; Appleby-Thomas and Hazell, 2012; Gautam *et al.*, 2017). The linear approximation of the shock velocity – particle velocity relation seems reasonable for the data obtained in this work. The coefficients of Equation 6.2.2 for the performed tests were determined as: $C = 2.84\ km/s$ and $S_1 = 1.42$.

The error bars in the graph were based on the earliest and latest possible arrival times deduced from the pressure traces.

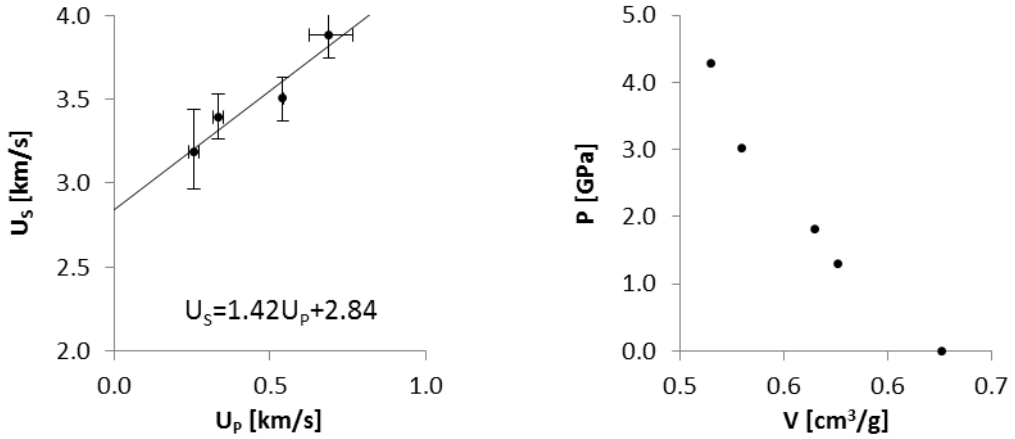

Figure 6.2.4 a) Shock velocity vs particle velocity, b) Pressure vs specific volume

A comparison of the calculated values of the coefficients C and S_1 against data found in literature is presented in Table 6.2.3. Dattelbaum and Coe (2012) investigated the unidirectional composite in the through thickness direction for impact velocities ranging from 0.670 to 3.307 km/s. The values of C and S_1 coefficients reported by Dattelbaum were 2.87 km/s and 1.17 respectively. Firstly, the small overlap of the particle velocities between two sets of data should be noted. The impact velocities used in (Dattelbaum and Coe, 2012) were generally higher than velocities used in our experiments. Secondly, the wider range of impact (and subsequently particle) velocities were investigated. However, given the small number of shots performed in this work and the narrower velocity range, the agreement of data is good.

The coefficients values presented here also exhibit a good agreement with the coefficients obtained by Millett et al. (2007) and Riedel, Nahme and Thoma (2004) – see Figure 2.1.1. Both publications considered woven composites rather than unidirectional. However, the suggestion of Millett et al. (2007) that the through thickness behaviour of composites is dominated by matrix properties encourages including also woven composites data. Moreover, it additionally justifies the comparison of the CFRP in through thickness direction with pure epoxy resins whose behaviour has been more extensively studied e.g. by Munson and May (1972); Boettger (1994); Millett, Meziere and Bourne, (2007); Hazell, Stennett and Cooper, (2008) and Appleby-Thomas, Hazell and Stennett, (2009) among others. The full

comparison of the data shock EOS parameters obtained in this work against the other available data is presented in Table 6.2.3.

Table 6.2.3 Plate impact test results comparison with available data

Specimen	Impact direction	ρ_0 [g/c^3]	C [km/s]	S_1 [-]
CFRP unidirectional	through thickness	1.597	2.84	1.42
CFRP unidirectional (Dattelbaum and Coe, 2012)	through thickness	1.536	2.87	1.17
CFRP woven (Millett *et al.*, 2007)	through thickness	1.5	3.23	0.92
CFRP woven (Riedel, Nahme and Thoma, 2004)	through thickness	-	2.54	1.41
CFRP woven (Hazell, Stennett and Cooper, 2009)	fibre	1.51	2.27	2.26
Epoxy (Millett, Bourne and Barnes, 2002)	-	1.14	2.58	1.47
Epoxy (Hazell, Stennett and Cooper, 2008)	-	1.41	2.65	1.55
Epoxy (Munson and May, 1972)	-	1.194	2.64	1.66
Epoxy (Boettger, 1994)	-	1.154	2.63	1.52

Therefore, it is clear from the table that the data obtained in this work are comparable to the CFRP data in literature (Riedel, Nahme and Thoma, 2004; Millett, Meziere and Bourne, 2007; Dattelbaum and Coe, 2012). Note that the through thickness impact properties of CFRP are very close to the pure epoxy impact properties reported in (Munson and May, 1972; Boettger, 1994; Millett, Bourne and Barnes, 2002; Hazell, Stennett and Cooper, 2008).

The comparison between the CFRP data from literature and data obtained in this work is given in Figure 6.2.5. The results obtained in this work are in good agreement with (Riedel, Nahme and Thoma, 2004; Millett *et al.*, 2007; Dattelbaum and Coe, 2012). Figure 6.2.5 shows the data points and the linear approximation of EOS parameters for a range of particle velocities from 0 to 2.5 km/s. The best match of the speed of sound C was obtained with

Dattelbaum and Coe, (2012). Coefficient S_1 determined in this work is closest to the one obtained by Riedel, Nahme and Thoma (2004) which is manifested by almost parallel lines in Figure 6.2.5. Note that results determined in this work and those generated by Millett *et al.* (2007) and Riedel, Nahme and Thoma (2004) considered the particle velocities up to 1 km/s. Dattelbaum and Coe (2012) investigated shock behaviour for a wider range – up to 2.2 km/s.

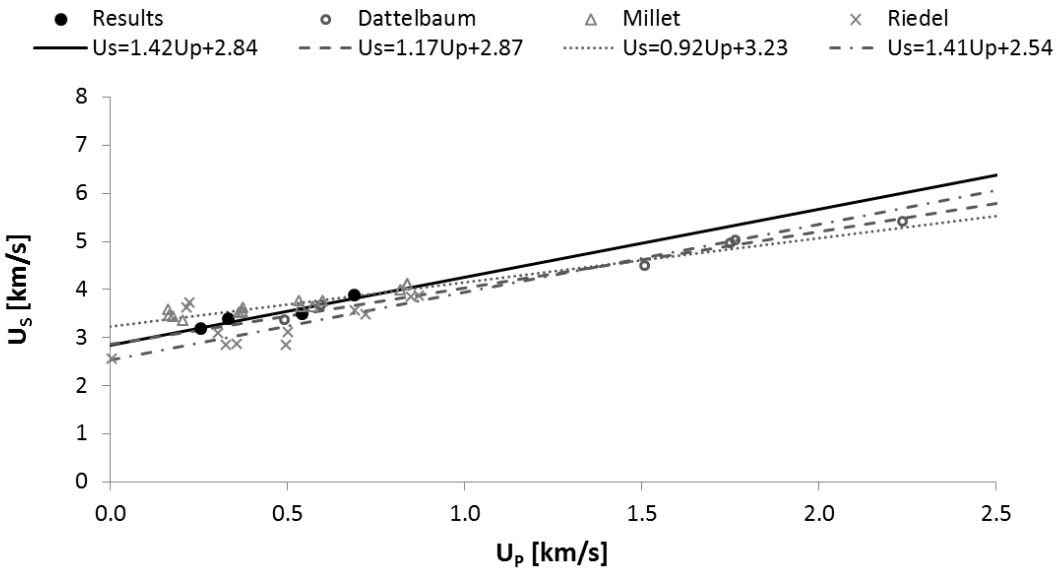

Figure 6.2.5 CFRP shock parameters comparison in particle velocity range: a) 0-1 kms^{-1}, b) 0-10 kms^{-1}

6.2.3 Summary

The purpose of this study was to determine the equation of state for CFRP 977-2 unidirectional composite. The characterisation in through thickness directions covered velocities in a range from 0.352 km/s to 0.806 km/s. The coefficients C and S_1 were found to be 2.84 km/s and 1.42 respectively. These results are in a good agreement with existing data for unidirectional CFRP (Dattelbaum and Coe, 2012). They also exhibited similarity with the properties of woven composite in through thickness direction (Riedel, Nahme and Thoma, 2004; Millett et al., 2007). A very good match between the current study and the pure epoxy equation of state (Munson and May, 1972; Boettger, 1994; Millett, Meziere and Bourne, 2007; Hazell, Stennett and Cooper, 2008; Appleby-Thomas, Hazell and Stennett, 2009) was found. This corroborates the hypothesis that matrix material drives the through thickness EOS for a composite. It cannot be underestimated, that the current findings add to a growing, but still insufficient, body of literature on composite shock equation of state.

6.3 Model implementation

The theoretical model presented in Section 6.1 was implemented in Dyna3D (Lin, 2004). The implementation required a direct calculation of the theoretically derived state variables from the input data and variables computed in Dyna3D solver. The model follows a standard FEM procedure which can be split into four major parts – input, initialisation, solution and output as presented schematically in Figure 6.3.1.

Figure 6.3.1 Model flow chart - general

Material constants that are required in the constitutive model are read from a material card in the input part. Model constants that are not defined in the input file, but are required in solution phase are defined and computed during initialisation. The major part of the model is the solution where all the variables are determined following the constitutive equations. The output consists of typical outputs, stress and strain, and model specific internal variables including modal damage variables and their conjugate forces.

6.3.1 Input

Input parameters in the model are material density (ρ) three Young's moduli (E_1, E_2, E_3), three shear moduli (G_{12}, G_{23}, G_{31}) and three Poisson's ratio $(\nu_{21}, \nu_{31}, \nu_{32})$. For transversely isotropic material, the nine elastic material parameters can be reduced to five. However, the model was implemented in a way to allow for future generalisation to other material symmetries than transverse isotropy. Additional variables that are required for damage part of the model are the energy limits $(\omega_0^I, \omega_0^{II}, \omega_0^{III}, \omega_0^{IV}, \omega_0^V, \omega_0^{VI})$. Damage evolution can be controlled by six damage evolution energies $(\kappa^I, \kappa^{II}, \kappa^{III}, \kappa^{IV}, \kappa^V, \kappa^{VI})$, whilst final material failure can be controlled by critical damage parameters $(d_{cr}^I, d_{cr}^{II}, d_{cr}^{III}, d_{cr}^{IV}, d_{cr}^V, d_{cr}^{VI})$. Setting the damage evolution energies to non-zero values allow for modelling of strain hardening or softening of the material. Critical damage variables set limits for damage state variable, used as the final failure criterion. When the critical damage parameter is reached, element is failed which results setting the element stresses to zero (for stability reasons it is performed in 100 time steps). Both damage evolution energies and critical damage variables are commented in more detail in Section 6.3.7. The input is shown in the flow chart in Figure 6.3.2.

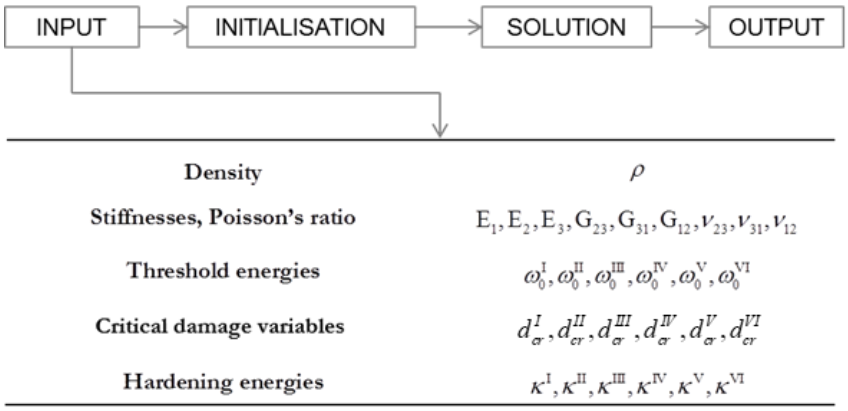

Figure 6.3.2 Model flow chart – input

6.3.2 Initialisation

During the initialisation step the model constants are declared and calculated and constitutive model specific variables are set to zero. All material constants including the undamaged material stiffness tensor, its eigenvalues and two coefficients (α and β) that uniquely define the eigenvectors are calculated. The initialisation is shown in the flow chart in Figure 6.3.3.

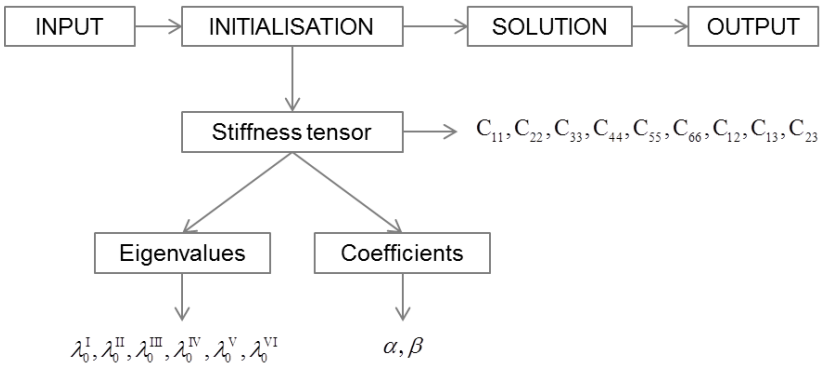

Figure 6.3.3 Model flow chart - initialisation

The stiffness tensor entries are calculated from the material constants as:

$$C_{11} = \frac{1-\nu_{23}\nu_{32}}{E_2E_3\Delta}, \qquad C_{12} = \frac{\nu_{21}+\nu_{31}\nu_{23}}{E_2E_3\Delta} = \frac{\nu_{12}+\nu_{32}\nu_{13}}{E_1E_3\Delta},$$

$$C_{22} = \frac{1-\nu_{13}\nu_{31}}{E_1E_3\Delta}, \qquad C_{13} = \frac{\nu_{31}+\nu_{21}\nu_{32}}{E_2E_3\Delta} = \frac{\nu_{13}+\nu_{12}\nu_{23}}{E_1E_2\Delta},$$

$$C_{33} = \frac{1-\nu_{12}\nu_{21}}{E_1E_2\Delta}, \qquad C_{23} = \frac{\nu_{32}+\nu_{12}\nu_{31}}{E_1E_3\Delta} = \frac{\nu_{23}+\nu_{21}\nu_{13}}{E_1E_2\Delta}, \qquad \text{6.3.1}$$

$$C_{44} = 2G_{12}, \qquad C_{55} = 2G_{23}$$

$$C_{66} = 2G_{31}, \qquad \Delta = \frac{1-\nu_{12}\nu_{21}-\nu_{23}\nu_{32}-\nu_{31}\nu_{13}-2\nu_{21}\nu_{32}\nu_{13}}{E_1E_2E_3}.$$

It is important to note that the order of shear related constants is different than it was described in the previous sections due to consistency with Dyna3D. In Voigt (or contracted tensor notation) the shear indices order is: 23, 31, 12 whilst in Dyna D it is 12, 23, 31. Thus, in the implementation, the fourth and sixth modes are equal (two fibre plane shear modes) and the fifth mode is the isotropy plane shear mode whose stiffness eigenvalue equals to the second mode stiffness eigenvalue.

The initial stiffness tensor eigenvalues $(\lambda_0^I, \lambda_0^{II}, \lambda_0^{III}, \lambda_0^{IV}, \lambda_0^V, \lambda_0^{VI})$ are calculated from the stiffness tensor members by:

$$\lambda_0^I = \frac{1}{2}\left[(C_{11}+C_{22}+C_{23}) + \sqrt{(C_{11}-C_{22}-C_{23})^2 + 8(C_{12})^2}\right], \qquad \lambda_0^{IV} = 2C_{44},$$

$$\lambda_0^{II} = C_{22} - C_{23}, \qquad \lambda_0^V = 2C_{55}, \qquad \textbf{6.3.2}$$

$$\lambda_0^{III} = \frac{1}{2}\left[(C_{11}+C_{22}+C_{23}) - \sqrt{(C_{11}-C_{22}-C_{23})^2 + 8(C_{12})^2}\right], \qquad \lambda_0^{VI} = 2C_{66}.$$

Material coefficients α and β are defined as:

$$\alpha = \frac{2C_{12}}{\lambda_0^I - C_{11}}, \qquad \beta = \frac{2C_{12}}{\lambda_0^{III} - C_{11}}. \qquad \textbf{6.3.3}$$

The assumption of not rotating eigenvectors is equivalent to the assumption that these coefficients are constant in the model.

6.3.3 Solution – damage part

Solution part of the model includes time integration, calculation of deformation rate tensor, processing of damage part of the model and update of the internal energy with stress update. It is shown in the flow chart in Figure 6.3.4. The solution steps down to a calculation of rate of deformation tensor are performed by Dyna3D existing algorithms.

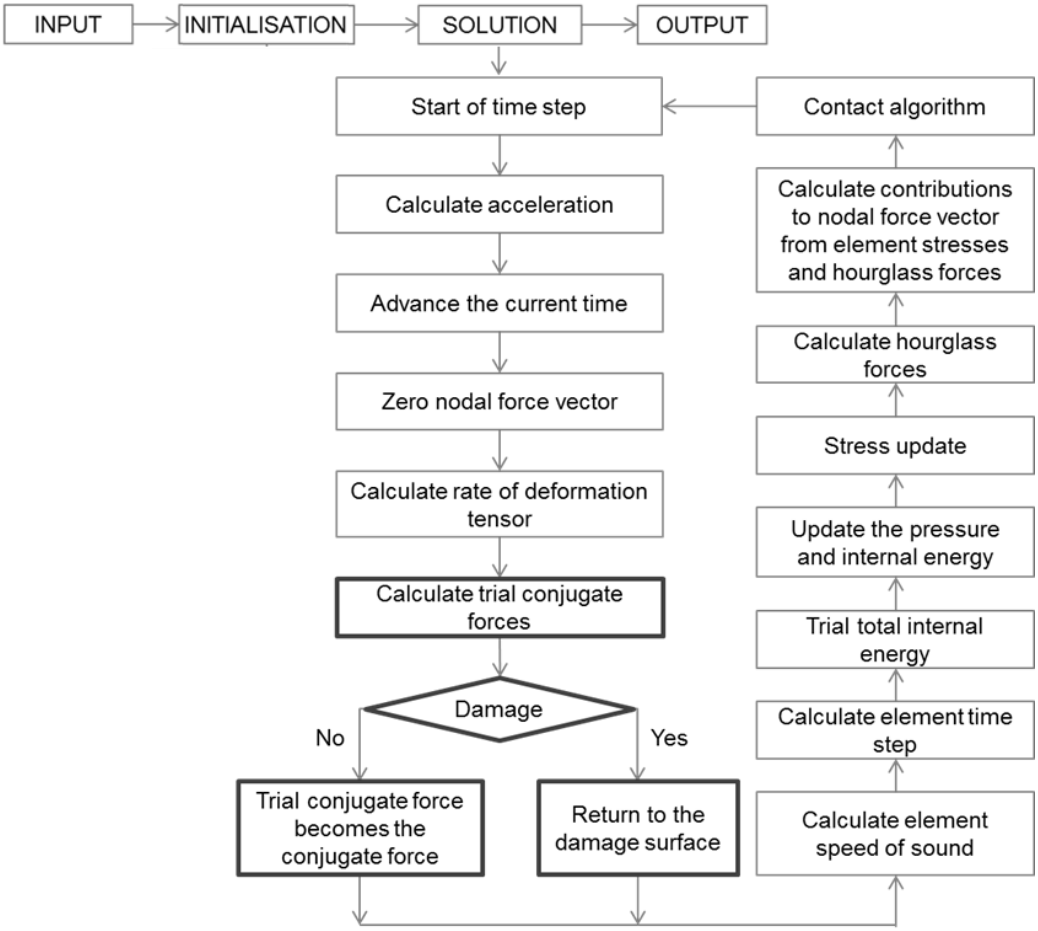

Figure 6.3.4 Model flow chart - solution

The implementation of the model presented in Section 6.1 starts with the calculation of the trial conjugate forces. This part of the solution is presented in detail in Figure 6.3.5.

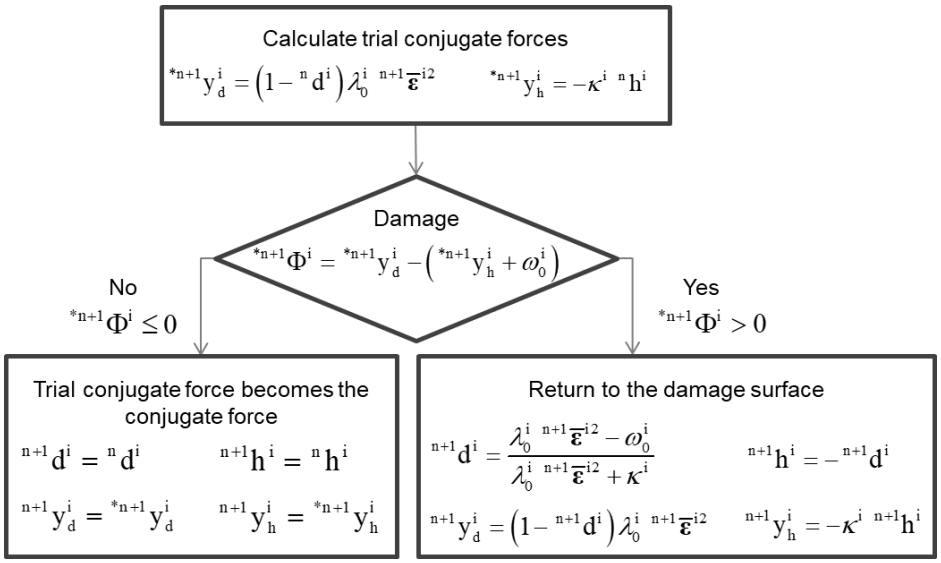

Figure 6.3.5 Model flow chart - solution - damage part

A calculation of trial conjugate forces is performed using Equations 6.3.4 consequently for all modes. The trial value is computed for the damage variable from the previous time step $({}^{n}d)$ and the current time step strain $({}^{n+1}\varepsilon)$.

$$ {}^{*n+1}y_d^i = \left(1 - {}^{n}d^i\right)\lambda_0^i\, {}^{n+1}\varepsilon^{i2}, \qquad {}^{*n+1}y_h^i = -\kappa^i\, {}^{n}h^i = \kappa^i\, {}^{n}d^i. \qquad \textbf{6.3.4} $$

The squares of the modal strains in the definition of the trial conjugate forces are determined from the strains at time step $n+1$ by:

$$ {}^{n+1}\varepsilon^{I2} = \frac{\left(\alpha\, {}^{n+1}\varepsilon_1 + {}^{n+1}\varepsilon_2 + {}^{n+1}\varepsilon_3\right)^2}{2+\alpha^2}, $$

$$ {}^{n+1}\varepsilon^{II2} = \frac{1}{2}\left({}^{n+1}\varepsilon_2 - {}^{n+1}\varepsilon_3\right)^2, $$

$$ {}^{n+1}\varepsilon^{III2} = \frac{\left(\beta\, {}^{n+1}\varepsilon_1 + {}^{n+1}\varepsilon_2 + {}^{n+1}\varepsilon_3\right)^2}{2+\beta^2} = \frac{\left(-2\, {}^{n+1}\varepsilon_1 + \alpha\, {}^{n+1}\varepsilon_2 + \alpha\, {}^{n+1}\varepsilon_3\right)^2}{2\left(2+\alpha^2\right)}, \qquad \textbf{6.3.5} $$

$$ {}^{n+1}\varepsilon^{IV2} = 2\, {}^{n+1}\varepsilon_4^2, $$

$$ {}^{n+1}\varepsilon^{V2} = 2\, {}^{n+1}\varepsilon_5^2, $$

$$ {}^{n+1}\varepsilon^{VI2} = 2\, {}^{n+1}\varepsilon_6^2. $$

Initial values of damage and damage evolution variables equal to zero. The trial values of damage potentials are calculated using damage and damage hardening forces (Equations 6.3.4) for all modes:

$$ {}^{*n+1}\Phi_i = {}^{*n+1}y_{di} - \left({}^{*n+1}y_{hi} + \omega_{0i}\right). \qquad \textbf{6.3.6} $$

If trial damage potential for all modes is lower or equal to zero damage does not evolve in any of the modes. Thus, the damage and damage evolution variables for the current time step are equal to the previous time step variables.

$$ {}^{n+1}d^i = {}^{n}d^i, \qquad {}^{n+1}h^i = {}^{n}h^i. \qquad \textbf{6.3.7} $$

Consequently, the damage and damage hardening conjugate forces are equal to their trial values:

$$ {}^{n+1}y_d^i = {}^{*n+1}y_d^i, \qquad {}^{n+1}y_h^i = {}^{*n+1}y_h^i. \qquad \textbf{6.3.8} $$

If the trial damage potential exceeds zero for any of the modes, the corresponding damage variable evolves, and its current value is determined as:

$$ {}^{n+1}d^i = \frac{\lambda_0^i \, {}^{n+1}\bar{\boldsymbol{\varepsilon}}^{i2} + \kappa^i - \omega_0^i}{\lambda_0^i \, {}^{n+1}\bar{\boldsymbol{\varepsilon}}^{i2} + \kappa^i}, \qquad {}^{n+1}h_i = -{}^{n+1}d_i . \tag{6.3.9} $$

And the conjugate forces for the current time step become:

$$ {}^{n+1}y_d^i = \left(1 - {}^{n+1}d^i\right) \lambda_0^i \, {}^{n+1}\bar{\boldsymbol{\varepsilon}}^{i2}, \qquad {}^{n+1}y_h^i = -\kappa_i \, {}^{n+1}h_i . \tag{6.3.10} $$

6.3.4 Solution – stress update

Stress in the model depends on the strains but also on the pressure calculated from the EOS (see Section 3.5). Stress update is therefore required to correctly determine the stress components within elements. To update the stress tensor, the deviatoric stress increment needs to be determined first. In the most general terms the new deviatoric stress is equal to:

$$ {}^{n+1}s_{ij} = {}^{n}s_{ij} + {}^{n+½}\dot{s}_{ij} \, {}^{n+½}\Delta t = {}^{n}s_{ij} + {}^{n+1}\Delta s_{ij}, \tag{6.3.11} $$

where ${}^{n}s_{ij}$ and ${}^{n+1}s_{ij}$ are deviatoric stress tensors for subsequent time steps and ${}^{n+½}\dot{s}_{ij}$ is rate of deviatoric stress which multiplied by increment of time gives an increment of deviatoric stress ${}^{n+1}\Delta s_{ij}$. The deviatoric stress rate depends on the deviatoric strain rate and damage rate, which can be expressed as:

$$ {}^{n+1}\Delta s_{ij} = {}^{n+½}\dot{s}_{ij} \, {}^{n+½}\Delta t = {}^{n+½}\dot{M}_{ijkl} \, {}^{n+½}\Delta t \, {}^{n+½}s_{kl}^0 + {}^{n+½}M_{ijkl} \, {}^{n+½}\dot{s}_{kl}^0 \, {}^{n+½}\Delta t, \tag{6.3.12} $$

where tensor M_{ijkl} is a damage effect tensor. Damage in the model is mode-characteristic, and thus the damage effect tensor can be constructed from damage variables multiplied by the corresponding projection operators:

$$ M_{ijkl} = \sum \left(1 - d^i\right)^2 P_{ijkl}^i \tag{6.3.13} $$

The increment of damage effect tensor is:

$$ {}^{n+½}\dot{M}_{ijkl} \, {}^{n+½}\Delta t = {}^{n+½}\Delta M_{ijkl} = {}^{n+1}M_{ijkl} - {}^{n}M_{ijkl} = \sum \left(\left(1 - {}^{n+1}d^i\right)^2 - \left(1 - {}^{n}d^i\right)^2 \right) P_{ijkl}^i . \tag{6.3.14} $$

Thus, the deviatoric stress increment coming from deviatoric strain:

$$
\begin{aligned}
{}^{n+1}\Delta s_{ij} = \sum \left(\left(1 - {}^{n+1}d^{i}\right)^{2} - \left(1 - {}^{n}d^{i}\right)^{2} \right) \lambda_0^i v_{mn}^i \, {}^{n+\frac{1}{2}}\varepsilon_{mn}^{'} v_{ij}^i + \\
+ \sum \left(1 - {}^{n+\frac{1}{2}}d^{i}\right)^{2} \lambda_0^i v_{mn}^i \, {}^{n+\frac{1}{2}}\Delta\varepsilon_{mn}^{'} v_{ij}^i
\end{aligned}
\qquad \textbf{6.3.15}
$$

where $\varepsilon_{mn}^{'}$ is the deviatoric strain and mid-step damage variables ${}^{n+\frac{1}{2}}d^{i}$ can be calculated from the mid step strains as:

$$
{}^{n+\frac{1}{2}}d^{i} = \frac{\lambda_0^i \, {}^{n+\frac{1}{2}}\varepsilon^{i\,2} - \omega_0^i}{\lambda_0^I \, {}^{n+\frac{1}{2}}\varepsilon^{i\,2} + \kappa^i}. \qquad \textbf{6.3.16}
$$

The explicit solution for the stress tensor can be determined after substitution of known eigenvectors:

$$
\begin{aligned}
{}^{n+1}\Delta s_1 &= \frac{\alpha}{\sqrt{2+\alpha^2}} x^I + \frac{\beta}{\sqrt{2+\beta^2}} x^{III}, \\
{}^{n+1}\Delta s_2 &= \frac{1}{\sqrt{2+\alpha^2}} x^I - \frac{1}{\sqrt{2}} x^{II} + \frac{1}{\sqrt{2+\beta^2}} x^{III}, \\
{}^{n+1}\Delta s_3 &= \frac{1}{\sqrt{2+\alpha^2}} x^I + \frac{1}{\sqrt{2}} x^{II} + \frac{1}{\sqrt{2+\beta^2}} x^{III}, \\
{}^{n+1}\Delta s_4 &= \lambda_0^{IV} \left(\left(1 - {}^{n+\frac{1}{2}}d^{IV}\right)^{2} \, {}^{n+\frac{1}{2}}\Delta\varepsilon_4^{'} + \left(\left(1 - {}^{n+1}d^{IV}\right)^{2} - \left(1 - {}^{n}d^{IV}\right)^{2} \right) {}^{n+\frac{1}{2}}\varepsilon_4^{'} \right), \\
{}^{n+1}\Delta s_5 &= \lambda_0^{V} \left(\left(1 - {}^{n+\frac{1}{2}}d^{V}\right)^{2} \, {}^{n+\frac{1}{2}}\Delta\varepsilon_5^{'} + \left(\left(1 - {}^{n+1}d^{V}\right)^{2} - \left(1 - {}^{n}d^{V}\right)^{2} \right) {}^{n+\frac{1}{2}}\varepsilon_5^{'} \right), \\
{}^{n+1}\Delta s_6 &= \lambda_0^{VI} \left(\left(1 - {}^{n+\frac{1}{2}}d^{VI}\right)^{2} \, {}^{n+\frac{1}{2}}\Delta\varepsilon_6^{'} + \left(\left(1 - {}^{n+1}d^{VI}\right)^{2} - \left(1 - {}^{n}d^{VI}\right)^{2} \right) {}^{n+\frac{1}{2}}\varepsilon_6^{'} \right),
\end{aligned}
\qquad \textbf{6.3.17}
$$

where x^i are variables introduced for the sake of clarity:

$$
\begin{aligned}
x^I &= \frac{\lambda_0^1}{\sqrt{2+\alpha^2}} \left(\begin{array}{l} \left(1 - {}^{n+\frac{1}{2}}d^{I}\right)^{2} \left(\alpha \, {}^{n+\frac{1}{2}}\Delta\varepsilon_1^{'} + {}^{n+\frac{1}{2}}\Delta\varepsilon_2^{'} + {}^{n+\frac{1}{2}}\Delta\varepsilon_3^{'} \right) + \\ \quad + \left(\left(1 - {}^{n+1}d^{I}\right)^{2} - \left(1 - {}^{n}d^{I}\right)^{2} \right) \left(\alpha \, {}^{n+\frac{1}{2}}\varepsilon_1^{'} + {}^{n+\frac{1}{2}}\varepsilon_2^{'} + {}^{n+\frac{1}{2}}\varepsilon_3^{'} \right) \end{array} \right), \\
x^{II} &= \frac{\lambda_0^{II}}{\sqrt{2}} \left(\begin{array}{l} \left(1 - {}^{n+\frac{1}{2}}d^{II}\right)^{2} \left({}^{n+\frac{1}{2}}\Delta\varepsilon_3^{'} - {}^{n+\frac{1}{2}}\Delta\varepsilon_2^{'} \right) + \\ \quad + \left(\left(1 - {}^{n+1}d^{II}\right)^{2} - \left(1 - {}^{n}d^{II}\right)^{2} \right) \left({}^{n+\frac{1}{2}}\varepsilon_3^{'} - {}^{n+\frac{1}{2}}\varepsilon_2^{'} \right) \end{array} \right), \\
x^{III} &= \frac{\lambda_0^{III}}{\sqrt{2+\beta^2}} \left(\begin{array}{l} \left(1 - {}^{n+\frac{1}{2}}d^{III}\right)^{2} \left(\beta \, {}^{n+\frac{1}{2}}\Delta\varepsilon_1^{'} + {}^{n+\frac{1}{2}}\Delta\varepsilon_2^{'} + {}^{n+\frac{1}{2}}\Delta\varepsilon_3^{'} \right) + \\ \quad + \left(\left(1 - {}^{n+1}d^{III}\right)^{2} - \left(1 - {}^{n}d^{III}\right)^{2} \right) \left(\beta \, {}^{n+\frac{1}{2}}\varepsilon_1^{'} + {}^{n+\frac{1}{2}}\varepsilon_2^{'} + {}^{n+\frac{1}{2}}\varepsilon_3^{'} \right) \end{array} \right).
\end{aligned}
\qquad \textbf{6.3.18}
$$

Following the stress decomposition suggested by Vignjevic *et al.* (2008) the final form of the deviatoric stress should be perpendicular to the pressure vector, which does not hold for the above expressions. The new deviatoric stress vectors can be determined from:

$$\Delta s = \frac{\Delta s_1 \psi_1 + \Delta s_2 \psi_2 + \Delta s_3 \psi_3}{\psi_1 \psi_1 + \psi_2 \psi_2 + \psi_3 \psi_3},$$

$$\begin{aligned} \Delta \tilde{s}_1 &= \Delta s_1 - \Delta s \psi_1, & \Delta \tilde{s}_2 &= \Delta s_2 - \Delta s \psi_2, \\ \Delta \tilde{s}_3 &= \Delta s_3 - \Delta s \psi_3, & \Delta \tilde{s}_4 &= \Delta s_4, \\ \Delta \tilde{s}_5 &= \Delta s_5, & \Delta \tilde{s}_6 &= \Delta s_6, \end{aligned} \qquad \textbf{6.3.19}$$

where pressure vector is defined as (repeated from Section 3.5.1):

$$\psi_i = \frac{\left(C_{i1} + C_{i2} + C_{i3}\right)}{\sqrt{\frac{\left(C_{11} + C_{12} + C_{13}\right)^2 + \left(C_{12} + C_{22} + C_{23}\right)^2 + \left(C_{13} + C_{23} + C_{33}\right)^2}{3}}}. \qquad \textbf{6.3.20}$$

Following Equations 6.3.19, the new deviatoric stress is determined:

$$\begin{aligned} {}^{n+1}\tilde{s}_1 &= {}^{n}s_1 + \Delta \tilde{s}_1, & {}^{n+1}\tilde{s}_2 &= {}^{n}s_2 + \Delta \tilde{s}_2, \\ {}^{n+1}\tilde{s}_3 &= {}^{n}s_3 + \Delta \tilde{s}_3, & {}^{n+1}\tilde{s}_4 &= {}^{n}s_4 + \Delta \tilde{s}_4, \\ {}^{n+1}\tilde{s}_5 &= {}^{n}s_5 + \Delta \tilde{s}_5, & {}^{n+1}\tilde{s}_6 &= {}^{n}s_6 + \Delta \tilde{s}_6. \end{aligned} \qquad \textbf{6.3.21}$$

The pressure in the model is calculated using the modified Gruneisen Equation of State where the total stress is calculated using the new deviatoric stress and the pressure (EOS) multiplied by pressure vector:

$$\begin{aligned} {}^{n+1}\sigma_1 &= {}^{n+1}\tilde{s}_1 - {}^{n+1}p_{EOS}\psi_1 & {}^{n+1}\sigma_2 &= {}^{n+1}\tilde{s}_2 - {}^{n+1}p_{EOS}\psi_2 \\ {}^{n+1}\sigma_3 &= {}^{n+1}\tilde{s}_3 - {}^{n+1}p_{EOS}\psi_3 & {}^{n+1}\sigma_4 &= {}^{n+1}\tilde{s}_4 \\ {}^{n+1}\sigma_5 &= {}^{n+1}\tilde{s}_5 & {}^{n+1}\sigma_6 &= {}^{n+1}\tilde{s}_6 \end{aligned} \qquad \textbf{6.3.22}$$

The minus sign results from sign convention in Dyna3D, where the tensile pressure is negative and compressive one is positive as opposed to the stresses which are positive when tensile and negative when compressive.

6.3.5 Output

The model output includes the stress and strain tensors components (given in global coordinates), modal strain magnitudes, damage variables, damage evolution variables and

damage conjugate forces. Pressure calculated from modified Gruneisen EOS is also written as a history variable. Note that the default pressure output in LS PrePost is calculated by the post processor as the average of the normal stresses. Therefore, it is not equal to the modified Gruneisen EOS pressure calculated in the model, unless the material is isotropic. The implementation was verified in the series of single element tests as described in the following section.

6.3.6 Single element tests

In order to check the implementation, single element tests were performed. Their objective was to investigate the single element behaviour under a simple load for which material response is known. The element behaviour was checked for the six deformation eigenmodes. The single element of edge length 1cm was generated and was subsequently loaded to activate the deformation eigenmodes depending on the load case. Model input data is presented in Table 6.3.1. Damage threshold for the first mode was determined from the failure strain of fibres (knowing that the first eigenstrain is almost exactly equal to the fibre strain). Shear modes critical strains were taken from the critical shear stresses. The second mode threshold is equal to the fifth mode threshold, as the modes share the same eigenvalue. The threshold energy of the last remaining mode – the third mode was taken from the mesoscale simulations.

Table 6.3.1 Input data of the model for single element validation

Density [g/cm3]	ρ	1.622
Stiffness [GPa]	E_1	165.00
	$E_2 = E_3$	9.84
	$G_{12} = G_{31}$	4.98
	G_{23}	3.00
Poisson's ratio [-]	$\nu_{21} = \nu_{31}$	0.0169
	ν_{32}	0.4535
Damage threshold [MPa]	ω^{I}	46.210
	$\omega^{II} = \omega^{V}$	2.096
	ω^{III}	7.836
	$\omega^{IV} = \omega^{VI}$	3.138
Critical damage variable	d^{I}	0.3
	$d^{II} = d^{III}$	0.5
	$d^{IV} = d^{V} = d^{VI}$	0.7

The single element tests were run without pressure update from Gruneisen EOS to directly check behaviour of the damage part of the model implementation. However, it was also proved that the EOS gives expected results. Figures below (Figure 6.3.6 to Figure 6.3.7) show material's strain, damage and damage conjugate force as a function of time as well as the eigenstress – eigenstrain curve. Only the first mode is presented here, however all the modes behave in the same way. Figure 6.3.6 clearly shows that an element was loaded to activate a single strain energy mode and indeed, only the first eigenstrain is present. Damage initiated when the damage conjugate force reached its critical value ($y_d = 46MPa$) for time $t_d = 160\mu s$ which is presented in Figure 6.3.8. At this time damage starts to grow which can be observed in Figure 6.3.7. Damage grows until its critical value ($d_{cr} = 0.3$) is reached at time $t_{fail} = 200\mu s$. Eigenstress – eigenstrain plot (Figure 6.3.9) shows that stress grows linearly up to the damage initiation (at strain ε_d and time t_d). With damage evolution stress is reduced and it is set to zero in 100 time steps after damage variable reached its critical value. The model behaves as expected in the first mode. All the graphs clearly show, that only one strain energy mode was activated in the simulation as only the variables corresponding to the first mode are non-zero.

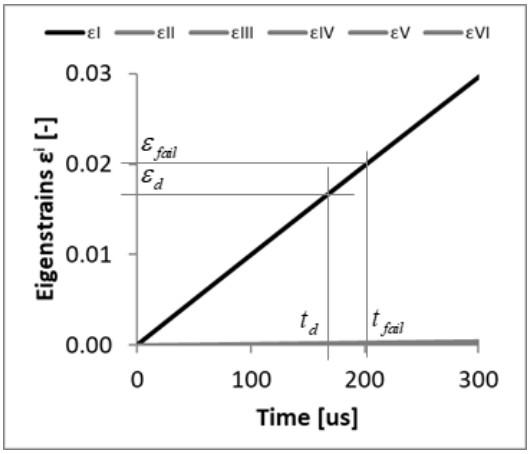

Figure 6.3.6 Strain vs time plot of the first deformation eigenmode single element simulation

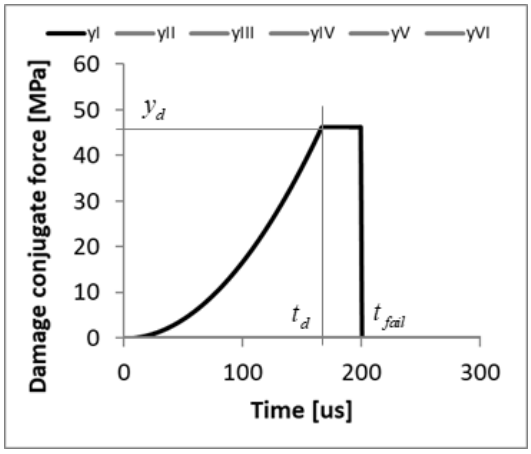

Figure 6.3.7 Damage conjugate force vs time plot of the first deformation eigenmode single element simulation

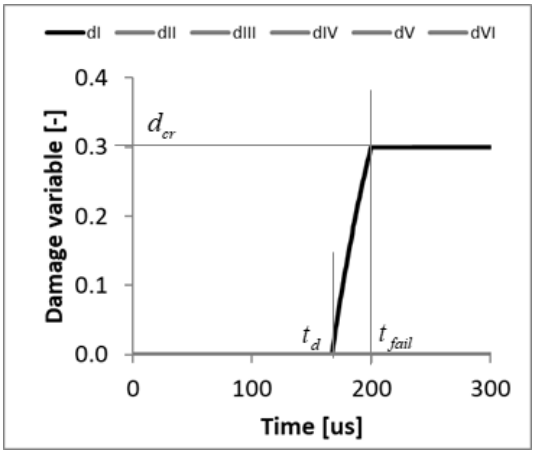

Figure 6.3.8 Damage vs time plot of the first deformation eigenmode single element simulation

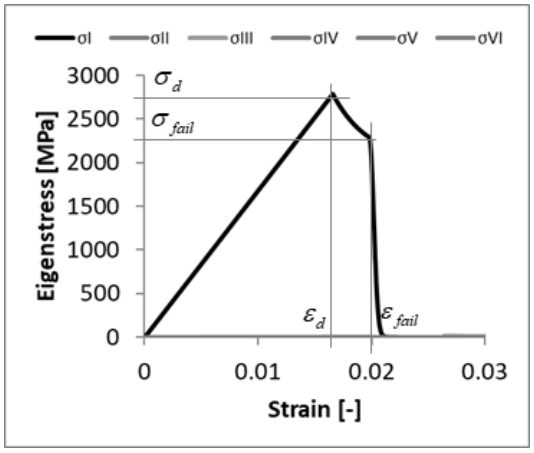

Figure 6.3.9 Stress – strain plot of the first deformation eigenmode single element simulation

The similar analysis was carried out for the remaining modes. It was confirmed that in all the modes damage was initiated when damage conjugate force reached the damage threshold. After initiation damage growth was observed up to the point of final failure after which stress was reduced to zero. This confirms that the experimental single element results follow the analytical expectations which proves that the model is implemented correctly.

6.3.7 Analysis of the hardening variables and critical damage variables

The previous section showed that the proposed model works at a single element level. The parameters used in the model were a basic set including density, stiffness constants, damage energy thresholds and the critical damage variables. However, the model also allows to introduce the damage evolution energies that can control damage evolution in the material. Having the full modal stress – modal strain curves for material would univocally describe the material behaviour. It would allow for determination of both damage threshold and damage evolution variables by curve fitting. Nevertheless, lacking the curves one can try to analytically estimate the hardening values or allowable ranges, which is the aim of this paragraph.

Damage evolution is controlled by hardening potential (κh) in Equation 6.3.23 which results in modal stress-strain curve shape being determined by the evolution energy (κ):

$$\Phi = y_d + \left(y_h - \omega_0\right) = 0, \tag{6.3.23}$$

$$y_d = \left(1-d\right)\lambda_0 \varepsilon^2, \qquad y_h = -\kappa h.$$

Note that damage conjugate force (y_d) is dependent on the sum of hardening potential (y_h) and energy threshold (ω_0). Moreover, damage evolution variable (h) grows from 0 to -1. It is therefore sensible to analyse the evolution energy as a multiplicity of energy threshold (ω_0). Figure 6.3.10 shows the theoretical predictions of damage conjugate force and stress-strain behaviour for different damage evolution energies.

a) b)

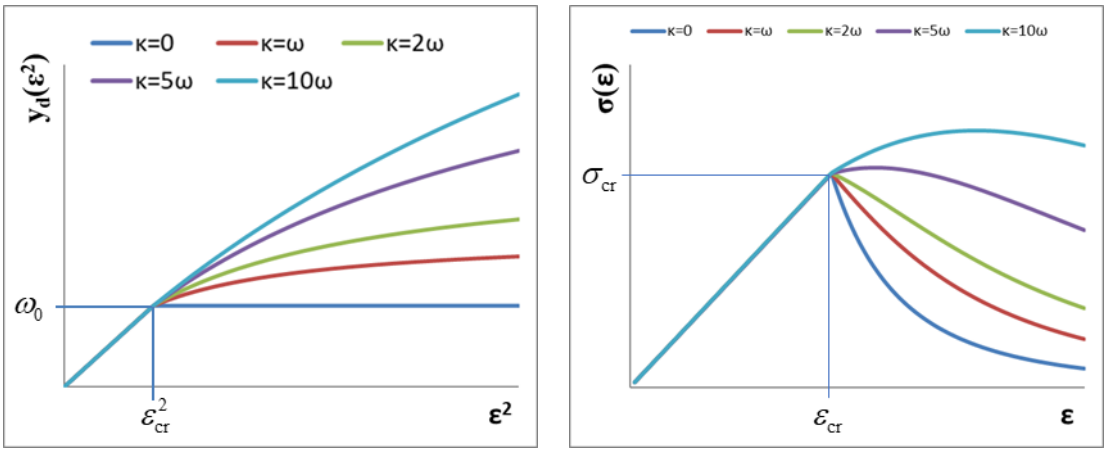

Figure 6.3.10 Theoretically predicted: a) damage conjugate force and b) stress strain behvaviour for different evolution energies

For $\kappa = 0$ perfect damage behaviour can be observed with damage conjugate force at the level of damage threshold after damage initiation. For higher values of κ damage conjugate force can increase after damage initiation. More information can be gained from Figure 6.3.10 - b). For $\kappa = 0$ stress after damage initiation drops rapidly. The higher the damage evolution energy, the less rapid is stress reduction. For $\kappa = 5\omega_0$ after damage initiation stress is almost constant (very slightly increasing), starting to drop gradually with increasing strain (and damage). Finally, for $\kappa = 10\omega_0$ the maximum stress that the material can withstand is significantly higher than stress at damage initiation. Such a behaviour is not observed in composites in normal load directions, thus $\kappa = 5\omega_0$ can be assumed to be a limit for the damage evolution energy. On the other hand, stress increase after damage initiation was observed in some mechanical tests in shear damage modes. Therefore, addition of damage evolution energies can provide more realistic modelling.

Another model parameter that needs to be determined is a critical damage variable (one for each mode). It is the parameter that defines what is the critical damage extent of a material

after which it completely loses the load carrying capability. Critical damage variable can be determined from a mechanical test activating a single strain energy mode. With knowledge of the stress-strain material behaviour and the final failure strain it is possible to determine the critical damage variable. Final failure usually occurs in material as rupture or loss of stability. Figure 6.3.11 - a) shows the stress strain graph of a material (no hardening) with several potential damaged principal stiffnesses each calculated using different damage variable. At the interception of stress-strain graph with the potentially determined stiffnesses, material has the critical damage variable corresponding to the respective stiffness line. Figure 6.3.11 - b) shows an example of determination of critical damage variable.

a) b)

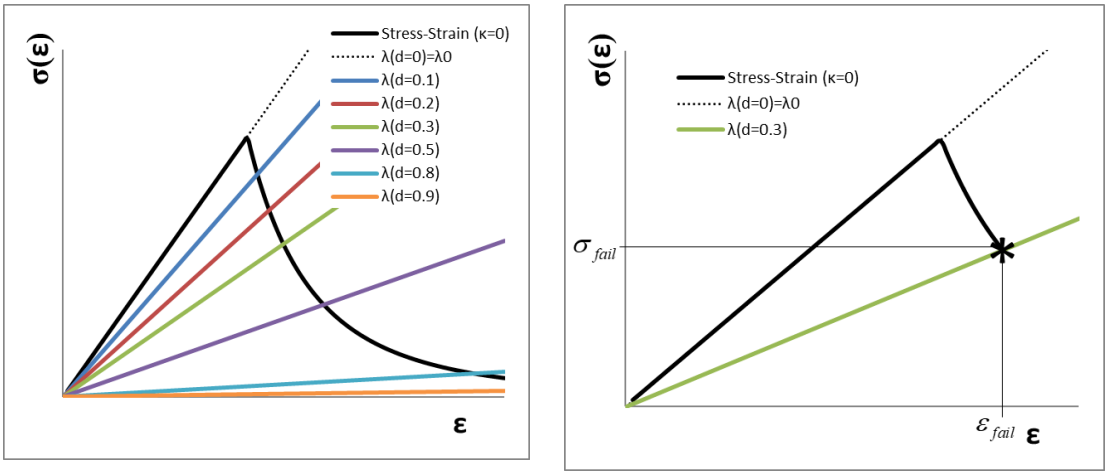

Figure 6.3.11 Damage dependency of principal stiffness: a) concept, b) example

The material in the example failed in the point marked with asterisk. By reading the stress and strain at failure it is possible to calculate the critical damage variable using:

$$\sigma_{fail} = \left(1 - d_{cr}\right)^2 \lambda_0 \varepsilon_{fail}, \qquad \textbf{6.3.24}$$

which leads to direct expression:

$$d_{cr} = 1 - \sqrt{\frac{\sigma_{fail}}{\lambda_0 \varepsilon_{fail}}}. \qquad \textbf{6.3.25}$$

Carbon fibre composites are brittle materials, and their rupture usually occurs not long after damage initiation for fibre direction (i.e. $d_{cr} \leq 0.3$). For other material directions, damage can attain higher values, but for normal directions $d_{cr} \leq 0.5$ seems a reasonable constraint.

Such analysis is also valid for materials (or single modes) with nonzero damage evolution energies.

Having a full material modal characterisation would allow to determine of all model parameters directly. However, there is lack of such experimental data available. Thus, in this work the parameters were assumed rather than experimentally determined.

6.4 Model validation

Having established the theoretical foundations and numerical calculation procedures the next step is to validate the model. Validation of the model was performed to check the model's accuracy, its capabilities and limitations. During validation, it became apparent that strong anisotropy of the material poses a serious threat to simulations numerical stability. In case of unidirectional composites fibre direction is stiffer by a factor of 15 than matrix direction. It was found to generate the significant numerical error in pressure calculation which grows constantly in time if applied to small elements. Thus, the model becomes visibly unstable after approximately 6 μs. To overcome this numerical stability problem the model was validated using an orthotropic material with two fibre directions of equal stiffness and strength. In such a material stiffness in all directions is of the same order of magnitude, which considerably improves pressure calculation. The symmetry class that corresponds to chosen material is called tetragonal. It can be modelled with the same approach as transversely isotropic material. Furthermore, the eigenvalues and eigenvectors of tetragonal material can be explicitly determined using the same equations as for the transversely isotropic material (obviously, yielding different results). The one exception is lack of equivalence of the second and the fifth mode (in Dyna3D numbering convention). Nevertheless, the current code can be successfully used for tetragonal material.

Material data for validation was taken from (Vignjevic *et al.*, 2008; Vignjevic, Djordjevic and de Vuyst, 2012) – presented in Table 6.4.1.

Table 6.4.1 Orthotropic material engineering constants used in model validation

Young's moduli GPa / [-]		Shear moduli GPa		Poisson's ratio [-]	
E_x	10.0	G_{yz}	4.57	ν_{yz}	0.039
E_y	68.5	G_{zx}	3.57	ν_{zx}	0.045
E_z	68.5	G_{xy}	3.57	ν_{yx}	0.045

The Y and Z directions were assumed to be fibre directions. It was dictated by the implementation, which requires those directions to be equal. Corresponding stiffness tensor and its eigenvalues and eigenvectors are:

$$C = \begin{bmatrix} 10.00 & 0.47 & 0.47 & 0 & 0 & 0 \\ 0.47 & 68.63 & 2.70 & 0 & 0 & 0 \\ 0.47 & 2.70 & 68.63 & 0 & 0 & 0 \\ 0 & 0 & 0 & 7.14 & 0 & 0 \\ 0 & 0 & 0 & 0 & 9.14 & 0 \\ 0 & 0 & 0 & 0 & 0 & 7.14 \end{bmatrix} GPa$$

$$\begin{aligned} \lambda^{I} &= 71.3\,GPa, & \mathbf{v}^{I} &= \begin{bmatrix} 0.011 & 0.707 & 0.707 & 0 & 0 & 0 \end{bmatrix}^{T}, \\ \lambda^{II} &= 65.9\,GPa, & \mathbf{v}^{II} &= \begin{bmatrix} 0 & -0.707 & 0.707 & 0 & 0 & 0 \end{bmatrix}^{T}, \\ \lambda^{III} &= 10.0\,GPa, & \mathbf{v}^{III} &= \begin{bmatrix} -0.9999 & 0.008 & 0.008 & 0 & 0 & 0 \end{bmatrix}^{T}, \\ \lambda^{IV} &= 7.1\,GPa, & \mathbf{v}^{IV} &= \begin{bmatrix} 0 & 0 & 0 & 1 & 0 & 0 \end{bmatrix}^{T}, \\ \lambda^{V} &= 9.1\,GPa, & \mathbf{v}^{V} &= \begin{bmatrix} 0 & 0 & 0 & 0 & 1 & 0 \end{bmatrix}^{T}, \\ \lambda^{VI} &= 7.1\,GPa = \lambda^{IV}, & \mathbf{v}^{VI} &= \begin{bmatrix} 0 & 0 & 0 & 0 & 0 & 1 \end{bmatrix}^{T}. \end{aligned} \qquad \textbf{6.4.1}$$

Coefficients α and β which define the material anisotropy can be determined as (repeated from Table 2.1.1):

$$\mathbf{v}^{I} = \frac{1}{\sqrt{2+\alpha^2}}\begin{bmatrix} \alpha & 1 & 1 & 0 & 0 & 0 \end{bmatrix}^{T}, \qquad \mathbf{v}^{III} = \frac{1}{\sqrt{2+\beta^2}}\begin{bmatrix} \beta & 1 & 1 & 0 & 0 & 0 \end{bmatrix}^{T}. \qquad \textbf{6.4.2}$$

For the orthotropic material used for validation coefficient α is equal to 0.015, and coefficient β is equal to -131. Due to such a high β coefficient, the third mode is aligned exactly with X direction with negligible influence of Y and Z direction. Note, that X direction only non-fibre direction here, so the third mode is the matrix plane strain in tension or compression. Modes I and II are the fibre related modes. The first one is the fibre tension – tension (or compression – compression) mode whilst the other one is fibre tension – compression mode. The graphical representation of the modes corresponding to the material

used in validation is presented in Figure 6.4.1. The fourth, fifth and sixth modes are the shear modes in XY, YZ and ZX planes respectively (in Dyna3D numbering).

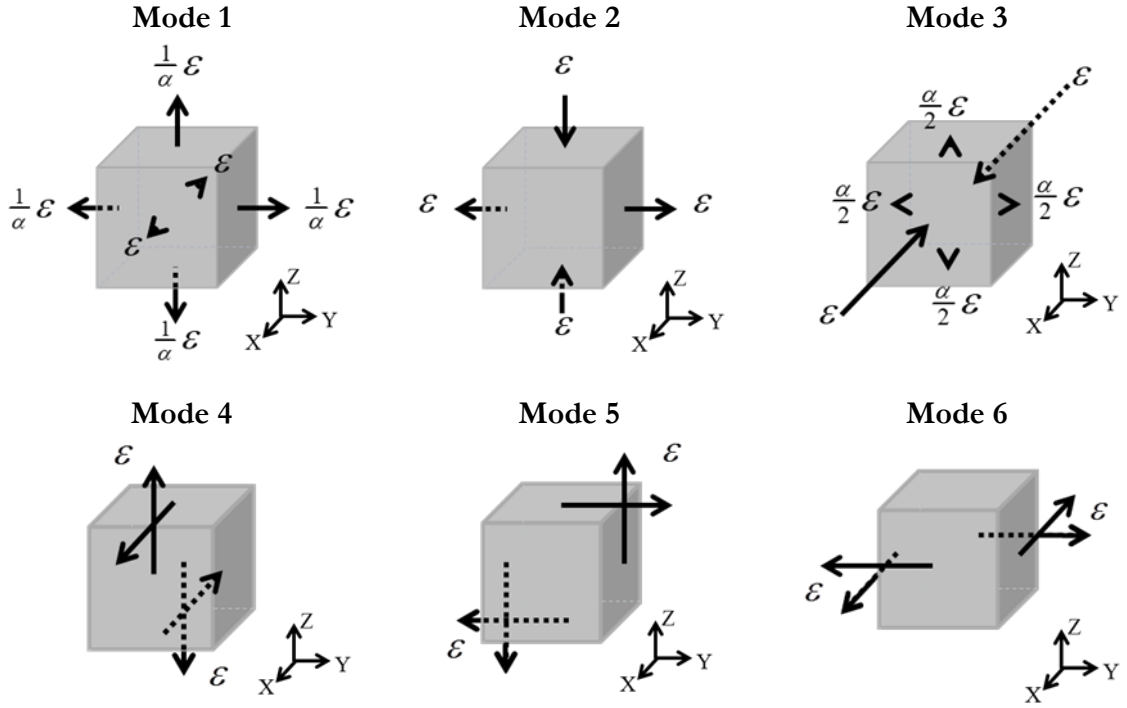

Figure 6.4.1 Graphical representation of the modes of orthotropic material used for validation

6.4.1 Plate impact test

Plate impact test was described in Section 6.2 for the purpose of determination of material's EOS parameters. The same test was also used for validation of the EOS part of the model.

The solid FE model of the plate impact test was created (Figure 6.4.2). To reduce the computational cost only a small part of the plate was modelled. Model dimensions in X and Y directions (which in experiment were considerably larger) were modelled by the periodic boundary conditions. Thus, only a small part of the model could be generated to avoid high computation cost. This allowed to generate the plane strain state in the material, which is the key assumption in the plate impact test. The model consists of four solid elements in X and Y directions that model the 4 mm x 4 mm section of the material. The flyer plate (5 mm) was modelled with 40 elements in Z direction, cover plate (1 mm) with eight elements. The woven material specimen for through thickness plate impact test was 5.7 mm thick which was modelled with 48 elements. The backing plate (12 mm) was modelled with 100 elements in Z direction.

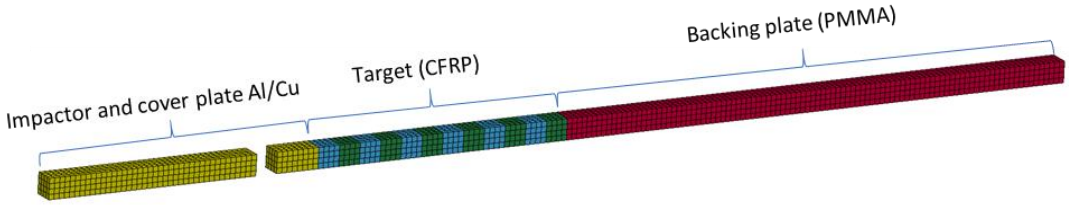

Figure 6.4.2 Plate impact test model for through thickness direction (square section of the plates)

The flyer and the cover plate were made of aluminium while the backing plate of PMMA. All were modelled using MAT_10 (isotropic-elastic-plastic-hydrodynamic) Material data for aluminium and PMMA was taken from (Steinberg, 1996). Contact between the flyer and the cover plate was modelled using a sliding interface with separation and friction (slide surface type 3 in Dyna 3D)(Lin, 2004). Velocity of the flyer in the experiment and simulation was 504m/s. Initially, the target was modelled using the isotropic epoxy material properties (Table 6.4.2).

Table 6.4.2 Input parameters for isotropic material for plate impact test

GPa / [-]		MPa		[-]		MPa	
E	3.52	ω_0^I	4x10^9	$d_{cr}^I = d_{cr}^{II}$	1.0	κ^I	0.0
G	1.35	ω_0^{II}	4.0	d^{III}	1.0	κ^{II}	0.0
ν	0.33	ω_0^{III}	4.0	d^{IV}	1.0	κ^{III}	0.0
		ω_0^{IV}	4.0	d^{IV}	1.0	κ^{IV}	0.0
		ω_0^V	4.0	d^V	1.0	κ^V	0.0
		ω_0^{VI}	4.0	d^{VI}	1.0	κ^{VI}	0.0

Modal critical energies that define damage initiation of the material were determined from the strength of epoxy. For isotropic materials the first mode is the volumetric mode. As it is assumed that volumetric deformation does not lead to damage the corresponding strength was set to a very high value. Simulation results were compared against the experimental (composite) results. Comparison is reasonable as epoxy properties are dominant in composites in through thickness direction. The stress traces are displayed in Figure 6.4.3. In the figure red and pink colours represent the experiment and blue and light blue to the simulation. The figure shows the good agreement of epoxy simulation results to the experimental results. Time of shock propagation through the specimen is equal in experiment and in simulation (1.6 μs). The shock-direction stress level of epoxy at the front gauge (dark blue line in Figure 6.4.3) was 1.66 GPa. It gives 10% discrepancy when compared to the experimental 1.85 GPa stress at the cover-target interface. The front gauge stress relaxation

is slightly steeper in the simulation than in the experiment. Stress level at the back surface (light blue in Figure 6.4.3) is in perfect agreement with the stress level in the experiment (pink). However, unloading of back surface of the target starts around 3.2 μs which is later than in the experiments (2.9 μs) and it is steeper than the experimental back gauge unloading.

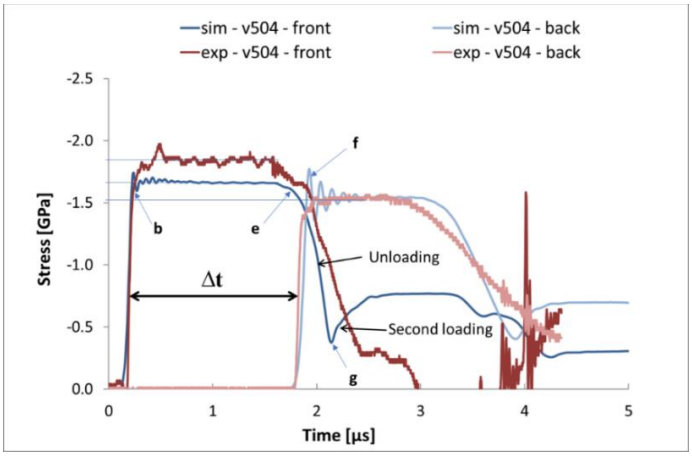

Figure 6.4.3 Plate impact test simulation vs experimental results - isotropic epoxy

Note that stress-reloading at the front gauge after 2 μs comes from the target side. This loading is a result of use of the cover plate. It is best illustrated on the X-t diagram given in Figure 6.4.4. The shock wave initiates when the flyer and cover plate get in contact (point 'a'). It results in the compressive wave travelling through the cover plate and the flyer– blue and orange lines. At the interface between the cover plate and the target (point 'b'), the shock wave is transferred into the target (grey line) but is also partially reflected as a release wave back into the cover plate (orange line), from where it progresses back to the flyer (points 'b' to 'd'). When the initial shock wave and the wave reflected from the cover plate – target interface reach back surface of the flyer they are reflected (points 'c' and 'd'). The release wave, generated by the reflection of the shock wave, define the loading pulse length. The loading pulse length is equal to the time required for the shock wave to travel twice the thickness of the flyer:

$$\Delta t = \frac{2s_f}{C_f}, \qquad \textbf{6.4.3}$$

where s_f is the flyer thickness and C_f is the speed of sound in flyer material. Points 'b' and 'e' mark the shock initiation in the target and start of the unloading, which correspond to the plateau observed in Figure 6.4.3 (also labelled with letters for clarity). The reflection of the cover plate – target interface release wave causes reloading of the target (point 'g' also marked

in both figures). Consequently, due to the superposition of the waves coming from the target and the sample, the loading in material becomes complicated and the experimental results are not reliable after approximately 2.5 μs.

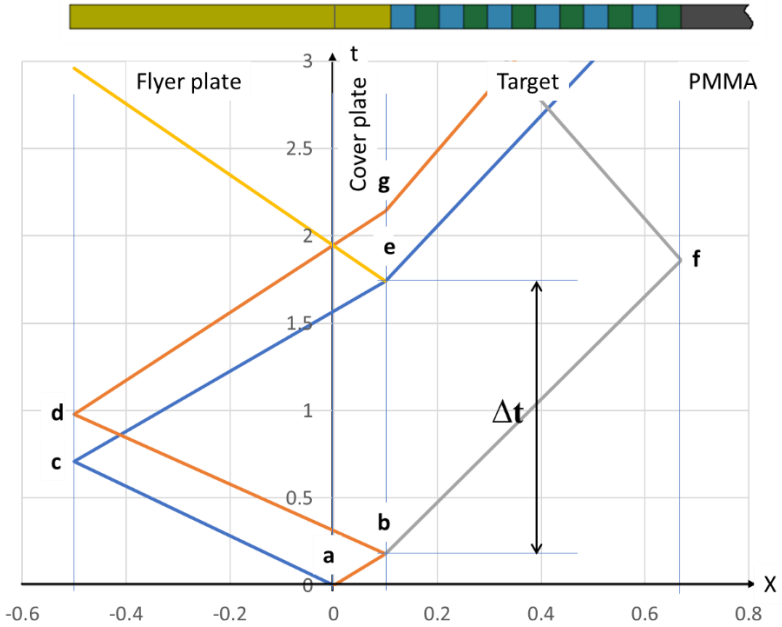

Figure 6.4.4 X-t diagram for shock waves travelling in the plate

Good agreement of the simulation and experimental results confirms that the through thickness composite behaviour is dominated by epoxy properties.

The next step in the validation was use of linear elastic woven composite properties in the plate impact test. The woven composite properties were taken from (Vignjevic and Djordjevic, 2010) with the EOS data determined in this work. The strengths were set to high values to assure no damage in the model. The model input is presented in Table 6.4.3.

Table 6.4.3 Input parameters for linear elastic woven composite for plate impact test

GPa / [-]		10^{10}*MJ/m^3		[-]		MJ/m^3	
E_x	10.0	ω_0^I	36.5	d_{cr}^I	1.0	κ^I	0.0
$E_y = E_z$	68.5	ω_0^{II}	16.0	d_{cr}^{II}	1.0	κ^{II}	0.0
G_{yz}	4.57	ω_0^{III}	6.3	d_{cr}^{III}	1.0	κ^{III}	0.0
$G_{zx} = G_{xy}$	3.57	ω_0^{IV}	3.1	d_{cr}^{IV}	1.0	κ^{IV}	0.0
ν_{yz}	0.039	ω_0^V	2.1	d_{cr}^V	1.0	κ^V	0.0
$\nu_{zx} = \nu_{xy}$	0.045	ω_0^{VI}	3.1	d_{cr}^{VI}	1.0	κ^{VI}	0.0

The simulation results were compared against the experimental results. Figure 6.4.5 shows the stress traces obtained with the linear elastic woven composite model.

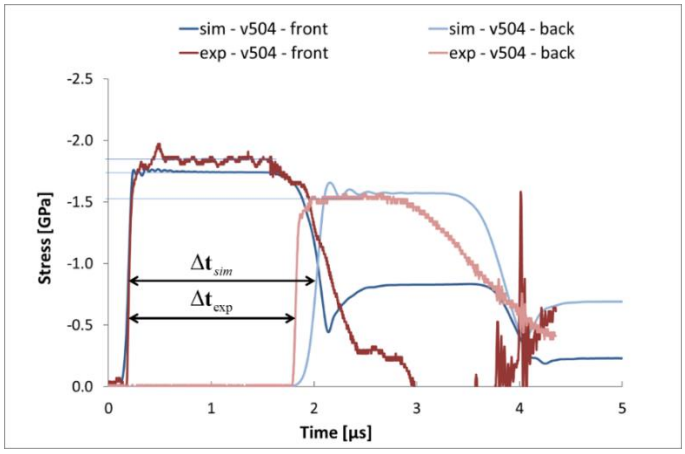

Figure 6.4.5 Stress traces from front and back gauges - through thickness plate impact test – linear elastic properties

Clearly, a good agreement was achieved in the stress magnitude both at the front and at the back gauge. The front stress trace has a good length and the unloading region is also well aligned with the experimental results. The shock arrival at the back surface was predicted quite well, but the stress rise is less rapid than in the simulations. The back-surface stress trace is longer than the experimental one and has a steeper unloading slope. However, its length matches the length of the front gauge signal. The simulation results are reasonable for the linear elastic material properties. The shape of the experimental back gauge trace (pink line in Figure 6.4.5) suggests damage in the material or the stress gauge.

Another modelled case was the woven material with modal damage initiation energies determined from the quasi-static strengths (see Table 6.4.4).

Table 6.4.4 Input parameters for woven composite for plate impact test

GPa / [-]		MJ/m³		[-]		MJ/m³	
E_x	10.0	ω_0^I	36.5	d_{cr}^I	1.0	κ^I	0.0
$E_y = E_z$	68.5	ω_0^{II}	16.0	d_{cr}^{II}	1.0	κ^{II}	0.0
G_{yz}	4.57	ω_0^{III}	6.3	d_{cr}^{III}	1.0	κ^{III}	0.0
$G_{zx} = G_{xy}$	3.57	ω_0^{IV}	3.1	d_{cr}^{IV}	1.0	κ^{IV}	0.0
ν_{yz}	0.039	ω_0^V	2.1	d_{cr}^V	1.0	κ^V	0.0
$\nu_{zx} = \nu_{xy}$	0.045	ω_0^{VI}	3.1	d_{cr}^{VI}	1.0	κ^{VI}	0.0

Note that the current code sets the stresses to zero after final failure (in subsequent 100 timesteps), disregarding the character of the load (tension/compression). In case of tensile stress this is accurate, as the material completely loses its integrity and load carrying capability. However, for compressive loads the bulk of material (even after failure) is still capable of transferring loads. The damage part of the model at its current stage cannot distinguish

between tensile and compressive loads. Thus, to overcome the problem of total loss of load carrying capability in compression due to failure, the final failure of the model was disabled in the plate impact tests (by setting the critical damage variables to 1).

Stress traces for that model are presented in Figure 6.4.6 together with the experimental data. The first thing that is clear is that the shock passage through the specimen does not follow the experiment. Time required for the shock wave to travel through the specimen was 2.5 μs, which is roughly 50% more than the experimental result (1.6 μs). The stress magnitude obtained for the front of the target was 1.31 GPa, which is 30% lower than the experimental stress. The back-surface stress has a magnitude of 1.42 GPa which agrees well with the experimentally obtained 1.52 GPa (error lower than 7%).

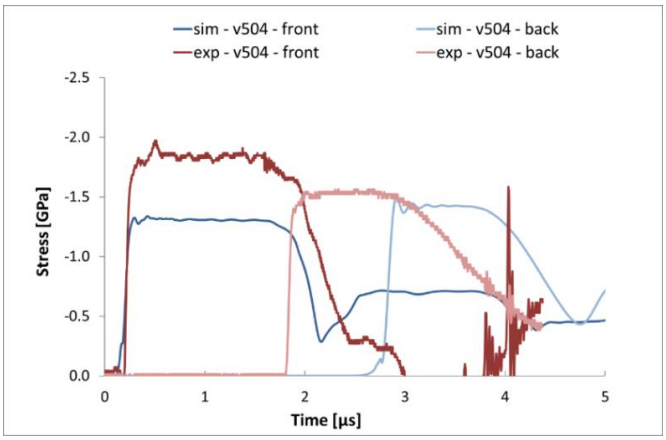

Figure 6.4.6 Stress traces from front and back gauges - through thickness plate impact test – material with finite strength

What is interesting is that the back surface trace of the damaged material has a similar length and a slope of the unloading region (see Figure 6.4.7). This confirms that the back-surface stress was affected by damage of the composite plate in the experiment.

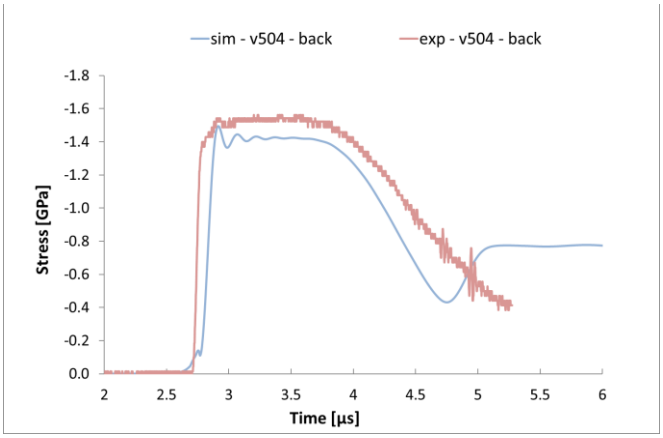

Figure 6.4.7 Stress traces from back gauge in through thickness plate impact test of woven material allowing for damage

To conclude, proposed material model can accurately predict the shock passage through material thickness if linear elastic properties are used. If a finite strength material is considered, the failure in material occurs too early and has significant influence on the stress both at the front and at the back of the specimen. It leads to the simulated stress at the beginning of the load being much lower in comparison to the experimental one. The reason for that is twofold. Firstly, material properties for the composite were estimated from the tensile properties rather than compressive, which may introduce an error in damage initiation. Current version of the damage part of the model does not have the functionality to distinguish between tension and compression, which may be addressed in future. Secondly, homogenisation of a strongly anisotropic material leads to different pressure vector orientation than for an isotropic homogeneous material. This may also affect the material stresses and damage behaviour especially for the through thickness direction, which is known to be matrix dependent. It points out to another subject of future investigations, namely, detailed analysis of coupling of the material model with EOS and its implications.

6.4.2 Plate impact test – fibre direction

Plate impact test performed in the fibre direction was carried out on the 6 mm long specimen of woven composite with stacking sequence [0/90,45] with fibres in XZ plane. The model dimensions perpendicular to the impact are 3.8 mm x 3.8 mm with eight elements in directions X and Y (Figure 6.4.8). The continuity of the material was achieved by using the periodic boundary conditions. The 5 mm flyer plate and 1 mm cover plate were modelled respectively with ten and two elements in the impact direction (Z). Both the flyer and the cover plate were modelled using MAT_15 (Johnson Cook material model) with copper properties taken from (Vignjevic *et al.*, 2008). The backing PMMA plate of 12 mm was modelled with 25 elements with MAT_10 (isotropic-elastic-plastic-hydrodynamic) and the material properties were taken from (Steinberg, 1996). The composite target consisted of eight layers each modelled with twelve elements in the impact direction.

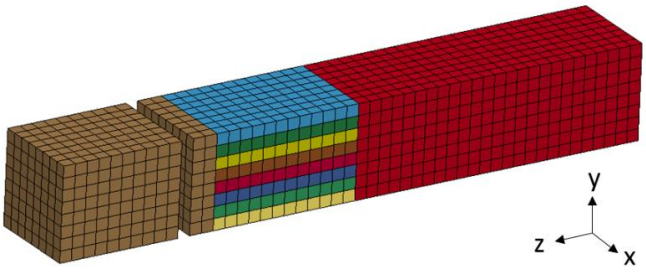

Figure 6.4.8 Plate impact test model in fibre direction

Due to different layer orientations, the stress traces at the front and at the back were averaged from the four front and back elements of the target. The experimental stress trace from the front gauge was not available because of the front gauge failure. Thus, simulation results were only compared against the back-surface stress trace. Initially, linear elastic material model was simulated (material input parameters can be found in Table 6.4.3). The linear elastic behaviour was modelled by setting the modal damage initiation energies to high values. The back-surface stress is presented in Figure 6.4.9. In general, the simulation results match the experimental results well. The stress rise was steep and its magnitude was only slightly overestimated. The simulation stress signal was longer than the experimental one.

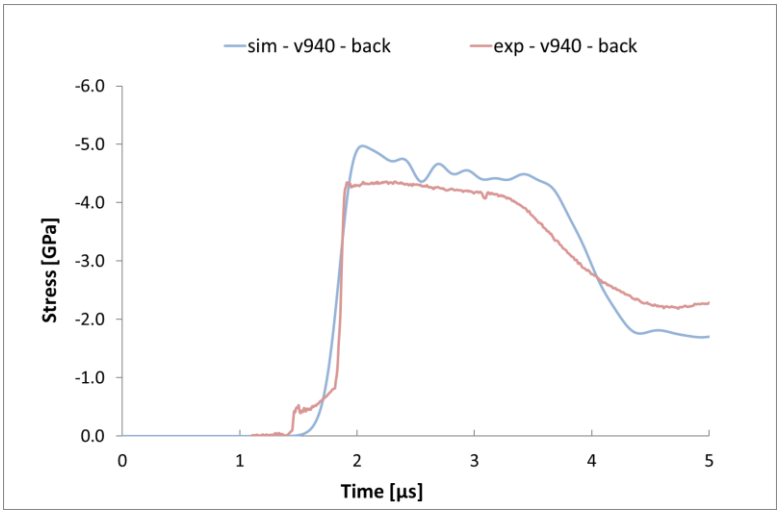

Figure 6.4.9 Back surface stress for plate imact test with linear elastic woven material

After setting the energy thresholds (ω) to the values given in Table 6.4.4, material strengths seem to be slightly underestimated (Figure 6.4.10). Moreover, stress starts to drop down quite early and rapidly in comparison to the experimental results.

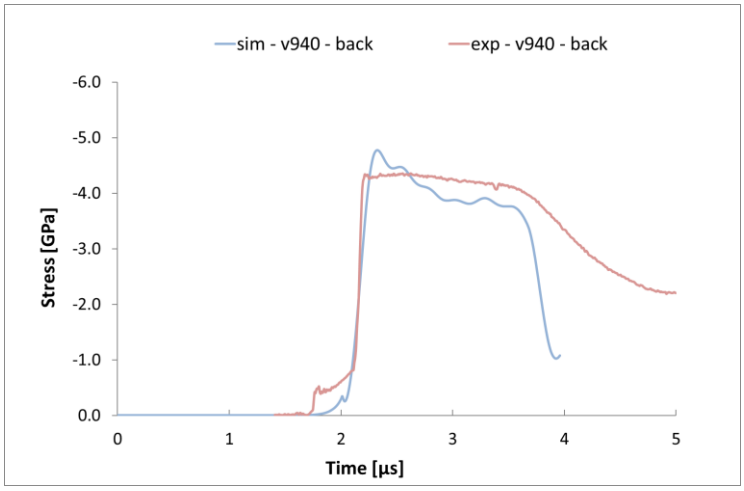

Figure 6.4.10 Back surface stress for plate imact test with woven material with nonzero hardening constants

The third case investigated in the fibre direction plate impact test was damage with hardening with input parameters given in Table 6.4.5.

Table 6.4.5 Input parameters for woven composite for plate impact test in fibre direction

GPa / [-]		MJ/m³		[-]		MJ/m³	
E_x	10.0	ω_0^I	36.5	d_{cr}^I	1.0	κ^I	73.0
$E_y = E_z$	68.5	ω_0^{II}	16.0	d_{cr}^{II}	1.0	κ^{II}	32.0
G_{yz}	4.57	ω_0^{III}	6.3	d_{cr}^{III}	1.0	κ^{III}	12.6
$G_{zx} = G_{xy}$	3.57	ω_0^{IV}	3.1	d_{cr}^{IV}	1.0	κ^{IV}	6.2
ν_{yz}	0.039	ω_0^V	2.1	d_{cr}^V	1.0	κ^V	4.2
$\nu_{zx} = \nu_{xy}$	0.045	ω_0^{VI}	3.1	d_{cr}^{VI}	1.0	κ^{VI}	6.2

Following the analysis from Section 6.3.7 damage evolution variable can attain values between two to five of the damage threshold value. In this case value of two was chosen for all the modes. Figure 6.4.11 shows the results of the stress trace obtained in the simulations compared against the experimental curve. It is evident, that these results follow the experimental curve well. The stress rise is steep and stress plateau has excellent agreement in terms of stress level. The only part that does not follow the experiments as well is the stress drop, which starts earlier in the simulations (around 3.3 μs) comparing to the experiments (3.6 μs).

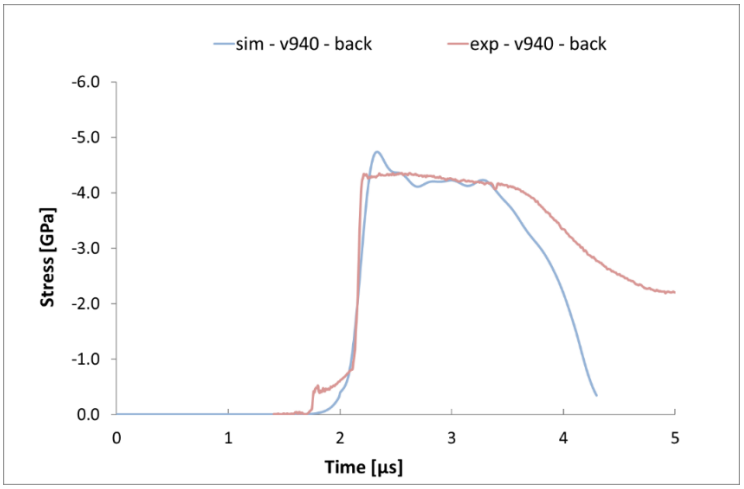

Figure 6.4.11 Back surface stress for plate imact test with woven material with nonzero hardening constants

In general, it can be concluded that the proposed model has the capability of modelling fibre direction plate impact test accurately.

6.4.3 Hard projectile impact

Another test that was used for the model validation was a hard projectile impact test. The test consists in firing a small steel sphere against a target panel. The sphere penetrates the panel generating a crater. Although, the craters dimensions are close to the spheres it was observed in experiments (e.g. (Vignjevic, Djordjevic and de Vuyst, 2012) and (Hazell et al., 2009)) that damage in the target is not contained to the crater. It propagates through the panel in the form of delamination, matrix or even fibre damage. The extent of damage in the composites after a sphere impact was investigated by Hazell *et al.* (2009), and thus, the same panel dimensions and layup was used in the simulation to assure the best results comparison.

The hard projectile test model was generated. The panel was a 6 mm thick, 16 layer woven composite laminate with asymmetric layup given in Figure 6.4.12. The full panel was modelled (dimensions 200 mm x 200 mm x 6 mm) with each of 16 layers being modelled with 200 x 200 x 1 elements. The resulting element size was 1 mm x 1 mm x 0.37 mm. The sphere was modelled with butterfly mesh with 2432 elements using Johnson Cook material model (steel properties taken from (Steinberg, 1996)). Initial velocity of the sphere was 1200 m/s.

a) b)

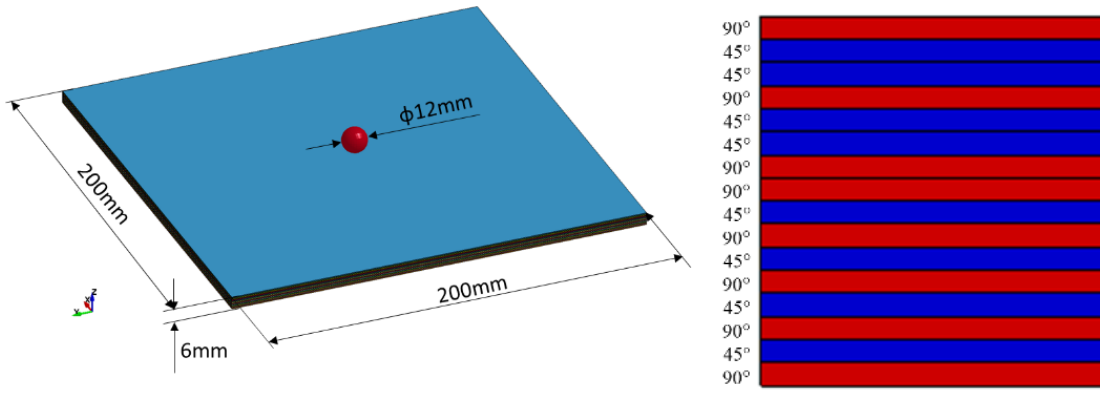

Figure 6.4.12 Hard projectile test: a) full model, b) material layup – red 0/90 layer, blue 45 layer

The same set of elastic and damage properties was used as in the plate impact test (see Table 6.4.5) but for the critical damage variables. The critical damage was allowed and the critical damage variables were chosen following the analysis in Section 6.3.7 to be: $d_{cr}^{I} = d_{cr}^{II} = 0.3$, $d_{cr}^{III} = 0.5$ and $d_{cr}^{IV} = d_{cr}^{V} = d_{cr}^{VI} = 0.7$. For consistency the full data set is given in Table 6.4.6.

Table 6.4.6 Input parameters in hard projectile impact simulations

GPa / [-]		MJ/m³		[-]		MJ/m³	
E_x	10.0	ω_0^I	36.5	d_{cr}^I	0.3	κ^I	73.0
$E_y = E_z$	68.5	ω_0^{II}	16.0	d_{cr}^{II}	0.3	κ^{II}	32.0
G_{yz}	4.57	ω_0^{III}	6.3	d_{cr}^{III}	0.5	κ^{III}	12.6
$G_{zx} = G_{xy}$	3.57	ω_0^{IV}	3.1	d_{cr}^{IV}	0.7	κ^{IV}	6.2
ν_{yz}	0.039	ω_0^V	2.1	d_{cr}^V	0.7	κ^V	4.2
$\nu_{zx} = \nu_{xy}$	0.045	ω_0^{VI}	3.1	d_{cr}^{VI}	0.7	κ^{VI}	6.2

Contact between sphere and panel initiated at 0.2 μs. This was calculated analytically given the sphere offset and velocity, because the output print frequency was rather low, due to memory limit. The output was set to be printed every 1 μs which determines the time resolution in all simulation results (time step was less than 0.01 μs). The largest sphere diameter passed the bottom layer at time 12 μs, which resulted in the sphere losing contact with all not fully damaged elements. Elements in the last layer were not removed. However, this is not a major problem. As stated before, element deletion was only introduced to avoid computational problems associated with poor element Jacobian. Elements of concern reached the critical damage and thus do not introduce any stress into the calculations. The sphere top passed the bottom layer at time 16 μs.

a) t=0 μs b) t=16 μs

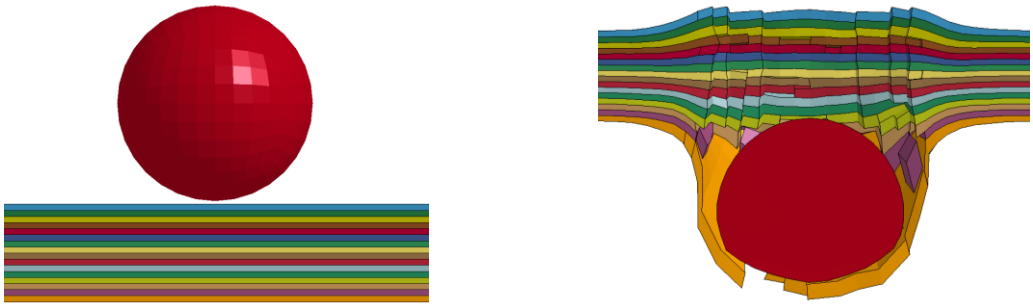

Figure 6.4.13 Panel and sphere at: a) t=0μs, b) t=16μs

The most interesting part of the results is the analysis of damage evolution and damage extent in the panel. There were six damage modes. Fibre-related modes (first and second) did not propagate far through the panel and they were contained close to the crater (Figure 6.4.14). The diameter of damage affected zone was 26 mm in the first layer and 22 mm in the middle (eighth) layer for the first mode. Damage distribution obtained at the back of the target panel (bottom layer in Figure 6.4.14) did not vary much from the front (top layer in Figure 6.4.14). In the second mode a diameter of the damage affected zone was 31 mm in the top layer (similar in the bottom layer) and 22 mm, in the middle layer (Figure 6.4.14 - b).

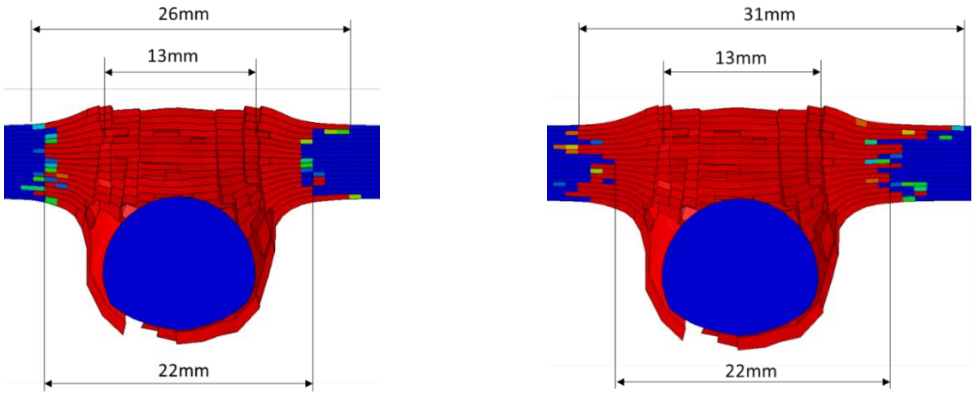

Figure 6.4.14 Damage affected zone in the: a) first mode, b) second mode in the XZ crossection

The third mode, related to matrix damage was more severe. Damage extent in the first layer reached 39 mm, in the middle layer 25 mm and 29 mm in the bottom layer (Figure 6.4.15). The characteristic hourglass shape of damage is evident just like in the first and second modes.

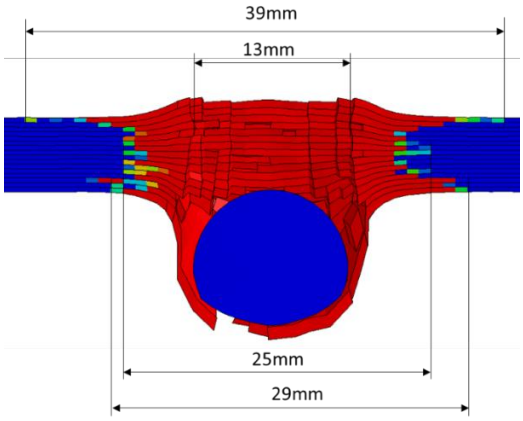

Figure 6.4.15 Damage affected zone in the third mode in the XZ cross-section

The remaining three modes are the shear modes of which the fifth mode was expected to behave differently as it is the only in-plane shear mode and it is not related to the impact (and through thickness) direction. Note that Dyna3D mode numbering convention was used here.

In the fourth mode damage extent in the first layer was 71 mm, in the eighth layer 32 mm and 61 mm in the last layer as presented in Figure 6.4.16.

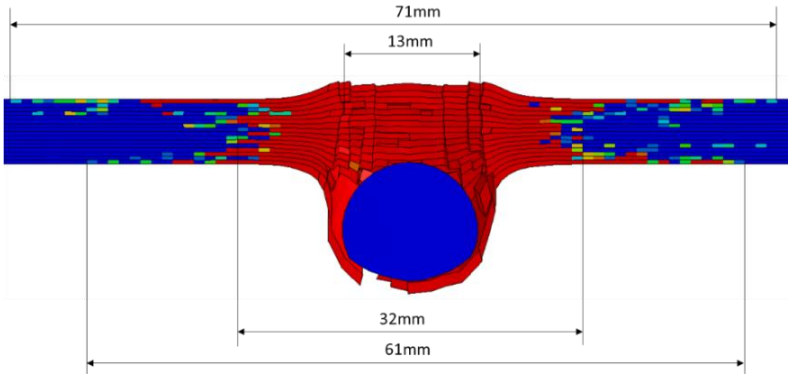

Figure 6.4.16 Damage affected zone in the fourth mode in the XZ cross-section

In the fifth mode damage extent in the first layer was 46 mm, in the middle layer 26 mm and in the bottom one 36 mm. Note that in this mode the layer direction clearly affects damage diameter which can be observed in Figure 6.4.17. It is evident that layers in which fibres are aligned with X and Y directions (red) develop more damage than the layers oriented at the 45° angle (blue).

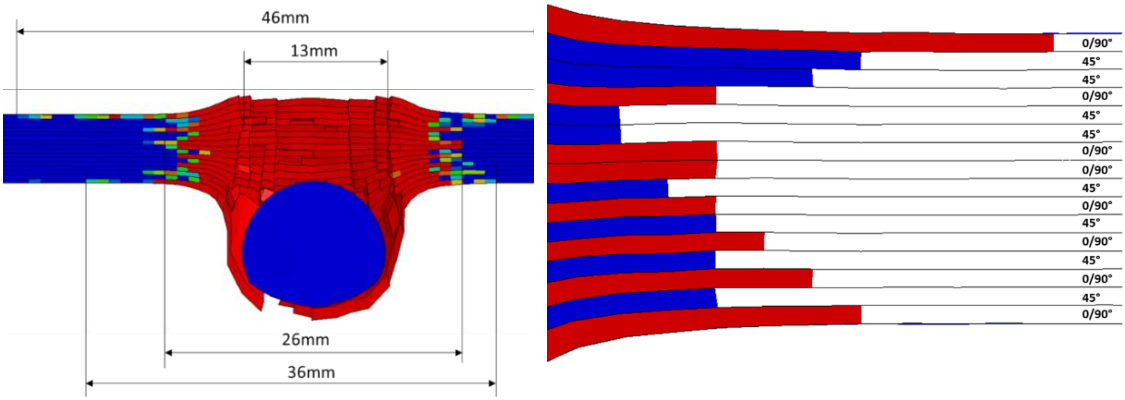

Figure 6.4.17 Damage affected zone in the fifth mode in the XZ cross-section

Damage in the sixth mode was slightly smaller than the damage in the fourth mode (Figure 6.4.18). The highest damage was found in the first layer. Its diameter reached 54 mm. The middle layer damage was 35 mm and the bottom one 47 mm.

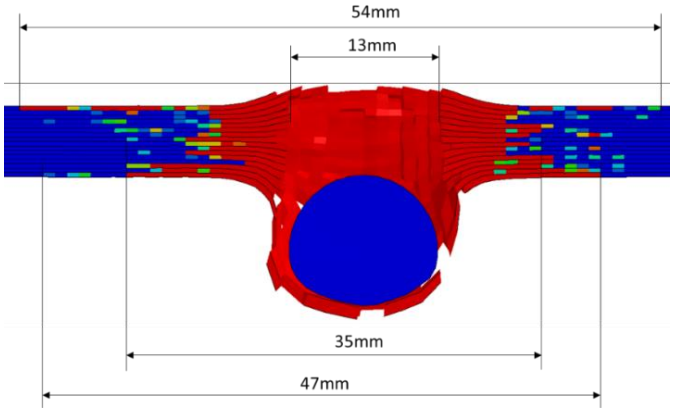

Figure 6.4.18 Damage affected zone in the sixth mode in the YZ cross-section

The results can be compared to the experimental results of the similar material (woven composite 12 mm in thickness) reported by Vignjevic, Djordjevic and de Vuyst (2012) presented in Figure 6.4.19. The figure shows the front and rear sides of the panel after impact.

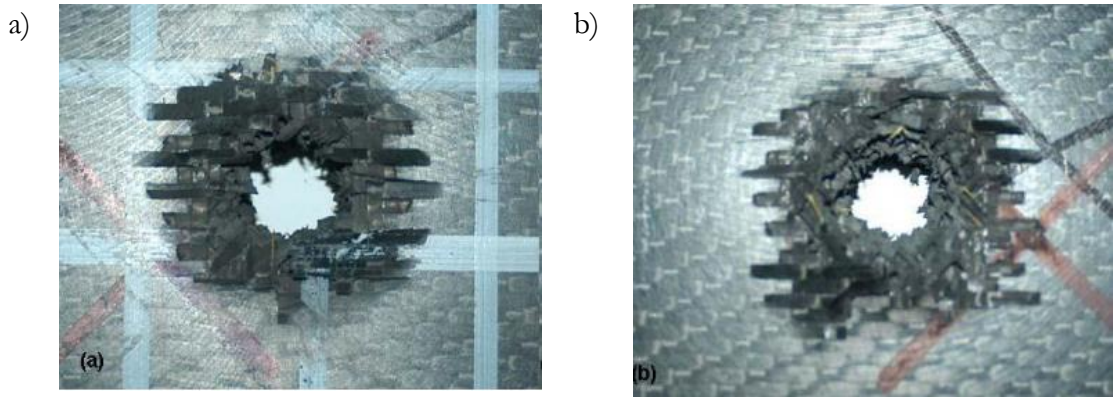

Figure 6.4.19 Distribution of damage in 12mm thickness woven composite impcated by 12mm sphere at 1219m/s: a) impact and b) rear face (Vignjevic, Djordjevic and de Vuyst, 2012)

There is a clear fibre failure on the both sides of the panel that are similar in size and shape to the first and second mode of damage presented in Figure 6.4.20.

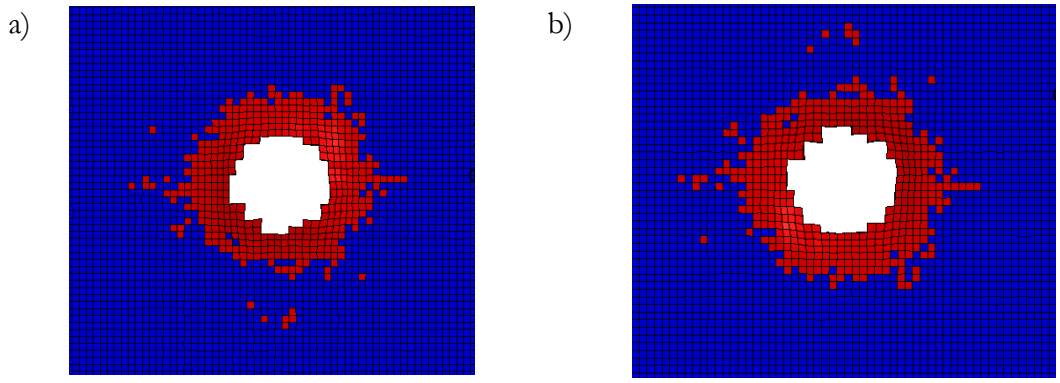

Figure 6.4.20 Distribution of the second damage mode in simulations: a) impact and b) rear face

According to Vignjevic, Djordjevic and de Vuyst (2012) delamination measured by C-scan ultrasonography in the experiments was between 35 mm and 43 mm in the front layers and between 41 mm and 45 mm in rear layers. The simulation results in shear modes varied from 46 mm and 71 mm in front layer to 36 mm and 61 mm for rear layers. It seems that the material model slightly overestimates damage in the panel. However, it is not clear that all of these damage modes can be correctly captured by the C-scan.

If the basic delamination modes are considered: opening mode, shearing mode and tearing mode (not to be confused with deformation eigenmodes), only the opening mode might be captured by the C-scan as shearing and tearing modes may not give any layer separation. The two latter delamination modes are likely to occur under the models' damage modes IV

and VI. Delamination in the opening mode can be reflected by model mode III, which is matrix mode for which damage in the front layers reached 39 mm and in the back 29 mm.

Comparing to experimental results obtained by Hazell *et al.* (2009) the model predicts matrix damage accurately. Delamination and matrix damage reported therein reached 20 mm in radius (Figure 6.4.21) whereas damage diameter in the matrix related mode III in simulation reached 39 mm.

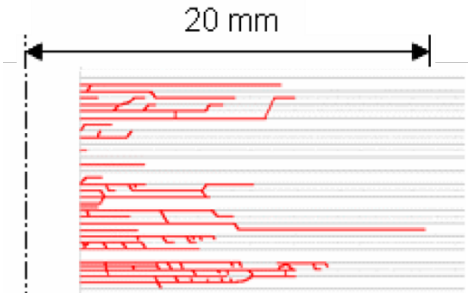

Figure 6.4.21 Matrix damage extent in hard projectile test in experiment by Hazell *et al.* (2009)

Analysis of damage evolution revealed that with progressing time damage started to evolve more unstably. It is clearly visible in Figure 6.4.22. Up to time t=16 μs damage evolved continuously Figure 6.4.22 - a). For time 20 μs significant amount of scatter (single damaged elements) can be observed around the continuous damage zone Figure 6.4.22 - b).

a) t = 16 μs b) t = 20 μs

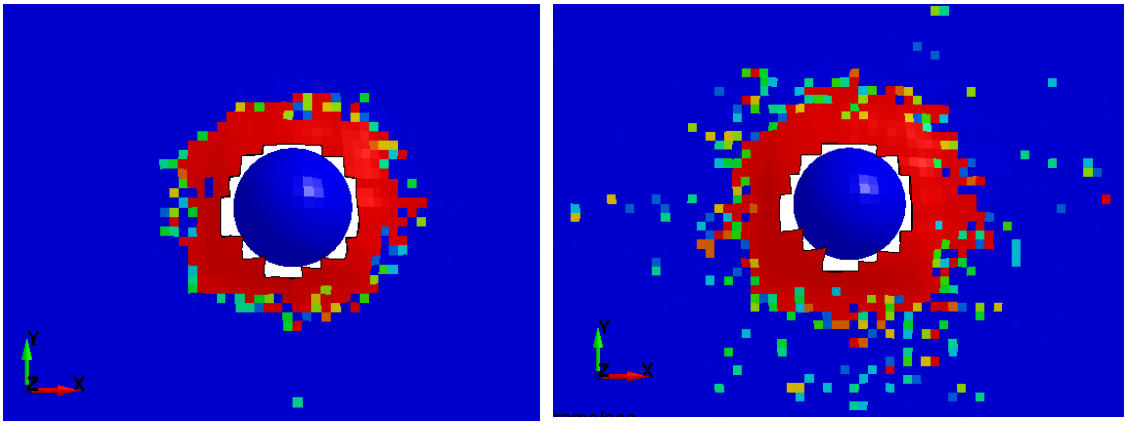

Figure 6.4.22 Damage in the first layer in the first mode for: a) t=16μs, b) t=20μs

It is worth noticing that stresses reach the boundaries of the panel roughly in 20 μs for all layers. Therefore, for simulation time exceeding 20 μs it is possible that the boundary conditions of the model affect the results by introducing additional stresses.

The sudden increase in the damage diameter is well captured in Figure 6.4.23. The graph shows the damage diameter as a function of time. Damage diameter was measured in the

first layer in XZ cross-section by checking for the most distant non-zero damage elements. It is clear that at the beginning damage evolution was stable. At time t_1=6 μs the sphere lost contact with the first layer which resulted in the slight change in damage evolution trend. Another noteworthy time is t_2=12 μs at which the sphere's largest diameter passed the bottom of the panel. After that point damage evolution should remain stable as there was no energy transferred into the panel. Around time t_3=20 μs there was a significant increase in the damage diameter. As it was commented before, this increase was attributed to reaching material boundaries.

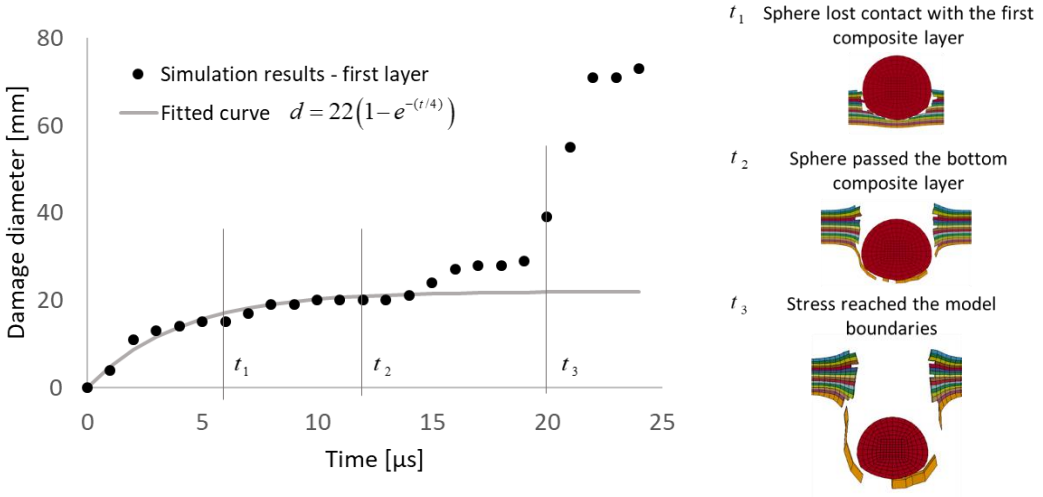

Figure 6.4.23 Simulations results of damage evolution in time for the first layer in the first mode

As this sudden increase of the damage extent hinders reliable measurement of the damage diameter a heuristic fit to the data (damage diameter vs time) was proposed as an attempt to effectively filter out numerical instabilities. Therefore, a function was fitted to the results in the range of sphere interaction with the panel (grey line in Figure 6.4.23). An exponential function was found to be most suitable for this purpose:

$$y = A\left(1-e^{-t/b}\right) \qquad 6.4.4$$

It allowed control of the function initial slope by time constant (b) as well as the asymptotic rise to certain value (A). It can be observed that a very good fit was achieved for the part of the function up to 15 μs. A similar analysis was carried out for the remaining modes. All the graphs are presented in Figure 6.4.24. The best fit was achieved for the first three modes. The fit for the shear modes seems a bit less accurate. One of the reasons might be the strong influence of neighbouring layers. Due to extremely large model each layer was modelled only

with one element in through thickness direction, which allowed for reasonable computational efficiency, but may have influenced the shear modes behaviour.

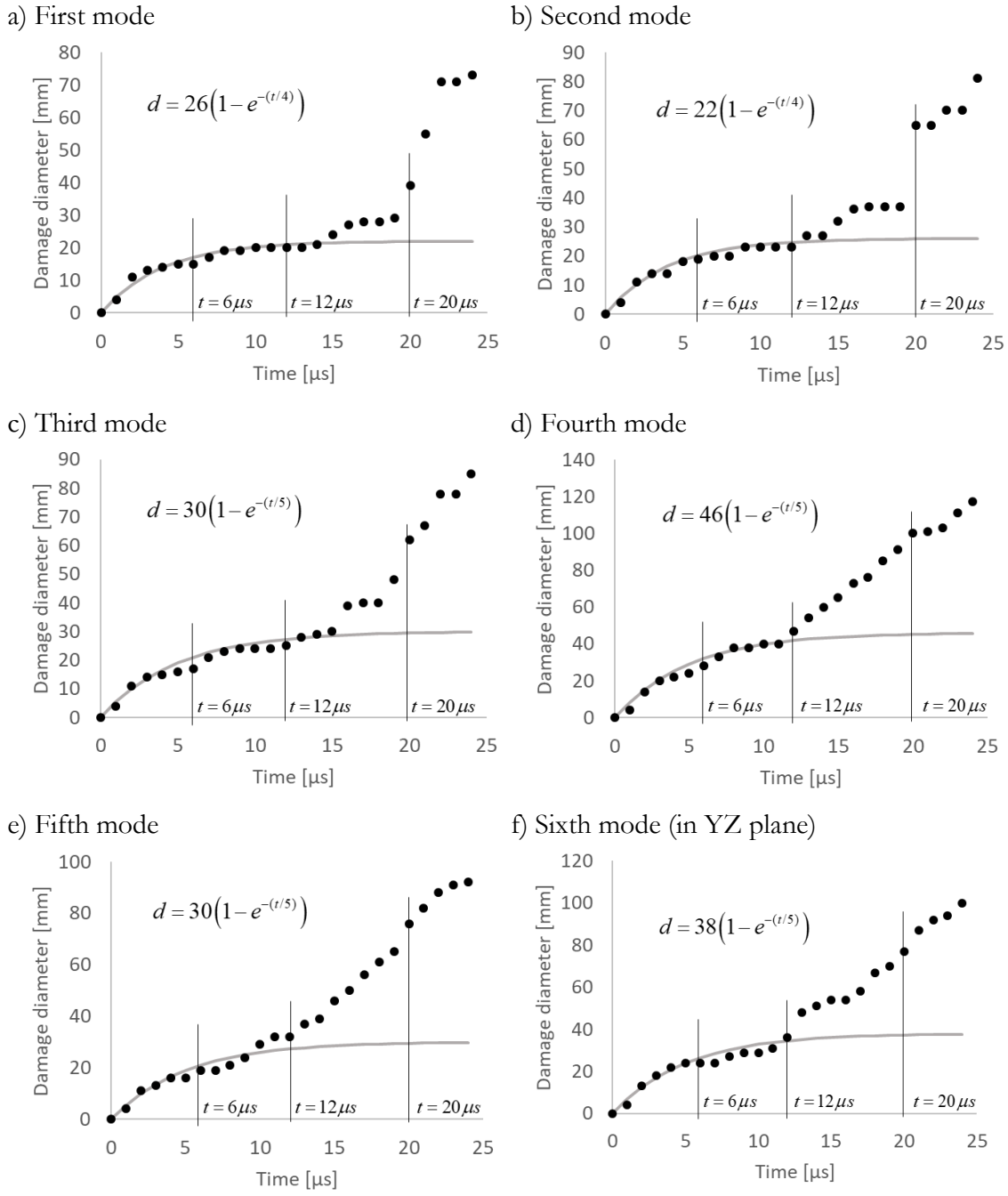

Figure 6.4.24 Damage evolution for the first layer in the: a) first, b) second, c) third, d) fourth, e) fifth, f) sixth mode

It is important to mention that the curve fitting parameter (A) is meaningful. It gives the damage diameter for an infinite time, so it can be treated as a maximum extent of damage in the mode (given stable damage growth). The similar analysis was carried out for the eighth

and the last layers (all the chosen layers had the same layer orientation). The curve fitting parameters are presented in Table 6.4.7 for selected layers.

Table 6.4.7 Fitting parameters (A) for modes for selected layers

Damage diameter	Layer 1	Layer 8	Layer 16
Mode I	22	22	30
Mode II	26	22	28
Mode III	30	25	30
Mode IV	46	30	30
Mode V	30	30	22
Mode VI	30	40	45

It can be observed, that the maximum extent of damage for different layers vary, however not significantly. In principle, the shear modes have higher parameters. It was expected, as these modes account for delamination (shearing mode and tearing mode) in the material, which has greater extent than other damage mechanisms in the material. Damage mode III may account for delamination opening mode as was mentioned before.

Figure 6.4.25 shows the comparison between damage extent measured from mechanical tests (Hazell *et al.*, 2009) and the overall damage from simulation results (highest damage disregarding the modes for the time assuring stable damage growth). The described experiments used exactly the same material along with the same composite layup as was assumed in the simulations, therefore direct comparison is possible.

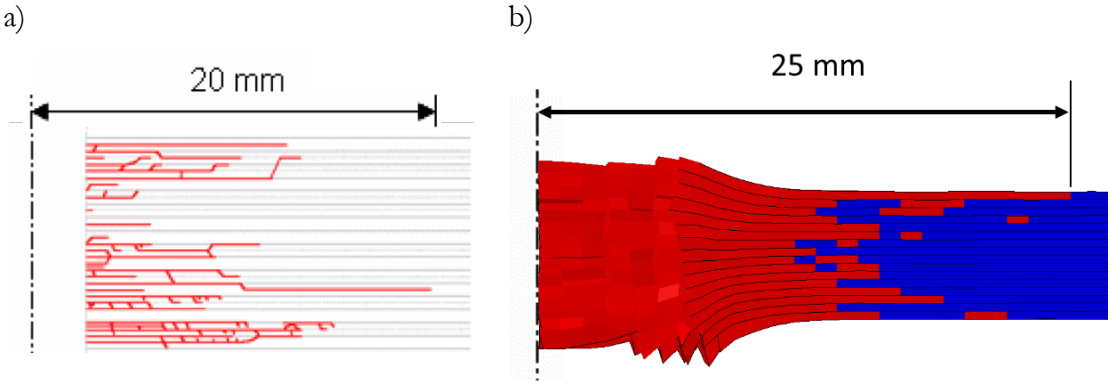

Figure 6.4.25 Comparison between damage extent in: a) experiment by Hazell et al. (2009) and b) simulation

The first thing to observe in Figure 6.4.25 - a) is that there is a large amount of scatter in damage diameter between the layers. This may be due to imperfections, that lead to higher damage evolving in some layers. It can also be stated that generally middle layers were less affected, however some of them still developed significant amount of damage. The highest

damage extent in the material reached 20 mm in experiments. The simulations predicted 25 mm as the highest damage extent in the chosen cross-section. Note that there was some randomness in damage in the middle layers, but the general trend of more severe damage being located close to the top and the bottom of the panel was preserved.

Concluding, the material model has the capability to accurately predict damage in the material due to high velocity impact. There are some stability issues that were presumably caused by the coupling with equation of state (building up the numerical error coming from the pressure vector) and introduced by boundary conditions. Nevertheless, up to the point of sphere exiting the panel, the model behaviour is stable, with stable damage growth. Damage extent seems reasonable, and could be significantly improved with reliable material characterisation tests that would allow to determine model input parameters accurately. The model distinguishes between damage modes that can be easily linked to different damage mechanisms such as fibre tensile damage (modes I and II), fibre compressive damage (mode II), matrix damage or opening mode of delamination (mode III), intralaminar shear (mode V) and shearing and tearing delamination (modes IV and VI).

6.5 Theoretical model with mode interaction

The material model presented in Section 6.1 was developed at continuum scale without looking at the influence of the combined mode loading on the material constituents. Analysis carried out in Section 5.3 revealed that combination of the modes leads to an increased stress levels within the fibres and matrix. This does not violate the existence of the non-interacting modes of strain energy at continuum level. However, it may lead to increase or decrease in the modal limit energy subject to the existence of the other modes. Such an approach was adopted in the second version of the model. The limit energy was defined as a function of the strain in the other modes:

$$\omega^i = \omega^i\left(\varepsilon^j\right) \qquad \textbf{6.5.1}$$

The exact forms of interactions were defined for a combination of the first three modes analytically in the subsequent sections. Moreover, they were compared against the simulation results. Note that this section describes the mode interaction for unidirectional composite, as this was the one investigated in simulations and initially derived. In following sections only interaction between first three modes is considered as an example. Nevertheless, the analysis

can be expanded in future to account for interactions with the shear modes. The implementation of the model proposed in this section lies beyond the scope of this work. It is however the suggested extension that can be applied to improve the basic model.

6.5.1 Fibre related modes interaction

The first mode was identified as a leading fibre mode. The longitudinal fibre stress generated by the first mode is dominant; however, the third mode also weakly affects it. As a consequence, the limit energy in the first (fibre) mode (ω^I) can be defined as a function of the strain in the third mode (ε^{III}):

$$\omega^I = \omega^I\left(\varepsilon^{III}\right). \qquad \textbf{6.5.2}$$

The longitudinal strain in fibres is the strain associated with X direction. Therefore, it is affected by the first components (X components) of the modal strain vectors (Table 6.5.1).

Table 6.5.1 Modal strain vectors of transversely isotropic material

Modal strain vectors $(\alpha = 22.73, \beta = -0.09)$	
$\boldsymbol{\varepsilon}^I = \frac{1}{\sqrt{2+\alpha^2}}\left[\alpha \quad 1 \quad 1 \quad 0 \quad 0 \quad 0\right]^T \varepsilon^I$	$\boldsymbol{\varepsilon}^{II} = \frac{1}{\sqrt{2}}\left[0 \quad -1 \quad 1 \quad 0 \quad 0 \quad 0\right]^T \varepsilon^{II}$
$\boldsymbol{\varepsilon}^{III} = \frac{1}{\sqrt{2+\beta^2}}\left[\beta \quad 1 \quad 1 \quad 0 \quad 0 \quad 0\right]^T \varepsilon^{III}$	$\boldsymbol{\varepsilon}^{IV} = \left[0 \quad 0 \quad 0 \quad 1 \quad 0 \quad 0\right]^T \varepsilon^{IV}$
$\boldsymbol{\varepsilon}^V = \left[0 \quad 0 \quad 0 \quad 0 \quad 1 \quad 0\right]^T \varepsilon^V$	$\boldsymbol{\varepsilon}^{VI} = \left[0 \quad 0 \quad 0 \quad 0 \quad 0 \quad 1\right]^T \varepsilon^{VI}$

As only first and third eigenstrains have non-zero first components $(\varepsilon_1^I, \varepsilon_1^{III})$ it can be concluded that these are the only modes affecting longitudinal fibre strain. The components of modal strains are proportional to the total modal strain magnitude, so the effective longitudinal strain is expressed by:

$$\varepsilon^f = \varepsilon_1^I + \varepsilon_1^{III} = \frac{\alpha}{\sqrt{\alpha^2+2}}\varepsilon^I - \frac{2}{\sqrt{2\alpha^2+4}}\varepsilon^{III}. \qquad \textbf{6.5.3}$$

If the fibres strength is characterised by a critical longitudinal strain ε_{cr}^f the failure of the fibres occurs when:

$$\varepsilon^f \geq \varepsilon_{cr}^f. \qquad \textbf{6.5.4}$$

The critical strain in the first mode can be defined as a function of the strain in the third mode by combining Equations 6.5.3 and 6.5.4:

$$\varepsilon_{cr}^{I} = \frac{\sqrt{\alpha^2 + 2}\varepsilon_{cr}^{f} + \sqrt{2}\varepsilon^{III}}{\alpha}. \qquad \textbf{6.5.5}$$

Limit energy and the critical strain are related by equating damage potential (introduced in Equation 6.1.29) to zero:

$$\Phi^{I}\left(\boldsymbol{\varepsilon}, d^{I}=0, h^{I}=0\right) = \lambda_0^{I}\varepsilon_{cr}^{I2} - \omega^{I} = 0, \qquad \omega^{I} = \lambda_0^{I}\varepsilon_{cr}^{I2}. \qquad \textbf{6.5.6}$$

In case of the investigated material $(\alpha = 22.73)$ the limit energy (ω^{I}) is:

$$\begin{aligned} \omega^{I} = \lambda_0^{I}\varepsilon_{cr}^{I2} = \lambda_0^{I}\left(\frac{\sqrt{\alpha^2+2}\varepsilon_{cr}^{f} + \sqrt{2}\varepsilon^{III}}{\alpha}\right)^2 \approx \\ = \lambda_0^{I}\varepsilon_{cr}^{f2} + 0.125\lambda_0^{I}\varepsilon_{cr}^{f}\varepsilon^{III} + 0.004\lambda_0^{I}\varepsilon^{III2} = \\ = \omega_0^{I} + 0.125\lambda_0^{I}\varepsilon_{cr}^{f}\varepsilon^{III} + 0.004\lambda_0^{I}\varepsilon^{III2}, \end{aligned} \qquad \textbf{6.5.7}$$

where $\lambda_0^{I}\varepsilon_{cr}^{f2}$ is equal to the limit energy of the first mode identified before as ω_0^{I}. The limit energy can increase or decrease depending on the sign of the third mode strain (signs were assigned arbitrarily and are used consistently). Note that the influence of the third mode on the first mode is weak. Unless the first mode strain is significantly lower than the third mode one this influence can be practically neglected leaving the first mode in the form unchanged from the initial formulation (repeated Equation 6.1.29):

$$\Phi^{I}\left(\boldsymbol{\varepsilon}, d^{I}, h^{I}\right) = \left(1 - d^{I}\right)\lambda_0^{I}\varepsilon^{I2} - \kappa^{I}h^{I} - \omega_0^{I} = 0. \qquad \textbf{6.5.8}$$

6.5.2 Matrix related modes interaction

Matrix itself is an isotropic material. Therefore, analytical considerations of matrix related modes interactions started by analysis of a stress state in an isotropic, homogeneous matrix subjected to deformation modes characteristic of a transversely isotropic material (Section 5.1.1). For isotropic materials there are only two distinct strain energy modes – volumetric and deviatoric. The purpose of this study was to define the relation between the isotropic and transversely isotropic deformation modes. The strain driven model is a great advantage in this case. The stress in the pure matrix and matrix in the presence of fibres

would vary only slightly because of the local influence of the microstructure. The strain tensors for the single modes are given by:

$$\boldsymbol{\varepsilon}^{I} = \frac{1}{\sqrt{\alpha^2+2}}\begin{bmatrix}\alpha & 1 & 1 & 0 & 0 & 0\end{bmatrix}^T \varepsilon^{I} = \begin{bmatrix}\alpha\varepsilon_2^{I} & \varepsilon_2^{I} & \varepsilon_2^{I} & 0 & 0 & 0\end{bmatrix}^T,$$

$$\boldsymbol{\varepsilon}^{II} = \frac{1}{\sqrt{2}}\begin{bmatrix}0 & -1 & 1 & 0 & 0 & 0\end{bmatrix}^T \varepsilon^{II} = \begin{bmatrix}0 & -\varepsilon_2^{II} & \varepsilon_2^{II} & 0 & 0 & 0\end{bmatrix}^T, \qquad \textbf{6.5.9}$$

$$\boldsymbol{\varepsilon}^{III} = \frac{1}{\sqrt{4+2\alpha^2}}\begin{bmatrix}-2 & \alpha & \alpha & 0 & 0 & 0\end{bmatrix}^T \varepsilon^{III} = \begin{bmatrix}\frac{-2}{\alpha}\varepsilon_2^{III} & \varepsilon_2^{III} & \varepsilon_2^{III} & 0 & 0 & 0\end{bmatrix}^T,$$

where ε^i denotes a modal strain magnitude. Equations above are given in terms of the second elements of the total strain vector for the sake of convenience. The volumetric strains of matrix subjected to the first three (transversely isotropic) modes are calculated following Equation 3.5.2 as:

$$\varepsilon_v^{I} = \frac{\alpha+2}{3}\varepsilon_2^{I}, \qquad \varepsilon_v^{II} = 0, \qquad \varepsilon_v^{III} = \frac{2\alpha-2}{3\alpha}\varepsilon_2^{III}. \qquad \textbf{6.5.10}$$

Note that the volumetric strain magnitude is proportional to the total modal strain magnitude. Deviatoric strain vectors, which are also proportional to the total strain magnitude, are defined as:

$$\boldsymbol{\varepsilon}_d^{I} = \frac{(1-\alpha)}{3}\begin{bmatrix}-2 & 1 & 1 & 0 & 0 & 0\end{bmatrix}^T \varepsilon_2^{I},$$

$$\boldsymbol{\varepsilon}_d^{II} = \begin{bmatrix}0 & -1 & 1 & 0 & 0 & 0\end{bmatrix}^T \varepsilon_2^{II}, \qquad \textbf{6.5.11}$$

$$\boldsymbol{\varepsilon}_d^{III} = \frac{(2+\alpha)}{3\alpha}\begin{bmatrix}-2 & 1 & 1 & 0 & 0 & 0\end{bmatrix}^T \varepsilon_2^{III}.$$

It is worth noticing that the deviatoric strain vectors defined from the first and third modes are mutually collinear and perpendicular to the third mode deviatoric strain. The magnitude of deviatoric strains can be calculated as the square root of the vectors dot product given by Equation 6.5.12:

$$\varepsilon_d^{I} = \sqrt{\boldsymbol{\varepsilon}_d^{I}\cdot\boldsymbol{\varepsilon}_d^{I}} = \sqrt{\tfrac{2}{3}}(\alpha-1)\left|\varepsilon_2^{I}\right|,$$

$$\varepsilon_d^{II} = \sqrt{\boldsymbol{\varepsilon}_d^{II}\cdot\boldsymbol{\varepsilon}_d^{II}} = \sqrt{2}\left|\varepsilon_2^{II}\right|, \qquad \textbf{6.5.12}$$

$$\varepsilon_d^{III} = \sqrt{\boldsymbol{\varepsilon}_d^{III}\cdot\boldsymbol{\varepsilon}_d^{III}} = \sqrt{\tfrac{2}{3}}\frac{\alpha+2}{\alpha}\left|\varepsilon_2^{III}\right|.$$

Therefore, deviatoric strain magnitudes are proportional to the total strain magnitude.

The combined mode strains are by definition the sums of modal strain vectors:

$$\boldsymbol{\varepsilon}^{I/II} = \boldsymbol{\varepsilon}^{I} + \boldsymbol{\varepsilon}^{II} = \left[\alpha\varepsilon_2^I \quad \varepsilon_2^I - \varepsilon_2^{II} \quad \varepsilon_2^I + \varepsilon_2^{II} \quad 0 \quad 0 \quad 0\right]^T,$$

$$\boldsymbol{\varepsilon}^{II/III} = \boldsymbol{\varepsilon}^{II} + \boldsymbol{\varepsilon}^{III} = \left[-\frac{2}{\alpha}\varepsilon_2^{III} \quad \varepsilon_2^{III} - \varepsilon_2^{II} \quad \varepsilon_2^{III} + \varepsilon_2^{II} \quad 0 \quad 0 \quad 0\right]^T, \qquad \textbf{6.5.13}$$

$$\boldsymbol{\varepsilon}^{III/I} = \boldsymbol{\varepsilon}^{I} + \boldsymbol{\varepsilon}^{III} = \left[\alpha\varepsilon_2^I - \frac{2}{\alpha}\varepsilon_2^{III} \quad \varepsilon_2^I + \varepsilon_2^{III} \quad \varepsilon_2^I + \varepsilon_2^{III} \quad 0 \quad 0 \quad 0\right]^T.$$

The calculation of the volumetric part of combined strains reveals that they are simple sums of the volumetric parts of single mode strains:

$$\varepsilon_v^{I/II} = \frac{(\alpha+2)}{3}\varepsilon_2^I = \varepsilon_v^I,$$

$$\varepsilon_v^{II/III} = \frac{2\alpha-2}{3\alpha}\varepsilon_2^{III} = \varepsilon_v^{III}, \qquad \textbf{6.5.14}$$

$$\varepsilon_v^{III/I} = \frac{(\alpha+2)}{3}\varepsilon_2^I + \frac{2\alpha-2}{3\alpha}\varepsilon_2^{III} = \varepsilon_v^{III} + \varepsilon_v^I.$$

It follows, that the deviatoric part of the combined strain vectors is also a sum of the modal deviatoric strain vectors

$$\boldsymbol{\varepsilon}_d^{I/II} = \left[\tfrac{2}{3}(\alpha-1)\varepsilon_2^I \quad -\tfrac{1}{3}(\alpha-1)\varepsilon_2^I - \varepsilon_2^{II} \quad -\tfrac{1}{3}(\alpha-1)\varepsilon_2^I + \varepsilon_2^{II} \quad 0 \quad 0 \quad 0\right]^T$$

$$\boldsymbol{\varepsilon}_d^{II/III} = \boldsymbol{\varepsilon}_d^{II} + \boldsymbol{\varepsilon}_d^{III} =$$

$$= \left[-\frac{2(2+\alpha)}{3\alpha}\varepsilon_2^{III} \quad \frac{(2+\alpha)}{3\alpha}\varepsilon_2^{III} - \varepsilon_2^{II} \quad \frac{(2+\alpha)}{3\alpha}\varepsilon_2^{III} + \varepsilon_2^{II} \quad 0 \quad 0 \quad 0\right]^T \qquad \textbf{6.5.15}$$

$$\boldsymbol{\varepsilon}_d^{III/I} = \boldsymbol{\varepsilon}_d^{I} + \boldsymbol{\varepsilon}_d^{III} =$$

$$= \left[\frac{2(\alpha-1)}{\alpha}\varepsilon_2^I - \frac{2(2+\alpha)}{3\alpha}\varepsilon_2^{III} \quad \frac{-(\alpha-1)}{3}\varepsilon_2^I + \frac{(2+\alpha)}{3\alpha}\varepsilon_2^{III} \quad \ldots\right.$$

$$\left.\ldots\frac{-(\alpha-1)}{3}\varepsilon_2^I + \frac{(2+\alpha)}{3\alpha}\varepsilon_2^{III} \quad 0 \quad 0 \quad 0\right]^T$$

Note that only for the combination of modes I and III the transverse strains are equal. The deviatoric strain magnitudes for the combined modes are:

$$\varepsilon_d^{I/II} = \sqrt{\boldsymbol{\varepsilon}_d^{I/II} \cdot \boldsymbol{\varepsilon}_d^{I/II}} = \sqrt{\tfrac{2}{3}(\alpha-1)^2 \varepsilon_2^{I2} + 2\varepsilon_2^{II2}} = \sqrt{\varepsilon_d^{I2} + \varepsilon_d^{II2}},$$

$$\varepsilon_d^{II/III} = \sqrt{\boldsymbol{\varepsilon}_d^{II/III} \cdot \boldsymbol{\varepsilon}_d^{II/III}} = \sqrt{2\varepsilon_2^{II2} + \tfrac{2}{3}\frac{(2+\alpha)^2}{\alpha^2}\varepsilon_2^{III2}} = \sqrt{\varepsilon_d^{II2} + \varepsilon_d^{III2}}, \qquad \textbf{6.5.16}$$

$$\varepsilon_d^{III/I} = \sqrt{\boldsymbol{\varepsilon}_d^{III/I} \cdot \boldsymbol{\varepsilon}_d^{III/I}} = \left| \sqrt{\tfrac{2}{3}}(\alpha-1)\varepsilon_2^{I} - \sqrt{\tfrac{2}{3}}\frac{(\alpha+2)}{\alpha}\varepsilon_2^{III} \right| = \left| \pm\varepsilon_d^{I} \pm \varepsilon_d^{III} \right|.$$

The deviatoric strain magnitudes of modes I and III can be simply added to obtain the total deviatoric strain in the combined modes. This is a consequence of the collinearity of the deviatoric strains in those modes. On the other hand, mode II is perpendicular to both mode I and mode III. Therefore, the combined strain magnitude in those cases is a square root of the modal strain magnitude squares. Concluding, the matrix deviatoric strain in a composite can be expressed in terms of transversely isotropic material modes as:

$$\varepsilon_d^m = \sqrt{\left(\pm\varepsilon_d^I \pm \varepsilon_d^{III}\right)^2 + \left(\varepsilon_d^{II}\right)^2}, \qquad \textbf{6.5.17}$$

The signs in the mode III/I correspond to the signs arbitrarily assigned to the modes in this work. The above equations show the possibility of defining the distortional strain magnitude in matrix from the transversely isotropic modal strain magnitudes. If there is a limit in material's elastic energy of distortion (Hencky's interpretation of von Mises yield criterion (Hill, 1950)) it is expressed by:

$$W^d = \tfrac{1}{2}\lambda_d \varepsilon_d^2 = \tfrac{1}{2}\lambda_d \left(\left(\pm\varepsilon_d^I \pm \varepsilon_d^{III}\right)^2 + \left(\varepsilon_d^{II}\right)^2 \right) \le W_{cr}^d, \qquad \textbf{6.5.18}$$

where W^d is distortional (deviatoric) strain energy, λ_d is an eigenvalue of an isotropic material deviatoric mode, ε_d^2 is deviatoric strain, ε_d^I, ε_d^{II} and ε_d^{III} are deviatoric strains coming from the first, second and third mode of transversely isotropic material. It is important to highlight that by definition an eigenvalue of an isotropic material deviatoric mode equals to twice its shear modulus, which can be expressed as:

$$G^m = \tfrac{1}{2}\lambda_d. \qquad \textbf{6.5.19}$$

Consequently, Equation 6.5.18 can be rewritten as:

$$W^d = G^m \varepsilon_d^2 = G^m \left(\left(\pm \varepsilon_d^I \pm \varepsilon_d^{III} \right)^2 + \left(\varepsilon_d^{II} \right)^2 \right) \leq W_{cr}^d . \qquad \textbf{6.5.20}$$

In the previous chapters, the second mode was identified as the principal matrix damage mode. By transforming Equation 6.5.20 the critical strain in the second mode can be determined as:

$$\varepsilon_{cr}^{II} = \sqrt{\frac{W_{cr}^d}{G^m} - \left(\pm \varepsilon_d^I \pm \varepsilon_d^{III} \right)^2} . \qquad \textbf{6.5.21}$$

Note that the second mode is purely deviatoric, so $\varepsilon^{II} = \varepsilon_d^{II}$. Thus, the critical matrix distortional strain energy (W_{cr}^d) can be easily related to the critical stress obtained from the uniaxial tensile test. Therefore, it can be treated as material model's input parameter just like the shear modulus (G^m). The damage potential for the second mode (ignoring influence of the fourth mode) was defined previously as (6.1.29):

$$\Phi^{II} \left(\boldsymbol{\varepsilon}, d^{II}, h^{II} \right) = \left(1 - d^{II} \right) \lambda_0^{II} \varepsilon^{II\,2} - \kappa^{II} h^I - \omega_0^{II} = 0 . \qquad \textbf{6.5.22}$$

Thus, for the damage onset the limit energy is defined as (using Equation 6.5.21):

$$\omega^{II} = \lambda_0^{II} \varepsilon_{cr}^{II\,2} = \lambda_0^{II} \left(\frac{W_{cr}^d}{G^m} - \left(\pm \varepsilon_d^I \pm \varepsilon_d^{III} \right)^2 \right) = \lambda_0^{II} \frac{W_{cr}^d}{G^m} - \lambda_0^{II} \left(\pm \varepsilon_d^I \pm \varepsilon_d^{III} \right)^2 , \qquad \textbf{6.5.23}$$

where the threshold energy for a single second mode activated can be defined as:

$$\omega_0^{II} = \frac{\lambda_0^{II}}{G^m} W_{cr}^d . \qquad \textbf{6.5.24}$$

Deviatoric strains in the modes can be related to the total modal strains leading to the final form of the threshold energy (substituting Equations 6.5.12 into Equation 6.5.23):

$$\begin{aligned} \omega^{II} &= \frac{W_{cr}^d \lambda_0^{II}}{G^m} - \lambda_0^{II} \left(\pm \varepsilon_d^I \pm \varepsilon_d^{III} \right)^2 = \\ &= \lambda_0^{II} \frac{W_{cr}^d}{G^m} - \frac{\lambda_0^{II}}{3\left(\alpha^2 + 2 \right)} \left(\sqrt{2} \left(\alpha - 1 \right) \varepsilon^I + \left(\alpha + 2 \right) \varepsilon^{III} \right)^2 . \end{aligned} \qquad \textbf{6.5.25}$$

If the second mode strain equals to zero, the third mode becomes the principal matrix failure mode. Then, by rearranging Equation 6.5.18 and substituting Equations 6.5.12 the relation between strains and constants becomes:

$$\frac{W_{cr}^{d}}{G^{m}} = \frac{\left(\sqrt{2}(\alpha-1)\varepsilon^{I} + (\alpha+2)\varepsilon^{III}\right)^{2}}{3\left(\alpha^{2}+2\right)}. \qquad \textbf{6.5.26}$$

After further transformations it becomes:

$$\sqrt{\frac{3\left(\alpha^{2}+2\right)W_{cr}^{d}}{G^{m}}} = \left|\sqrt{2}(\alpha-1)\varepsilon^{I} + (\alpha+2)\varepsilon^{III}\right|. \qquad \textbf{6.5.27}$$

It leads to two solutions for the critical third mode strain ε_{cr}^{III}:

$$\varepsilon_{cr}^{III} = \begin{cases} \dfrac{1}{\alpha+2}\sqrt{\dfrac{3\left(\alpha^{2}+2\right)W_{cr}^{d}}{G^{m}}} - \dfrac{\sqrt{2}(\alpha-1)}{\alpha+2}\varepsilon^{I}, & \sqrt{2}(\alpha-1)\varepsilon^{I} + (\alpha+2)\varepsilon^{III} \geq 0 \\ -\dfrac{1}{\alpha+2}\sqrt{\dfrac{3\left(\alpha^{2}+2\right)W_{cr}^{d}}{G^{m}}} - \dfrac{\sqrt{2}(\alpha-1)}{\alpha+2}\varepsilon^{I}, & \sqrt{2}(\alpha-1)\varepsilon^{I} + (\alpha+2)\varepsilon^{III} < 0 \end{cases} \qquad \textbf{6.5.28}$$

Finally, the threshold energy in the third mode can be obtained by substituting the critical energy in Equation 6.5.29 by the critical strain from Equation 6.5.28:

$$\omega^{III} = \lambda_{0}^{III}\varepsilon_{cr}^{III\,2}. \qquad \textbf{6.5.29}$$

6.5.3 Effect of microstructure

In the previous section the matrix was analysed as a continuum homogeneous constituent. It was shown in Chapter 5 that the effective stress (and thus effective strain) was not uniform within the RVE. Existence of a microstructure introduces local variations in strains and stresses. The assumption that was adopted for simplification is that the microstructure changes elements of the (continuum) modal strain vector proportionally, which can be expressed by:

$$\boldsymbol{\varepsilon}_{micro}^{i} = m^{i}\begin{bmatrix}\varepsilon_{1}^{i} & \varepsilon_{2}^{i} & \varepsilon_{3}^{i} & 0 & 0 & 0\end{bmatrix} = m^{i}\boldsymbol{\varepsilon}^{i}, \qquad \textbf{6.5.30}$$

where $\boldsymbol{\varepsilon}^{micro}$ is a local strain vector accounting for microstructure influence and m^{i} is coefficient of proportionality.

Thus, the local deviatoric strain magnitude in the material under i-th deformation mode is proportional to the modal strain magnitude:

$$\tilde{\varepsilon}_d^i = z^i \varepsilon^i , \qquad \textbf{6.5.31}$$

where factor z^i accounts for the microstructure strain variation (m^i) but also includes terms that transform the total modal strain magnitude to distortional strain magnitude (depending on material constant α). The total local deviatoric strain in the material is therefore described by:

$$\tilde{\varepsilon}_d^{I/II/III} = \sqrt{\left(\tilde{\varepsilon}_d^I + \tilde{\varepsilon}_d^{III}\right)^2 + \tilde{\varepsilon}_d^{II\,2}} = \sqrt{\left(z^I \varepsilon^I + z^{III} \varepsilon^{III}\right)^2 + z^{II\,2} \varepsilon^{II\,2}} . \qquad \textbf{6.5.32}$$

For such an assumption the distortional strain energy in matrix can be expressed by:

$$W^d = G^m \tilde{\varepsilon}_d^2 = G^m \left(\left(z^I \varepsilon^I + z^{III} \varepsilon^{III}\right)^2 + z^{II\,2} \varepsilon^{II\,2}\right) \le W_{cr}^d . \qquad \textbf{6.5.33}$$

Consequently, the second mode critical strain can be defined as:

$$\omega^{II} = \lambda_0^{II} \varepsilon_{cr}^{II\,2} = \frac{\lambda_0^{II}}{z^{II\,2}} \left(\frac{W_{cr}^d}{G^m} - \left(z^I \varepsilon^I + z^{III} \varepsilon^{III}\right)^2 \right). \qquad \textbf{6.5.34}$$

In the absence of the second mode strain, the third mode becomes the principal matrix mode with the threshold energy:

$$\omega^{III} = \lambda_0^{III} \varepsilon_{cr}^{III\,2} = \frac{\lambda_0^{III}}{z^{III\,2}} \left(\frac{W_{cr}^d}{G^m} + z^{I\,2} \varepsilon^{I\,2} \pm 2 z^I \sqrt{\frac{W_{cr}^d}{G^m}} \varepsilon^I \right). \qquad \textbf{6.5.35}$$

6.5.4 Mode summation – mesoscale model check

The accuracy of the mode addition presented in the previous sections was checked against the mesoscale models' simulations. Maximum distortional strain magnitudes $\tilde{\varepsilon}_d^{sim}$ were obtained by averaging distortional strains for twenty critical elements. The analytical results were calculated using Equation 6.5.33. Coefficients z^i were determined from single mode simulation results by dividing nominal modal strains (ε^i) by maximum distortional strain magnitudes $(\tilde{\varepsilon}_d^{sim})$:

$$z^i = \frac{\varepsilon^i}{\tilde{\varepsilon}_d^{sim}} , \qquad \textbf{6.5.36}$$

Comparison between the analytical and simulation results is presented in Figure 6.5.1.

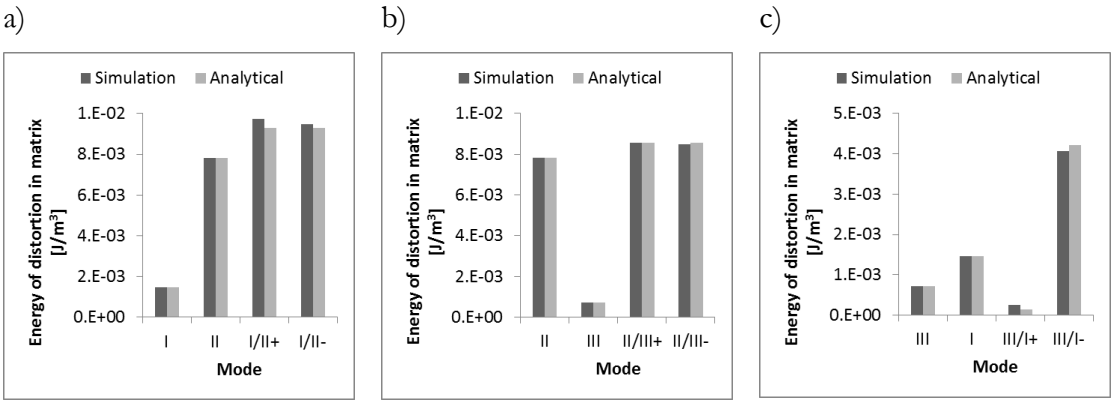

Figure 6.5.1 Comparison between the modal distortional energy obtained in simulations and calculated analytically for a) I/II modes, b) II/III modes, c) III/I modes

Note that the analytical results, although subjected to the number of simplifying assumptions, are very close to the simulation results for all loading cases. They are also much more accurate than the simple summation of the modal distortional energies. The closest match between the simulation and analytical results was obtained for modes II/III. The error did not exceed 1%. The discrepancy between the modes I/II reached 5% for mode I/II+ and 2% for mode I/II-. The error of mode III/I- was 4%. The highest difference was found for the mode III/I+, it reached 47%, but in this case the energies were subtracted. Therefore, although an absolute error was similar to III/I- case, relative error was much larger. The coefficients z^i obtained from the mesoscale model simulations were equal to:

$$z^I = 0.79, \qquad z^{II} = 1.83, \qquad z^{III} = 0.55. \qquad \textbf{6.5.37}$$

6.6 Summary

Two versions of the composite constitutive damage model were presented in this section. The first one is the basic version based on the spectral decomposition leading to identification of the non-interacting strain energy modes. The basic version of the model is a purely continuum approach without looking at the constituent stresses and strains. This version of the model was implemented in Dyna3D software.

Validation of the model was based on two dynamic test cases for which experimental data was available. These were plate impact tests and a hard projectile test. The former tested the EOS part and proved that the model can accurately predict the shock wave passage through the plate. It also revealed some issues related to coupling with EOS and determination of damage vector, that may be researched and developed further. The hard projectile test

showed that the model is capable of predicting damage in the panel. The six damage modes available can be linked to damage mechanisms such as fibre failure, matrix failure and different modes of delamination. Comparison with the experimental results showed that the damage was predicted accurately. The definite improvement may be achieved with more reliable material input data after the full material characterisation for this specific material model and possibly accounting for differences in tension and compression behaviour. Nevertheless, the current approach that used commonly available composite strengths to determine model input proved to be successful.

The extended version of the model was proposed. It accounts for the mesoscale stress interaction between the deformation eigenmodes by change in the limit energies in the modes. This version of the model has not yet been implemented.

7 Conclusions

The new composite damage constitutive model was developed, which was the principal aim of this work. The model was developed within the thermodynamic framework. State potentials are used to define the material's state and the state variables are rigorously determined based on thermodynamics laws. The foundation of the model was a spectral decomposition of the stiffness tensor. It allows the diagonalisation of the stiffness tensor and determination of the non-interacting strain energy (deformation) modes. The modes are specific to the material symmetry class and can be linked to damage mechanisms evolving in the material. In the case of transversely isotropic material, the first mode was identified as a fibre mode, modes II and IV as the isotropy plane shear modes, mode III as the matrix damage mode and modes V and VI as the fibre plane shear modes.

In this newly developed constitutive model, damage is associated with the deformation eigenmodes. Damage is assumed to occur if the strain energy in a mode exceeds a set limit. The proposed model is a progressive damage model in which damage evolution leads to degradation of the material principal stiffnesses (eigenvalues of the material stiffness tensor) corresponding to the damage modes. The principal stiffnesses degradation was modelled using continuum damage mechanics concepts – effective stress with strain energy equivalence hypothesis. Possibility of modelling different damage evolution behaviour was assured by defining the damage potential (included in the Helmholtz free energy). If no damage evolution energies are set, the model is a perfect damage model, i.e. limit energy of deformation remains constant with damage evolution. Otherwise, it can change depending on the sign of the hardening constant – either increase or decrease.

Model development was supported by a wide range of mesoscale model simulations which provided an insight into the material mesoscale behaviour. They led to formulation of the assumption that the eigensystem of a material remains unchanged with progressing damage. Furthermore, mesoscale models were used to determine modal threshold energies. Additionally, mechanical tests allowing extraction of threshold energies were proposed as a first step towards real-life application of the model.

The model was coupled with the EOS adapted for non-isotropic materials, which makes it applicable to dynamic load cases. It is a significant progress in composites modelling, as none

of the commercially available constitutive models has this capability. The Gruneisen EOS parameters were defined for unidirectional CFRP.

The model was validated against experimental data for composites with tetragonal symmetry by two mechanical tests – plate impact and hard projectile test. The model accurately predicted shock waves and damage extent in the material. Some instabilities of the model were observed at large times of simulation. Nevertheless, the analysis carried out allowed to determine damage extent before instabilities appear.

Below, the model summary is presented in bullet points to emphasize the most important aspects of this work. It includes: features of the developed model, novel aspects of this work and recommended future work.

Features of the composite model:

- Developed at continuum scale
- Applicable to transversely isotropic materials with hyperelastic behaviour
- Applicable to orthotropic materials (of tetragonal symmetry) with hyperelastic behaviour
- Capable of predicting of HVI response including shock wave modelling
- Rigorously derived in the framework of continuum thermodynamics with internal variables
- Energy based, physically justified damage initiation criteria – assuming that damage starts when the modal strain energy exceeds the limit value
- Scalar damage variables
- Damage affecting only the mode in which critical energy was exceeded (mode characteristic)
- Associative damage evolution
- Strain driven
- Relatively few, easy to determine input parameters

The novel aspects of this work include:

- Mesoscale modelling of damage – investigation of the influence of material damage mechanisms on its stiffness tensors and its eigenvalues and eigenvectors

- Investigation of the material mesoscale response to single and combined deformation mode loading
- Definition of the new transversely isotropic material damage initiation criteria that are based on the critical modal strain energy
- Linking damage variables with principal strain energy modes and definition of their conjugate forces
- Determination of the EOS parameters for the transversely isotropic CFRP material

The recommended future work is:

- Expanding the model to be applicable to wider range of materials (especially generally orthotropic)
- Adjusting the damage part of the model to differentiate between the tensile and compressive material failure
- Further work on coupling with EOS to assure stability and more accurate pressure prediction
- Implementation and validation of the extended model accounting for mode interaction
- Development of the method to investigate laminates using the spectral decomposition approach

Bibliography

Ahrens, T. J. and Johnson, M. L. (1994) *Shock wave data for minerals*. Wiley Online Library.

Anderson, C. E. *et al.* (1994) 'A constitutive formulation for anisotropic materials suitable for wave propagation computer programs—II', *Computational Mechanics*, 15(3), pp. 201–223.

Appleby-Thomas, G. J. and Hazell, P. J. (2012) 'The impact of structural composite materials. Part 2: hypervelocity impact and shock', *The Journal of Strain Analysis for Engineering Design*, 47(7), pp. 406–418.

Appleby-Thomas, G. J., Hazell, P. J. and Stennett, C. (2009) 'The variation in lateral and longitudinal stress gauge response within an RTM 6 epoxy resin under one-dimensional shock loading', *Journal of materials science*, 44(22), pp. 6187–6198.

Askeland, D., Fulay, P. and Wright, W. (2010) 'The Science and engineering of materials', *The Science and Engineering of Materials*, p. 949. doi: 10.1016/0921-5107(92)90012-X.

Betten, J. (1986) 'Applications of tensor functions to the formulation of constitutive equations involving damage and initial anisotropy', 25, pp. 573–584.

Betten, J. (1992) 'Applications of tensor functions in continuum damage mechanics', *International Journal of Damage Mechanics*, 1(1), pp. 47–59.

Boettger, J. C. (1994) *SESAME equation of state for epoxy*. Los Alamos National Lab., NM (United States).

Broughton, W. R., K, M. and Hull, D. (1990) 'Analysis of the Iosipescu Shear Test as Applied to Unidirectional Carbon-Fibre Reinforced Composites', 38, pp. 299–325.

Callen, H. B. (1998) 'Thermodynamics and an Introduction to Thermostatistics'. AAPT.

Carbon Fiber- All Patterns Explained (2015) *Carbon.Ee*. Available at: http://www.carbon.ee/en/n/carbon-fiber-all-patterns-explained (Accessed: 1 March 2017).

Cauvin, A. and Testa, R. B. (1999) 'Damage mechanics: basic variables in continuum theories', *International Journal of Solids and Structures*, 36(5), pp. 747–761.

Chaboche, J. L. (1988) 'Continuum damage mechanics: Part I—General concepts; Part II—Damage growth, crack initiation and crack growth', *J. appl. Mech.*, 55, pp. 59–72.

Chaboche, J. L., Lesne, P. M. and Maire, J. F. (1995) 'Continuum damage mechanics, anisotropy and damage deactivation for brittle materials like concrete and ceramic composites', *International Journal of Damage Mechanics*, 4(1), pp. 5–22.

Chang, F. and Chang, K.-Y. (1987) 'Laminated Composites Containing Stress Concentrations', *Journal of Composite Materials*, 21(September), pp. 834–855.

Cordebois, J. P. and Sidoroff, F. (1982) 'Damage induced elastic anisotropy', in *Mechanical Behavior of Anisotropic Solids/Comportment Méchanique des Solides Anisotropes*. Springer, pp. 761–774.

Cowin, S. C. and Mehrabadi, M. M. (1985) 'On the identification of material symmetry for anisotropic elastic materials', *Quarterly Journal of Mechanics and Applied Mathematics*, 40(Part 4), pp. 451–476.

Cowin, S. C. and Mehrabadi, M. M. (1992) 'The structure of the linear anisotropic elastic symmetries', *Journal of the Mechanics and Physics of Solids*, 40(7), pp. 1459–1471. doi: 10.1016/0022-5096(92)90029-2.

Cytec Engineered Materials (2012) 'Cycom 977-2 Epoxy Resin System', *Cytec - Engineered Materials*, pp. 1–4. Available at: https://www.cytec.com/sites/default/files/datasheets/CYCOM_977-2_031912.pdf%0Ahttp://www.cemselectorguide.com/pdf/CYCOM_977-2_031912.pdf.

Dattelbaum, D. M. and Coe, J. D. (2012) 'The dynamic loading response of carbon-fiber-filled polymer composites', in *Dynamic Deformation, Damage and Fracture in Composite Materials and Structures*. Elsevier, pp. 225–277.

Dávila, C. G. and Camanho, P. P. (2003) 'Failure criteria for FRP laminates in plane stress', *NASA TM*, 212663(613).

Dávila, C. G., Camanho, P. P. and Rose, C. A. (2005) 'Failure criteria for FRP laminates', *Journal of Composite materials*, 39(4), pp. 323–345.

Davison, L. and Graham, R. A. (1979) 'Shock compression of solids', *Physics Reports*, 55(4), pp. 255–379. doi: https://doi.org/10.1016/0370-1573(79)90026-7.

Djordjevic, N. (2011) *Modelling of Inelastic Behaviour of Orthotropic Materials Under Dynamic Loading Including High Velocity Impact*. Cranfield University.

Echaabi, J., Trochu, F. and Gauvin, R. (1996) 'Review of failure criteria of fibrous composite materials', *Polymer Composites*, 17(6), pp. 786–798. doi: 10.1002/pc.10671.

Fischer, F. D. and Svoboda, J. (2007) 'A Note on the Principle of Maximum Dissipation Rate', *Journal of Applied Mechanics*, 74(5), p. 923. doi: 10.1115/1.2722304.

Gama, B. A. (2015) 'User Manual: A Progressive Composite Damage Model For Unidirectional and woven fabric', (215). doi: 10.1021/ef100926v.

Gautam, P. C. *et al.* (2017) 'Determination of Hugoniot Elastic Limit (HEL) and Equation of State (EOS) of Ceramic Materials in the Pressure Region 20 GPa to 100 GPa', *Procedia Engineering*, 173, pp. 198–205.

Gitman, I. M. (2007) 'Representative volume : Existence and size determination', 74, pp. 2518–2534. doi: 10.1016/j.engfracmech.2006.12.021.

Gitman, I. M., Askes, H. and Sluys, L. J. (2007) 'Representative volume: existence and size determination', *Engineering fracture mechanics*, 74(16), pp. 2518–2534.

Hallquist, J. O. (2006) 'LS-DYNA theory manual', *Livermore software Technology corporation*. Livermore Software Technology Corporation, pp. 25–31.

Hansen, N. R. and Schreyer, H. L. (1994) 'A thermodynamically consistent framework for theories of elastoplasticity coupled with damage', *International Journal of Solids and Structures*, 31(3), pp. 359–389.

Hashin, Z. (1980) 'Failure criteria for unidirectional fiber composites', *Journal of applied mechanics*, 47(2), pp. 329–334.

Hazell, P. J. *et al.* (2009) 'Penetration of a woven CFRP laminate by a high velocity steel sphere impacting at velocities of up to 1875 m/s', *International Journal of Impact Engineering*, 36(9), pp. 1136–1142. doi: 10.1016/j.ijimpeng.2008.12.001.

Hazell, P. J., Stennett, C. and Cooper, G. (2008) 'The shock and release behavior of an aerospace-grade cured aromatic amine epoxy resin', *Polymer Composites*, 29(10), pp. 1106–1110.

Hazell, P. J., Stennett, C. and Cooper, G. (2009) 'The effect of specimen thickness on the shock propagation along the in-fibre direction of an aerospace-grade CFRP laminate',

Composites Part A: Applied Science and Manufacturing, 40(2), pp. 204–209. doi: https://doi.org/10.1016/j.compositesa.2008.11.002.

Hebda, M. (2006) 'Zastosowanie energetycznego kryterium wytężeniowego do analizy wytrzymałościowej kompozytów włóknistych', *Praca doktorska, Politechnika Krakowska, Kraków*.

Helbig, K. (1994) 'Chapter 11 Eigentensors of the elastic tensor and their relationship with material symmetry', in *Foundations of anisotropy for exploration seismics*. Pergamon,.

Van Hemelrijck, D. *et al.* (2008) 'Biaxial testing of fibre-reinforced composite laminates', *Proceedings of the institution of mechanical engineers, part L: Journal of Materials: Design and Applications*, 222(4), pp. 231–239.

Hexcel Corporation (2016) 'HexTow ® AS7 carbon fiber', pp. 1–2.

Hill, R. (1950) *The mathematical theory of plasticity*. Oxford university press.

Holzapfel, G. A. (2000) *Nonlinear solid mechanics*. Wiley Chichester.

Huang, K. (1963) 'Statistical Mechanics, John Wily & Sons', *New York*.

Jones, R. M. (1998) *Mechanics of composite materials*. CRC press.

Kachanov, L. (1999) 'Rupture Time Under Creep Conditions', *International Journal of Fracture*, 97(8), pp. 11–18. doi: 10.1023/A:1018671022008.

Kaddour, Hinton, Li, *et al.* (2013) 'Recent progress on benchmarking craking and damage models for fibre reinforced polymer composites The third world wide failure excercise', in *THE 19TH INTERNATIONAL CONFERENCE ON COMPOSITE MATERIALS*.

Kaddour, Hinton, Smith, *et al.* (2013) 'The background to the third world-wide failure exercise', *Journal of Composite Materials*, 47(20–21), pp. 2417–2426.

Kaddour *et al.* (2014) 'The world-wide failure exercises: How can composites design and manufacture communities build their strength', in *Proceedings of the 16th European Conference on Composite Materials (ECCM16), Seville, Spain*, pp. 22–26.

Kamiński, M. and Pawlak, A. (2015) 'Various approaches in probabilistic homogenization of the CFRP composites', *Composite Structures*, 133, pp. 425–437. doi:

https://doi.org/10.1016/j.compstruct.2015.07.090.

Kanit, T. *et al.* (2003) 'Determination of the size of the representative volume element for random composites: statistical and numerical approach', *International Journal of solids and structures*, 40(13), pp. 3647–3679.

Khisaeva, Z. F. and Ostoja-Starzewski, M. (2006) 'On the size of RVE in finite elasticity of random composites', *Journal of elasticity*, 85(2), pp. 153–173.

Kim, J. K. (2000) 'Recent developments in impact damage assessment of fibre composites', *Impact behaviour of fibre-reinforced composite materials and structures*, pp. 33–74.

Krajcinovic, D. and Fonseka, G. U. (1981) 'The continuous damage theory of brittle materials', *J. appl. Mech*, 48(4), pp. 809–824.

Krajcinovic, D. and Silva, M. A. G. (1982) 'Statistical aspects of the continuous damage theory', *International Journal of Solids and Structures*, 18(7), pp. 551–562. doi: 10.1016/0020-7683(82)90039-7.

Lemaitre, J. (1985) 'A Continuous Damage Mechanics Model for Ductile Fracture', *Journal of Engineering Materials and Technology*, 107(January 1985), pp. 83–89. doi: 10.1115/1.3225775.

Lempriere, B. M. (1968) 'Poisson's ratio in orthotropic materials.', *AIAA Journal*, 6(11), pp. 2226–2227. doi: 10.2514/3.4974.

Li, S., Singh, C. V. and Talreja, R. (2009) 'A representative volume element based on translational symmetries for FE analysis of cracked laminates with two arrays of cracks', *International Journal of Solids and Structures*, 46(7–8), pp. 1793–1804. doi: 10.1016/j.ijsolstr.2009.01.009.

Lin, J. I. (2004) 'DYNA3D: A Nonlinear, Explicit, Three-Dimensional Finite Element Code for Solid and Structural Mechanics; User Manual'.

LSTC (2014) 'LS-Dyna Keyword User's Manual; Volume II Material Models: (R 7.1 edition)'. Livermore Software Technology Corporation.

Lubarda, V. and Chen, M. (2009) 'On the elastic moduli and compliances of transversely isotropic and orthotropic materials', *Journal of Mechanics of Materials and Structures*, 3(1), pp. 153–171. doi: 10.2140/jomms.2008.3.153.

Maimí, P. *et al.* (2007a) 'A continuum damage model for composite laminates: Part I–Constitutive model', *Mechanics of Materials*, 39(10), pp. 897–908.

Maimí, P. *et al.* (2007b) 'A continuum damage model for composite laminates: Part II–Computational implementation and validation', *Mechanics of Materials*, 39(10), pp. 909–919.

Malvern, L. E. (1969) *Introduction to the Mechanics of a Continuous Medium*.

Marsh, S. P. (1980) *LASL shock Hugoniot data*. Univ of California Press.

Mase, G. T. and Mase, G. E. (1999) 'Continuum mechanics for engineers, Boca Raton-London-New York-Washington D. C'. CRC Press.

Matzenmiller, A., Lubliner, J. and Taylor, R. L. (1995) 'A constitutive model for anisotropic damage in fiber-composites', *Mechanics of materials*, 20(2), pp. 125–152.

Mehrabadi, M. M. and Cowin, S. C. (1990) 'Eigentensors of Linear Anisotropic Elastic Materials', *The Quarterly Journal of Mechanics and Applied Mathematics*, 43(1), pp. 15–41. doi: 10.1093/qjmam/43.1.15.

Meyers, M. A. (1994) *Dynamic behavior of materials*. John wiley & sons.

Millett, J. C. F. *et al.* (2007) 'The effect of orientation on the shock response of a carbon fibre–epoxy composite', *Composites Science and Technology*, 67(15–16), pp. 3253–3260.

Millett, J. C. F., Bourne, N. K. and Barnes, N. R. (2002) 'The behavior of an epoxy resin under one-dimensional shock loading', *Journal of applied physics*, 92(11), pp. 6590–6594.

Millett, J. C. F., Meziere, Y. J. E. and Bourne, N. K. (2007) 'The response to shock loading of a glass-fibre–epoxy composite: effects of fibre orientation to the loading axis', *Journal of Physics D: Applied Physics*, 40(17), p. 5358.

Munson, D. E. and May, R. P. (1972) 'Dynamically Determined High-Pressure Compressibilities of Three Epoxy Resin Systems', *Journal of Applied Physics*, 43(3), pp. 962–971.

Murakami, S. (1987) 'Progress of continuum damage mechanics', *JSME international journal*, 30(263), pp. 701–710.

Murakami, S. (2012) *Continuum damage mechanics: a continuum mechanics approach to the analysis of*

damage and fracture. Springer Science & Business Media.

Nye, J. F. (1985) *Physical properties of crystals: their representation by tensors and matrices*. Oxford university press.

Onat, E. T. and Leckie, F. A. (1988) 'Representation of mechanical behavior in the presence of changing internal structure', *Journal of Applied Mechanics*, 55(1), pp. 1–10.

Orifici, A. C., Herszberg, I. and Thomson, R. S. (2008) 'Review of methodologies for composite material modelling incorporating failure', *Composite structures*, 86(1–3), pp. 194–210.

Orlowski, M. (2014) *Experimental and Numerical Investigation on the Bird Impact Resistance of Novel Composite Sandwich Panels*. Cranfield University.

Ostoja-Starzewski, M. (2002) 'Microstructural randomness versus representative volume element in thermomechanics', *Journal of Applied Mechanics*, 69(1), pp. 25–35.

Pinho, S. T., Iannucci, L. and Robinson, P. (2006a) 'Physically based failure models and criteria for laminated fibre-reinforced composites with emphasis on fibre kinking. Part I: Development', *Composites Part A: Applied Science and Manufacturing*, 37(1), pp. 63–73.

Pinho, S. T., Iannucci, L. and Robinson, P. (2006b) 'Physically based failure models and criteria for laminated fibre-reinforced composites with emphasis on fibre kinking. Part II: FE implementation', *Composites Part A: Applied Science and Manufacturing*, 37(5), pp. 766–777.

Puck, A. and Schürmann, H. (1998) 'Failure analysis of FRP laminates by means of physically based phenomenological models', *Composites Science and Technology*, 58(7), pp. 1045–1067.

Puck, A. and Schürmann, H. (2002) 'Failure analysis of FRP laminates by means of physically based phenomenological models', *Composites Science and Technology*, 62(12), pp. 1633–1662.

Rabotnov, Y. N. (1969) 'Creep rupture', in *Applied mechanics*. Springer, pp. 342–349.

Reid, S. R. and Zhou, G. (2000) *Impact behaviour of fibre-reinforced composite materials and structures*. Elsevier.

Riedel, W., Nahme, H. and Thoma, K. (2004) 'Equation of state properties of modern composite materials: modeling shock, release and spallation', in *AIP Conference Proceedings*. AIP, pp. 701–706.

Rosenberg, Z., Yaziv, D. and Partom, Y. (1980) 'Calibration of foil-like manganin gauges in planar shock wave experiments', *Journal of Applied Physics*, 51(7), pp. 3702–3705.

Ruoff, A. L. (1967) 'Linear Shock-Velocity-Particle-Velocity Relationship', *Journal of Applied Physics*, 38(13), pp. 4976–4980.

Rychlewski, J. (1984) 'On Hooke's law', *Journal of Applied Mathematics and Mechanics*, 48(3), pp. 303–314. doi: 10.1016/0021-8928(84)90137-0.

Schreyer, H. L. (1995) 'Continuum Damage Based on Elastic Projection Operators', *International journal of damage mechanics*, 4(2), pp. 171–195.

Schreyer, H. L. and Zuo, Q. H. (1995) 'Anisotropic yield surfaces based on elastic projection operators', *Trans. ASME: J. Appl. Mech.*, 62(September), pp. 780–785. doi: 10.1115/1.2897014.

Schweizerhof, K. *et al.* (1998) 'Crashworthiness analysis with enhanced composite material models in LS-DYNA-Merits and Limits', in *LS-DYNA World Conference, Detroit, MI*.

Soden, P. D., Kaddour, A. S. and Hinton, M. J. (2004) 'Recommendations for designers and researchers resulting from the world-wide failure exercise', *Composites Science and Technology*, 64(3), pp. 589–604.

Steinberg, D. J. (1996) 'Equation of State and Strength Properties of Selected Materials'. Lawrence Livermore National Laboratory.

Talreja, R. and Singh, C. V. (2012) *Damage and failure of composite materials*. Cambridge University Press.

Thomson, W. (1857) 'I. Elements of a mathematical theory of elasticity', *Proceedings of the Royal Society of London*, (8), pp. 85–87.

Trias, D. *et al.* (2006) 'Random models versus periodic models for fibre reinforced composites', *Computational materials science*, 38(2), pp. 316–324.

Tsai, S. W. and Melo, J. D. D. (2014) 'An invariant-based theory of composites', *Composites Science and Technology*, 100, pp. 237–243.

Tsai, S. W. and Wu, E. M. (1971) 'A general theory of strength for anisotropic materials', *Journal of composite materials*, 5(1), pp. 58–80.

Vakulenko, A. A. and Kachanov, M. (1971) 'Continuum theory of medium with cracks', *Mekhanika tverdogo tela*, 4, pp. 159–166.

Vignjevic, R. *et al.* (2008) 'Modeling shock waves in orthotropic elastic materials', *Journal of Applied Physics*, 104(4). doi: 10.1063/1.2970160.

Vignjevic, R. and Djordjevic, N. (2010) 'Modelling of High Velocity Impact on Carbon Fibre Composite Materials', *Scientific Technical Review*, 60(3–4), pp. 3–8.

Vignjevic, R., Djordjevic, N. and de Vuyst, T. A. I. (2012) 'PROGRESSIVE DAMAGE IN WOVEN CFRPP IN PRESENCE OF SHOCK WAVES'.

Walrath, D. E. and Adams, D. F. (1983) 'The Iosipescu shear test as applied to composite materials', *Experimental mechanics*, 23(1), pp. 105–110.

Wu, E. and Tsai, C.-Z. (2000) 'Impact behaviour and analysis of CFRP laminated plates', in Reid, S. R. and Zhou, G. (eds) *Impact behaviour of fibre-reinforced composite materials and structures*. Woodhead Publishing Ltd. Cambridge, p. 212.

Yamada, S. E. and Sun, C. T. (1978) 'Analysis of laminate strength and its distribution', *Journal of Composite Materials*, 12(3), pp. 275–284.

Zhang, J. *et al.* (2016) 'A micromechanics-based degradation model for composite progressive damage analysis', *Journal of Composite Materials*, 50(16), pp. 2271–2287.

Zhao, L. *et al.* (2018) 'A novel material degradation model for unidirectional CFRP composites', *Composites Part B: Engineering*, 135, pp. 84–94.

Appendix A Failure criteria in composite models in LS-Dyna

MAT_022:

Failure criteria:

$$F_M^T = \left(\frac{\sigma_2}{Y_T}\right)^2 + \frac{\left(\frac{\sigma_6^2}{2G_{12}}\right) + \frac{3}{4}\alpha\sigma_6^4}{\left(\frac{S_{12}^2}{2G_{12}}\right) + \frac{3}{4}\alpha S_{12}^4} > 1$$

$$F_M^C = \left(\frac{\sigma_2}{2S_{12}}\right)^2 + \left[\left(\frac{Y_C}{2S_{12}}\right)^2 - 1\right]\frac{\sigma_2}{Y_C} + \frac{\left(\frac{\sigma_6^2}{2G_{12}}\right) + \frac{3}{4}\alpha\sigma_6^4}{\left(\frac{S_{12}^2}{2G_{12}}\right) + \frac{3}{4}\alpha S_{12}^4} > 1$$

$$F_F = \left(\frac{\sigma_1}{X_T}\right)^2 + \frac{\left(\frac{\sigma_6^2}{2G_{12}}\right) + \frac{3}{4}\alpha\sigma_6^4}{\left(\frac{S_{12}^2}{2G_{12}}\right) + \frac{3}{4}\alpha S_{12}^4} > 1$$

MAT_054:

Failure criteria:

$$F_f^t = \left(\frac{\sigma_1}{X_t}\right)^2 + \beta\left(\frac{\sigma_6}{S_6}\right) - 1 \geq 0$$

$$F_f^c = \left(\frac{\sigma_2}{X_c}\right)^2 - 1 \geq 0$$

$$F_m^t = \left(\frac{\sigma_2}{Y_t}\right)^2 + \left(\frac{\sigma_6}{S_{12}}\right)^2 - 1 \geq 0$$

$$F_m^c = \left(\frac{\sigma_2}{2S_{12}}\right)^2 + \left[\left(\frac{Y_c}{2S_{12}}\right)^2 - 1\right]\frac{\sigma_2}{Y_c} + \left(\frac{\sigma_6}{S_{12}}\right)^2 - 1 \geq 0$$

MAT_055:

Failure criteria:

$$F_f^t = \left(\frac{\sigma_1}{X_t}\right)^2 + \beta\left(\frac{\sigma_6}{S_6}\right) - 1 \geq 0$$

$$F_f^c = \left(\frac{\sigma_2}{X_c}\right)^2 - 1 \geq 0$$

$$F_m = \left(\frac{\sigma_2}{Y_c Y_t}\right)^2 + \frac{(Y_c - Y_t)\sigma_2}{Y_c Y_t} + \left(\frac{\sigma_6}{S_{12}}\right)^2 - 1 \geq 0$$

MAT_059:

Failure criteria:

$$F = \frac{4\left(\sigma_1 - \frac{X_t - X_c}{2}\right)^2}{(X_t + X_c)^2} + \frac{4\left(\sigma_2 - \frac{Y_t - Y_c}{2}\right)^2}{(Y_t + Y_c)^2} + \frac{\sigma_4^2}{S_c^2} + \frac{\sigma_5^2}{S_c^2} + \frac{\sigma_6^2}{S_c^2} - 1 \geq 0$$

MAT_261:

Failure criteria:

$$F_f^t = \left(\frac{\sigma_1}{X_t}\right)^2 \geq 1$$

$$F_f^c = \begin{cases} \left(\frac{\tau_T}{S_T - \mu_T \sigma_n}\right)^2 + \left(\frac{\tau_L}{S_L - \mu_L \sigma_n}\right)^2 \geq 1 & \sigma_{b^m} \leq 0 \\ \left(\frac{\sigma_n}{Y_T}\right)^2 + \left(\frac{\tau_T}{S_T}\right)^2 + \left(\frac{\tau_L}{S_L}\right)^2 \geq 1 & \sigma_{b^m} > 0 \end{cases}$$

$$F_m^t = \left(\frac{\sigma_n}{Y_T}\right)^2 + \left(\frac{\tau_T}{S_T}\right)^2 + \left(\frac{\tau_L}{S_L}\right)^2 \geq 1 \qquad \sigma_n \geq 0$$

$$F_m^c = \left(\frac{\tau_T}{S_T - \mu_T \sigma_n}\right)^2 + \left(\frac{\tau_L}{S_L - \mu_L \sigma_n}\right)^2 \geq 1 \qquad \sigma_n < 0$$

MAT_261 – variables:

$$S_T = \frac{Y_c}{2\tan(\phi_0)}$$

$$\mu_T = -\frac{1}{\tan(2\phi_0)}$$

$$\mu_L = S_L \frac{\mu_T}{S_T}$$

$$\sigma_n = \frac{\sigma_{2^m} + \sigma_{3^\psi}}{2} + \frac{\sigma_{2^m} - \sigma_{3^\psi}}{2}\cos(2\phi) + \tau_{2^m 3^\psi}\sin(2\phi)$$

$$\tau_T = -\frac{\sigma_{2^m} - \sigma_{3^\psi}}{2}\sin(2\phi) + \tau_{2^m 3^\psi}\cos(2\phi)$$

$$\tau_L = \tau_{1^m 2^m}\cos(\phi) + \tau_{3^\psi 1^m}\sin(\phi)$$

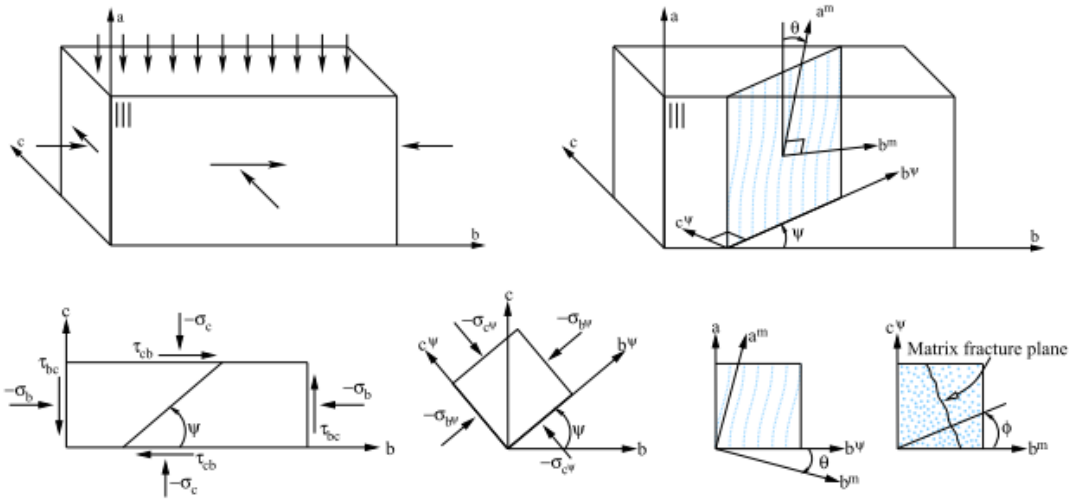

MAT_262:

Failure criteria:

$$F_f^t = \left(\frac{\sigma_1 - \nu_{12}\sigma_2}{X_t} \right)^2 \geq 1$$

$$F_f^c = \frac{\left\langle \left| \sigma_6^m \right| + \mu_L \sigma_2^m \right\rangle}{S_L} \geq 1$$

$$F_m^c = \left(\frac{\tau_T}{S_T} \right)^2 + \left(\frac{\tau_L}{S_L} \right)^2 \geq 1 \qquad \sigma_2 < 0$$

$$F_m^t = \begin{cases} \sqrt{(1-g)\frac{\sigma_2}{Y_T} + g\left(\frac{\sigma_2}{Y_T} \right)^2 + \left(\frac{\sigma_6}{S_L} \right)^2} \geq 1 & \sigma_2 \geq 0 \\ \frac{\left\langle \left| \sigma_6 \right| + \mu_L \sigma_2 \right\rangle}{S_L} \geq 1 & \sigma_2 < 0 \end{cases}$$

MAT_262 – variables:

$$\mu_L = -\frac{S_L \cos(2\phi_0)}{Y_C \cos^2(2\phi_0)}$$

$$\mu_T = -\frac{1}{\tan(2\phi_0)}$$

$$\varphi^c = \arctan\left(\frac{1 - \sqrt{1 - 4\left(\frac{S_L}{X_c} + \mu_L \right)\frac{S_L}{X_c}}}{2\left(\frac{S_L}{X_c} + \mu_L \right)} \right)$$

$$\sigma_2^m = \sigma_1 \sin^2(\varphi^c) + \sigma_2 \cos^2(\varphi^c) - 2|\sigma_6| \sin(\varphi^c)\cos(\varphi^c)$$

$$\sigma_6^m = (\sigma_2 - \sigma_1)\sin(\varphi^c)\cos(\varphi^c) + |\sigma_6|\left(\cos^2(\varphi^c) - \sin^2(\varphi^c)\right)$$

$$S_T = Y_C \cos(\phi_0)\left[\sin(\phi_0) + \frac{\cos(\phi_0)}{\tan(2\phi_0)} \right]$$

$$\theta = \arctan\left(\frac{-|\sigma_6|}{\sigma_2 \sin(\phi_0)} \right)$$

$$\tau_T = \left\langle -\sigma_2 \cos(\phi_0)\left[\sin(\phi_0) - \mu_T \cos(\phi_0)\cos(\theta) \right] \right\rangle$$

$$\tau_L = \left\langle \cos(\phi_0)\left[|\sigma_6| + \mu_L \sigma_2 \cos(\phi_0)\sin(\theta) \right] \right\rangle$$

Appendix B Derivation of Gruneisen Equation of State

The Mie – Gruneisen EOS was derived from principal physics laws with use of quantum and statistical mechanics concepts. It necessitates understanding of the micromechanics of material especially its resistance to an externally applied force or pressure.

An average distance between atoms in a material is governed by the balance of long range attractive and short range repulsive forces. Therefore, atoms are experiencing potential energy as shown in Figure A1. Due to material's temperature, the atoms are not staying simply in the minimum energy but they are vibrating around their equilibrium position (Meyers, 1994).

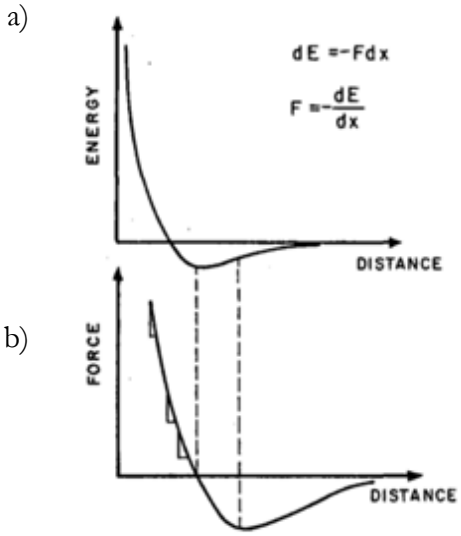

Figure A1 a) Energy vs Distance, b) Force vs Distance (Meyers, 1994)

Thus, at the microscopic scale the atoms in a material can be represented as oscillators that vibrate in three dimensions. According to the quantum theory, the oscillator has discrete energy levels, which have energies equal to:

$$u_i = ih\upsilon + \tfrac{1}{2}h\upsilon\,, \qquad \text{A.1}$$

where h is Planck constant ($h \approx 6.626*10^{-34} m^2 kgs^{-1}$), i denotes the energy level, and υ is a vibration frequency. The total vibrational energy of a material is given by a sum of the oscillators' vibrational energies:

$$\tilde{u} = \sum_{j=1}^{3N} \bar{u}_j \,, \qquad \text{A.2}$$

where N is a number of oscillators and $\bar{u}_j$ is a mean vibrational energy of an oscillator. The energies are summed over $3N$ because each atom has three degrees of freedom that define the three components of the vibrational energy each related to one of the dimensions.

The mean energy of an oscillator $\bar{u}_j$ can be calculated using the quantum statistics. The relative probability of finding an oscillator in the i-th energy level depends on temperature and is given by (Meyers, 1994):

$$p_i = g_i e^{-u_i/k\theta}, \qquad \text{A.3}$$

where g_i is degeneracy, k is the Boltzmann's and θ is absolute temperature (in K).

The absolute probability is the relative probability divided by the sum of the probabilities of the whole system given as:

$$P_i = \frac{g_i e^{-u_i/k\theta}}{\sum_j g_j e^{-u_j/k\theta}} \,. \qquad \text{A.4}$$

As in any kind of material there are numerous atoms, using the above probability distribution allows to calculate relevant properties. Thus, the mean vibrational energy can be expressed as:

$$\tilde{u} = \sum_i P_i u_i = \frac{\sum_i u_i g_i e^{-u_i/k\theta}}{\sum_j g_j e^{-u_j/k\theta}} = -\frac{d}{d\left(1/k\theta\right)} \log\left(\sum_i g_i e^{-u_i/k\theta} \right) = -\frac{d}{d\left(1/k\theta\right)} \log\left(f \right), \qquad \text{A.5}$$

where partition function f is introduced for convenience:

$$f = \sum_i g_i e^{-u_i/k\theta} \,. \qquad \text{A.6}$$

The energy levels are not degenerate in this case, as the energy level univocally defines the state of the oscillator, so $g_i = 1$.

After substitution of Equation A.1A. to Equation A.5 and summing for all the energy levels i, the partition function becomes:

$$f = e^{-\frac{1}{2}h\upsilon/k\theta}\sum_{i=0}^{\infty}e^{-ih\upsilon/k\theta} = e^{-\frac{1}{2}h\upsilon/k\theta}\sum_{n=0}^{\infty}\left(e^{-h\upsilon/k\theta}\right)^{i} = e^{-\frac{1}{2}h\upsilon/k\theta}\left(1+e^{-h\upsilon/k\theta}+\left(e^{-h\upsilon/k\theta}\right)^{2}+...\right) \qquad \textbf{A.7}$$

This forms a geometric series with a scale factor equal to $e^{-\frac{1}{2}h\upsilon/k\theta}$ (related to the ground state's energy) and the common ratio being $e^{-h\upsilon/k\theta}$. The sum of such a geometric series is easily found as:

$$f = e^{-\frac{1}{2}h\upsilon/k\theta}\sum_{i=0}^{\infty}\left(e^{-h\upsilon/kT}\right)^{i} = e^{-\frac{1}{2}h\upsilon/k\theta}\lim_{i\to\infty}\frac{1-\left(e^{-h\upsilon/k\theta}\right)^{i}}{1-e^{-h\upsilon/k\theta}}. \qquad \textbf{A.8}$$

Knowing that:

$$\lim_{i\to\infty}\left(e^{-h\upsilon/k\theta}\right)^{i} = 0. \qquad \textbf{B.9}$$

The partition function simplifies further to:

$$f = \frac{e^{-\frac{1}{2}h\upsilon/k\theta}}{1-e^{-h\upsilon/k\theta}}. \qquad \textbf{A.10}$$

Therefore, the mean vibrational energy of an oscillator is:

$$\bar{u} = -\frac{d}{d\left(1/k\theta\right)}\ln\left(f\right) = \frac{d}{d\left(1/k\theta\right)}\left[\left(\tfrac{1}{2}h\upsilon/k\theta\right)\ln\left(1-e^{-h\upsilon/k\theta}\right)\right] = \qquad \textbf{A.11}$$

$$= \tfrac{1}{2}h\upsilon + \frac{h\upsilon e^{-h\upsilon/k\theta}}{1-e^{-h\upsilon/k\theta}} = \tfrac{1}{2}h\upsilon + \frac{h\upsilon}{e^{h\upsilon/k\theta}-1}.$$

The total vibration energy of a system of oscillators is:

$$\tilde{u} = \sum_{j=1}^{3N}\bar{u} = \sum_{j=1}^{3N}\left(\frac{h\upsilon}{e^{h\upsilon/k\theta}-1}+\tfrac{1}{2}h\upsilon\right). \qquad \textbf{A.12}$$

The total energy comprises the potential energy and vibration energy. It is therefore given by:

$$u = \phi + \sum_{j=1}^{3N}\left[\frac{1}{2}h\upsilon_{j}+\frac{h\upsilon_{j}}{e^{h\upsilon_{j}/k\theta}-1}\right]. \qquad \textbf{A.13}$$

Knowing that entropy of the system can be expressed as (Huang, 1963):

$$\begin{aligned} s &= -k\sum P^i \ln P^i = -k\sum P^i \ln \frac{e^{-u_i/k\theta}}{f} = -k\sum P^i \left(\ln\left(e^{-u_i/k\theta}\right) - \ln f\right) = \\ &= -k\sum P^i \left(-u_i / k\theta - \ln f\right) = \frac{1}{\theta}\sum P^i u_i + k\ln f \sum P^i = \\ &= \frac{1}{\theta}\bar{u} + k\ln f. \end{aligned} \qquad \text{A.14}$$

By multiplying both sides of Equation A.14 by temperature and rearranging it the following relation is obtained:

$$-k\theta \ln f = \bar{u} - \theta s. \qquad \text{A.15}$$

Note that it gives the Helmholtz free energy. To define the Helmholtz free energy for a system of oscillators, each having three vibration directions Equation A.14 needs to be summed as follows (adding a potential energy ϕ):

$$\begin{aligned} \Psi &= \phi - \sum_{j=0}^{3N} k\theta \ln f = \phi - k\theta \sum_{j=0}^{3N} \ln \frac{e^{-\frac{1}{2}h\upsilon_j/k\theta}}{1-e^{-h\upsilon_j/k\theta}} = \\ &= \phi - k\theta \sum_{j=0}^{3N} \ln e^{-\frac{1}{2}h\upsilon_j/k\theta} + k\theta \sum_{j=0}^{3N} \ln\left(1-e^{-h\upsilon_j/k\theta}\right) = . \\ &= \phi + \sum_{j=0}^{3N} \tfrac{1}{2} h\upsilon_j + k\theta \sum_{j=0}^{3N} \ln\left(1-e^{-h\upsilon_j/k\theta}\right) \end{aligned} \qquad \text{A.16}$$

Derivative of Helmholtz free energy with respect to volume (at constant temperature) is, by definition, negative pressure:

$$p = -\left(\frac{\partial \Psi}{\partial V}\right)_\theta = -\frac{d\phi}{dV} - \frac{d\sum_{j=1}^{3N} \frac{1}{2} h\upsilon_j}{dV} - \frac{d\left(k\theta \sum_{j=1}^{3N} \ln\left(1-e^{-h\upsilon_j/k\theta}\right)\right)}{dV}. \qquad \text{A.17}$$

At this point one can introduce the Gruneisen constant γ_j being:

$$\gamma_j = -\frac{V}{\upsilon_j}\left(\frac{\partial \upsilon_j}{\partial V}\right)_\theta = -\left(\frac{\partial \ln \upsilon_j}{\partial \ln V}\right)_\theta. \qquad \text{A.18}$$

And use it in the following expressions:

$$\frac{d\sum_{j=1}^{3N}\frac{1}{2}h\upsilon_j}{dV}=\sum_{j=1}^{3N}\frac{1}{2}\frac{d\left(h\upsilon_j\right)}{dV}=\frac{1}{V}\sum_{j=1}^{3N}\frac{1}{2}h\upsilon_j\frac{V}{\nu_j}\frac{d\upsilon_j}{dV}=-\frac{1}{V}\sum_{j=1}^{3N}\frac{1}{2}\gamma_j h\upsilon_j\,,$$

$$\frac{d\left(k\theta\sum_{j=1}^{3N}\ln\left(1-e^{-h\upsilon_j/k\theta}\right)\right)}{dV}=k\theta\sum_{j=1}^{3N}\frac{d\ln\left(1-e^{-h\upsilon_j/k\theta}\right)}{dV}= \qquad \textbf{A.19}$$

$$=k\theta\sum_{j=1}^{3N}\frac{d\left(1-e^{-h\upsilon_j/kT}\right)}{dV}\frac{d\ln\left(1-e^{-h\upsilon_j/kT}\right)}{d\left(1-e^{-h\upsilon_j/kT}\right)}=k\theta\sum_{j=1}^{3N}\frac{d\left(1-e^{-h\upsilon_j/k\theta}\right)}{dV}\frac{1}{1-e^{-h\upsilon_j/k\theta}}=$$

$$=k\theta\sum_{j=1}^{3N}\frac{-e^{-h\upsilon_j/k\theta}}{1-e^{-h\upsilon_j/k\theta}}\frac{d\left(-h\upsilon_j/k\theta\right)}{dV}=\frac{1}{V}\sum_{j=1}^{3N}\frac{h\upsilon_j}{e^{h\upsilon_j/k\theta}-1}\frac{V}{\upsilon_j}\frac{d\upsilon_j}{dV}=-\frac{1}{V}\sum_{j=1}^{3N}\gamma_j\frac{h\upsilon_j}{e^{h\upsilon_j/k\theta}-1}.$$

Finally, substituting Equations A.19 to A.17, pressure is obtained as:

$$p=-\left(\frac{\partial\Psi}{\partial V}\right)_\theta=-\frac{d\phi}{dV}+\frac{1}{V}\sum_{j=1}^{3N}\gamma_j\left(\frac{1}{2}h\upsilon_j+\frac{h\upsilon_j}{e^{h\upsilon_j/k\theta}-1}\right)=-\frac{\partial\phi}{\partial V}+\frac{\gamma}{V}\tilde{u}_{vib}\,, \qquad \textbf{A.20}$$

where $\tilde{u}_{vib}$ stands for vibrational energy including the ground state.

Assuming that all oscillators have the same vibrational frequency, γ_j becomes γ - the Gruneisen constant defined as:

$$\gamma=-\frac{V}{\upsilon}\left(\frac{\partial\upsilon}{\partial V}\right)_\theta=-\left(\frac{\partial\ln\upsilon}{\partial\ln V}\right)_\theta. \qquad \textbf{A.21}$$

Pressure in the material for 0K can be calculated by Equation A.22 as:

$$p_{0K}=-\frac{\partial\phi}{\partial V}+\frac{\gamma}{V}u_{0K}\,. \qquad \textbf{A.22}$$

Subtracting Equation A.22 from Equation A.20 yields:

$$p-p_{0K}=\frac{\gamma}{V}\left(u-u_{0K}\right), \qquad \textbf{A.23}$$

which is the Gruneisen equation of state.

One can also use other reference state. The often used reference state is the state on the Hugoniot curve that is established experimentally. It gives pressure p_H and corresponding energy u_H of a material. The relation is expressed as:

$$p - p_H = \frac{\gamma}{V}\left(u - u_H\right). \qquad \textbf{A.24}$$

The most universal formula is the incremental form of pressure (Equation A.25). It simply relates the change in pressure to the change in energy at any reference point.

$$dp = \frac{\gamma}{V} du_{vib} \qquad \textbf{A.25}$$

The Gruneisen constant can be written in a form that allows it to be linked with the macroscopic material properties as:

$$\gamma = V\left(\frac{\partial p}{\partial u}\right)_V = V\left(\frac{\partial p}{\partial \theta}\right)_V \left(\frac{\partial \theta}{\partial u}\right)_V = \frac{V}{c_v}\left(\frac{\partial p}{\partial \theta}\right)_V = -\frac{V}{c_v}\left(\frac{\partial p}{\partial V}\right)_\theta \left(\frac{\partial V}{\partial \theta}\right)_p \qquad \textbf{A.26}$$

And $\left(\partial u / \partial \theta\right)_V$ is the heat capacity at constant volume $\left(c_v\right)$, $\left(1/V\right)\left(\partial V / \partial \theta\right)_p$ is volumetric thermal expansion and $-\left(V\right)\left(\partial p / \partial V\right)_\theta$ is isothermal bulk modulus $\left(K\right)$. Note that for isotropic materials volumetric thermal expansion is equal to $3\alpha_\theta$ where α_θ is longitudinal thermal expansion coefficient. Finally, the Gruneisen constant for isotropic materials is related to these material properties by:

$$\frac{\gamma}{V} = \frac{3\alpha_\theta K}{c_v} \qquad \textbf{A.27}$$

Appendix C Material data used in mesoscale models

Table A.1 Undamaged matrix properties

Matrix			
E	Young's modulus	4668	MPa
ν	Poisson's ratio	0.400	MPa

Table A.2 Undamaged fibre properties

Fibres			
E_x	Young's modulus, x-direction	$2.654 \cdot 10^5$	MPa
E_y	Young's modulus, y-direction	$1.298 \cdot 10^4$	MPa
E_z	Young's modulus, z-direction	$1.298 \cdot 10^4$	MPa
ν_{yz}	Poisson's ratio, yx-plane	0.0126	-
ν_{zx}	Poisson's ratio, zx-plane	0.0126	-
ν_{xy}	Poisson's ratio, yz-plane	0.2060	-
G_{yz}	Shear modulus, yz-plane	$5.380 \cdot 10^3$	MPa
G_{zx}	Shear modulus, zx-plane	$1.550 \cdot 10^4$	MPa
G_{xy}	Shear modulus, xy-plane	$1.550 \cdot 10^4$	MPa

Table A.3 Broken fibre layer properties used for broken fibre and combined damage mesoscale model

Broken fibres layer			
x	Damage factor	1, 4, 10, 40, 100, 400, 1000, 10000	
E_x	Young's modulus, x-direction	$2.654 \cdot 10^5$/x	MPa
E_y	Young's modulus, y-direction	$1.298 \cdot 10^4$/x	MPa
E_z	Young's modulus, z-direction	$1.298 \cdot 10^4$/x	MPa
ν_{yz}	Poisson's ratio, yx-plane	0.0126	-
ν_{zx}	Poisson's ratio, zx-plane	0.0126	-
ν_{xy}	Poisson's ratio, yz-plane	0.2060	-

G_{yz}	Shear modulus, yz-plane	$5.380 \cdot 10^3/x$	MPa
G_{zx}	Shear modulus, zx-plane	$1.550 \cdot 10^4/x$	MPa
G_{xy}	Shear modulus, xy-plane	$1.550 \cdot 10^4/x$	MPa

Table A.4 Damaged matrix properties used for uniform matrix damage, fibre-matrix debonding and combined damage mesoscale models

Matrix			
x	Damage factor	1, 4, 10, 40, 100, 400, 1000, 10000	
E	Young's modulus	4668/x	MPa
ν	Poisson's ratio	0.400/x	MPa

Appendix D Integration of damage variable

To describe damage behaviour of the proposed material model determination of damage variables is vital. Following theoretical considerations in Section 6.1 damage variable rate was related to the strain rate (Equation 6.1.24). However, the equation requires integration which is presented in this appendix. Integration consists of purely mathematical operations with no additional assumptions, thus it was not seen as important part of the thesis main body. Nevertheless, it is presented here for completeness.

The integration starts with Equation 6.1.24 (repeated below for convenience):

$$\frac{1}{\left(1-d^i\right)}\dot{d}^i = \frac{2\lambda_0^i \boldsymbol{\varepsilon}^i}{\kappa^i + \lambda_0^i \bar{\boldsymbol{\varepsilon}}^{i2}}\dot{\boldsymbol{\varepsilon}}^i \qquad \textbf{A.28}$$

In this form damage variable and its time derivative are at the left side of the equation and strain and its time derivative are at the right side. If equation is rewritten as:

$$\frac{1}{\left(1-d^i\right)}\frac{dd^i}{dt} = \frac{2\lambda_0^i \boldsymbol{\varepsilon}^i}{\kappa^i + \lambda_0^i \bar{\boldsymbol{\varepsilon}}^{i2}}\frac{d\boldsymbol{\varepsilon}^i}{dt} \qquad \textbf{A.29}$$

one can observe that the equation can be integrated as:

$$\int \frac{1}{\left(1-d^i\right)} dd^i = \int \frac{2\lambda_0^i \boldsymbol{\varepsilon}^i}{\kappa^i + \lambda_0^i \bar{\boldsymbol{\varepsilon}}^{i2}} d\boldsymbol{\varepsilon}^i \qquad \textbf{A.30}$$

It results in the following steps:

$$-\ln\left(1-d^i\right) = \ln\left(\kappa^i + \lambda_0^i \bar{\boldsymbol{\varepsilon}}^{i2}\right) + c_0$$

$$e^{-\ln\left(1-d^i\right)} = e^{\ln\left(\kappa^i + \lambda_0^i \bar{\boldsymbol{\varepsilon}}^{i2}\right)+c_0}$$

$$\frac{1}{\left(1-d^i\right)} = \left(\kappa^i + \lambda_0^i \bar{\boldsymbol{\varepsilon}}^{i2}\right)e^{c_0} = \left(\kappa^i + \lambda_0^i \bar{\boldsymbol{\varepsilon}}^{i2}\right)c \qquad \textbf{A.31}$$

$$d^i = 1 - \frac{1}{\left(\kappa^i + \lambda_0^i \bar{\boldsymbol{\varepsilon}}^{i2}\right)c}$$

Finally, recalling that damage potential must be equal to zero (for damage evolution):

$$ {}^{n+1}\Phi^{i} = \left(1 - {}^{n+1}d^{i}\right)\lambda_0^{i}\,{}^{n+1}\bar{\boldsymbol{\varepsilon}}^{i2} - \left(\kappa^{i}\,{}^{n+1}d^{i} + \omega_0^{i}\right) = 0 \qquad \textbf{A.32} $$

integration constant can be obtained as:

$$ c = \frac{1}{\omega_0^{i} + \kappa^{i}} \qquad \textbf{A.33} $$

Appendix E Woven material properties

Table A.5 Woven material properties

	Stiffness		
E_x	Young's modulus, x-direction	10.0	GPa
E_y	Young's modulus, y-direction	68.5	GPa
E_z	Young's modulus, z-direction	68.5	GPa
ν_{yz}	Poisson's ratio, yx-plane	0.0390	-
ν_{zx}	Poisson's ratio, zx-plane	0.0301	-
ν_{xy}	Poisson's ratio, yz-plane	0.0044	-
G_{yz}	Shear modulus, yz-plane	3.00	GPa
G_{zx}	Shear modulus, zx-plane	4.98	GPa
G_{xy}	Shear modulus, xy-plane	4.98	GPa
	Strength		
X_t	Tensile strength in x-direction	2690.0	MPa
X_c	Compressive strength in x-direction	1580.0	MPa
Y_t	Tensile strength in y-direction	81.4	MPa
Y_c	Compressive strength in y-direction	158.0	MPa
Z_t	Tensile strength in z-direction	87.2	MPa
Z_c	Compressive strength in z-direction	158.0	MPa
S_{yz}	Shear strength in fibre plane	125.0	MPa
S_{zx}	Out of plane shear strength	79.3	MPa
S_{xy}	Out of plane shear strength	79.3	MPa